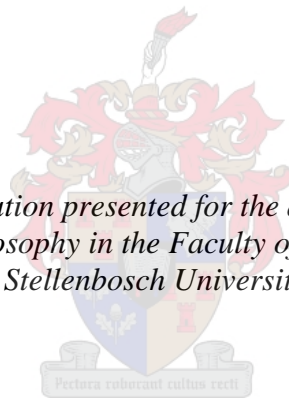


**Laser Powder Bed Fusion-Centred Approach to Enable Local Drug Delivery from a  
Cementless Hip Stem**

by  
Martin Botha Bezuidenhout

*Dissertation presented for the degree of  
Doctor of Philosophy in the Faculty of Engineering at  
Stellenbosch University*



Supervisor: Professor Oliver Frank Rudolf August Damm  
Co-supervisor: Professor Natasha Sacks  
Co-supervisor: Professor Leon Milner Theodore Dicks

March 2021

## **Declaration**

By submitting this dissertation electronically, I declare that the entirety of the work contained therein is my own, original work, that I am the sole author thereof (save to the extent explicitly otherwise stated), that reproduction and publication thereof by Stellenbosch University will not infringe any third party rights and that I have not previously in its entirety or in part submitted it for obtaining any qualification.

Date: 28 February 2021

Copyright ©2021 Stellenbosch University

All rights reserved

---

## Abstract

Periprosthetic joint infection (PJI) resulting from colonisation of implant surfaces by pathogenic bacteria and subsequent biofilm formation is a devastating complication following total hip arthroplasty. It significantly reduces a patient's quality of life and, in severe cases, can result in amputation or mortality. Treatment of PJI is associated with a substantial burden on healthcare and economic resources. The importance of research towards innovations in PJI prevention and treatment is emphasised.

Local delivery of antimicrobial drugs is an effective approach to prevent and treat PJI as it enables high local drug concentrations while avoiding systemic side effects. Current practice is considered sub-optimal and appreciable research exists on the improvement of local drug delivery strategies. For cementless hip stems the focus tends to be on coatings and conditioning of the external implant surface. A significant research gap exists between external and internal drug delivery strategies where 'internal' refers to the incorporation of reservoir structures within the implant. Therefore, a prototype strategy utilising the internal volume of a cementless stem for a reservoir from which an antimicrobial drug can be delivered directly to the implant surface was investigated. The challenge of fabricating a cementless hip stem with intricate internal geometries can be effectively addressed through metal additive manufacturing (MAM).

Industry is steadily incorporating MAM into process chains as the main production technology for the fabrication of high-value functional components. Laser powder bed fusion (LPBF) was applied in this study as MAM technology to fabricate a Ti6Al4V ELI demonstrator cementless hip stem with local drug delivery functionality. This required an interdisciplinary approach, for which a problem solving framework has been synthesised to aid in process chain development from an LPBF-centred perspective.

The overall problem was decomposed into integrated partial and single problems which were systematically investigated through literature study and experimentation. An LPBF-centred solution was developed for the direct integration of permeable structures in a dense part using an in-process assembly method. Different levels of porosity were induced into permeable thin walls according to a systematically identified window for ranges of the process parameters, laser power and scanning speed. This resulted in tailorable release profiles for the model antibiotic vancomycin from an aqueous formulation. Released vancomycin retained its antibiotic efficacy against *Staphylococcus aureus* Xen 36 (methicillin sensitive) and *Staphylococcus aureus* Xen 31 (methicillin resistant), representing two of the most frequent pathogens in PJI.

---

Solutions for single problems were recomposed for integrated solutions to partial problems, and subsequently for an overall prototype solution. The overall solution cementless hip stem prototype effectively prevented surface colonisation by *Staphylococcus aureus* Xen 31, confirming the efficacy of the developed local drug delivery strategy. These results were used to inductively refine the LPBF-centred interdisciplinary problem solving framework.

The original contribution of the research corresponds to the experimentation and framework development phases respectively. This involves the systematic investigation of LPBF to enable local drug delivery and an LPBF-centred approach for interdisciplinary problem solving. Lastly, it contributes to the advancement of LPBF by demonstrating the application efficacy of the prototype solution.

---

## Opsomming

Periprostetiese gewrigsinfeksie (PJI) as 'n gevolg van implantaatoppervlak kolonisasie deur patogeniese bakterieë en biofilm formasie is 'n ernstige komplikasie na totale heupartroplastiek. Dit verlaag 'n pasiënt se lewenskwaliteit merkwaardig en kan in ernstige gevalle lei tot amputasie of sterfte. Behandeling van PJI word geassosieer met 'n substansiële las op gesondheids- en ekonomiese middele. Die belangrikheid van navorsing vir innovasies in PJI voorkoming en behandeling word benadruk.

Lokale toediening van antimikrobiese medikamente is 'n effektiewe benadering om PJI te voorkom en te behandel deurdat hoë lokale antimikrobiese konsentrasies gehandhaaf kan word sonder sistemiese newe-effekte. Huidige praktyk word beskou as suboptimaal en veel navorsing bestaan vir die verbetering van lokale toedieningsstrategieë. Vir ongesementeerde heupstamme is die fokus op bedekkings en kondisionering van die eksterne implantaatoppervlak. 'n Beduidende gaping bestaan tussen eksterne en interne lokale toedieningsstrategieë waar 'intern' verwys na die inkorporasie van reservoirstrukture binne die implantaat. Daarom was 'n prototipestrategie vir die benutting van die interne volume van 'n ongesementeerde heupstam vir 'n reservoir waar vanuit medikamente direk na die implantaatoppervlak toegedien kan word ondersoek. Die uitdaging om 'n ongesementeerde heupstam met ingewikkelde interne geometrieë te vervaardig kan effektief aangespreek word deur metaal toevoegingsvervaardiging (MAM).

Industrie is stelselmatig besig om MAM in proseskettings te inkorporeer as die hoof produksietegnologie vir die vervaardiging van hoë-waarde funksionele komponente. Laser poeierbed fusie (LPBF) is toegepas in hierdie studie as MAM-tegnologie om 'n Ti6Al4V ELI demonstrasie ongesementeerde heupstam met lokale medikament toedieningsfunksie te vervaardig. Dit het 'n interdisiplinêre benadering vereis waarvoor 'n probleemoplossingsraamwerk gesintetiseer was om die proseskettingontwikkeling vanuit 'n LPBF-gesentreerde perspektief te ondersteun.

Die algehele probleem was opgebreek in geïntegreerde deel- en enkelprobleme wat sistematies ondersoek was deur literatuur studie en eksperimentasie. 'n LPBF-gesentreerde oplossing was ontwikkel vir die direkte integrasie van poreuse strukture in 'n digte part met 'n in-proses monteermethode. Verskeie vlakke van porositeit was geïnduseer in deurlaatbare dun wande volgens 'n stelselmatige geïdentifiseerde venster vir waardes vir die prosesparameters laser sterkte en skandeer spoed. Dit het geresulteer in aanpasbare vrystellingsprofile vir die modelantibiotika vankomisien vanuit 'n wateroplossing. Vrygestelde vankomisien het antibiotiese effektiwiteit behou teen *Staphylococcus aureus* Xen 36 (metisillien sensitief)

---

en *Staphylococcus aureus* Xen 31 (metisillien weerstandig), verteenwoordigend van twee van die mees frekwente patogene in PJI.

Oplossings vir enkelprobleme was geherkombineer tot geïntegreerde oplossings vir deelprobleme, en gevolglik vir 'n algehele prototipe-oplossing. Die algehele oplossing ongesementeerde heupstam prototipe het oppervlakkolonisasie deur *Staphylococcus aureus* Xen 31 effektief verhoed wat die funksionaliteit van die ontwikkelde lokale medikament toedieningsstrategie bevestig. Die resultate was inductief gebruik om die LPBF-gesentreerde interdisiplinêre probleemoplossingsraamwerk te verfyn.

Die oorspronklike bydrae van die navorsing korrespondeer respektiewelik tot die eksperimentele- en raamwerkontwikkelingsfases. Dit betrek die sistematiese ondersoek van LPBF om lokale medikamenttoediening te bewerkstellig en 'n LPBF-gesentreerde raamwerk vir interdisiplinêre probleemoplossing. Laastens dra dit by tot die bevordering van LPBF deur die toepassingseffektiwiteit van die prototipe-oplossing te demonstreer.

---

## Acknowledgements

The Fraunhofer Institute for Machine Tools and Forming Technology (IWU) for funding the majority of the work on which the dissertation is based. I am grateful for the opportunity to have been part of such an international project and especially would like to thank Mr C. Rotsch, Mr M. Oettel, and Mr T. Töppel for the insightful and inspirational collaboration.

Prof O.F.R.A. Damm: for stepping in as the main supervisor near the end of the study, thereby enabling its completion. I am grateful for the insights, critical discussion of results, and guidance towards writing and revision of the dissertation.

Prof N. Sacks: for adopting the project as co-supervisor and securing additional funding. The constructive feedback and discussions were invaluable for revision and finalisation of the dissertation.

Prof L.M.T. Dicks: for enthusiastically supporting the project, availability of his laboratory, and continual motivation through his effective guidance, insights and creativity.

Ms E. Booyen: for her openness to share expertise and selfless dedication to the collaborative environment established for the execution of the work.

To Dr J. Joubert: for kindly donating a commercial cementless stem.

To the staff of the Industrial Engineering Department and the Stellenbosch Technology Centre at Stellenbosch University: for providing support and being accommodating with access to the required resources during challenging times.

To the staff of the Central Analytical Facilities at Stellenbosch University: for valuable insights and creative approaches towards customising analysis procedures.

To my colleagues, Mr P. Hugo, Mr D. Hagedorn-Hansen, and Mr G. Ter Haar for their scientific and technical support, advice, critical discussions, friendship, and many coffees.

To Dr E.H.A. Uheida, whose advice I hold in high regard. I am grateful for your engagement in critical discussions of the results, mentorship in both research and life, and honest friendship.

My family: for their love and support of immeasurable value, especially during the final stages of the dissertation. Your efforts are greatly appreciated and I shall always carry it with me.

To my friends for their support, especially Mr Ian van Vuuren who does not yield in the forge.

My late supervisor Prof D.M. Dimitrov: without whom the PhD would not have been possible. Prof's vision, dedication to progress and development of new ideas, encouraging character, and ironclad commitment to duty have left a lasting impression on me.

*In memory of Professor Dimiter Marinov Dimitrov*

## Table of Contents

<b>Declaration</b>	<b>ii</b>
<b>Abstract</b>	<b>iii</b>
<b>Opsomming</b>	<b>v</b>
<b>Acknowledgements</b>	<b>vii</b>
<b>1. Introduction</b>	<b>1</b>
1.1 Background	1
1.1.1 Total Hip Arthroplasty Overview	1
1.1.2 Periprosthetic Joint Infection	2
1.1.3 Metal Additive Manufacturing-based Process Chains for Medical Implants	4
1.2 Problem Statement	5
1.3 Research Objectives	6
1.4 Research Approach	7
1.5 Limits and Exclusions	8
1.6 Scientific Contribution of the Research	9
1.7 Document Roadmap	10
<b>2. Strategy to Apply LPBF for Local Drug Delivery: Literature Study</b>	<b>12</b>
2.1 Infection in Total Hip Arthroplasty	12
2.1.1 Costs and Burden of Infection	13
2.1.2 Microbial Infection	15
2.1.3 Treatment Procedures	19
2.2 Local Drug Delivery	21
2.2.1 Clinically Applied Local Antimicrobial Delivery for Cementless Hip Stems	21
2.2.2 Investigated Local Antimicrobial Delivery Strategies for Cementless Implants	23
2.2.3 Opportunity for Novel Prophylactic Strategy	26
2.3 Laser Powder Bed Fusion (LPBF)	27
2.3.1 Overview of LPBF Process Chain	28
2.3.2 Overview of the LPBF Building Process	33
2.3.3 LPBF of Ti6Al4V ELI	37

<i>Table of Contents</i>	x
2.3.4 Influence of Selected Process Parameters	42
2.3.5 Post Processing Considerations	47
2.3.6 Design Constraints	47
2.4 Frameworks for Deriving an LPBF-Centred Interdisciplinary Approach	48
2.5 Conclusion	61
<b>3. High-Level LPBF-Centred Interdisciplinary Framework</b>	<b>63</b>
3.1 Positioning of Framework Application within Product Life Cycle Phases	63
3.2 High-Level Framework	64
3.3 Project Problem Breakdown Structure	71
<b>4. Sustained Release Vancomycin Drug Formulation</b>	<b>72</b>
4.1 Gaining Insight for Formulation Material Selection	72
4.1.1 Sustained Vancomycin Release Formulation	72
4.1.2 Gaining Insight into PLGA Erosion and Drug Release	76
4.2 Vancomycin Encapsulated Nanoparticles Preparation and Release Testing	88
4.3 Conclusion	91
<b>5. Inducing Porosity in LPBF for Drug Release</b>	<b>92</b>
5.1 LPBF Machine and Material	92
5.2 Influence of Key Parameters - Experimental Setup and Design	94
5.2.1 Process Parameter Variation	94
5.2.2 Relative Porosity Measurement	95
5.3 Influence of Key Parameters - Results and Discussion	95
5.4 Permeable Thin Walls for Vancomycin Release Screening	109
5.4.1 Fabrication of Thin Wall Specimens	109
5.4.2 Experimental Setup and Design	110
5.4.3 Experimental Results	111
5.5 Conclusion	112
<b>6. Tailored Drug Release with LPBF-Produced PTWs – Experimental Setup and Design</b>	<b>113</b>
6.1 PTWs	113
6.1.1 Part Fabrication	114

<i>Table of Contents</i>	xi
6.1.2 Part Inspection	115
6.1.2.1 Water Contact Angle	115
6.1.2.2 Surface Roughness	118
6.1.2.3 Relative Porosity	118
6.1.3 Antimicrobial Efficacy	120
6.1.3.1 Vancomycin Release through PTWs	120
6.1.3.2 Activity of Released Vancomycin	121
6.2 Integrated Reservoir Specimens	121
6.2.1 Part Fabrication	122
6.2.2 Antimicrobial Efficacy	123
6.2.2.1 Vancomycin Release from Integrated Reservoirs	123
6.2.2.2 <i>S. aureus</i> Xen 36 Colonisation Prevention Potential	125
<b>7. Tailored Drug Release with LPBF-Produced PTWs – Results and Discussion</b>	<b>126</b>
7.1 PTWs	126
7.1.1 Fabricated PTWs Part Inspection	126
7.1.1.1 Water contact angle	127
7.1.1.2 Relative Porosity	130
7.1.2 Vancomycin Release Testing	136
7.1.3 Activity of Released Vancomycin	144
7.2 Integrated Reservoir Specimens	145
7.2.1 Fabricated Integrated Reservoir Specimens	145
7.2.2 Vancomycin Release Testing	145
7.2.3 Colonisation Prevention Potential	152
7.3 Conclusion	152
<b>8. Implant Internal Structure Functionalisation</b>	<b>155</b>
8.1 Internal Channel Layout Design	155
8.1.1 Implant Bulk Geometry and ZOI parameters	156
8.1.2 Placement of Channel Openings	157
8.1.3 Internal Channel Generation	158
8.1.4 Static Stress Analysis Simulation	161
8.2 Implant Prototype Manufacture	165

<i>Table of Contents</i>	xii
8.2.1 First Iteration Prototype Fabrication	165
8.2.2 Post Processing	168
8.2.3 Part Inspection	168
8.3 Antimicrobial Testing of Prototype	169
8.3.1 Experimental Setup and Design	169
8.3.2 Results	171
8.4 Conclusion	172
<b>9. Framework Update and Implementation</b>	<b>174</b>
9.1 Updated Interdisciplinary Problem Solving Framework	174
9.2 Framework Implementation Summary	176
<b>10. Conclusion and Future Research</b>	<b>184</b>
<b>11. References</b>	<b>187</b>
<b>Appendix A: Supplementary Information to Chapter 1</b>	<b>225</b>
<b>Appendix B: Vancomycin Encapsulation Biodegradable Polymers</b>	<b>227</b>
<b>Appendix C: LPBF-Induced Porosity Screening</b>	<b>237</b>
<b>Appendix D: PTWs for Vancomycin Release</b>	<b>250</b>
<b>Appendix F: Prototype Design and Manufacturing</b>	<b>256</b>

## List of Figures

FIGURE 1-1: REVISION THA RECORDED IN THE NORWEGIAN ARTHROPLASTY REGISTER FOR THE PERIOD 2005 TO 2017 (ADAPTED FROM FURNES ET AL., 2018).....	2
FIGURE 1-2: PROJECTED NUMBER OF IMPLANTS MANUFACTURED WITH MAM TO THE YEAR 2026 (ADAPTED FROM PARK, 2018) .....	4
FIGURE 1-3: ROADMAP OF DOCUMENT.....	11
FIGURE 2-1: REPORTED COSTS FOR TREATMENT OF PJI AS REPORTED BY (A) KAPADIA ET AL. (2016) (B) AKINDOLIRE ET AL. (2020) AND (C) KLOUCHE ET AL. (2010).....	14
FIGURE 2-2: SIMPLIFIED SCHEMATIC REPRESENTATION OF BIOFILM FORMATION, (ADAPTED FROM ARCIOLA ET AL., 2012; OTTO, 2013; BRESKO ET AL., 2017).....	17
FIGURE 2-3: SCANNING ELECTRON MICROSCOPY IMAGES OF AN <i>S. AUREUS</i> BIOFILM ON Ti6Al7Nb DISCS AFTER 7 DAYS OF INCUBATION (POST ET AL., 2017) .....	18
FIGURE 2-4: IMPLANT FUNCTIONALISATION STRATEGIES FOR DRUG DELIVERY.....	26
FIGURE 2-5: SIMPLIFIED SCHEMATIC REPRESENTATION OF THE LPBF PROCESS INSIDE THE BUILD CHAMBER....	28
FIGURE 2-6: BASIC LPBF HIGH LEVEL PROCESS CHAIN (ADAPTED FROM HUGO ET AL., 2018).....	29
FIGURE 2-7: SOLID CAD MODEL ON THE LEFT WITH STL APPROXIMATION FORMAT ON THE RIGHT (IN-HOUSE EXAMPLE) .....	30
FIGURE 2-8: DEFECTS ON Ti6Al4V ELI PARTS FABRICATED BY LPBF WITH (A) EXCESSIVE OXIDATION, (B) CRACKING, (C) DELAMINATION, (D) DISTORTION (HAGEDORN-HANSEN ET AL., 2017), (E) FAILED FEATURES (IN-HOUSE EXAMPLES) .....	32
FIGURE 2-9: MAIN PROCESSES AND FACTORS INFLUENCING THE LPBF PROCESS AND PART PERFORMANCE (ADAPTED FROM SPIERINGS ET AL., 2016) .....	34
FIGURE 2-10: SCHEMATIC REPRESENTATION OF SCANNING AND MELTING THE COATED POWDER LAYER WITH A GAUSSIAN LASER BEAM WITH (A) SCAN TRACK LONGITUDINAL VIEW AND (B) SCAN TRACK CROSS SECTIONAL VIEW (ADAPTED FROM SOLA & NOURI, 2019; WESSELS ET AL., 2019; ZHENG ET AL., 2019) .....	36
FIGURE 2-11: TITANIUM PHASES WITH (A) $\alpha$ PHASE IN HCP UNIT CELL ARRANGEMENT, (B) $\beta$ PHASE IN BCC UNIT CELL ARRANGEMENT, AND (C) POSITIONING OF $\alpha+\beta$ Ti6Al4V ON A PSEUDOINARY PHASE DIAGRAM WITH REGARDS TO THE $\beta$ STABILISING ELEMENT CONCENTRATION (ADAPTED FROM DONACHIE, 2000; LÜTJERING & WILLIAMS, 2007).....	38
FIGURE 2-12: AS-BUILT MICROSTRUCTURE OF LPBF PRODUCED Ti6Al4V WITH (A) TOP VIEW (PERPENDICULAR TO BUILD DIRECTION) AND (B) SIDE VIEW (PARALLEL TO BUILD DIRECTION) (ADAPTED FROM ZHOU ET AL., 2018).....	39
FIGURE 2-13: EXAMPLE DEFECTS (A) POROSITY FROM ENTRAPPED GAS, (B) LACK OF FUSION, AND (C) SURFACE ROUGHNESS (ALI ET AL., 2018; WYCISK ET AL., 2014; FOUSSOVA ET AL., 2018).....	41

FIGURE 2-14: SUMMARY OF LPBF PROCESS PARAMETERS (RECREATED FROM ABOULKHAIR ET AL., 2014) .....	43
FIGURE 2-15: GRAPHIC REPRESENTATION OF POROSITY AS A FUNCTION OF LASER POWER AND SCANNING SPEED AT CONSTANT HATCH SPACING OF 0.1 MM, LAYER THICKNESS OF 0.03 MM, AND LASER SPOT SIZE OF 0.1 MM (ADAPTED FROM MIERZEJEWSKA, 2019) .....	44
FIGURE 2-16: SINGLE SCAN TRACKS PRODUCED AT 400 W LASER POWER AND 200 $\mu$ M LAYER THICKNESS Ti6Al4V WITH (A) SUFFICIENT ENERGY INPUT (TOP TO BOTTOM SCANNING SPEEDS OF 40, 60, AND 80 $\text{MM.S}^{-1}$ ) AND (B) INSUFFICIENT ENERGY INPUT (TOP TO BOTTOM SCANNING SPEEDS OF 160, 180, AND 200 $\text{MM.S}^{-1}$ ) (ADAPTED FROM SHI ET AL., 2016) .....	45
FIGURE 2-17: CLASSIFICATION OF DFAM APPROACH ACCORDING TO KUMKE ET AL. (2016) (RECREATED).....	48
FIGURE 2-18: IPPD WITH (A) THE GENERIC METHODOLOGY AND (B) THE HIERARCHICAL TRADE-OFF ASSESSMENT PROCESS FLOW, (RECREATED FROM SCHRAGE, 1999).....	50
FIGURE 2-19: IPPD WITH AM POTENTIALS AND FACTORS TO ACHIEVE THEM (ZAMAN ET AL., 2018).....	51
FIGURE 2-20: INTEGRATED DESIGN ORIENTED FRAMEWORK FOR RESOURCE SELECTION IN AM (ZAMAN ET AL., 2018) .....	52
FIGURE 2-21: INTEGRATED AM PRODUCT DEVELOPMENT FRAMEWORK WITH FOCUS ON POST PROCESSING AND QUALITY MANAGEMENT (KASPAR ET AL., 2019) .....	53
FIGURE 2-22: OVERVIEW OF IPPE FRAMEWORK (STOFFELS ET AL., 2018) .....	55
FIGURE 2-23: INTEGRATED DESIGN ORIENTED FRAMEWORK FOR RESOURCE SELECTION IN AM (RECREATED FROM KREHMER ET AL., 2009) .....	56
FIGURE 2-24: GENERAL STRUCTURE OF LEVEL BASED MECPro <sup>2</sup> MODEL FRAMEWORK (RECREATED FROM EIGNER ET AL., 2016) .....	57
FIGURE 2-25: DWAM MODEL FOR CONCEPTUAL AND EMBODIMENT DESIGN PHASES (RECREATED FROM LAVERNE ET AL., 2017) .....	59
FIGURE 2-26: DBAM FRAMEWORK FOR ENHANCING INNOVATION (RECREATED FROM SEGONDS, 2018) .....	60
FIGURE 3-1: POSITIONING OF FRAMEWORK (INDICATED WITH DASHED LINE) WITHIN PLC PHASES, (ADAPTED FROM CHEN ET AL., 2009; ALI ET AL., 2019) .....	63
FIGURE 3-2: HIGH LEVEL OVERALL INTERDISCIPLINARY PROBLEM SOLVING FRAMEWORK.....	65
FIGURE 3-3: HIGH-LEVEL INTERDISCIPLINARY FRAMEWORK FOR DEVELOPING AN INTEGRATED LPBF PROCESS CHAIN FOR DRUG DELIVERY .....	67
FIGURE 3-4: SYSTEMATIC PROCEDURE FOR INTEGRATIVE DECOMPOSITION AND RECOMPOSITION OF PROBLEMS AND SOLUTIONS.....	68
FIGURE 3-5: INTERACTION OF INTEGRATED KNOWLEDGE PACKAGES WITH DIVERGENT AND CONVERGENT PROCESSES DURING PROBLEM DECOMPOSITION AND RECOMPOSITION .....	69
FIGURE 3-6: PROBLEM BREAKDOWN STRUCTURE .....	71
FIGURE 4-1: VANCOMYCIN MOLECULE 2D REPRESENTATION .....	72

FIGURE 4-2: BIODEGRADABLE POLYMERS FOR DRUG DELIVERY (RECREATED FROM PRAJAPATI ET AL., 2015) .....	73
FIGURE 4-3: PLGA ENCAPSULATED VANCOMYCIN MICROPARTICULATE FORMULATIONS WITH (A) SHOWING BURST RELEASE (PLGA 50:50, 33,000 DA) (HSU ET AL., 2018) AND (B) SHOWING SUSTAINED RELEASE WITH A SUPPRESSED BURST RELEASE (PLGA 75:25, 30,000) (WANG ET AL., 2011)) .....	75
FIGURE 4-4: NUMBER OF RELEVANT PUBLICATIONS OF BIODEGRADABLE POLYMERS FROM SCOPUS SEARCH....	76
FIGURE 4-5: PLGA STRUCTURE (RECREATED FROM MAKADIA & SIEGEL, 2011) .....	76
FIGURE 4-6: HYDROLYSIS OF PLGA (RECREATED FROM MAKADIA & SIEGEL, 2011) .....	77
FIGURE 4-7: 2D COMPUTATIONAL GRID FOR SIMULATION OF PLGA BULK EROSION AND DRUG RELEASE .....	78
FIGURE 4-8: SCHEMATIC OF COMMUNICATION BETWEEN MATRICES.....	79
FIGURE 4-9: OUTPUT MATRIX OF THE STARTING POLYMER MATRIX.....	80
FIGURE 4-10: PIXEL MATRICES REPRESENTING (A) POLYMER STATE AT INITIATION OF PROGRAM AND (B) POLYMER STATE AFTER PROGRAM EXECUTION.....	81
FIGURE 4-11: SIMULATED DRUG DISTRIBUTION (A) AT THE START OF THE PROGRAM AND (B) AT THE END OF THE PROGRAM .....	81
FIGURE 4-12: DEGRADATION AND EROSION PROFILES OF (A) SIMULATION PROGRAM, (B) FROM THE SIMULATION OF GÖPFERICH (1997), AND (C) EXPERIMENTALLY OBTAINED MASS LOSS PROFILE FOR RESOMER RG 502H (TRIANGLES), RESOMER RG 504H (SQUARES), AND RESOMER RG 502 (CIRCLES) (GÖPFERICH, 1997).....	82
FIGURE 4-13: DEGRADATION (BLACK) AND EROSION (RED) FROM A SINGLE PROGRAM EXECUTION .....	83
FIGURE 4-14: DRUG RELEASE PROFILE FROM (A) SINGLE PROGRAM EXECUTION, (B) AVERAGE OF THREE EXECUTIONS, (C) MODELLED RELEASE PROFILES IN LITERATURE (KEY INDICATES LACTIC ACID TO GLYCOLIC ACID RATIO) (AMANN ET AL., 2010), (D) CUMULATIVE RELEASE PROFILE OF GANCICLOVIR FROM RESOMER RG 502H IN LITERATURE (DUVVURI & GAURAV JANORIA, 2006).....	85
FIGURE 4-15: AVERAGE DEGRADATION AND EROSION (A), AVERAGE CUMULATIVE FRACTIONAL DRUG RELEASE (B) FOR A DRUG PROBABILITY OF 0.2, AND AVERAGE DEGRADATION AND EROSION (C) WITH AVERAGE CUMULATIVE FRACTIONAL DRUG RELEASE (D) FOR A DRUG PROBABILITY OF 0.35.....	87
FIGURE 4-16: FE-SEM IMAGE OF VANCOMYCIN ENCAPSULATED PLGA NANOPARTICLES.....	89
FIGURE 4-17: CUSTOM MADE DIFFUSION CELL WITH (A) CAD MODEL (ADAPTED FROM BOOYSEN ET AL., 2019), (B) ASSEMBLED CELL, AND (C) DIFFUSION CELLS IN RELEASE TESTING WITH MAGNETIC STIRRING AT 600 RPM.....	90
FIGURE 4-18: VANCOMYCIN RELEASE PROFILE FROM PLGA NANOPARTICLES (BOOYSEN ET AL., 2019).....	91
FIGURE 5-1: (A) LPBF MACHINE AND (B) Ti6Al4V ELI POWDER .....	92
FIGURE 5-2: DEFAULT ISLAND SCANNING STRATEGY WITH (A) A LAYER BEING EXPOSED INSIDE THE BUILDING CHAMBER, (B) A SCHEMATIC OF THE ISLANDS AND FILL VECTOR DIRECTIONS, AND (C) A SCHEMATIC OF THE PATTERN SHIFT BETWEEN SUBSEQUENT LAYERS .....	93

FIGURE 5-3: CYLINDRICAL SPECIMENS FOR POROSITY MEASUREMENT .....	95
FIGURE 5-4: POROSITY FROM $\mu$ CT ANALYSES FOR (A) RUN 1, (B) RUN 7, AND (C) RUN 4.....	97
FIGURE 5-5: SCATTER PLOT OF THE RELATION OF RELATIVE POROSITY TO THE INPUT VED .....	100
FIGURE 5-6: ESTIMATED EFFECTIVE VED AT SCAN TRACK APEX.....	100
FIGURE 5-7: DIAGNOSTIC PLOTS FOR (A-B) RAW DATA AND (C-D) TRANSFORMED DATA.....	102
FIGURE 5-8: TWO FACTOR INTERACTION PLOTS WITH HIGH AND LOW VARIATIONS FOR THIRD FACTOR WITH (A-B) LASER POWER AND SCANNING SPEED, (C-D) LASER POWER AND HATCH SPACING, AND (E-F) SCANNING SPEED AND HATCH SPACING .....	106
FIGURE 5-9: DETECTED LASER EXPOSURE ISSUE ON MACHINE WITH REGARDS TO POSITIONING OF SCAN VECTORS WITH (A) THE ENTIRE ISLAND VISIBLE, (B) A JUNCTION OF FOUR ISLANDS WITH PERPENDICULARLY ALTERNATING ISLAND FILL VECTOR DIRECTIONS, (C) MEASUREMENTS SHOWING THE POSITIONING TO BE DOUBLE THE HATCH SPACING, AND (D) SCHEMATIC DESCRIBING THE OBSERVATIONS OF THE PHENOMENON .....	107
FIGURE 5-10: 3D RECONSTRUCTIONS FOR RUN1 WITH TOP (LEFT) REVEALING EXPOSURE IRREGULARITY AND BOTTOM (RIGHT) REVEALING CORRECT LASER POSITIONING.....	108
FIGURE 5-11: CUSTOM 3D-PRINTED DIFFUSION WELLS FOR VANCOMYCIN RELEASE SCREENING OF PARAMETER SET 6.....	110
FIGURE 5-12: VANCOMYCIN DIFFUSION SCREENING ACROSS LPBF Ti6Al4V ELI THIN WALLS .....	111
FIGURE 5-13: QUALITATIVE REPRESENTATION OF BLUE DYE DIFFUSION THROUGH PTWS.....	112
FIGURE 6-1: PTW EXPERIMENTAL STUDY ROADMAP.....	113
FIGURE 6-2: PTW AND SUPPORT FRAME SHOWING INTERFERENCE OF GEOMETRIES.....	114
FIGURE 6-3: STATIC WATER CONTACT ANGLE MEASUREMENT EXPERIMENTAL SETUP WITH (A) THE PHYSICAL CONFIGURATION, AND (B) IMAGE EXAMPLE.....	116
FIGURE 6-4: CONTACT ANGLE MEASUREMENT PROCEDURE USING <i>IMAGE J</i> AND <i>CONTACT ANGLE</i> PLUGIN SHOWING (A) THE IMAGE ADJUSTMENT AND POINTS SELECTION AND (B) THE BEST FIT OUTPUT .....	117
FIGURE 6-5: SPECIFICATION OF 5 MM X 5 MM X 0.1 MM VOI WITH (A) 2D VIEW IN X-Z PLANE, (B) 2D VIEW IN X-Y PLANE, AND (C) 3D VOI VIEW.....	119
FIGURE 6-6: PHOTOGRAPHS OF PTWS ASSEMBLED IN ABS CUSTOM MADE DIFFUSION WELLS (A) SHOWING THE BUFFER SIDE OF THE PTW AND (B) SHOWING THE RESERVOIR SIDE OF THE PTW.....	120
FIGURE 6-7: INTEGRATED RESERVOIR SPECIMENS STUDY LAYOUT .....	122
FIGURE 6-8: EXAMPLES OF INTEGRATED RESERVOIR SPECIMEN DESIGN VARIATIONS WITH (A) 2 MM HOLE AND 0.4 MM PTW, (B) 5 MM HOLE AND 0.95 MM PTW, (C) 8 MM HOLE AND 1.5 MM PTW, AND (D) FABRICATED SPECIMEN WITH 5 MM HOLE AND 0.95 MM PTW.....	122
FIGURE 6-9: PHOTOGRAPHIC REPRESENTATION OF EXPERIMENTAL SETUP FOR VANCOMYCIN RELEASE FROM INTEGRATED RESERVOIR SPECIMENS .....	124
FIGURE 7-1: AS-BUILT PTWS WITHIN SUPPORT FRAME ON BUILD PLATE.....	126

FIGURE 7-2: STATIC WATER CONTACT ANGLES ON REFERENCE AND 400 $\mu\text{M}$ PTW SPECIMENS .....	127
FIGURE 7-3: IMAGE FRAMES FOR CREATION OF A TIME SERIES OF WATER DROPLET IMBIBED INTO 950 $\mu\text{M}$ THICK PERMEABLE WALL FABRICATED WITH PS-10 .....	128
FIGURE 7-4: SCHEMATIC OF MODELS FOR WETTING WITH (A) THE YOUNG MODEL, (B) THE WENZEL MODEL, AND (C) THE CASSIE-BAXTER MODEL (HAN ET AL., 2019) .....	129
FIGURE 7-5: RELATIVE POROSITIES WITH FE-SEM IMAGES OF THE FRONT SURFACES FOR 400 $\mu\text{M}$ PTW SAMPLES IN ORDER OF ASCENDING VED WITH (A) PS-3, (B) PS-10, (C) PS-7, (D) PS-6, (E) PS-9, (F) PS-1, AND (G) PS-5 .....	135
FIGURE 7-6: SCATTER PLOT OF OBTAINED RELATIVE POROSITY FOR DIFFERENT INPUT VED .....	135
FIGURE 7-7: AVERAGE VANCOMYCIN RELEASE PROFILES ACROSS PTWS WITH (A) THE PROCESS PARAMETER SETS WITH LASER POWER OF 40 AND 50 W, AND (B) THE PROCESS PARAMETER SETS WITH LASER POWER OF 70 W. ERROR BARS REPRESENT THE STANDARD DEVIATION ( $N = 3$ ) FOR PS-7 AND THE RANGE ( $N = 2$ ) FOR ALL OTHER PARAMETER SETS. THE VED ( $\text{J}\cdot\text{MM}^{-3}$ ) VALUES ARE INDICATED AT THE END OF THE PROFILES (ADAPTED FROM BEZUIDENHOUT ET AL., 2018).....	137
FIGURE 7-8: EFFECT OF PROCESS PARAMETERS ON VANCOMYCIN RELEASE WITH (A) RESPONSE SURFACE OF TWO FACTOR INTERACTION MODEL AND (B) INTERACTION EFFECTS PLOT (ADAPTED FROM BEZUIDENHOUT ET AL., 2018).....	140
FIGURE 7-9: PAIRWISE COMPARISON ON PREDICTIONS FOR (A) LOW SCANNING SPEED AND LOW LASER POWER AND (B) LOW SCANNING SPEED AND HIGH LASER POWER (ADAPTED FROM BEZUIDENHOUT ET AL., 2018) .....	142
FIGURE 7-10: GRAPHIC REPRESENTATION OF (A) INVESTIGATED VOLUMETRIC ENERGY DENSITY AND 12 H CUMULATIVE RELEASE PERCENTAGE AND (B) RELATIVE POROSITY TO 12 H CUMULATIVE VANCOMYCIN RELEASE PERCENTAGE (ADAPTED FROM BEZUIDENHOUT ET AL., 2018) .....	143
FIGURE 7-11: ACTIVITY AGAINST <i>S. AUREUS</i> XEN 36 OF VANCOMYCIN RELEASED THROUGH PTWS PRODUCED WITH PS-10 FOR DIFFERENT TIME POINTS (0, 5, AND 18 H) AS INDICATED ON THE PETRI DISHES (ADAPTED FROM BEZUIDENHOUT ET AL., 2018) .....	144
FIGURE 7-12: LPBF-PRODUCED INTEGRATED RESERVOIR SPECIMENS (ENCIRCLED) .....	145
FIGURE 7-13: AVERAGE VANCOMYCIN RELEASE PROFILES FROM INTEGRATED RESERVOIR SPECIMENS FOR (A) THE FACTORIAL POINTS (ERROR BARS REPRESENT THE RANGE, $N = 2$ ), (B) THE AXIAL POINTS (ERROR BARS REPRESENT THE RANGE, $N = 2$ ), AND (C) THE CENTRE POINT (ERROR BARS REPRESENT STANDARD DEVIATION, $N = 3$ ). THE HOLE DIAMETER, $\varnothing$ (MM), AND PTW THICKNESS (MM) VALUES ARE INDICATED AT THE END OF THE PROFILES. ....	147
FIGURE 7-14: FIT OF MODEL TO THE AVERAGE EXPERIMENTAL DATA FOR (A) THE FACTORIAL POINTS ( $N = 2$ ), (B) THE AXIAL POINTS ( $N = 2$ ), AND (C) THE CENTRE POINT ( $N = 3$ ) .....	151

FIGURE 7-15: INHIBITION ZONES SHOWING EFFECTIVE PREVENTION OF COLONISATION OF THE SURFACE WHERE THE INTEGRATED PTW IS SITUATED (INDICATED WITH ARROWS) FOR INTEGRATED RESERVOIR SPECIMENS WITH DOE TREATMENT ‘C’ (ADAPTED FROM BEZUIDENHOUT ET AL., 2018) .....	152
FIGURE 8-1: PROTOTYPE MODEL DESIGN AND FABRICATION PROCESS FLOW .....	155
FIGURE 8-2: CHANNEL OPENING PLACEMENT APPROACH WITH (A) FULL HEXAGONAL ARRANGEMENT OVER IMPLANT PROFILE AND (B) STARTING POINT IDENTIFICATION FOR PSEUDO-HEXAGONAL PACKING.....	157
FIGURE 8-3: PSEUDO-HEXAGONAL CIRCLE PACKING WITH (A) PLACEMENT OF CHANNEL OPENINGS ON ANTERIOR SURFACE (B) ON THE MEDIAL AND ANTERIOR SURFACES AND (C) ON THE LATERAL AND ANTERIOR SURFACES .....	158
FIGURE 8-4: INTERNAL CHANNEL LAYOUT WITH (A) ANTERIOR-POSTERIOR VIEW OF CHANNEL FILL VARIANT, (B) REPOINTED SPLINE, (C) SMOOTHED SPLINE WITH ENTRY AND EXIT POINTS, (D) CHANNEL OF CONSTANT 2.5 MM DIAMETER, (E) MEDIAL-LATERAL VIEW.....	159
FIGURE 8-5: INTERNAL CHANNEL GENERATION IN HIP STEM WITH (A) CHANNEL SOLID MODEL AND CUTTER INSERTS AND (B) HIP STEM SOLID MODEL WITH INTERNAL CHANNEL.....	160
FIGURE 8-6: PROTOTYPE HIP STEM STATIC STRESS ANALYSIS SETUP WITH (A) ORIENTATION, LOAD, AND BOUNDARY CONDITIONS OF MODEL AND (B) MESH SETUP IN ANSYS 2020 R2 WITH INSET SHOWING NODES MATCHING AT CONTACT SURFACES.....	162
FIGURE 8-7: SELECTED STATIC STRESS ANALYSIS RESULTS WITH (A) FULL PROTOTYPE MODEL VIEW, (B) VIEW OF MAXIMUM STRESS AREAS, AND (C) TOTAL DEFORMATION APPROXIMATION, AND (D) ZOOMED VIEW OF TOTAL DEFORMATION IN MAX VON MISES EQUIVALENT STRESS AREA.....	165
FIGURE 8-8: IMPLANT PROTOTYPE CAD MODEL WITH OVERSIZED INDIVIDUAL PERMEABLE STRUCTURES AT CHANNEL OPENINGS .....	166
FIGURE 8-9: FIRST ITERATION OF LPBF PROTOTYPE BUILD WITH (A) <i>MAGICS</i> BUILD SETUP AND (B) ACTUAL PARTS.....	167
FIGURE 8-10: FIRST ITERATION PROTOTYPES FOR INSPECTION AND DEMONSTRATION PURPOSES .....	168
FIGURE 8-11: DISTAL PART OF PROTOTYPE BLUE DYE DIFFUSION SCREENING WITH (A) DYE LOADING, (B) STEM IMMERSION, (C) CONTINUED DIFFUSION OF BLUE DYE .....	169
FIGURE 8-12: PHYSICAL SETUP OF VANCOMYCIN SOLUTION LOADING PROCEDURE .....	170
FIGURE 8-13: PHOTOGRAPHS AFTER 24 HOURS INCUBATION OF (A) PROTOTYPE STEM, (B) COMMERCIAL STEM, (C) ENLARGEMENT OF PROTOTYPE STEM, (D) ENLARGEMENT OF COMMERCIAL STEM, (E) SURROUNDING MEDIA OF PROTOTYPE AND COMMERCIAL STEM VISIBLE AFTER STEM REMOVAL.....	172
FIGURE 9-1: UPDATED OVERALL FRAMEWORK .....	175
FIGURE 9-2: COMMUNICATION LINES THAT DEVELOPED BETWEEN SINGLE PROBLEMS DURING EXECUTION OF THE PROJECT.....	176
FIGURE C-1: $\mu$ CT POROSITY ANALYSIS OF CYLINDRICAL SPECIMENS (SECTION 5.3).....	244

---

FIGURE C-2: RESPONSE SURFACES FOR THE QUADRATIC MODEL WITH (A-B) THE LOW LEVEL OF HATCH SPACING AND (C-D) THE HIGH LEVEL OF HATCH SPACING.....	246
FIGURE C-3: DIAGNOSTIC PLOTS FOR QUADRATIC MODEL OF POROSITY.....	248
FIGURE C-4: BCA ASSAY CALIBRATION CURVES FOR A) 0 MIN, B) 15 MIN, C) 30 MIN, D) 45 MIN, AND E) 60 MIN .....	249
FIGURE D-1: : RELATIVE POROSITIES OF 400 $\mu$ M IN ORDER OF ASCENDING VED WITH (A) PS-3, (B) PS-7, (C) PS-7, (D) PS-1, AND (E) PS-5.....	253
FIGURE F-1: STATIC STRESS ANALYSIS SETUP FOR REFERENCE STEM WITH (A) ORIENTATION, LOAD, AND BOUNDARY CONDITIONS AND (B) MESH SETUP IN ANSYS 2020 R2 WITH INSET SHOWING NODES MATCHING AT CONTACT SURFACES.....	256
FIGURE F-2: SIMULATION RESULTS FOR REFERENCE STEM WITH (A) VON MISES EQUIVALENT STRESS DISTRIBUTION AND (B) THE TOTAL DEFORMATION .....	257

## List of Tables

TABLE 2-1: EXAMPLES OF EXTERNAL, INTERNAL, AND POROUS METAL LOCAL ANTIMICROBIAL DELIVERY STRATEGIES IN RESEARCH FOR METALLIC IMPLANTS .....	24
TABLE 2-2: SPECIFIED COMPOSITION OF Ti6Al4V ELI AFTER LPBF PROCESSING (ASTM INTERNATIONAL, 2014) .....	37
TABLE 2-3: SUMMARY OF TENSILE PROPERTIES OF AS-BUILT LPBF Ti6Al4V ELI .....	40
TABLE 2-4: FATIGUE LIFE OF AS-BUILT AND HIPED LPBF PRODUCED SPECIMENS .....	42
TABLE 3-1: SUMMARY OF IDENTIFIED DISCIPLINES, SATELLITE TOPIC, AND REQUIRED KNOWLEDGE AREAS FOR PROCESS INTEGRATED LPBF CENTRED PROCESS CHAIN DEVELOPMENT .....	70
TABLE 4-1: FDA APPROVED BIODEGRADABLE POLYMERS FOR DRUG RELEASE (PRAJAPATI ET AL., 2015; SONG ET AL., 2018) .....	74
TABLE 5-1: CHEMICAL COMPOSITION OF THE Ti6Al4V ELI POWDER (WT%).....	93
TABLE 5-2: SPHERICAL CCD DoE INVESTIGATION OF INFLUENCES OF KEY PARAMETERS ON PART POROSITY .....	94
TABLE 5-3: CORRELATION MATRIX FOR RELATIVE POROSITY INVESTIGATION INPUT FACTORS AND RESPONSES.....	98
TABLE 5-4: ANOVA RESULTS FOR QUADRATIC MODEL OF THE EFFECTS OF LASER POWER, SCANNING SPEED, AND HATCH SPACING ON THE RELATIVE POROSITY .....	102
TABLE 5-5: EQUATION OF THE FITTED QUADRATIC EMPIRICAL MODEL IN TERMS OF CODED AND ACTUAL.....	103
TABLE 5-6: PROCESS PARAMETER SETTINGS FOR INDUCED POROSITY SCREENING .....	109
TABLE 6-1: PARAMETER VARIATION DoE FOR PRODUCTION OF PTWS .....	115
TABLE 6-2: MASS MEASUREMENT OF WATER DROPLET ON PTW .....	117
TABLE 6-3: MOBILE PHASE ELUTION PROTOCOL FOR RP-UHPLC.....	121
TABLE 6-4: DESIGN PARAMETER VARIATION FOR PRODUCTION OF INTEGRATED RESERVOIR SPECIMENS.....	123
TABLE 6-5: MOBILE PHASE ELUTION PROTOCOL FOR RP-HPLC .....	124
TABLE 7-1: SUMMARY OF FABRICATED 400 $\mu$ M PTWS .....	130
TABLE 7-2: CORRELATION MATRIX FOR CUMULATIVE VANCOMYCIN RELEASE AFTER 12 HOURS TO LASER POWER AND SCANNING SPEED .....	138
TABLE 7-3: ANOVA FOR FITTED 2FI MODEL.....	139
TABLE 7-4: EQUATION OF THE FITTED 2FI EMPIRICAL MODEL IN TERMS OF CODED AND ACTUAL .....	139
TABLE 7-5: MODEL PARAMETERS FOR VANCOMYCIN RELEASE PROFILES FROM INTEGRATED RESERVOIR SPECIMENS.....	150
TABLE 8-1: ZOIs REPORTED FOR VANCOMYCIN AS POSITIVE CONTROL AGAINST <i>S. AUREUS</i> STRAINS .....	156
TABLE 8-2: MATERIAL PROPERTIES USED IN THE STATIC STRESS ANALYSIS SIMULATION .....	162
TABLE 8-3: FIRST PROTOTYPE BUILD ITERATION SUPPORT STRUCTURE PARAMETERS .....	167

---

TABLE 9-1: SUMMARY OF OVERALL FRAMEWORK IMPLEMENTATION.....	177
TABLE A-1: COMMERCIALY PRODUCED MAM MEDICAL IMPLANTS (NON-EXHAUSTIVE LIST).....	225
TABLE B-1: SUMMARY OF PUBLICATIONS FOR SUSTAINED VANCOMYCIN DRUG DELIVERY FORMULATIONS....	228

## List of Abbreviations

2FI	Two factor interaction
ABS	Acrylonitrile butadiene styrene
AcN	Acetonitrile
AD	Axiomatic design
AED	Area energy density
ALBC	Antibiotic loaded bone cement
AHP	Analytical hierarchy process
AM	Additive manufacturing
AMK	Additive manufacturing knowledge
ANOVA	Analysis of variance
ASTM	American society for testing and materials
ATCC	American type culture collection
BCA	Bicinchoninic acid
BCC	Body centred cubic
BHI	Brain heart infusion
BSA	Bovine serum albumin
CAD	Computer aided design
CAF	Central analytical facilities
CCD	Central composite design
CIE	Computer integrated environment
CNC	Computer numerical control
cpTi	Commercially pure titanium
CT	Computed tomography
CTAM	Creativity through additive manufacturing
DBAM	Design by additive manufacturing
DFAM	Design for additive manufacturing
DFX	Design for X
DI	Deionised
DMP	Direct metal printing
DMLS	Direct metal laser sintering

---

DoE	Design of experiments
DWAM	Design with additive manufacturing
DWX	Design with X
EBM	Electron beam melting
ECMx	Extracellular matrix
ELI	Extra low interstitial
FCC	Face centred cubic
FDA	Food and drug administration
FDM	Fused deposition modelling
FE-SEM	Field emission scanning electron microscope
HA	Hyaluronic acid
HAp	Hydroxyapatite
HCP	Hexagonal close packed
HIP	Hot isostatic pressing
IKP	Integrated knowledge package
IPPD	Integrated product/process development
IPPE	Integrated product and production engineering
ISO	International organization for standardization
LC-MS	Liquid chromatography – Mass spectrometry
LPBF	Laser powder bed fusion
MAM	Metal additive manufacturing
MCDM	Multi criteria decision making
MIC	Minimum inhibitory concentration
MRSA	Methicillin resistant <i>Staphylococcus aureus</i>
MSSA	Methicillin sensitive <i>Staphylococcus aureus</i>
MSCRAMM	Microbial surface component recognising adhesive matrix molecules
NCTC	National collection of type cultures
NDT	Non-destructive testing
PBF	Powder bed fusion
PBS	Phosphate buffered saline
PCL	Poly( $\epsilon$ -caprolactone)
PDLA	Poly D-lactic acid

---

PGA	Poly(glycolic acid)
PEG	Poly(ethylene glycol)
PELA	Poly(lactide-co-poly(ethylene glycol))
PHBV	Poly(3-hydroxybutyrate-co-3-hydroxyvalerate)
PHV	Poly(3-hydroxyvalerate)
PI	Polydispersity index
PJI	Periprosthetic joint infection
PLA	Poly(lactic acid)
PLC	Product life cycle
PLGA	Poly(lactic-co-glycolic acid)
PLLA	Poly L-lactic acid
PMMA	Poly(methyl methacrylate)
PTW	Permeable thin wall
PVC	Poly(vinyl chloride)
PVDF	Poly(vinylidene fluoride)
QE	Quality engineering
RP-HPLC	Reversed phase high performance liquid chromatography
RP-UHPLC	Reversed phase ultra-high performance liquid chromatography
<i>S. aureus</i>	<i>Staphylococcus aureus</i>
SE	Systems engineering
SEM	Scanning electron microscope
SLM	Selective laser melting
SU	Stellenbosch university
T3DS	Top down decision support
TFA	Trifluoroacetic acid
THA	Total hip arthroplasty
TJA	Total joint arthroplasty
TKA	Total knee arthroplasty
TRIZ	Theory of inventive problem solving
UTS	Ultimate tensile strength
UV	Ultraviolet
VDI	Verein Deutscher Ingenieure

---

VED	Volumetric energy density
VOI	Volume of interest
w-EDM	Wire electrical discharge machining
Xen	Xenogen
ZOI	Zone of inhibition

## Nomenclature

Symbol	Description	Unit
$A$	Area	$\text{cm}^2$
$A_p$	Absorptivity of the powder layer	
$C_A$	Concentration in buffer at time $t$	$\text{mol}/\text{cm}^3$
$C_{Ae}$	Concentration at equilibrium	$\text{mol}/\text{cm}^3$
$C_i$	Measured concentration at previous sampling point	$\mu\text{g}/\text{mL}$
$C_n$	Measured concentration at sampling point $n$	$\mu\text{g}/\text{mL}$
$f$	Area fraction of solid surface in contact with water droplet	
$h$	Hatch spacing	$\text{mm}$
$i$	Matrix index of element in x-direction (column)	
$j$	Matrix index of element in y-direction (row)	
$M_b$	Total mass of drug released into buffer	$\mu\text{g}$
$M_b/M_{\infty}/t = 12$	Cumulative drug release at 12 hours	%
$N_A$	Molar flux	$\text{mol}/\text{cm}^2 \cdot \text{s}$
$P$	Laser power	$\text{W}$
$P_{rel}$	Relative porosity	%
$q_m$	Average heat flux density	$\text{W} \cdot \text{m}^{-2}$
$q(r)$	Radial heat flux density	$\text{W} \cdot \text{m}^{-2}$
$R$	Drug release into buffer at time $t$	%
$R_a$	Mean surface roughness	$\mu\text{m}$
$R_e$	Drug release into buffer at equilibrium	%
$R_z$	Five point mean peak to valley height	$\mu\text{m}$
$r$	Radial distance from beam centre	$\text{m}$

$r_b$	Effective beam radius	m
$r_W$	Roughness parameter of actual to projected surface area	
$t$	Time	s
$t_{i,j}$	Lifetime for pixel at row $i$ and column $j$ in terms of iterations	
$t_l$	Layer thickness	mm
$V$	Volume	cm <sup>3</sup>
$V_b$	Volume of buffer	mL
$V_{s,i}$	Volume of sample previous sampling point	mL
$v$	Scanning speed	mm.s <sup>-1</sup>
$x_{i,j}$	Matrix index row $i$ and column $j$	
$\epsilon$	Random variable between 0 and 1	
$\theta$	Measured contact angle	°
$\theta_C$	Cassie-Baxter contact angle	°
$\theta_{Crit}$	Critical contact angle for imbibition	°
$\theta_W$	Wenzel contact angle	°
$\theta_{Young}$	Young contact angle	°
$\lambda_{i,j}$	Degradation rate for pixel at row $i$ and column $j$	
$\sigma_y$	Tensile yield stress	MPa
$\emptyset$	Diameter	mm
$\emptyset_s$	Emerged fraction of solid surface	

## 1. Introduction

The aim of this chapter is to provide the reader with a context for the study. Relevant background information is presented, from which the problem statement was derived. Based on this, the research aim and objectives were formulated, along with an overview of the research methodology followed throughout various stages of the project. Considerations regarding the scope and novelty of the study are highlighted and the chapter is concluded with a roadmap for the remainder of the document.

### 1.1 Background

#### 1.1.1 Total Hip Arthroplasty Overview

Systematic deterioration or the occurrence of trauma can leave joints within the human body in a state of permanent disrepair (Mancuso et al., 1996). Primary total joint arthroplasty (TJA) is a procedure during which a joint is reconstructed with implanted artificial components, for example total knee arthroplasty (TKA) for knee joints and total hip arthroplasty (THA) for hip joints (Siopack & Jergesen, 1995). Implant components are fixed either by the application of polymer bone cement between the implant and the host bone, or by osseointegration in the absence of bone cement, where the implant surface directly integrates with the host's physiological environment (Laupacis et al., 2002). The aim is to restore functionality to the joint and quality of life (Salih & Hamer, 2013). In general, THAs are highly successful procedures, with a vast repository of literature testifying to its state of continual refinement (Learnmonth et al., 2007; Soffin & YaDeau, 2016).

The average functional lifetime of an implant is 12-15 years for THA (Rack & Qazi, 2006), but several complications can occur, resulting in premature failure and the need for revision surgery. The two main categories of revision surgery are aseptic and septic (Barrack et al., 2000; Romanò et al., 2010). Aseptic revision indicates failure mainly due to mechanical, biochemical, and physiological phenomena in the absence of microorganisms whereas septic revision refers to failure due to periprosthetic joint infection (PJI) (Lombardi Jr et al., 2014). Revision rates are reported to vary between 4 and 15% for primary THA (Labek et al., 2011; Bozic et al., 2015) (Kandala et al., 2015). Figure 1-1 presents the aetiology of revision THA surgeries recorded in the *Norwegian Arthroplasty Register* for the period 2005 to 2017 (Furnes et al., 2018).

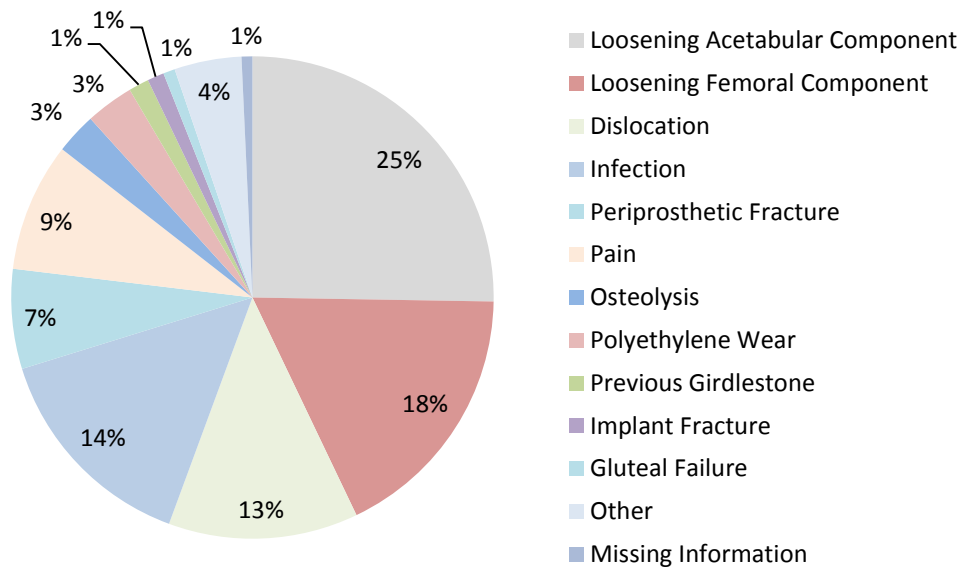


**Figure 1-1: Revision THA recorded in the Norwegian Arthroplasty Register for the period 2005 to 2017 (adapted from Furnes et al., 2018)**

The majority of revision surgeries for primary THA is represented by aseptic causes owing to its greater encompassing definition. However, trends are showing an increase in the fraction of primary revision due to PJI (Ayers et al., 2018; Springer et al., 2017). Languerrand *et al.* (2017) reported an increase in PJI within three months after surgery incidence during the years 2005-2013 of 2.3- and 3.0-fold for primary and revision hip arthroplasty, respectively. The risk of infection also increases significantly after revision surgery, regardless of reason for revision (Wyles et al., 2014; Languerrand et al., 2017). Infection has been reported to have become the main cause of multiple revisions (Kärrholm et al., 2018).

### 1.1.2 Periprosthetic Joint Infection

The leading cause of PJI is the colonisation of implant surfaces by pathogenic bacteria and subsequent biofilm formation (Zmistowski et al., 2013). Upon introduction into the human body, biomaterial surfaces are rapidly covered with host proteins (Kamath et al., 2008). This surface conditioning provides adhesion sites to bacteria with corresponding adhesins (Costerton et al., 2005). Once adhered, bacteria can multiply, form microcolonies, and produce an extracellular matrix which encases the organisms, enabling evasion of the host innate immune system and effecting antibiotic resistance (Høiby et al., 2010; Ter Boo et al., 2015). Systemic antibiotic treatment is generally not effective and surgical intervention is central to treatment procedures (Braem et al., 2014).

Different treatment procedures exist for PJI, the selection of which is primarily based on the time after surgery (Zimmerli & Ochsner, 2003). Within 6 weeks after primary surgery, irrigation and debridement with implant retention can be considered (Grammatopoulos et al., 2017). Thereafter, infection is treated with one- or two-stage exchange procedures. If the pathogens are known and the patient has sufficient healthy bone and soft tissue, or the risk of repeated surgery is high, a one-stage exchange is preferred (Osmon et al., 2013). However, the two-stage exchange protocol is considered the standard treatment for deep PJI. The first stage includes implant removal, debridement of infected tissue, and an initial antibiotic treatment for a typical period of six weeks (Puhto et al., 2014). This period can be extended significantly in the case of persistent pathogens, during which the patient has impaired mobility (Lai et al., 1996; Hsieh et al., 2004). Only once evidence of complete eradication is obtained can the second stage commence where a new functional implant is introduced (Scharfenberger et al., 2007). Reported treatment success rates are challenged due to prolonged interim periods, repeated surgeries, and increasing mortality (Jhan et al., 2017; Gomez et al., 2015). The need to research and develop innovations to aid in PJI prevention and treatment is therefore emphasised (Kheir et al., 2017).

When administering antibiotic drugs it is important to maintain effective concentration levels to the respective site without eliciting systemic side effects. Local drug delivery directly to the site of infection, as opposed to systemic administration, allows for maintaining effective drug concentrations without eliciting systemic toxicity (Young et al., 2014). To achieve effective local drug administration, delivery vehicles are required from which the drug can be released without degradation. For cementless hip stems, local drug delivery strategies are less available (Winkler, 2009). Although bone substitute and biodegradable augmentation materials such as calcium phosphate cements and collagen fleece are available, drug release and biodegradation rates often do not match (Ginebra et al., 2006; Kluin et al., 2013). Studies tend to focus on coatings and conditioning of the outer implant surface (Campoccia et al., 2013; Lyndon et al., 2014; Raphael et al., 2016). Drug delivery from implant surfaces remains challenging (Ter Boo et al., 2015). Rethinking implant design to utilise the implant itself as a drug reservoir has received much less attention. This is likely due to constraints regarding the conventional design and manufacture of commercialised cementless hip stems. Metal additive manufacturing (MAM) is a process that allows the developing of innovative designs to produce cementless implants for drug delivery (Müller et al., 2012). This study, therefore, aims to develop an interdisciplinary MAM-centred approach to enable local drug delivery from implants, with the emphasis on cementless hip stems.

### 1.1.3 Metal Additive Manufacturing-based Process Chains for Medical Implants

In the past decade, various studies have investigated MAM for the fabrication of a diverse range of medical devices (Vandenbroucke & Kruth, 2007; Petrovic et al., 2012; Jardini et al., 2014). The utilisation of MAM-produced medical implants is occurring in human patients and the innovative use of MAM in the fabrication of custom medical devices is on the increase (Murr et al., 2012). Figure 1-2 demonstrates this trend with a projection for the number of implants fabricated with MAM technologies.

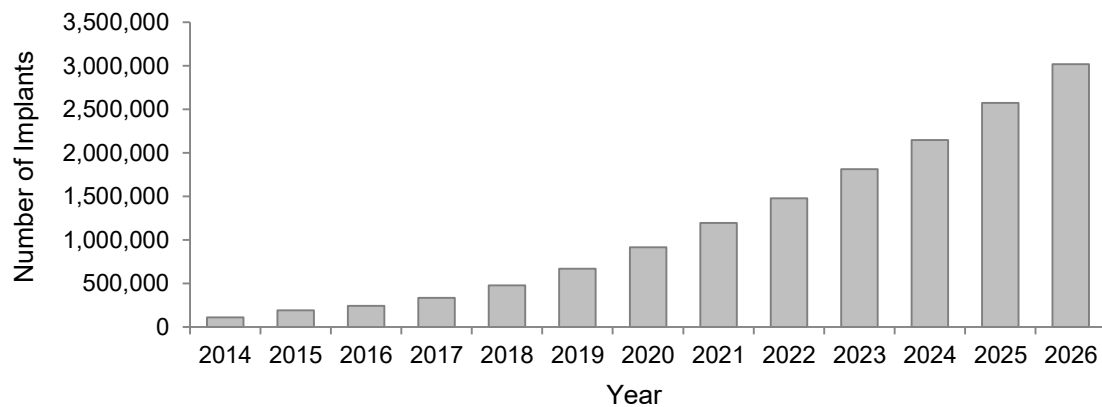


**Figure 1-2: Projected number of implants manufactured with MAM to the year 2026 (adapted from Park, 2018)**

The projection, unfortunately, does not include details with regards to the specific implants other than consisting of metal. Furthermore, although many implants have been successfully manufactured and introduced into patients, reported cases are often study-specific and only a few companies have commercialised MAM-produced implants (Table A-1 in Appendix A). With MAM, high value components such as medical implants can be re-engineered to enhance functionality of the final part, to shorten manufacturing process chains, and to reduce waste (Holmström et al., 2010). Laser powder bed fusion (LPBF) is an MAM technology which has been used to produce conceptual titanium alloy specimens with internal reservoirs containing antibiotic loaded bone cement (ALBC) to prevent bacteria from forming biofilms (Bezuidenhout et al., 2015; Cox et al., 2016). These studies serve as a point of departure for evaluating the concept of drug delivery from LPBF specimens with conceptual features, which is expanded in this project to the application of LPBF for the production of a demonstrator cementless hip stem with drug delivery functionality.

---

## 1.2 Problem Statement

Colonisation of THA cementless femoral stems by opportunistic pathogenic bacteria, most frequently staphylococci (Oliveira et al., 2018), and subsequent biofilm formation is one of the most devastating complications following THA. The protective biofilm shields the bacteria from both the host's immune system and presents a barrier to the diffusion of antibiotic molecules, thus enabling the bacteria to persist on the implant surface (Arciola et al., 2018). Exogenous sources of pathogenic contamination during the arthroplasty procedure include microorganisms present on the skin and mucous membranes of the patients and operating theatre staff as well as environmental aspects such as surfaces, surgical instruments and operating theatre airflow (Zimmerli & Moser, 2012; Graves et al., 2016). Pathogens can also adhere to implant surfaces through endogenous contamination via haematogenous routes due to bacteraemia or the presence of other infected sites (Murdoch et al., 2001; Luthringer et al., 2016).

Current strategies for local drug delivery approved by regulatory boards and implemented for prophylaxis and treatment of PJI are considered to be sub-optimal. Furthermore, in literature it is expressly stated that there is an urgent need for innovations that could aid in prevention and treatment of PJI (Rezapoor & Parvizi, 2015; Kheir et al., 2017).

Reported research tends to focus on the development of antimicrobial coatings and surface modifications, interfacial material chemistry and topography, with comprehensive reviews published (Campoccia et al., 2013; Ter Boo et al., 2015; Chouirfa et al., 2019). Significantly less literature exists on the utilisation of the bulk implant as a drug reservoir for local drug delivery. A potential reason is the geometrical constraints imparted on implant design by conventional manufacturing processes. Most cementless femoral stem bulk parts are produced from wrought titanium alloys (Garellick et al., 2014) with conventional manufacturing processes such as casting, forging, and machining. To overcome these constraints, an alternative would be the MAM route, which affords the realisation of highly complex geometries.

It is important to note that MAM, and specifically LPBF, is not constraint free and that within each step of the process several aspects need to be considered, which are material- and machine-specific. Furthermore, with LPBF as enabler technology, aspects from other disciplines critical to the drug delivery functionality of the implant are also included throughout the entire process chain. The utilisation of LPBF for internal drug delivery features is not yet applied in the current range of

cementless hip stems. An area therefore exists for the development of novel manufacturing process chains towards the production of such products which are interdisciplinary in nature. A cementless hip stem with enhancements such as a built-in drug delivery system requires the design of a new integrated process chain with the manufacturing focus centred on enabling the functional requirements from the beginning of the product's life cycle (Wu & Grainger, 2006).

### **1.3 Research Objectives**

The overall aim of this research was to contribute a prototype strategy for the potential prevention of PJI related to cementless hip stems. Supporting this aim was the development of a framework for interdisciplinary problem solving that guided the creation of an LPBF-centred process chain aimed at enabling local drug delivery from cementless hip stems. This included the identification of the required interdisciplinary knowledge areas to be integrated into the LPBF-centred process chain. It should provide insight for potential manufacturers into the necessary skills requirements for such projects whilst emphasising the need for interdisciplinary education programmes and collaborative research. In support of the overall aim, the following objectives were identified to provide a systematic roadmap for execution of the research:

- Identify the disciplines and required subsets of knowledge for developing the LPBF-centred manufacturing process chain and derive a high-level framework aimed at interdisciplinary problem solving from an LPBF-centred perspective
- Study the LPBF process, investigate how it can be utilised to create permeable structures for local drug delivery, and evaluate the drug release of a demonstrator vancomycin formulation
- Collaboratively study, specify, and develop a custom experimental setup for evaluating an alternative vancomycin formulation for sustained release demonstration
- Determine a method for integration of permeable structures with solid reservoir components and evaluate drug release from integrated reservoir specimens
- Expand the integrated reservoir specimens to design and fabricate a cementless femoral stem implant prototype with internal reservoir and integrated permeable structures
- Evaluate the potential of the prototype to prevent bacterial colonisation through the release of an antibiotic from the implant internal reservoir

- 
- Update the interdisciplinary problem solving framework with knowledge gained from the previous objectives

#### **1.4 Research Approach**

The research in this thesis followed a mixed-methods approach. The bulk of the research was executed under the work package title “*Passive Functionalisation of the Implant Inner Structure*” as part of an international collaborative project on intelligent implants that involved several disciplines. It was divided into four phases namely 1) analysis, 2) synthesis, 3) experimentation and integration, and 4) refinement. Phases 1 and 3 followed a deductive approach while phases 2 and 4 followed an inductive approach.

**Phase one** (analysis) concerned the undertaking of a literature review on the various aspects of applying LPBF for the enabling of local drug delivery for infection prevention. This encompassed studying the relevant aspects of microbiology, polymer science, and engineering. Frameworks for an LPBF-centred interdisciplinary approach to process chain development and problem solving were reviewed to establish a basis from which a high-level interdisciplinary framework for the problem in this study could be synthesised.

In **phase two** (synthesis), the high-level framework was synthesised. This involved consolidating the relevant information obtained in phase 1 to the context of this study, identifying the main knowledge areas within the different disciplines that required integration. A point of departure was identified from the VDI 2221 standard which concerns a level based representation of decomposing the overall problem into single problems and recomposing single solutions into an eventual overall solution (VDI, 1993). Viewing this approach from an LPBF-perspective formed the basis of the interdisciplinary process chain development process. A breakdown of the overall problem into partial and single problems was then performed to guide the experimental section of the project.

The **third phase** (experimentation and integration) involved a series of experimental investigations based on the breakdown structure developed in phase 2. Insight was obtained regarding the sustained release of vancomycin from a poly(lactic-co-glycolic acid) (PLGA) matrix after which a sustained release formulation was developed by the Department of Microbiology at Stellenbosch University (SU). The experimental setup for vancomycin release testing from the developed drug formulation required a collaborative effort during which custom release wells were designed and manufactured.

The bulk of the experimental work, however, encompassed studying the LPBF process and how it can be utilised for drug delivery application. Porosity was especially important in this study for its effects on drug release. Typically, the focus within LPBF is towards minimising porosity by identifying appropriate process parameter settings for specific machine and material combinations (Gong et al., 2014). Viewed from a perspective of functional enhancement, this implies the existence of parameter setting windows that would induce controllable levels of porosity.

One of the key aspects of the LPBF-centred process chain was based on the proposition of integrating features with tailorable porosity through varying the process parameters. This strategy was investigated through a series of design of experiments (DoE) approaches. Firstly, a DoE was performed to ascertain the influence of the three main process parameters, laser power, scanning speed, and hatch spacing. A subsequent experiment was aimed at establishing a range of volumetric energy density (VED) values within which permeable thin walls (PTWs) could be produced. Once this range was established a DoE was set up to investigate the effects of the selected process parameters on resulting vancomycin release. The main reason for this strategy is that process induced porosity created smaller pore sizes than the geometric limitations of current commercial LPBF machines. Where current lattices are typically constraint to feature size designs greater than 300  $\mu\text{m}$  (Hassanin et al., 2018), process induced pores are reported to be in the order of 50  $\mu\text{m}$  (Kasperovich et al., 2016). The integration part of phase three involved two aspects. Firstly, the PTWs were integrated with solid reservoir specimens and the drug release evaluated. The resulting knowledge gained was then utilised as input for integration in the design and manufacture of a demonstrator prototype which proved to be able to prevent bacterial colonisation.

**Phase four** (refinement), in essence, ran concurrently with phase three and utilised the generated knowledge in an inductive manner to update and improve the high-level framework. The implementation of the framework was then summarised to demonstrate a concrete example within the boundaries of the application case of this study, namely a cementless hip stem.

### ***1.5 Limits and Exclusions***

To evaluate antimicrobial efficacy, a model drug and pathogen combination was specified as vancomycin and two strains of *Staphylococcus aureus* (*S. aureus*), one methicillin sensitive (MSSA) and one methicillin resistant (MRSA), two of the most frequent offending pathogens with the ability to colonise implant surfaces and form biofilms, leading to serious PJI (Parvizi et al., 2010;

Triantafyllopoulos et al., 2017). The drug formulation for release and antimicrobial efficacy testing from LPBF-produced specimens was fixed as an aqueous vancomycin solution as this formulation could be prepared freshly for testing at any given time and did not depend on the progress of other stages within the collaborative project. Vancomycin is a glycopeptide antibiotic drug which is clinically endorsed for prophylactic use due to its efficacy against both MSSA and MRSA (Young et al., 2014).

For manufacturing of the prototype, LPBF was used as the MAM technology. In the current state of commercial MAM technologies, LPBF has the capability to produce components at the highest resolution and with the greatest dimensional accuracy (Schmidt et al., 2017; De Pasquale et al., 2019).

Challenges to the large scale adoption of LPBF technologies for load-bearing components include anisotropy in the mechanical properties of as-built parts due to the resulting grain morphology, crystallographic texture, and processing defects such as porosity and insufficient layer bonding (Kok et al., 2018). However, mechanical properties comparable to the wrought counterpart can be obtained through appropriate finishing and thermomechanical post processing methods (Li et al., 2016; Ter Haar & Becker, 2018). For this study, it was therefore assumed, based on literature, that the required mechanical properties are achievable with appropriate post processing techniques.

The body of the cementless stem was based on a commercial design that was fixed within the larger project mentioned in Section 1.4. The focus was therefore on design of the internal reservoir only and not the implant body.

### ***1.6 Scientific Contribution of the Research***

On a high level, the research contributes to local drug delivery strategies for the prevention of bacterial colonisation onto a cementless hip stem surface. An interdisciplinary framework has been synthesised to aid in problem solving and process chain development to enable such local drug delivery from an LPBF-centred perspective. The framework is also intended to be sufficiently generic to be applicable to interdisciplinary problem solving for local drug delivery within a broad range of implants and drugs.

More specific contributions regarding the LPBF process is the development of a method to produce permeable structures with smaller pores than is currently achievable with lattice structure designs on commercial LPBF machines. A method was developed to integrate such permeable structures with solid components with an in-process assembly approach without the need for expensive machine

---

manufacturer add-on software. In order to further the industrialisation of MAM, it is of high importance to demonstrate novel applications with the production of physical prototypes. Thus, in this study it was demonstrated that LPBF as an MAM technology provides the possibility to enhance the functionality of a cementless hip stem by enabling local drug delivery and prevent bacterial colonisation. It therefore contributes to the application examples of MAM to promote its relevance as manufacturing technology for implants of the future. A list of journal and conference papers published during the duration of the project, with either direct relevance or required background work to the research reported in this thesis, is presented in Appendix A.

### ***1.7 Document Roadmap***

A schematic of the document roadmap is presented in Figure 1-3. The preceding introduction described the context of the study. The problem statement addressed why the research is relevant and the objectives that were to be reached in order to achieve the overall aim. The research approach briefly described how the study was undertaken. Chapter 2 begins with an overview of infection in total hip arthroplasty to elaborate on the seriousness of the problem. This is followed by an overview of drug delivery within which the research gap of utilising an inner implant bulk as reservoir for drug delivery is emphasised. The LPBF process is then analysed with specific implications for its utilisation for inducing porosity for the generation of permeable structures. Chapter 2 ends with a review of frameworks for interdisciplinary problem solving from an LPBF-centred perspective. Chapter 3 presents the derivation of the high-level framework and is concluded with a problem breakdown structure which systematically organises the experimentation required to converge on an overall solution. The respective experiments, results and conclusions are presented in Chapters 4-7. The insights obtained from the experimentation are then utilised in the design and manufacture of a demonstrator prototype which was evaluated for its efficacy in Chapter 8. The high-level framework, updated with an inductive approach is discussed in Chapter 9. It was built on the insights obtained throughout the systematic experimentation according to the initial problem structure defined in Chapter 3. An implementation summary of the framework is also provided. The document is brought to a conclusion in Chapter 10 with recommendations for future research.

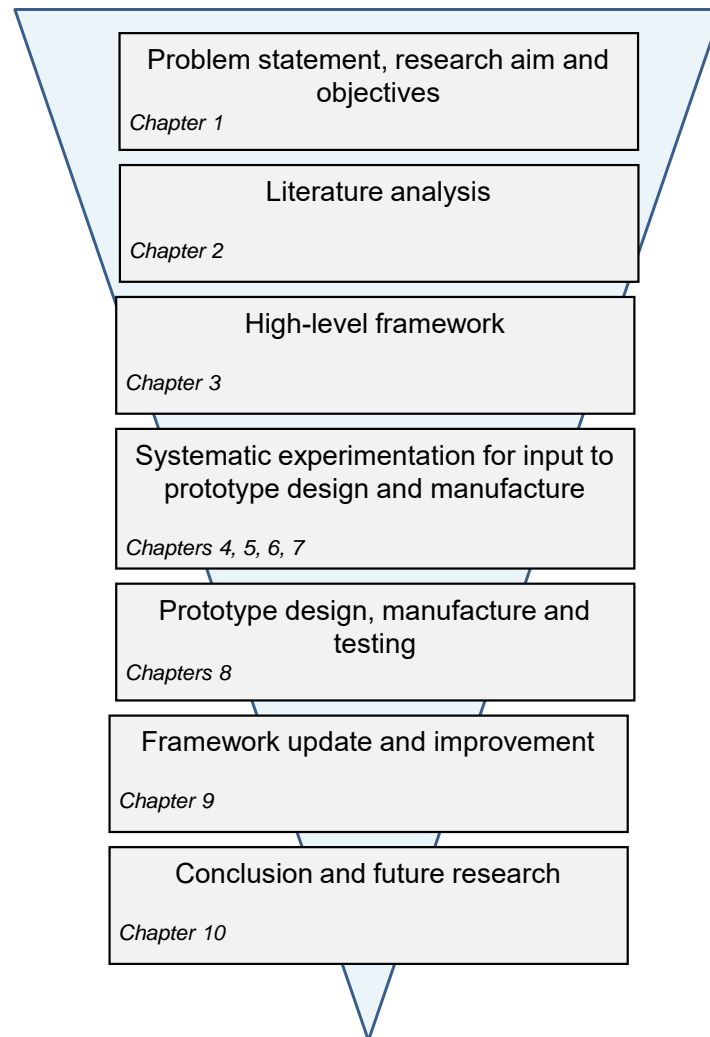


**Figure 1-3: Roadmap of document**

## **2. Strategy to Apply LPBF for Local Drug Delivery: Literature Study**

The application of LPBF for enabling drug delivery from a cementless hip stem to prevent bacterial colonisation encompasses knowledge areas of different disciplines. To gain an understanding of how to develop a strategy, it was important to study the basic principles of the relevant aspects within each of the involved disciplines. The review starts by describing the problem of infection in THA, its burden on resources, selected aspects of microbial infection, and the available treatment procedures which emphasise the need for local drug delivery innovations. Clinically applied local drug delivery strategies as well as strategies in development are then discussed, after which the scientific gap and opportunity regarding the application of LPBF for fabricating internal reservoirs are identified. Relevant aspects of LPBF for the processing of Ti6Al4V extra low interstitial (ELI) are then discussed, followed by an overview of frameworks to provide a basis for the derivation of an interdisciplinary problem-solving framework with an LPBF-centred perspective.

### ***2.1 Infection in Total Hip Arthroplasty***

Infection is one of the most serious complications following THA (Tsang et al., 2018). Colonisation of hip replacement implants by pathogenic bacteria and the formation of biofilms is the leading cause of PJI (Costerton et al., 2005; Zmistowski et al., 2013). Although PJI is relatively uncommon, occurring in 0.5-2.2% of primary arthroplasties, the implications are devastating (Shukla & Della Valle, 2015; Davidson et al., 2019). This includes poor clinical outcomes, heavy burden on healthcare and financial resources, and a significant risk of patient mortality (Shahi et al., 2017). Furthermore, PJI occurrence is steadily increasing (Springer et al., 2017). Lenguerrand et al. (2017) reported an increase in the PJI incidence per 1000 of 2.3- and 3.0-fold within 3 months following primary and revision hip arthroplasty, respectively, between the years 2005 and 2013. The number of reported PJI cases caused by antibiotic resistant Gram-positive bacteria is also increasing (Triantafyllopoulos et al., 2017). The importance of the development of novel antibiotic formulations and innovative drug delivery methods in joint replacement surgery is therefore underlined (Parvizi et al., 2010). This section discusses the costs and burden of infection, mechanisms of infection after hip replacement surgery, treatment procedures and prophylactic strategies. It is important to note that many themes with regard to the pathogenesis and persistence of infection, microbial behaviour and communication, are expert fields in their own right and therefore the review is presented at a level of detail as to maintain relevance to the aim of the current study.

### 2.1.1 Costs and Burden of Infection

Revision due to infection poses a greater challenge than aseptic complications (Ulrich et al., 2008). An average increase in costs has been reported as 1.6- and 4.44 times that of primary THA for aseptic and septic revision respectively (Bozic & Ries, 2005). As a quantitative indication, separate studies have reported estimated treatment costs around \$60,000.00 to \$100,000.00 per patient (Bozic & Ries, 2005; Springer, 2015; Kapadia et al., 2016). These estimations exclude secondary costs that may arise from economic effects such as sick leave and disability claims.

The main cost drivers include multiple operations required, length of hospital stay, expensive long term antibiotics, and new prostheses (Parvizi et al., 2010; Briggs 2015; Kapadia et al., 2016). Figure 2-1 presents cost breakdowns from three different studies for comparison. The charts are adapted or created from data reported on the contributions of various cost drivers to the overall treatment cost at the respective care centre (Klouche et al., 2010; Kapadia et al., 2016; Akindolire et al., 2020). The hospital bed cost is not explicitly indicated by Klouche et al. (2010) which make the direct comparison of this cost driver not clear in Figure 2-1(c), however their results reported an average length of stay of septic revision was  $30.6 \pm 14.9$  days in comparison to an average aseptic length of stay of  $8.9 \pm 2.2$  days.

The cost of prostheses and anaesthesia is included in Figures 2-1(a) and (b) under operating room costs, but only anaesthesia is included in the “*Surgical unit + anaesthesia*” costs in Figure 2-1(c). The main two cost drivers in all three studies can be identified as hospital stay and operating theatre costs. This would imply that costs can be reduced with strategies that would lead to shortening of hospital stay or reduction in number of surgeries required. Springer et al. (2017) evaluated infection burden as the number of septic revisions to the total number of primary arthroplasties for a given period from information reported in national arthroplasty registries from 6 different countries and found that the infection burden steadily increased. As the incidence of PJI is continuing to rise, this amounts to a significant economic treatment burden on resources.

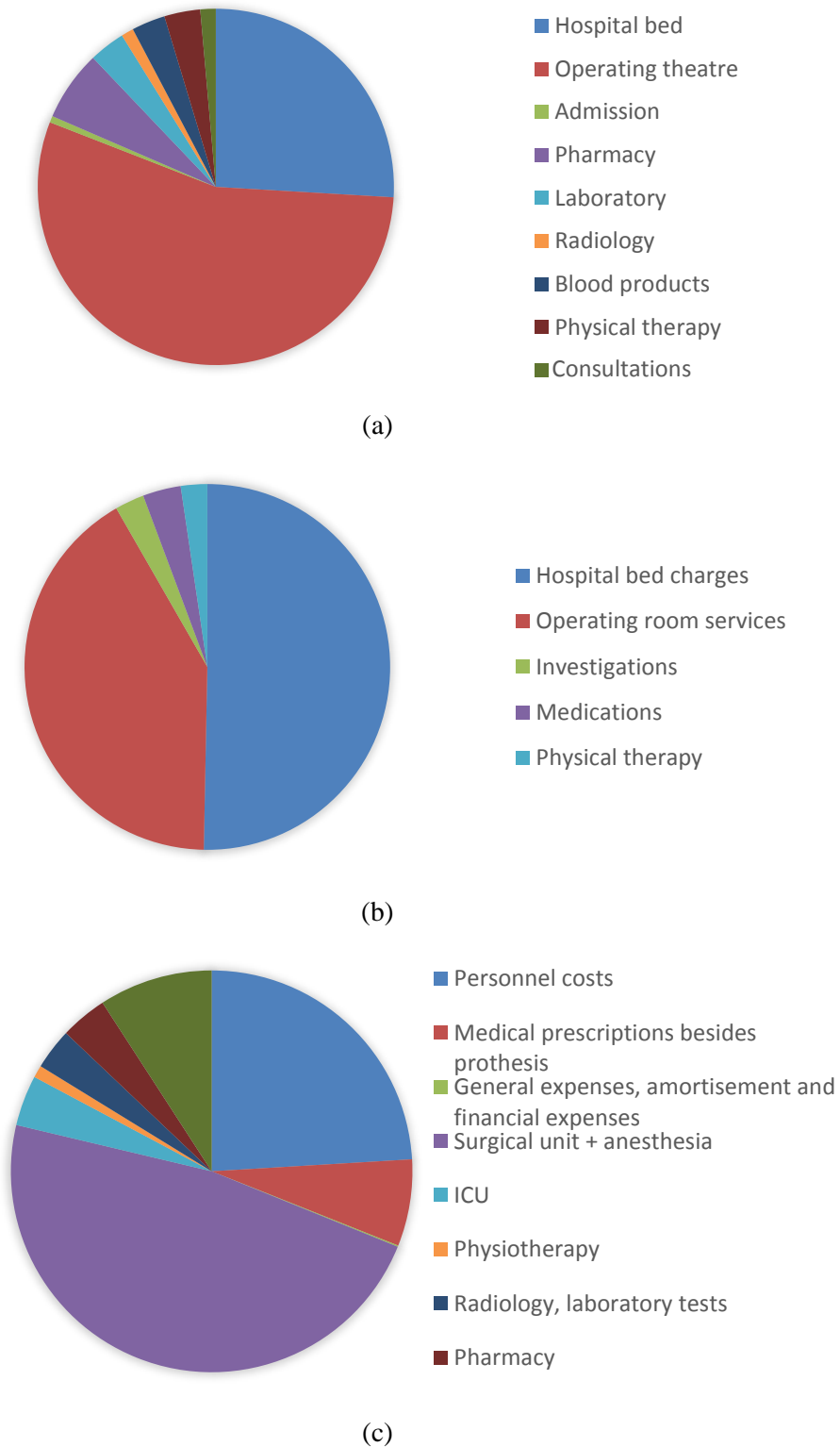


**Figure 2-1: Reported costs for treatment of PJI as reported by (a) Kapadia et al. (2016) (b) Akindolire et al. (2020) and (c) Klouche et al. (2010)**

However, not only the economic burden, but also the reduced quality of life and risks of amputation and mortality should be emphasized. Gundtoft et al. (2017) evaluated the Danish Arthroplasty Register for the years 2005 to 2014 and found that patients who underwent septic revision had a significant higher risk of mortality than aseptic revision ( $p = 0.019$ ) within one year after surgery. These findings are corroborated by other studies regarding increased risks of mortality after septic revision (Zmistowski et al., 2013; Patel et al., 2016; Shahi et al., 2017). It should be noted that PJI risk is also elevated after aseptic revision (Wyles et al., 2014; Goldman et al., 2020). Furthermore, septic revision often requires multiple surgeries during treatment (Bozic & Ries, 2005), with the risk of patient mortality compounding with each surgical admission, leading to an elevated mortality rate (Shahi et al., 2017). In fact, for septic revision, a mortality rate of 5 times higher than that for aseptic revision has been reported together with a re-infection rate of up to 20% (Davidson et al., 2019).

The above discussed issues do not differentiate between the pathogenic origins. In the case of bacteria resistant to antibiotics, however, the outcomes are typically worse (Parvizi et al., 2010). This encompasses increased treatment failure, longer hospital stay, and poor quality of life for the patient (Walls et al., 2008). Zmistowski et al. (2013) found trends of increased mortality regarding PJI caused by MRSA as opposed to MSSA with 15.9% and 7.4% of investigated cases respectively.

A worrying statistic is reports of increasing incidence of infection by resistant organisms (Kapadia et al., 2016). The variety of resistant microorganisms is also increasing, further adding pressure on the problem (Kapadia et al., 2016). It therefore comes as no surprise that the importance of improving both PJI treatment and prevention strategies is unanimously emphasised throughout literature.

### **2.1.2 Microbial Infection**

Infection can be regarded as a disturbance in the homeostatic balance between microorganisms and the host cells (Zilberman & Elsner, 2008). It starts with the adherence of microorganisms to the surface of the implanted biomaterial (Darouiche, 2001; Arciola et al., 2012). The origin of the microorganisms can vary and is classified as follows, perioperative if contamination occurred during surgery or shortly thereafter, haematogenous if the organisms reached the implant surface through blood circulation or lymph which transported the organism from a distant site, and contiguous if the pathogen has spread from one or more nearby foci of infection (Trampuz & Zimmerli, 2005). Time lapse since primary surgery is also a key parameter in classifying PJI. If PJI occurs within three months after primary THA

it is termed ‘early’, ‘delayed’ if occurrence is 3-24 months after primary THA, and ‘late’ after 24 months (Trampuz & Zimmerli, 2005; Anagnostakos et al., 2009).

The leading cause of PJI is the colonisation of joint replacement implant surfaces by pathogenic bacteria and subsequent biofilm formation (Zmistowski et al., 2013). A biofilm consists of surface-adhering microorganisms which are embedded in an extracellular matrix (ECMx). The ECMx is generated from secretions of the microorganisms and components from the surrounding environment (Gallo et al., 2003).

After implantation, the surface of an implant is covered with host extracellular matrix (ECMx) proteins including fibrinogen, fibronectin, collagen and elastin (Garcia-Gareta et al., 2016). This conditioning of the surface with host ECMx proteins provides sites to which planktonic bacterial cells can adhere through cellular features referred to as microbial surface component recognising adhesive matrix molecules (MSCRAMMs) (Patti et al., 1994). On unconditioned areas of the surface, initial attachment can be mediated through hydrophobic effects, van der Waals, acid-base, and electrostatic forces (Arciola et al., 2018). The risk of bacterial cell adhesion to the conditioned implant surface is further increased by the existence of an immune-compromised zone in the vicinity of the implant which impairs the ability of the host to clear intrusive microorganisms (Rochford et al., 2012). Once adhered, bacteria can multiply, form microcolonies, and produce an ECMx which encases the organisms, enabling evasion of the host innate immune system and effecting antibiotic resistance (Høiby et al., 2010; Ter Boo, et al., 2015).

To address the problem of infection in an interdisciplinary environment, it is required for all parties involved in such a project to have a basic understanding of the process of biofilm formation. A fundamental understanding, however, would entail an extensive amount of detail regarding the differences in gene expression and virulence factors of a wide variety of pathogens which is not necessarily relevant. The following sections thus aim to present a description of the biofilm formation process at a level of detail which would be required in order for the various disciplines involved in such a manufacturing process chain to take cognisance of the factors which could either increase or decrease the risk of bacterial colonisation and biofilm formation.

Biofilm formation can be regarded as a four step process, attachment, accumulation, maturation, and dispersal (Arciola et al., 2012). These are presented in the simplified schematic in Figure 2-2, which serves as the basis for the process description.

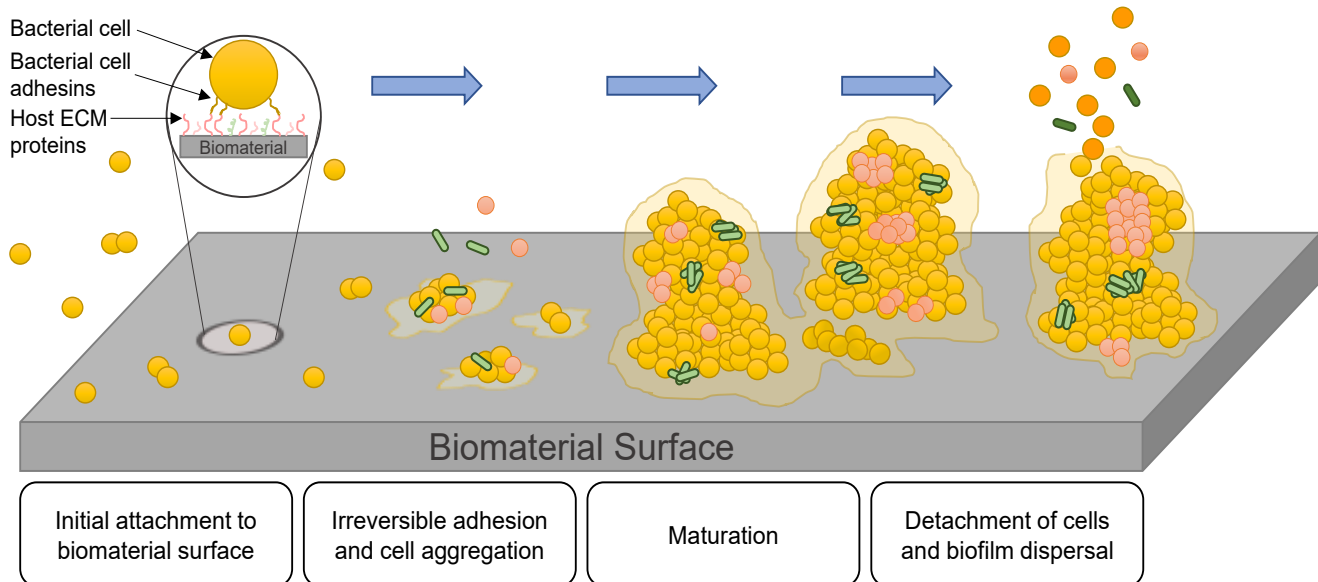


**Figure 2-2: Simplified schematic representation of biofilm formation, (adapted from Arciola et al., 2012; Otto, 2013; Bresco et al., 2017)**

Initial cell attachment to the biomaterial is a reversible adhesion and can be effected by different mechanisms as described above. The administering of prophylactic antibiotics strives to eliminate planktonic and reversibly attached bacteria, prohibiting them from reaching the state of irreversible adhesion (Garcia-Gareta et al., 2016). Once adhered, a rapid increase in the number of adhering bacteria follows, leading to the progressive establishment of the biofilm (Gallo et al., 2003). *S. aureus* can detect the cell density or “quorum” through a process termed “quorum sensing” with the accessory gene regulator (*agr*) system which signals the cells to respond with changes in gene expression, typically accompanied by an increase in expression of virulence factors (Yarwood et al., 2004; Le & Otto, 2015).

During the maturation phase, the biofilm develops structural features which are specific to the primary bacterial species (Arciola et al., 2012). Figure 2-3 shows a SEM image of an *S. aureus* biofilm on a Ti6Al7Nb substrate which has been incubated for seven days (Post et al., 2017). This involves the production of an extracellular polymer matrix which provides structural stability and protects the organisms, adhesive processes that link the cells, as well as processes that create channels in the

biofilm which serve as conduits for nutrients between the multiple layers of cells (Højby et al., 2010; Otto 2013). In addition to the diffusional barriers provided by the structural components of the biofilm, bacteria in biofilm mode of growth undergo changes in metabolic activity, which typically slows down in lower layers due to decreased availability of oxygen and nutrients. These changes in metabolism further reduce the efficacy of antibiotics (Kiamco et al., 2018). The high cell density in biofilms further provides an environment for mutation and amplification of both natural and acquired resistance (Francolini & Donelli, 2010).

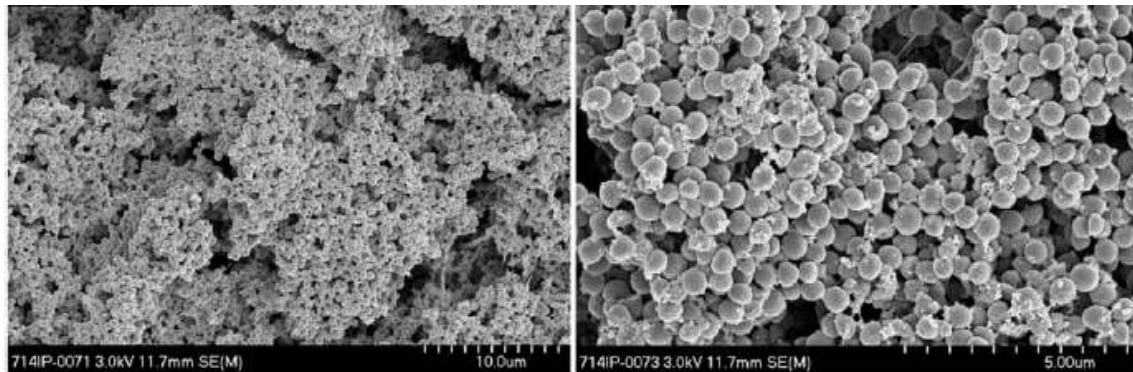


**Figure 2-3: Scanning electron microscopy images of an *S. aureus* biofilm on Ti6Al7Nb discs after 7 days of incubation (Post et al., 2017)**

In the fourth phase, a range of different surfactants and exo-enzymes are produced which degrades the ECMx with cells being able to revert from the biofilm to the planktonic state (Lister & Horswill, 2014). This enables the cells, now possibly with acquired mutations as indicated by the slight change in colour in Figure 2-2, to further spread over the biomaterial surface and initiate the biofilm process anew (Arciola et al., 2012).

Several factors regarding the physico-chemical properties of the implant material surface affect the attachment of *S. aureus* (Crawford et al., 2012). Two key parameters are the combined roughness and topographical features of the surface as well its hydrophobicity (Kasimanickam et al., 2013). Rough surfaces, although useful for osseointegration, tend to also promote the adhesion of bacteria if prophylactic measures are not taken (Campoccia et al., 2013). This is especially true in the case of LPBF where a significant reduction in biofilm growth has been observed on manually polished compared to as-built surfaces (McGaffey et al., 2019). Sarker et al. (2019) found that *S. aureus* biofilm area coverage reduced with decreasing hydrophobicity on LPBF-produced Ti6Al4V coupons. These issues should be taken into consideration when producing Ti6Al4V implants with LPBF.

### 2.1.3 Treatment Procedures

Treatment of a PJI in hip replacement aims to completely eradicate all offending microorganisms and restore functionality to the articulating implant components (Haddad et al., 2000). Current treatment procedures include irrigation and debridement with implant retention, one-stage exchange arthroplasty, and two-stage exchange arthroplasty (Zimmerli & Ochsner, 2003).

The option of PJI treatment with debridement and retention of the implant is subdued to strict selection criteria if it is to be successful, such as, the implant must be stable, infection is in its early stage and that the patient must be able to tolerate an aggressive and an extensive period of antibiotic therapy, both intravenously and orally (Zimmerli et al., 1998). This strategy consists of a thorough debridement of all infectious evidence at the prosthetic site without the removal of the prosthesis, accompanied by an intensive and prolonged period of antibiotic treatment (Brandt et al., 1997; Zimmerli et al., 1998). More than one debridement procedure might be required and the period between debridement procedures can vary (Westberg et al., 2012) The advantages of this treatment, if successful, are reduction in patient morbidity, lengths of hospital stay, resource burden and costs in comparison to one- or two-stage exchange arthroplasty (Fisman et al., 2001).

The one-stage exchange procedure involves thorough debridement of all infected soft tissue, complete removal of the prosthesis and associated components (for example bone cement in the case of cemented components), and debridement of the bone-implant interface in the medullary canal, after which a new prosthesis is fixed in place (Buchholz et al., 1981). Between removal of infected components and re-implantation, a full rescrub and re-preparation is required to reduce the risk of recontamination (Jiranek et al., 2015). Traditionally, cemented components and the use of antibiotic loaded bone cement (ALBC) are indicated, but, successful treatment has also been demonstrated with cementless components (Hansen et al., 2013). It is however, subject to strict patient selection criteria. This includes the absence of any host comorbidities, the presence of adequate and healthy host soft tissue and bone stock, accurate preoperative identification of the infecting microorganisms, and absence of a sinus tract (Masri & Salvati, 1998; Klouche et al., 2012). Advantages of successful one-stage to two-stage exchange are reduced risks for patient morbidity, less surgical procedures and hospital stay time, and a reduced cost (Klouche, et al., 2012).

Two-stage exchange is regarded as the standard procedure for PJI, especially for patients with developed abscesses and sinus tracts (Scharfenberger et al., 2007; Nett, 2015). During the first stage, the implant is resected together with a thorough debridement of all infected tissue. This is followed by a period of both local and systemic antibiotic treatment to target organisms identified from tissue biopsies (Sukeik & Haddad, 2009). There is controversy around the optimal period between stages, and subsequently a wide range has been reported. While some studies have shown little to no benefit of periods longer than 6 weeks, a delay between stages of 12 months or more have been reported for resistant pathogens (Zimmerli & Ochsner, 2003; Bernard et al., 2010; Babis et al., 2015). A temporary spacer which can be either static or articulating, typically made from ALBC, is utilised to locally elute antibiotics at the target infection site while maintaining limb length and allowing a certain amount of mechanical support (Rava et al., 2019). Evidence of complete eradication of the infecting microorganisms is required before the second stage, re-implantation of new components, can commence (Scharfenberger et al., 2007). Successful eradication can however not be guaranteed and repetition of the whole procedure might be required, which is associated with poor outcomes (Brown et al., 2018).

Despite continual efforts in improving the treatment of PJI, for some patients, treatment or repeated procedures eventually fail (Jiranek et al., 2015). In these cases, the remaining options are resection arthroplasty, arthrodesis, amputation, or chronic antibiotic suppression (Fagotti et al., 2018). In resection arthroplasty (also termed modified Girdlestone arthroplasty) all infected components are completely removed and the patient is left with a rough articulation and shortened limb (Vincenten et al., 2019). In some cases the femur may be fused to the acetabulum (arthrodesis) (Kliushin et al., 2016). These procedures are performed as a last resort and are clearly undesired outcomes.

Prophylaxis for PJI aims to reduce the bacterial presence at the bone-implant interface (Meehan et al., 2009). Currently this is done through parenteral and local delivery of antibiotics. Despite optimisation efforts in clinical practise, several studies emphasises the need for the development of innovative prophylactic approaches (Getzlaf et al., 2016; Kapadia et al., 2016; Kheir et al., 2017). Winkler et al. (2018) argues that if even a single infection could be prevented through the use of local drug delivery, a care institution would save a significant amount of money.

## 2.2 Local Drug Delivery

In local drug delivery, drugs are delivered in close proximity to the target site. As the focus in this study is on microbial colonisation of the foreign body implant, the target site can be regarded as the immediate volume surrounding the implant surface. Since a significant portion of this volume is situated within the proximal and distal femur, it can therefore also be considered in this particular case as intraosseous drug delivery. Administering drugs locally to the target site for prevention and treatment of PJI is an accepted practice and demonstrated to be safe (Gogia et al., 2009; Hafeman et al., 2010). Furthermore, with local antibiotic delivery, the burden on healthcare resources is reduced which is reflected in its lower cost compared to parenteral administration (Gogia et al., 2009). Wu and Grainger (2006) summarised the advantages of local drug delivery as follows:

- Smaller doses of the drug are needed
- More control can be achieved over the toxicity and bioavailability of the dose
- It is less likely to promote antibiotic resistance
- An extended release duration is possible
- Local drugs can be combined with systemic drugs exhibiting different kinetics
- From surfaces of combination devices drugs can be released directly to the required site
- Systemic exposure of the drug can be avoided
- It offers a direct method to mitigate device related infection

The following subsections briefly present methods in clinical use and those in development. It also serves to indicate the opportunity that exists for the development of a local drug delivery strategy based on the utilisation of the implant itself as a reservoir.

### 2.2.1 Clinically Applied Local Antimicrobial Delivery for Cementless Hip Stems

The application of PMMA beads and spacers as local drug delivery vehicles has been a standard in both prophylaxis and treatment for decades (Wu & Grainger, 2006). Commercial preparations are available and suitable antimicrobial agents able to withstand the exothermic polymerisation reaction can additionally be added manually prior to polymerisation. For example, vancomycin can be delivered locally via PMMA in concentrations far greater than the respective minimum inhibitory concentration (MIC) of the *S. aureus* strain in question (Kelm et al., 2004; Wu & Grainger, 2006; Anagnostakos et al., 2009). Limitations for the use of PMMA, however, exist which raise serious questions to its continued use. PMMA is non-biodegradable, requiring additional invasive procedures for removal,

risking renewed pathogen intrusion (Hanssen & Spanghehl, 2004; Swearingen et al., 2016). Drug release efficiency is low with the majority of the drug remaining in the polymer matrix. This can lead to prolonged drug leaching in sub-effective concentrations, promoting the development of resistant bacterial mutations, and the PMMA material can present a new substrate for colonisation (van de Belt et al., 2001; Campoccia et al., 2010). Nevertheless, it is still employed clinically as a local drug delivery medium for both infection prophylaxis and treatment (Kluin et al., 2013; Bistolfi et al., 2019).

Bone substitute and biodegradable augmentation materials such as calcium phosphate cements and collagen fleece are available for local drug delivery, but drug release and biodegradation rates often do not match (Ginebra et al., 2006; Kluin et al., 2013). Biodegradable drug delivery vehicles offer the advantage of not requiring removal surgery and can also be used to manage dead space during its degradation period (Waghmare et al., 2019). Wahl et al. (2017) used a biodegradable calcium sulphate cement to both manage dead space and locally deliver vancomycin. Concentrations above the MIC were maintained for at least 4 weeks with no systemic side effects. Calcium sulphate can be mixed with vancomycin into either pellets or a paste and typically are absorbed within three months (George et al., 2015). In addition to calcium-based bone cements, natural and synthetic biodegradable polymers also offer promising alternative solutions for the local delivery of vancomycin. Rai et al. (2016) used poly( $\epsilon$ -caprolactone) (PCL) as carrier and demonstrated vancomycin delivery sufficient to successfully treat osteomyelitis in a rabbit model. Liu et al. (2002) described the use of PLGA biodegradable beads in a rabbit model and found effective levels of vancomycin for over 55 days.

Recently, a hydrogel based on hyaluronic acid (HA) and poly(lactic acid) (PLA) has been clinically approved for cementless implants. Evidence has been reported in support of its efficacy, however publicly available literature at this time is still sparse and the use of coatings is not yet defined in treatment algorithms (Zagra et al., 2019). It is nevertheless evident that biodegradable alternatives are receiving more attention for local drug delivery. When combined with a drug eluting functionally enhanced implant as proposed in this study, it has the potential to offer a novel configuration of device and drug delivery combination for both prophylaxis and treatment of implant-related infections. Antibiotic prophylaxis can also be augmented by direct application of antibiotic powder in the open wound.

### 2.2.2 Investigated Local Antimicrobial Delivery Strategies for Cementless Implants

The literature on local drug delivery strategies in development is vast. Examples of investigated strategies are presented in Table 2-1. Strategies are classified here as either external, internal, or the use of porous metal. For the purpose of demonstration, selected examples were restricted to specimens consisting of a metallic substrate and bacterial target pathogens. Furthermore, the selected examples include the application of different types of antimicrobial agents such as antibiotics, metallic cations, and antimicrobial peptides to convey the different possibilities for enhancing antibacterial functionality from cementless metallic implants.

External strategies mostly regard the development of coatings. For titanium implants this especially involves bioactive or biodegradable formulations. Typical approaches for external strategies are, but not limited to, the application of hydroxyapatite, films, hydrogels, microparticles, nanoparticles, electrospun nanofibers, TiO<sub>2</sub> nanotubes, TiO<sub>2</sub> layers formed by plasma electrolytic oxidation, and direct immobilisation of drugs onto the implant surface (Hickock & Shapiro, 2012; Barik & Chakravorty, 2019). Nevertheless, drug delivery from coated implant surfaces remains challenging, especially as it offers once-off release only and coatings bear the risk of excessive abrasion and delamination under the forces exerted on the implants during surgery (Ter Boo et al., 2015).

Internal strategies, as is the focus of this study, refer to the utilisation of a reservoir inside a cementless implant for drug loading and subsequent release. Rethinking implant design to utilise the implant itself as a drug reservoir has received much less attention than external strategies. This is likely due to constraints regarding the conventional design and manufacture of commercialised cementless hip stems.

Porous metal encompasses commercially available options such as tantalum trabecular metal as well as lattice structures manufacturable with MAM. With the geometrical freedoms afforded by MAM, researchers are investigating the use of various lattice structure designs for local drug delivery by either using the pores as reservoir sites or the large surface area for coatings or direct antimicrobial agent implantation (Bakhshandeh et al., 2017).

**Table 2-1: Examples of external, internal, and porous metal local antimicrobial delivery strategies in research for metallic implants**

Parent Strategy	Specific Strategy	Microorganism	Antimicrobial	Reference
External	Antimicrobial agent covalently bonded to surface of Ti6Al4V rods	<i>S. aureus</i> ATCC 25923	Vancomycin	(Antoci et al., 2007)
	Polyelectrolyte multilayers of HA and chitosan on Ti foil	<i>S. aureus</i> 25923	Chitosan	(Chua et al., 2008)
	Formation of Cu / Ti oxide layer on Ti6Al4V plate	<i>S. aureus</i> 25923	Cu <sup>2+</sup>	(Burghardt et al., 2015)
	Formation of Zn / TiO <sub>2</sub> coating on Ti plate	<i>S. aureus</i> 25923 <i>E. coli</i> <sup>a</sup>	Zn <sup>2+</sup>	(Hu et al., 2012)
	Formation of Ag / TiO <sub>2</sub> film on NiTi plate	<i>E. coli</i> ATCC 2259	Ag <sup>+</sup>	(Luo et al., 2013)
	Drug loaded mesoporous TiO <sub>2</sub> coating on Ti discs	<i>E. coli</i> (DH5 $\alpha$ )	Cephalothin	(Xia et al., 2012)
	Ag nanoparticle containing hydroxyapatite (HAp) coating on Ti discs	<i>S. epidermidis</i> <sup>b</sup> (ATCC <sup>c</sup> 12228) <i>E. coli</i> (ATCC 8739)	Ag <sup>+</sup>	(Xie et al., 2014)
	PLGA covered gentamicin coating on Ti6Al4V coupons	<i>S. aureus</i> ATCC 12600 <i>S. aureus</i> 7323 CNS <sup>d</sup> 7391 <i>S. aureus</i> 7388 <i>S. aureus</i> 5298	Gentamicin	(Neut et al., 2011)
	Electrospun PLGA coating containing vancomycin on Ti implants	<i>S. aureus</i> ATCC 29213	Vancomycin	(Zhang et al., 2014)
	Antimicrobial loaded TiO <sub>2</sub> nanotubes on Ti plates	<i>F. nucleatum</i> ATCC 25586 <i>P. gingivalis</i> ATCC 33277	GL13K AMP <sup>e</sup>	(Li et al., 2017)

	Drug loaded chitosan microspheres with nano-HAp precipitate	<i>S. aureus</i> ATCC 29213	Ciprofloxacin	(Doymus et al., 2021)
Internal	PMMA ALBC in LPBF produced Ti6Al4V specimens	<i>S. aureus</i> Xen 36 (MSSA) <i>S. aureus</i> Xen 31 (MRSA)	Gentamicin	(Bezuidenhout et al., 2015)
	Brushite ALBC in LPBF produced Ti6Al4V specimens	<i>S. aureus</i> NCTC 8532 <i>S. epidermidis</i> <sup>b</sup> NCTC 11047	Gentamicin	(Cox et al., 2016)
	Drug loaded mesoporous silica microparticles inside a commercial hollow stainless steel pin with porous wall	<i>S. aureus</i> ATCC 29213	Linezolid	(Perez et al., 2011)
	Drug loaded mesoporous silica inside a macroporous Ti dental implant	<i>S. mutans</i> <sup>f</sup> (Clarke)	Chlorhexidine	(De Cremer et al., 2017)
Porous metal / lattice reservoir	PLGA microspheres manually loaded into Ta trabecular metal specimens	<i>S. aureus</i> ATCC 49230	Tobramycin	(Ambrose et al., 2014)
	PMMA ALBC in Ta trabecular metal acetabular cup	n/a (release only test)	Gentamicin	(Mooney et al., 2019)
	Bacterial cellulose saturated with drug loaded into LPBF produced Ti6Al7Nb lattice	<i>S. aureus</i> ATCC 6538	Gentamicin	(Dydak et al., 2018)
	Multi-drug chitosan/gelatin based coating deposited on DMP <sup>g</sup> produced Ti lattice	<i>S. aureus</i> ATCC 6538	Ag <sup>+</sup> Vancomycin	(Bakhshandeh et al., 2017)
	Drug loading in EBM <sup>h</sup> produced and micro arc oxidised Ti6Al4V lattice	MRSA (hospital isolate)	Vancomycin	(Zhang et al., 2020)

<sup>a</sup>*Escherichia coli*; <sup>b</sup>*Staphylococcus epidermidis*; <sup>c</sup>American Type Culture Collection; <sup>d</sup>Coagulase Negative Staphylococci; <sup>e</sup>Antimicrobial peptide;

<sup>f</sup>*Streptococcus mutans*; <sup>g</sup>Direct Metal Printing; <sup>h</sup>Electron Beam Melting

### 2.2.3 Opportunity for Novel Prophylactic Strategy

Much research has and is being done in the area of developing prophylactic measures against bacterial colonisation of implant surfaces with comprehensive reviews published on the topic (Campoccia et al., 2013; Ter Boo et al., 2015; Getzlaf et al., 2016; Mohammed et al., 2020). The research focus up to the present was by far on external strategies, for example coatings, topographical and physico-chemical modifications to the outer surface of the implants, and tailoring of the material chemistry to render intrinsic antibacterial properties. Conversely, a limited number of studies reported on the delivery of antibiotics through utilisation of the inner implant as a reservoir. This is demonstrated in Figure 2-4. For simplicity, as in the previous section, the classification is split between internal, external, and the use of porous metal or lattice structure approaches. To construct the figure, 171 relevant publications from reference lists in the respective reviews were classified according to the predominant approach followed for functionalisation as described above (Campoccia et al., 2013; Lyndon et al., 2014; Getzlaf et al., 2016; Mohammed et al., 2020).

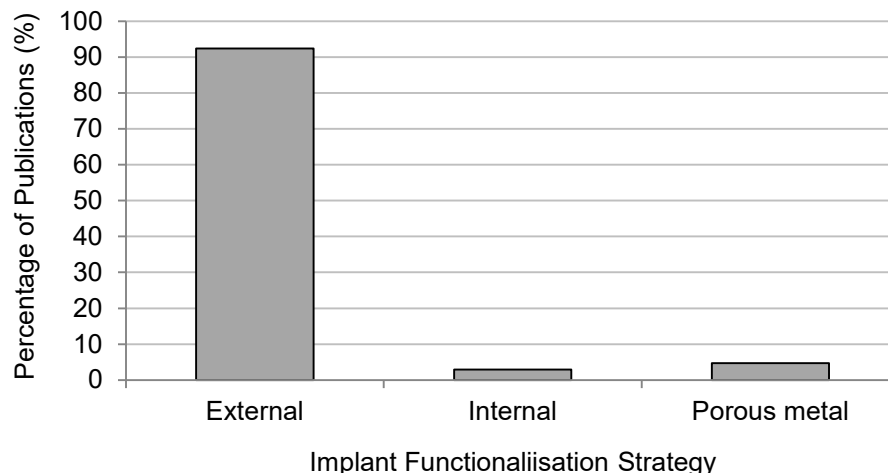


**Figure 2-4: Implant functionalisation strategies for drug delivery**

Currently there is paucity in the research of internal and porous metal functionalisation compared to that of external. A possible reason for this is the limitations imposed on internal geometries of implants with conventional manufacturing methods. This argument is supported by the fact the cited internal approaches in the reviews pertains to specimens manufactured by additive manufacturing methods (Bezuidenhout et al., 2015; Cox et al., 2016; Bezuidenhout et al., 2018; Hassanin et al., 2018).

With powder bed MAM being a reasonably new technology, this could also explain the large difference in research focus between external and internal approaches. Nonetheless, the opportunity for functionalisation of inner implant volumes through LPBF is emphasised with promising results in these studies.

The above identified opportunity thus forms the main theme of the research presented in this thesis. Furthermore, the application of LPBF as an MAM method to address this scientific gap not only contributes to local drug delivery strategies for cementless implants, but also to the arsenal of demonstrator applications for furthering of the industrial uptake of the LPBF technology. In the following sections the LPBF process is discussed in the context of processing a biomaterial used for the manufacturing of cementless hip stems, Grade 23 titanium (Ti6Al4V ELI).

### **2.3 Laser Powder Bed Fusion (LPBF)**

LPBF is an MAM process in which thermal energy from a laser beam is used to fuse material powder particles. The term AM has collectively been defined as “the process of joining materials to make parts or objects from 3D model data, usually layer upon layer, as opposed to subtractive manufacturing methodologies” (ASTM International, 2012). Due to this layer-by-layer nature, part fabrication is often referred to as “building” and jobs can be referred to as “builds”.

Fabrication of near net shape titanium alloy functional parts with MAM processes is being incorporated in the aerospace and biomedical industries for the production of high-value components in small batches (Caggiano et al., 2019). MAM offers production benefits through its efficient use of material, integration of components, topologically optimised and lightweight structures, and the capability for free form internal features (Petrovic et al., 2011). Such parts entail complex geometries unsuited to conventional manufacturing processes. Furthermore, geometrically complex parts can be fabricated by MAM processes with reduced lead times and tooling requirements (Holmström et al., 2010).

At present, LPBF processes offer the greatest dimensional accuracy and highest resolution in powder based MAM (De Pasquale et al., 2019). The term LPBF consolidates the previously used terms such as selective laser melting (SLM), LaserCUSING, and direct metal laser sintering (DMLS), to refer to the manufacturing process without directly distinguishing between machine manufacturers. A simplified schematic of the LPBF process inside the build chamber is presented in Figure 2-5.

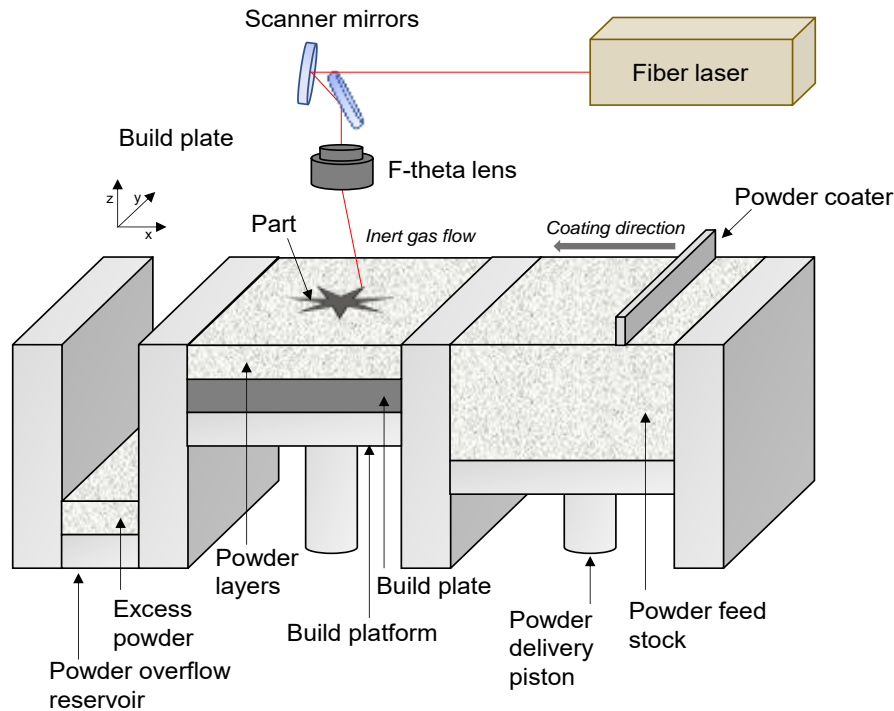


**Figure 2-5: Simplified schematic representation of the LPBF process inside the build chamber**

The LPBF process fabricates three dimensional (3D) parts one layer at a time. A thin layer of metal powder is coated onto a horizontal building platform. A laser beam is then used to selectively irradiate and heat the powder particles in the x-y plane to beyond its melting temperature. Consequently, powder particles are fused according to the part's two-dimensional (2D) geometry at the respective z-coordinate. The building platform is then lowered by the specified layer thickness and the process repeats until the full 3D-part is built. To shield the material being processed from excessive oxidation and hydrogen pickup, the building chamber is flooded with an inert gas, typically nitrogen or argon (Sing et al., 2016).

### 2.3.1 Overview of LPBF Process Chain

In generic terms, the high-level process chain of producing components with LPBF reflects that of the general AM process chain to a large extent. Figure 2-6 presents the general LPBF process chain. Each of the high-level processes in Figure 2-6 contains several specific steps, which can have differing details regarding the intended application of the part to be manufactured.

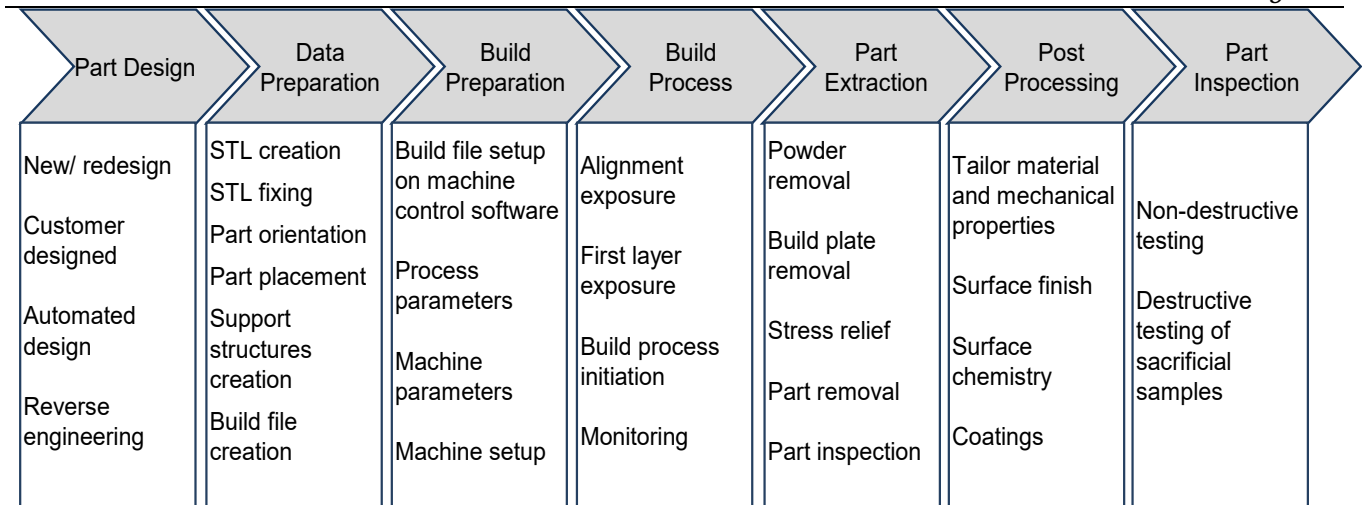


**Figure 2-6: Basic LPBF high level process chain (adapted from Hugo et al., 2018)**

The part design process involves the description of the part to be manufactured in the form of a digital solid 3D model. This model could be obtained in several different ways, for example, customer supplied, in-house designed and evaluated, generated through software which runs a solid model optimisation algorithm based on user specified boundary conditions, reverse engineering methods, or any combination of such methods. The digital integrity of the model to not contain any geometrical descriptive flaws such as any parts of the solid not enclosed is essential for streamlining subsequent model processing during downstream processes (Kim et al., 2015). Commercial CAD software packages have built in functions for evaluating the “water tightness” of the solid model which the user should utilise to confirm model integrity.

In the data processing procedure, the 3D model is digitally translated into different formats containing specific details for eventual input into the LPBF machine control software. The first step is the generation of an STL file, which is a mesh of triangles that approximates the surfaces of the solid model (Ma et al., 2001). The file can be exported in either binary or ASCII format and consist of all the coordinates of the vertices of the triangles which collectively approximate the original 3D CAD model (Grimm 2004). Figure 2-7 presents a solid model and its triangulated STL approximation.

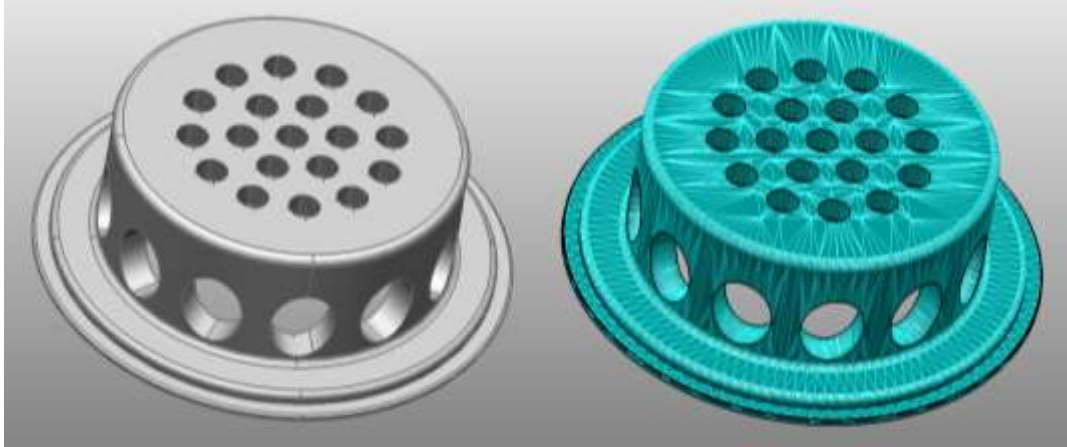


**Figure 2-7: Solid CAD model on the left with STL approximation format on the right (in-house example)**

Apart from potential accuracy issues due to the discretisation effect, several errors can exist in the triangulated mesh. These include inward facing surface normals, intersecting triangles, gaps between triangles, holes in the mesh caused by missing triangles, bad edges from adjacent triangles not sharing two vertices, and shell (cloud of uninterrupted triangles) errors such as noise shells or intersecting shells (Yau et al., 2003; Materialise, 2020). Care should be taken to fix all these errors before continuing with data preparation. In some instances, it might be necessary to revise the CAD solid model and re-export it as an STL file to fix or eliminate some of the features that could lead to difficult-to-fix errors.

The next step in data preparation is part orientation and support generation. Part orientation can affect several aspects of the component. One of the aspects is the need for support structures when certain features are oriented in a certain way. Support structures serve as attachment of these features to the building platform, to aid in heat dissipation during the process, and to help prevent part warping or collapse (Salmi et al., 2018). For example, supports are typically required for overhangs, holes or channels greater than a certain diameter (depending on machine), and features angled lower than a certain threshold with the horizontal (x-y plane) (typically  $45^\circ$  but can differ according to machine). Support structures not only increases the total amount of material required and building time, but also need to be removed afterwards and therefore influence part removal and post processing strategies, which further affect other properties of the final part and can significantly increase the production costs (Mirzendehtdel & Suresh, 2016; Jiang et al., 2018).

Next in the data preparation process is the generation of the build file. Machine manufacturers typically have specific software plugin(s) for their respective machines to translate the build configuration for communication with the machine control. These plugins are typically implemented in third party commercial pre-processing software such as *MAGICS* by *Materialise*. It encompasses the specification of parameters to use during slicing of the part as configured by the upstream processes. This includes the layer thickness and some parameters regarding the laser scanning strategy of each layer. Once build files are created successfully, they can be transferred to the machine control software for build preparation.

The build preparation process involves both digital and physical steps. Build files of parts created in the data preparation process are loaded on the machine control software and process parameters for each build file are specified. Machine parameters for the build job are also configured. Depending on the machine control software and output of the respective data preparation process, part orientation can still be adjusted by translation in the x-y plane and rotation around the z-axis. Machine setup typically involves preventative cleaning of any residue from the previous build, monitoring of the gas supply, sieving and loading of the power feed stock, mounting and levelling of the powder coater blade, preparation and mounting of the building plate as well as confirmation of even powder coating across the entire building platform. Preparation of the building plate involves levelling of the building plate surface with CNC milling, sand blasting to prevent laser reflection, and demagnetisation to avoid magnetic effects on the powder particles obstructing powder flow.

Prior to initiating the building process, a contour exposure scan can be performed to confirm correct translation of all part placements on the building plate from machine software to hardware. Next it is important to expose the first layer a few times in order to ensure strong fusion between this layer and the building plate. If no errors or malfunctions have been detected, the building process can be started. The building process should ideally be monitored periodically by the operator either on site or remotely so that corrective actions can be taken if possible, in order to save the build. Build failures are costly and online process monitoring options are being introduced in commercial machines and intensively researched, the details of which are outside of the scope of this study (Clijsters et al., 2014; Everton et al., 2016; Kolb et al., 2018).

When the build is finished, unconsolidated powder is present around the fabricated parts as well as on various surfaces of the machine's building module. As much as possible of this powder should be recycled and difficult to access powder can be removed by an immersion separating vacuum. Powder is also removed from the individual parts and part features. Details regarding the powder recycling steps vary from machine to machine and can either be manual or automated. The build plate can then be safely removed, and it is recommended to first be stress relieved before the parts are removed. Parts are generally removed by wire electrical discharge machining (w-EDM), bandsaw, or manual processes in special cases. After removal, parts should first be inspected visually for obvious defects such as excessive oxidation (Figure 2-8(a)), cracks (Figure 2-8(b)), delaminated layers (Figure 2-8(c)), excessive distortion (Figure 2-8(d)), and failed features (Figure 2-8(e)). Causes of defects need to be traced and if it is due to effects from actions in the data and build preparation steps, these need to be revised before rebuilding the parts, whereas hardware problems typically need to be addressed by a machine manufacturer certified technician.

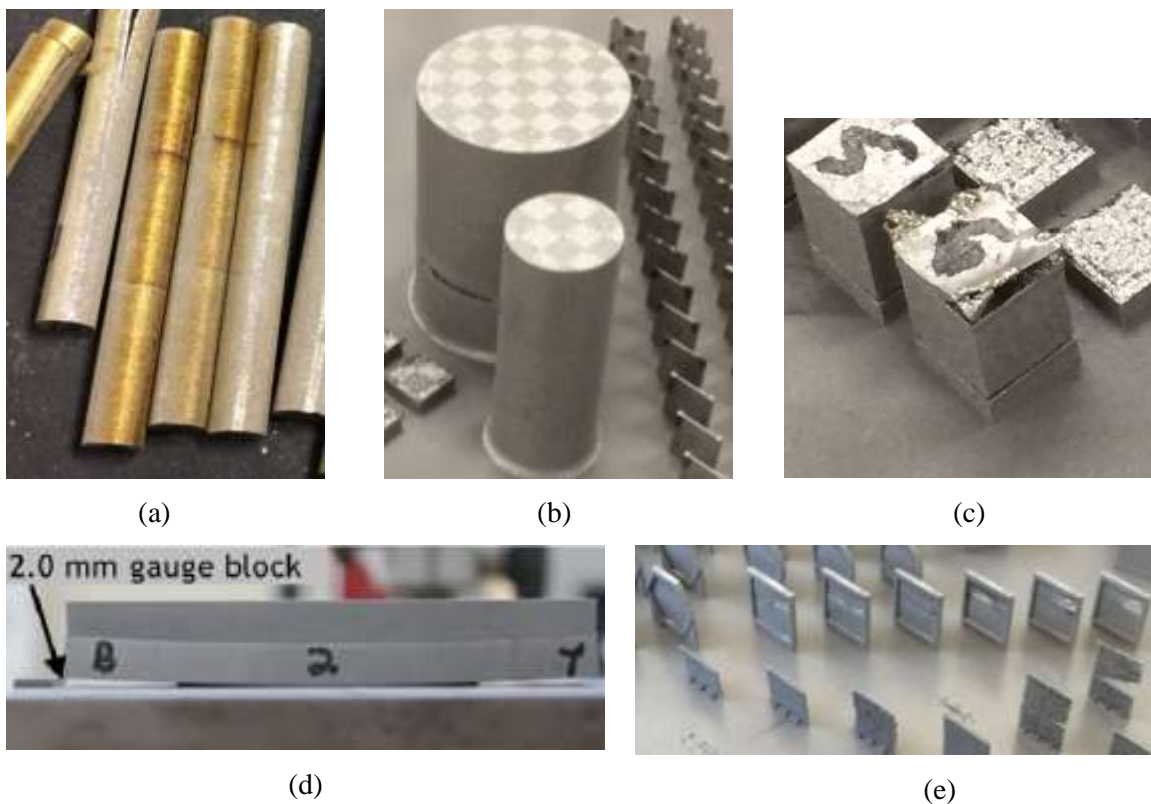


**Figure 2-8: Defects on Ti6Al4V ELI parts fabricated by LPBF with (a) excessive oxidation, (b) cracking, (c) delamination, (d) distortion (Hagedorn-Hansen et al., 2017), (e) failed features (in-house examples)**

Post processing of fabricated parts depends on the application and required mechanical and material properties (Wauthle et al., 2015). It includes steps to alter the microstructure and mechanical properties, reduce porosity, improve surface finish, and modify surface chemistry (Liu & Shin, 2019). Post processing steps are important for parts intended for load bearing applications (Masuo et al., 2018). It is possible that parts are designed for applications which require little to no post processing.

Parts intended for functional application can be inspected through non-destructive testing (NDT) techniques while sacrificial samples which accompanied the actual parts through the same process chain can be tested destructively. Sacrificial specimens provide information on the microstructural and mechanical properties that could be expected from the actual part (Roach et al., 2018). However, the limitations should be noted which arises from the nature of the LPBF process and the effects of several process parameters and part geometries on defect generation and subsequent mechanical behaviour (Dordlofva & Törlind, 2018). Furthermore, when applying NDT techniques to LPBF produced parts, it should be respected that generated defects would be not similar to defects arising during conventional processes such as casting and welding. Due to the highly customisable ability, once-off part designs, and lack of standardised NDT detection limits for associated defects, acceptance criteria would currently be part-specific (Waller et al., 2016; Seifi et al., 2017). Destructive testing refers to standard testing methods for evaluation of material and mechanical properties as specified in the respective international standards.

### **2.3.2 Overview of the LPBF Building Process**

The cyclic nature of the LPBF process together with the main processes and influencing factors are presented in Figure 2-9. The powder layer deposition process is influenced by the properties of the metal powder and the powder coating subsystem. The powder coating subsystem configuration is machine specific and subject to the manufacturer's design. Typically a roller or blade (flexible or rigid) is used to evenly coat a layer of powder. Properties of the coated powder layer are powder packing density, layer thickness, absorptivity, and thermal conductivity (Spierings et al., 2016). Powder layer properties are affected by the following parameters from the coating system and powder properties, coater type, layer thickness, coating speed, dose step, powder chemical composition, particle morphology, particle size distribution, van der Waals forces, moisture, powder flowability, and powder apparent and tap density (Sutton et al., 2017).

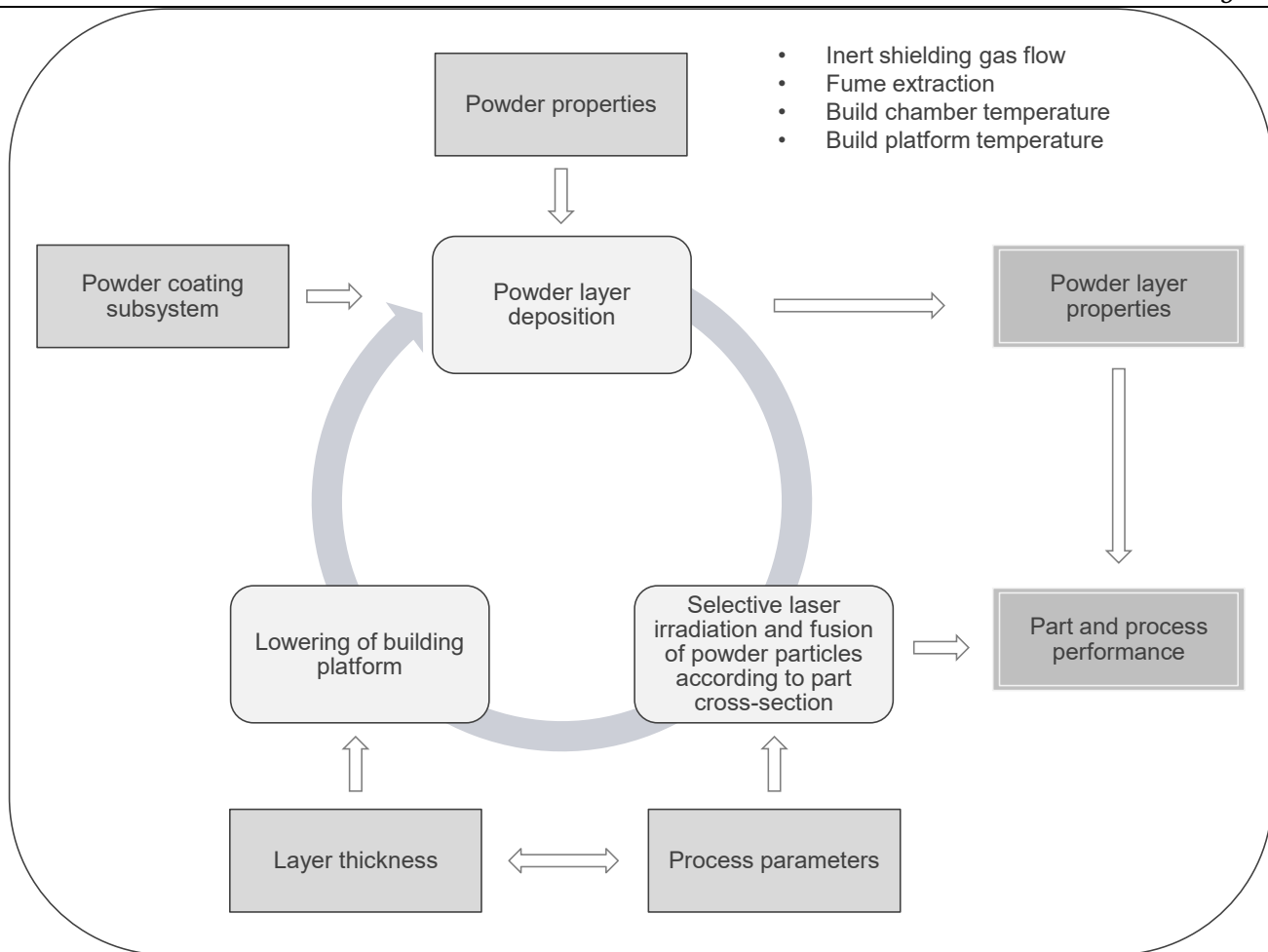


**Figure 2-9: Main processes and factors influencing the LPBF process and part performance (adapted from Spierings et al., 2016)**

The powder layer in turn affects the performance of the specified processing parameters for the exposure, melting, and fusion of the powder layer with the laser beam according to the part cross section geometry (Strondl et al., 2015). In reality, a multitude of process parameters affect the melting process, many of which are predefined according to machine and material supplier and therefore outside of user control (Spears & Gold, 2016). The key controllable process parameters however, which affect the melting process are laser power, laser spot size, scanning speed, scanning pattern, hatch spacing, powder size distribution, powder layer thickness, build plate temperature, and oxygen content in the build chamber (Song et al., 2012; Kasperovich et al., 2016; Li et al., 2018).

Figure 2-10 presents a schematic of the scanning and melting of powder particles in the coated layer to generate scan tracks. Scan tracks are the result of the vectors that define the laser path, and can be considered as a multitude of mini-welds (Ladewig et al., 2016). The active volume of melting is the

melt pool, demonstrated in Figure 2-10(a) together with its simplified heat transfer aspects. These tracks need to be sufficiently fused both to the preceding layers (or build plate in case of the first layer) as well as to adjacent tracks. The scan tracks are spaced in reference to each other with the parameter, hatch spacing (Figure 2-10(b)).

Stability and fusion of the tracks to the preceding layers are largely influenced by the properties of the melt pool (Gusarov et al., 2007). Formation and behaviour of the melt pool is a complex procedure and is governed by multiple physical mechanisms, which is outside the scope of this study (Yadroitsev et al., 2010; Khairallah et al., 2016). Nevertheless, these properties are largely influenced by the controllable laser beam parameters such as type of beam, spot size, power, scanning speed, and exposure mode (pulsed or continuous). Generally, laser beams with Gaussian intensity profiles are applied with heat flux density according to Equation 2-1, indicated by the Gaussian curves side and top views in Figure 2-10 (Hann et al., 2011; Song et al., 2012; Xiang et al., 2018).

$$q(r) = \frac{2A_p P}{\pi r_b^2} e^{\left(\frac{-2r^2}{r_b^2}\right)} \quad (2-1)$$

Where  $r$  is the radial distance from the beam centre,  $A_p$  is the absorptivity of the powder layer,  $P$  is the laser power, and  $r_b$  is the effective beam radius at which the laser intensity decreases to  $\frac{1}{e^2}$  of its peak value at the centre. The average area heat flux density across the spot size can then be written as,

$$q_m = \frac{1}{\pi r_b^2} \int_0^{r_b} q(2\pi r) dr \quad (2-2)$$

$$q_m = \frac{0.865A_p P}{\pi r_b^2} \quad (2-3)$$

The performance of the melting step has direct influences on part properties, performance, and quality. Once this process has finished, the building platform is lowered by the layer thickness and the cycle continues with coating of a new powder layer.

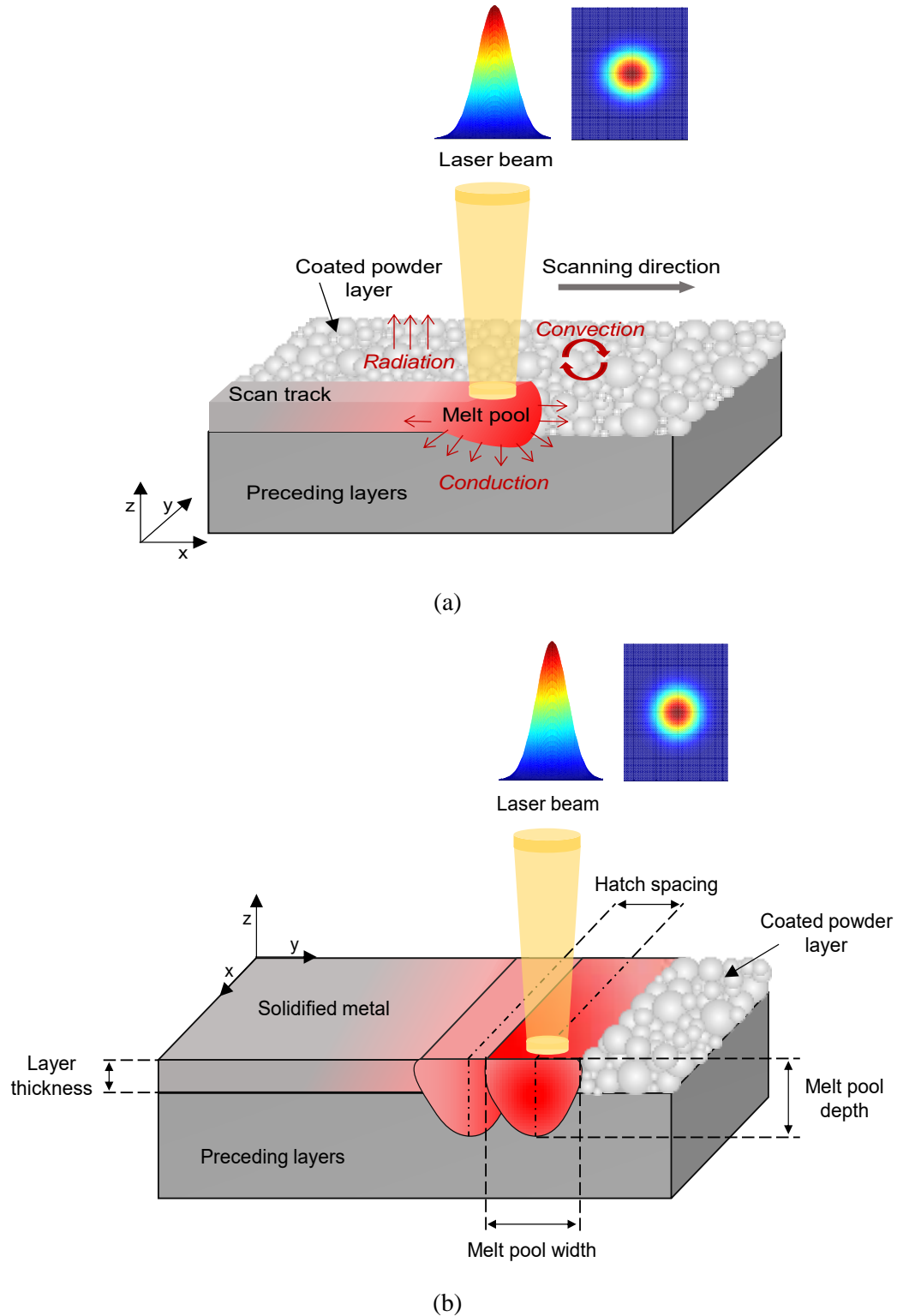


**Figure 2-10: Schematic representation of scanning and melting the coated powder layer with a Gaussian laser beam with (a) scan track longitudinal view and (b) scan track cross sectional view (adapted from Sola & Nouri, 2019; Wessels et al., 2019; Zheng et al., 2019)**

### 2.3.3 LPBF of Ti6Al4V ELI

Grade 23 titanium alloy, Ti6Al4V extra low interstitial (ELI), is a material widely used for the manufacture of femoral hip stems due to its biocompatibility, lower Young's modulus compared to the approved alternative metals of stainless steels and cobalt-chromium (CoCr) alloys, high strength-to-weight ratio, and corrosion resistance (Long & Rack, 1998; Geetha et al., 2009). It contains less interstitial impurities in the lattice structure of the elements Iron (Fe), Carbon (C), and Oxygen (O) than the known Grade 5 Ti6Al4V (Murr et al., 2009). The chemical composition (wt%) of Ti6Al4V ELI after LPBF processing, as specified in the ASTM F3001-14 (2014) standard is presented in Table 2-2.

**Table 2-2: Specified composition of Ti6Al4V ELI after LPBF processing (ASTM International, 2014)**

Element	Minimum	Maximum
Aluminium	5.50	6.50
Vanadium	3.50	4.50
Iron	...	0.25
Oxygen	...	0.13
Carbon	...	0.08
Nitrogen	...	0.05
Hydrogen	...	0.012
Yttrium	...	0.005
Other elements, each	...	0.10
Other elements, total	...	0.40
Titanium	remainder	

Titanium is an allotropic element that can exist in two different crystal structures, an  $\alpha$  phase with a hexagonal close packed (HCP) atomic arrangement (Figure 2-11(a)) and a  $\beta$  phase with a body centred cubic (BCC) atomic arrangement (Figure 2-11(b)). A solid-state phase transformation from  $\alpha$  to  $\beta$  phase occurs when commercially pure titanium (cpTi) is heated through 882.5 °C at atmospheric pressure (Long & Rack, 1998). To retain a percentage of  $\beta$  phase in the microstructure at lower temperatures, Ti is alloyed with phase stabilising elements (Figure 2-11(c)) (Donachie, 2000). The temperature above which a complete transformation to  $\beta$  phase occurs is termed the transus temperature and it depends on the mass fraction of phase stabilising alloying elements. Ti6Al4V ELI contains Al which strengthens and stabilises the  $\alpha$  phase while raising the  $\beta$ -transus temperature, which is  $980 \pm 20$  °C, and V as  $\beta$  stabiliser, which stabilises the  $\beta$  phase and allows a fraction of it to be retained at

temperatures below the  $\beta$ -transus temperature (Chavez-Diaz et al., 2018; Liu & Shin, 2019). The presence of  $\beta$  phase enhances the ductility and toughness of the alloy (Wauthle et al., 2015). In a commercially produced wrought Ti6Al4V ELI bar with a slightly elongated  $\alpha$  and intergranular  $\beta$  microstructure, the percentage  $\beta$  phase has been estimated at 12 % (Elmer et al., 2004).

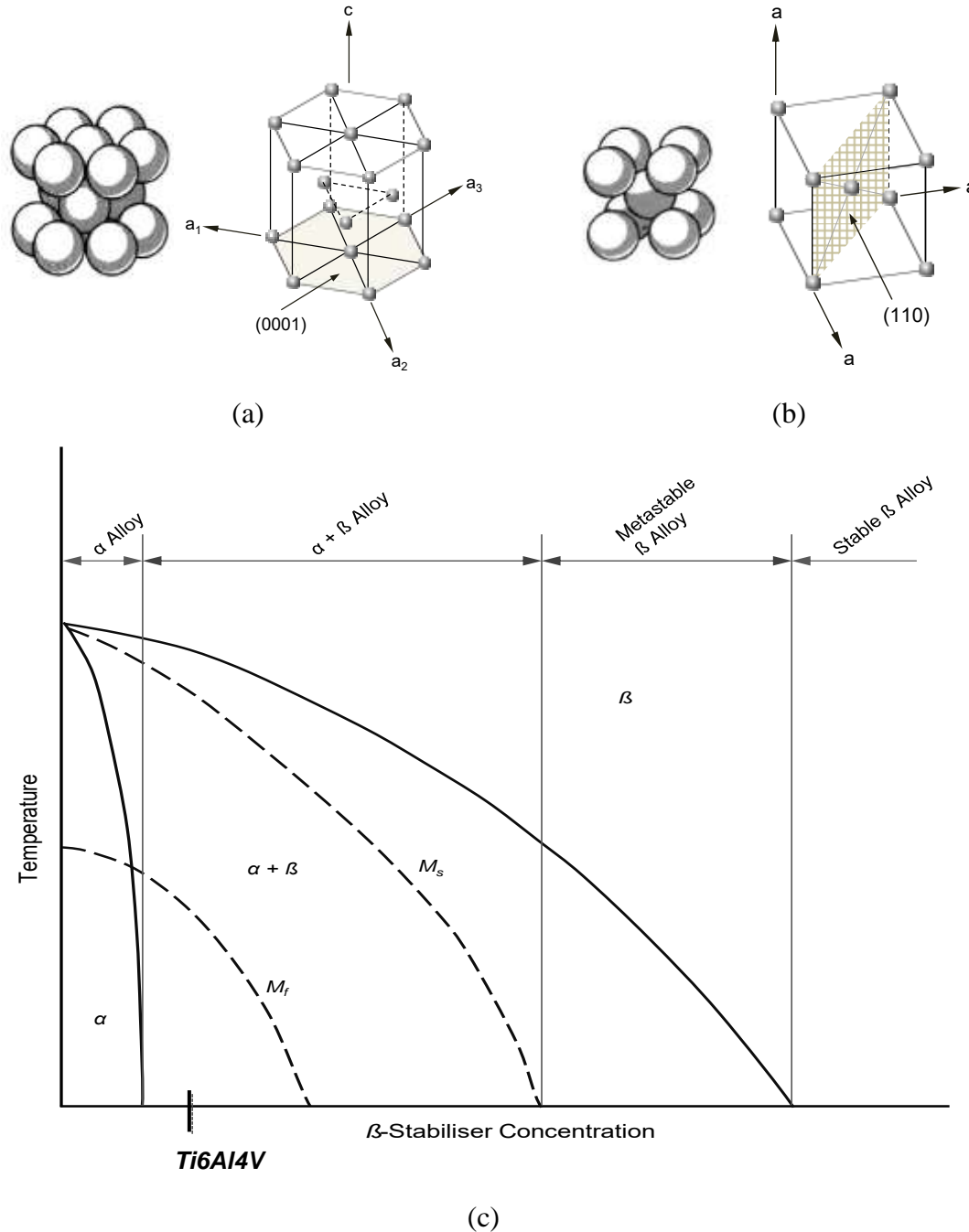


**Figure 2-11: Titanium phases with (a)  $\alpha$  phase in HCP unit cell arrangement, (b)  $\beta$  phase in BCC unit cell arrangement, and (c) positioning of  $\alpha + \beta$  Ti6Al4V on a pseudobinary phase diagram with regards to the  $\beta$  stabilising element concentration (adapted from Donachie, 2000; Lütjering & Williams, 2007)**

During LPBF processing of Ti6Al4V ELI, however, the generated microstructure is dominated by an acicular  $\alpha'$  martensitic phase (Figure 2-12(a)). As the melt pool temperature nears that of the solidus temperature ( $\sim 1604$  °C), prior  $\beta$  grains are formed, after which a fine acicular  $\alpha'$  martensitic phase forms within prior  $\beta$  grains due to the high cooling rate (in the order of  $10^6$  K/s (Rafi et al., 2013)). The orientation and morphology of the prior  $\beta$  grains are affected by the thermal cycles experienced within the material during laser exposure of each new layer and presents a characteristic columnar structure preferentially elongated in the building direction (Figure 2-12(b)) (Thijs et al., 2010; Qiu et al., 2013; Ali et al., 2018; Zhao et al., 2018).

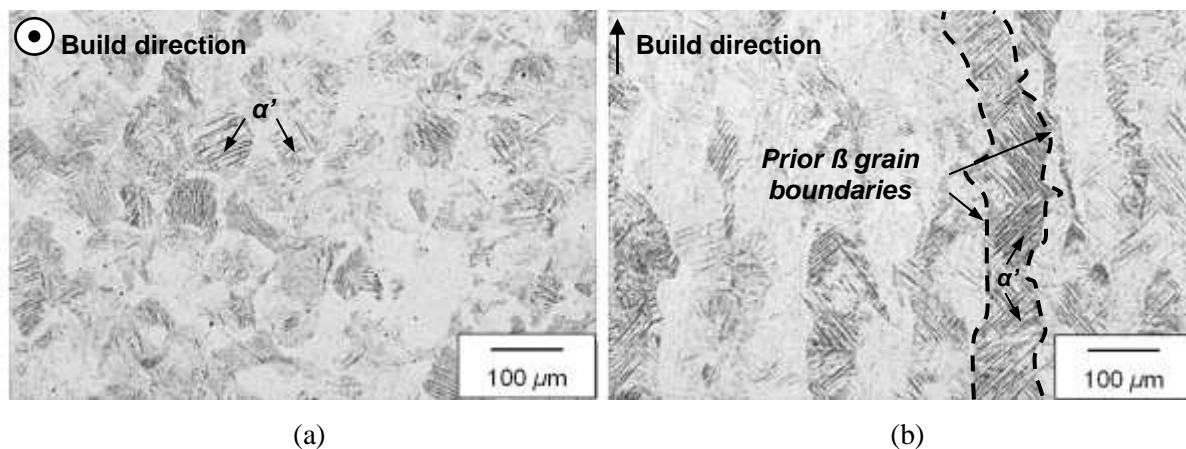


**Figure 2-12: As-built microstructure of LPBF produced Ti6Al4V with (a) top view (perpendicular to build direction) and (b) side view (parallel to build direction) (adapted from Zhou et al., 2018)**

This microstructural texturing effect imparts anisotropy to the mechanical properties and the arrangement of the texture throughout the part features depends on the build orientation of the part on the build plate (de Formanoir et al., 2020). Table 2-3 presents a summary of some of the mechanical properties of as-built tensile specimens from various LPBF machines with ASTM F136-13 specification of wrought Ti6Al4V ELI for reference. The referenced data were reported for specimens with microstructure in the as-built condition. Although the tensile strength of the as-built condition is typically higher than that of the wrought material, the ductility can be significantly lower and also tend to differ considerably more between studies compared to the ultimate tensile strength (UTS) and yield strength ( $\sigma_y$ ). The percentage difference in the data between the referenced studies of the UTS is around 20% for both the vertical and horizontal orientations whereas the yield strength differs by 44% in the vertical and by 21% in the horizontal direction respectively. The % elongation, however, differs by 150%. This highlights a major challenge in the standardisation of LPBF produced components. Not

only does anisotropy exist in the mechanical properties of parts built on the same machine, but differences in the properties are present in parts built on different machines with different process parameters, environmental conditions, and powder stock.

**Table 2-3: Summary of tensile properties of as-built LPBF Ti6Al4V ELI**

LPBF Machine	Specimen Orientation / Surface Finish	UTS (MPa)	$\sigma_y$ (MPa)	Elongation (%)	References
SLM Solutions 250HL	Vertical / As-built	1080	1008	1.6	(Thöne et al., 2012)
LM-Q <sup>a</sup>	Horizontal / Wire EDM	1267 ± 5	1110 ± 9	7.28 ± 1.12	(Vrancken et al., 2012)
Concept Laser M2	Horizontal / As-built	1250 ± 50	1070 ± 50	5.5 ± 1	(Qiu et al., 2013)
	Vertical / As-built	1050 ± 40	1180 ± 30	8.5 ± 1.5	
EOS M270	Horizontal / Machined	1269 ± 19	1195 ± 19	5 ± 0.5	(Rafi et al., 2013)
	Vertical / Machined	1219 ± 20	1143 ± 30	4.89 ± 0.6	
MTT 250	Horizontal / As-built	1035 ± 29	910 ± 10	3 ± 0.8	(Edwards & Ramulu, 2014)
Concept Laser M2 <sup>b</sup>	Vertical / As-built	1040-1062 (1051)	664-802 (733)	11.3-12.7 (12.0)	(Kasperovich & Hausmann, 2015)
	Vertical / Machined	1151-1157 (1154)	984-988 (986)	10.2-11.3 (10.75)	
LSNF-1 <sup>a</sup>	Not specified	1268 ± 10	1030 ± 60	4.2 ± 0.4	(Han et al., 2017)
EOS M280 <sup>d</sup>	Horizontal / As-built	~1265 ± ~5	~1125 ± 70	~9.2 ± ~0.6	(Yadroitsev et al., 2018)
	Vertical / As-built	~1240 ± ~13	~1110 ± ~10	~8.3 ± ~0.75	
3D Systems ProX®	Horizontal / As-built	1257 ± 2	1082 ± 55	9.2 ± 0.9	(de Formanoir et al., 2020)
	Vertical / As-built	1289 ± 1	1146 ± 33	9.3 ± 0.5	

DMP 320	build				
	Diagonal / As-	1229 ± 4	1084 ± 45	9.3 ± 0.6	
	built				
ASTM F136-13 <sup>e</sup>		860 (min)	795 (min)	10 (min)	(ASTM International, 2013)

<sup>a</sup> custom developed machines

<sup>b</sup> mean value in brackets

<sup>c</sup> orientation not specified, but based on standard specimen dimensions it is likely to be vertical due to custom build volume reduction unit of 66 mm x 66 mm x 125 mm used

<sup>d</sup> estimated from graph

With appropriate post processing heat treatments, the microstructure can be altered to yield tensile strength and ductility comparable to that of the wrought counterpart (Ter Haar & Becker, 2018). However, defects in parts can arise from the LPBF process such as porosity from entrapped gas (Figure 2-13(a)), lack of fusion (Figure 2-13(b)), and surface roughness (Figure 2-13(c)) which significantly reduce the number of cycles to failure of standard axial fatigue test specimen geometries (Leuders et al., 2014). These defects act as stress concentration areas and promote early crack initiation (Kasperovich & Hausmann, 2015).

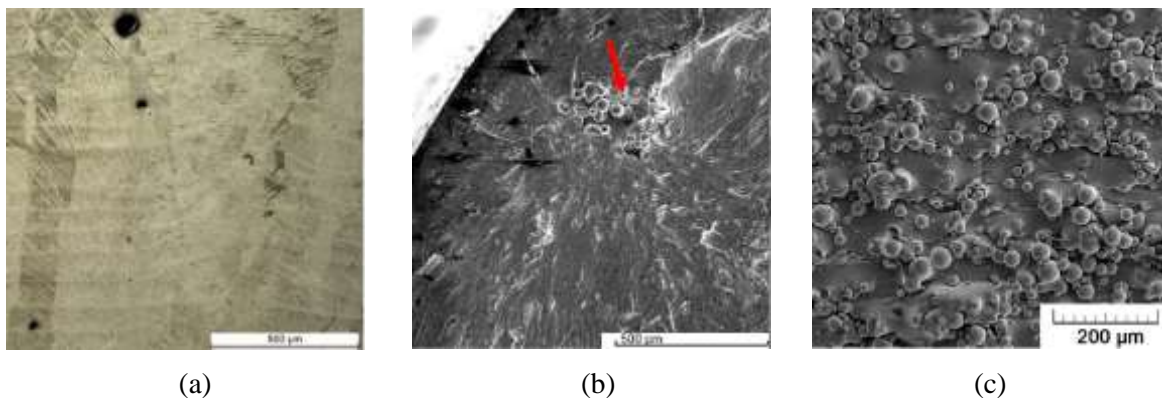


**Figure 2-13: Example defects (a) porosity from entrapped gas, (b) lack of fusion, and (c) surface roughness (Ali et al., 2018; Wycisk et al., 2014; Fousova et al., 2018)**

Currently, the most effective way of addressing these are through a combination of hot isostatic pressing (HIP) and surface finishing post processing operations (examples are presented in Table 2-4) (Kasperovich & Hausmann, 2015; Li et al., 2016; Du Plessis & Macdonald, 2020). HIPing is typically performed for two hours at a temperature of 920 °C and a pressure of 1000 bar. Although the details regarding the mechanisms behind phase transformations and precipitation of phases in the microstructure are outside the scope of this study, it is important to bear knowledge of the different

microstructures and resulting mechanical properties when developing a LPBF centred process chain as it significantly influences the functional performance of the part.

**Table 2-4: Fatigue life of as-built and HIPed LPBF produced specimens**

LPBF Machine	Specimen Condition	Maximum Reported Cycles	Maximum Stress (MPa)	Stress Ratio R	Reference
SLM 250HL	Vertical build; As-built; Machined;	$2 \times 10^6$	275	-1	(Leuders et al., 2014)*
	Vertical build; HIP; Machined	$1 \times 10^6$	675		
3D Systems ProX 300	Vertical build; As-built	$5 \times 10^7$	250	-1	(Benedetti et al., 2018)*
	Vertical build; HIP	$5 \times 10^7$	400		
SLM 250HL	Vertical build; stress relieved; machined	$2 \times 10^9$	250	-1	(Günther et al., 2017)*
	Vertical build; HIP; Machined	$1 \times 10^9$	425		
Concept Laser M2	Vertical build; HIP	$1 \times 10^7$	200	-1	(Kasperovich & Hausmann, 2015)
	Vertical build; HIP; machined	$1 \times 10^7$	350		

\*values estimated from graphs in respective publication

### 2.3.4 Influence of Selected Process Parameters

The LPBF process is influenced by many parameters. Spears and Gold (2016) lists fifty parameters which they classified into four groups, laser and scanning parameters, powder material parameters, powder bed properties and recoat parameters, and build environment parameters. Many of these parameters, however, are fixed based on for example, machine hardware such as laser wavelength and focal diameter or on third party suppliers such as powder material properties and shielding gas purity (Spears & Gold, 2016). Figure 2-14 presents a summary of LPBF process parameters as presented by Aboulkhair et al. (2014). Although their classification is not exhaustive, it demonstrates the complexity of the process, as a multitude of possible settings exist for each parameter, rapidly increasing the computational requirements for more comprehensive simulation studies (Khairallah et al., 2016). Studies therefore rely largely on empirical approaches in order to elucidate the effects of parameters on different aspects of LPBF produced parts.

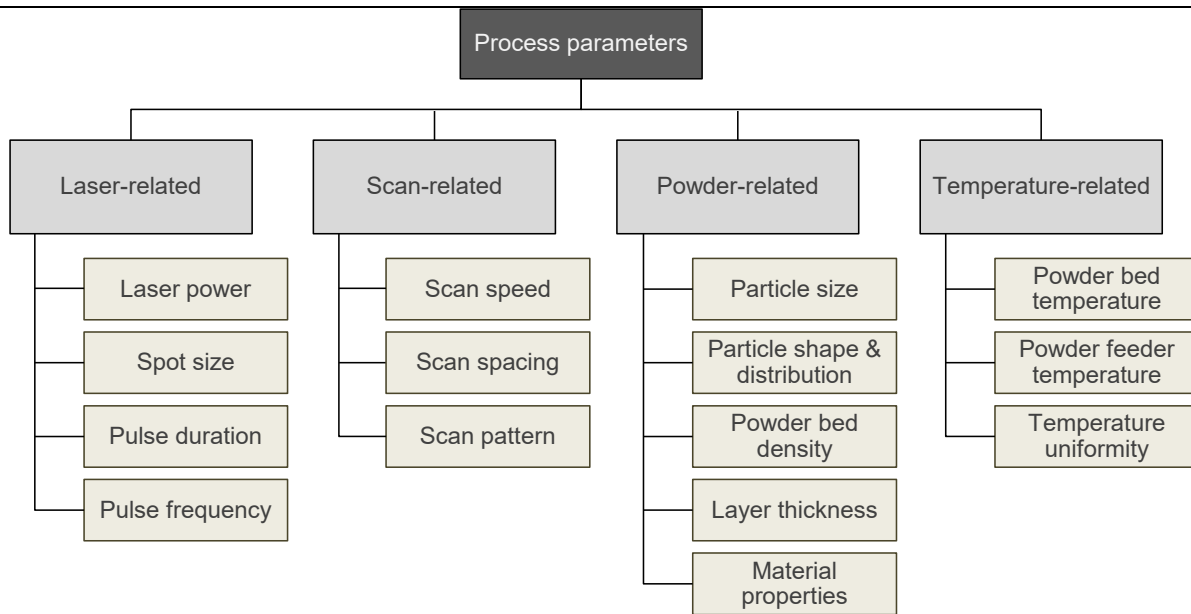


**Figure 2-14: Summary of LPBF process parameters (recreated from Aboulkhair et al., 2014)**

In order to relate a combination of the main controllable parameters listed in Figure 2-14, volumetric energy (VED) is often used. The VED ( $\text{J}\cdot\text{mm}^{-3}$ ) is expressed as a function of laser power, scanning speed, layer thickness, and hatch spacing according to Equation 2-4,

$$VED = \frac{P}{vht_l} \quad (2-4)$$

where,  $P$  is laser power (W),  $v$  the scanning speed ( $\text{mm}\cdot\text{s}^{-1}$ ),  $h$  the hatch spacing (mm), and  $t_l$  the layer thickness (mm). Although the VED is a useful expression incorporating the key process parameters, concerns exist in using VED as a key criterion (Bertoli et al., 2017). For example, it is evident that aliasing exist within the expression where different values of the parameters can yield the same VED.

It also does not account for the complex physics during melt pool formation and solidification (Bertoli et al., 2017). Nevertheless, it is a useful tool to relate the parameter settings to process performance, especially with regards to stable melting zones, microstructure, mechanical properties, and resulting porosity within applicable ranges for the respective parameters (Dilip et al., 2017) (Han et al., 2017). Depending on the specific LPBF machine hardware configuration and limitations, different value ranges for VED have been identified in literature for processing of Ti6Al4V ELI. This suggests the existence of local optimum points in the parameter settings which all provide acceptable outcomes. For example Gong et al. (2015) achieved a local maximum in density at a VED of  $42 \text{ J}\cdot\text{mm}^{-3}$  (120 W laser power,  $960 \text{ mm}\cdot\text{s}^{-1}$  scanning speed, 0.1 mm hatch spacing, and 0.03 mm layer thickness), Thijs et

al.(2010) reported their optimal parameters at  $93 \text{ J.mm}^{-3}$  (42 W laser power,  $200 \text{ mm.s}^{-1}$  scanning speed, 0.075 mm hatch spacing, and 0.03 mm layer thickness), and Mierzejewska (2019) reported an optimal VED range of  $78 - 127 \text{ J.mm}^{-3}$ .

Strong corroboration exists between studies with regards to the porosity effects when deviating from the respective value ranges identified for VED (Kasperovich et al., 2016; Mierzejewska, 2019; Du Plessis, 2019). Identification of suitable VEDs is generally based on minimising the porosity. Deviation from the identified values in both lower and higher directions results in increased porosity as demonstrated in Figure 2-15. For each level of laser power, the energy density decreases from left to right with increasing scanning speed.

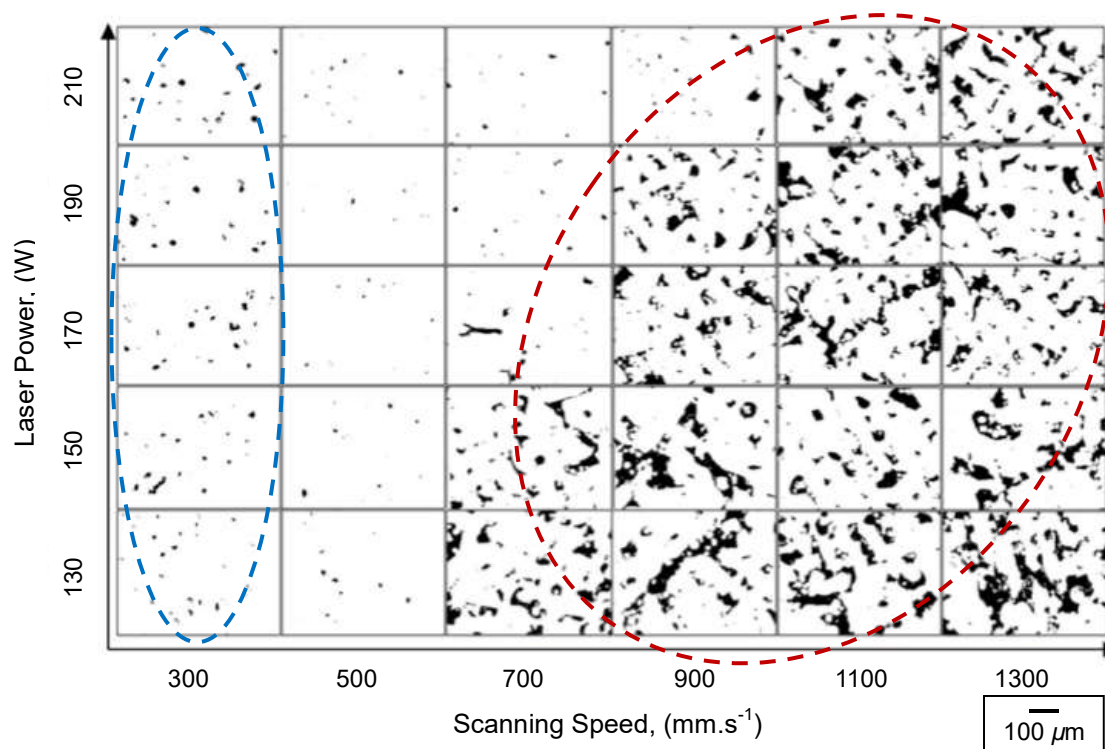


**Figure 2-15: Graphic representation of porosity as a function of laser power and scanning speed at constant hatch spacing of 0.1 mm, layer thickness of 0.03 mm, and laser spot size of 0.1 mm (adapted from Mierzejewska, 2019)**

The porosity in Figure 2-15 can be classified into two main categories, porosity due to overheating when the energy input is too high (region indicated with blue dashed line) or porosity due to insufficient energy input (region indicated with red dashed line) (Kasperovich et al., 2016). It can be observed in Figure 2-15 that pores formed due to insufficient energy input tend to be larger and more

irregular in shape than pores generated from excessive energy input. In both cases the pore formation mechanisms are complex with regards to melt pool physics and are addressed here more qualitatively.

When the energy input is too high, near spherical defects are typically observed. Gong et al. (2014) attributed these defects to a combination of the formation and entrapment of gas bubbles near the bottom of the melt pool during keyhole mode of melting, ejection of material from the molten pool due to recoil pressure from the generated vapour, and pitting from spherical particles which were ejected from the melt pool, weakly bonded to the top surface during solidification (also observed for suitable energy input levels as shown in Figure 2-16(a)) and subsequently removed by the powder coater during deposition of a new layer. Porosity due to inclusions of inert gas in the melt pool released upon solidification has also been reported (Kasperovich et al., 2016).

With low energy input, phenomena such as insufficient and intermittent melting, lack of fusion between layers, lack of overlap between scan tracks, and balling occurs (Gong et al., 2014; Kasperovich et al., 2016). During balling, the scan tracks contain discontinuities from the formation of spheroid particles of solidified material Figure 2-16(b). When the melt pool does not sufficiently wet the preceding layers, the surface tension of the melt pool tends to generate bead like particles (Cardaropoli et al., 2012). Balling is likely to occur when the total surface area of the melt pool becomes larger than that of a sphere with the same volume (Kruth et al., 2004).

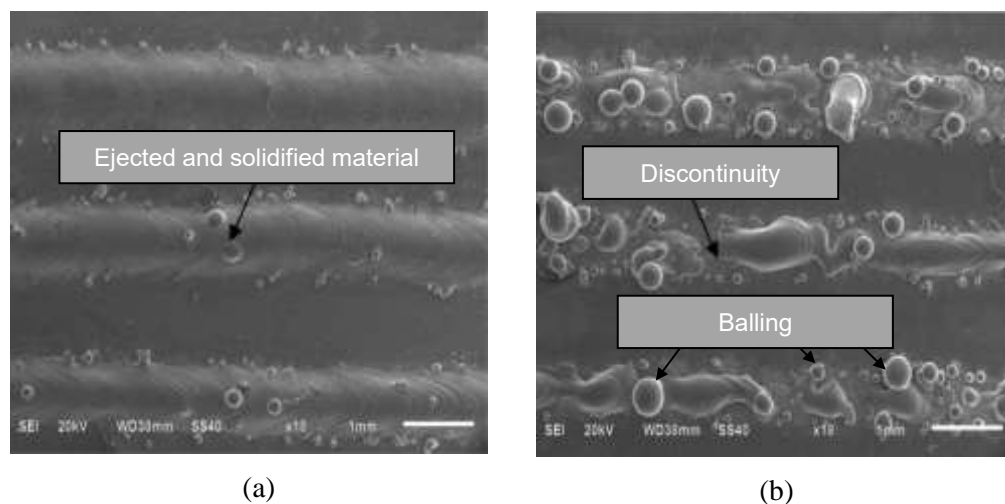


**Figure 2-16: Single scan tracks produced at 400 W laser power and 200  $\mu\text{m}$  layer thickness Ti6Al4V with (a) sufficient energy input (top to bottom scanning speeds of 40, 60, and 80  $\text{mm}\cdot\text{s}^{-1}$ ) and (b) insufficient energy input (top to bottom scanning speeds of 160, 180, and 200  $\text{mm}\cdot\text{s}^{-1}$ ) (adapted from Shi et al., 2016)**

The focus within MAM part quality is typically towards minimizing porosity by identifying appropriate process parameter settings for specific machine and material combinations. For this study, however, the interest is in identifying a process window for the parameter settings that would induce different levels of porosity to impart permeability. Whereas the abovementioned studies demonstrated the two different porosity cases generated either by overheating or insufficient energy input, permeability of resulting specimens containing different levels of porosity was not investigated.

Reported permeable structures produced with LPBF are typically designed as lattices and fabricated with parameters optimized for minimum strut porosity (Ghouse et al., 2017; Zadpoor, 2019; Burton et al., 2019). Consequently, pore sizes are limited by pre-processing (data preparation) software and machine capabilities. These minimum dimensions are, at present, limited to around 450 - 500  $\mu\text{m}$  for pore size depending on the machine (Warnke et al., 2009; Zhang et al., 2014). Furthermore, unit cell designs are by their nature highly structured and pores typically align (Wang et al., 2016; Bobbert et al., 2017). The relatively large size of the pores combined with the low tortuosity potentially risks the passage of *S. aureus* into the implant, allowing for colonisation of the internal surfaces.

Pores induced by incomplete melting or overheating are stochastically distributed through the material with smaller diameters than that of lattice structures currently achievable with LPBF machines. The stochastic distribution of the pores throughout the material would significantly increase the tortuosity, possibly obstructing free movement of pathogens as well as provide the ability to tailor drug release by constraining the diffusion of vancomycin molecules.

Little readily available literature exists on tailoring of porosity for permeability through the process parameters itself. A possible reason for this sparsity of reported literature is the laser control software limitations regarding assigning different process parameters for various volumetric regions within a part. Abele et al. (2015) reported LPBF produced gas permeable thin wall structures of 250  $\mu\text{m}$  thickness in 1.4542 stainless steel, investigated according to a Design of Experiments (DoE) approach with hatch spacing, laser power, and scanning speed as independent variables. Within the ranges investigated for the independent variables, hatch spacing was identified as the main factor influencing porosity. Pore morphology and distribution and the effects on permeability of molecules in liquid solution were not reported (Abele et al., 2015). Integration of such permeable structures, built with parameters for induced porosity, into larger components with a dense bulk was also not addressed.

### 2.3.5 Post Processing Considerations

Depending on application, parts fabricated by LPBF may require further processing in order to impart properties that would enable it to meet the functional requirements (Benedetti et al., 2017). This includes, among others, the geometrical and dimensional accuracy, surface roughness, surface chemistry, surface and internal residual stresses, porosity, and microstructure. For reference, these are termed part properties, which in turn affect the mechanical properties of a part and its functionality. Some of these part properties can be addressed simultaneously during a single post processing operation, for example, porosity and microstructure can both be addressed through HIP treatment. Geometrical and dimensional accuracy, surface roughness, and surface residual stresses can be addressed simultaneously through material removal processes, or surface residual stresses can be addressed individually through, for example shot peening (Benedetti et al., 2017; Conradie et al., 2017; Bezuidenhout et al., 2020). The eventual process chain is therefore highly dependent on part application. For LPBF components, as presented in Table 2-4, one of the main challenges regarding part functionality is the relatively low fatigue strength of as-built LPBF parts compared to conventionally processed Ti6Al4V (Benedetti et al., 2018). Consequently, the focus of post processing tends to be on reducing surface roughness, eliminating porosity, and recrystallization of the as-built  $\alpha'$  martensite dominated microstructure to a more ductile  $\alpha + \beta$  configuration (Kasperovich & Hausmann, 2015; Li et al., 2016).

### 2.3.6 Design Constraints

Although much design freedom is afforded with MAM, it is not entirely constraint free. Attention is required to process details as well as machine limitations. Design for additive manufacturing (DFAM) approaches therefore plays an important role in achieving successful builds. Practical guidelines and frameworks are continuously being developed and some have been published by researchers for the considerations of alterations to features to ensure AM suitable designs and build orientations (Kranz et al., 2015; Vaneker et al., 2020). Specifically this encompasses considerations for angled and overhanging surfaces, edges and corners, walls, radii, holes, cavities and internal channels, support structures, access for powder removal, and material tolerances for finishing post processing operations (Kranz et al., 2015). These aspects are subject to machine capability and also machine hardware setup and software control system configuration.

## 2.4 Frameworks for Deriving an LPBF-Centred Interdisciplinary Approach

An opportunity exists for the expansion of available AM frameworks, which generally focus on the challenges and characterisation of the emerging design paradigm, DFAM, and its relation to existing bodies of knowledge (Rosen, 2007; Kranz et al., 2015; Laverne et al., 2017; Mingareev & Richardson, 2017; Zaman et al., 2018). Renjith et al. (2020) presents a summary of published DFAM approaches classified according to focus area. The main areas identified involve design problem analysis, idea generation, the design phases, and incorporation of AM capabilities in the conceptualisation phase. A framework that is applicable to the specific requirements of this study does not appear to exist. In this section, AM-centred and interdisciplinary problem solving frameworks are discussed. The reviewed frameworks provide a base from which an interdisciplinary framework for this study was derived.

To highlight the relevance of DFAM to the product development process, Kumke et al. (2016) divides the term into ‘DFAM in the strict sense’ and ‘DFAM in the broad sense’. ‘DFAM in the strict sense’ regards the core design process and refers to the appropriate application of emerging AM design rules in order to ensure appropriate designs while respecting AM’s unique capabilities, and ‘DFAM in the broad sense’ encompasses generic upstream and downstream DFAM-related processes, for example process selection, part or application selection, manufacturability analysis, and the AM building process itself Figure 2-17 (Kumke et al., 2016).

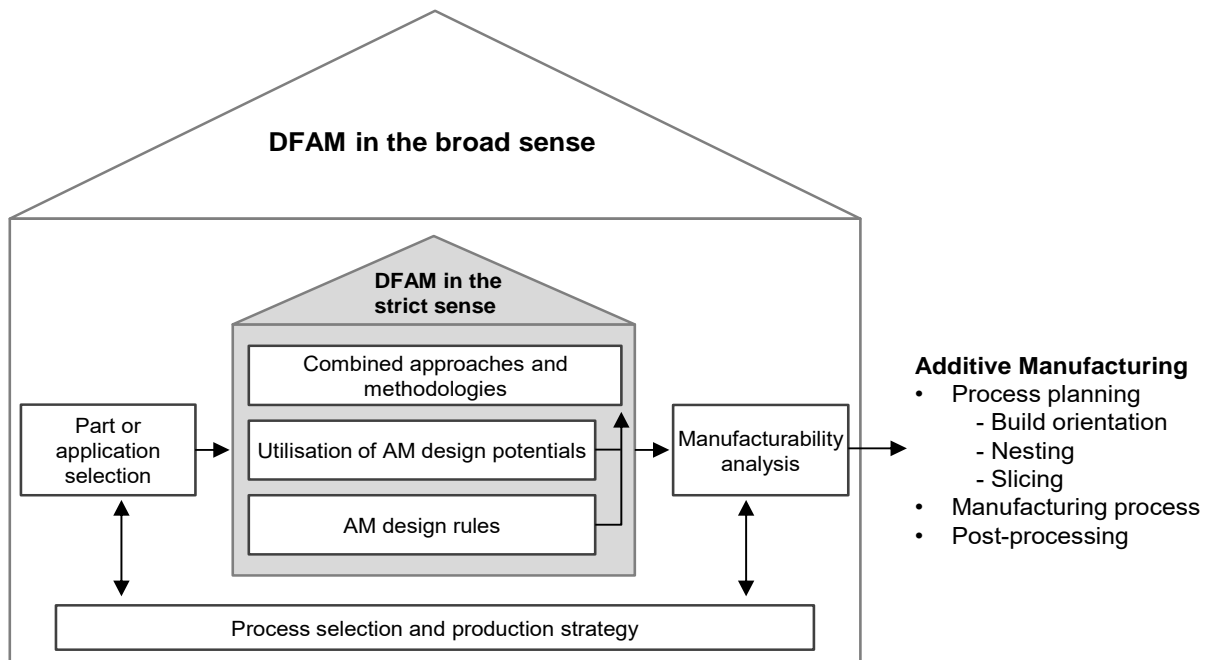
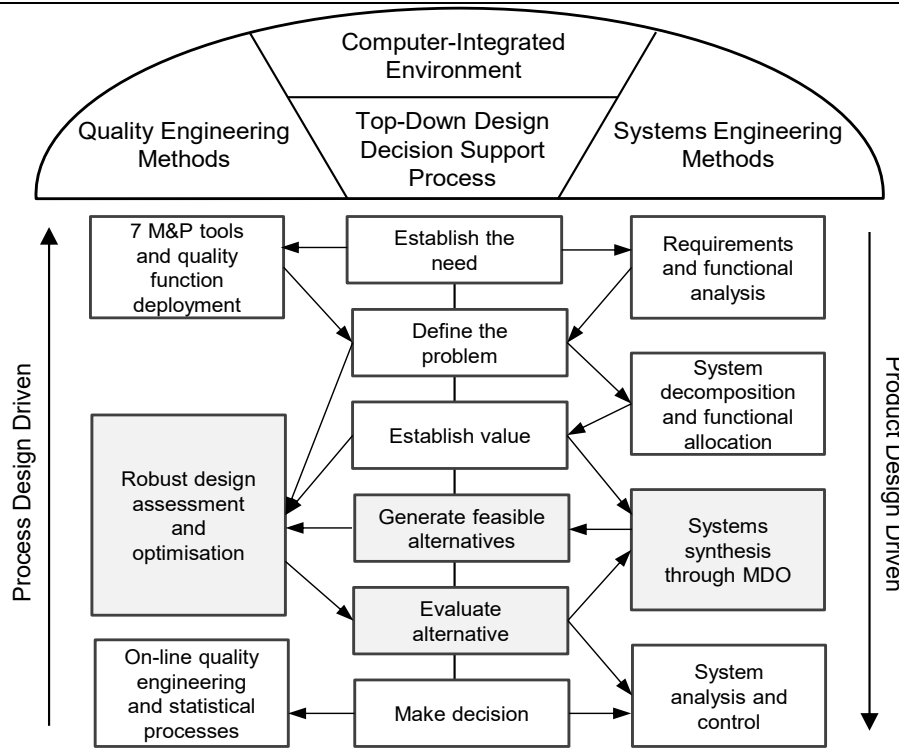


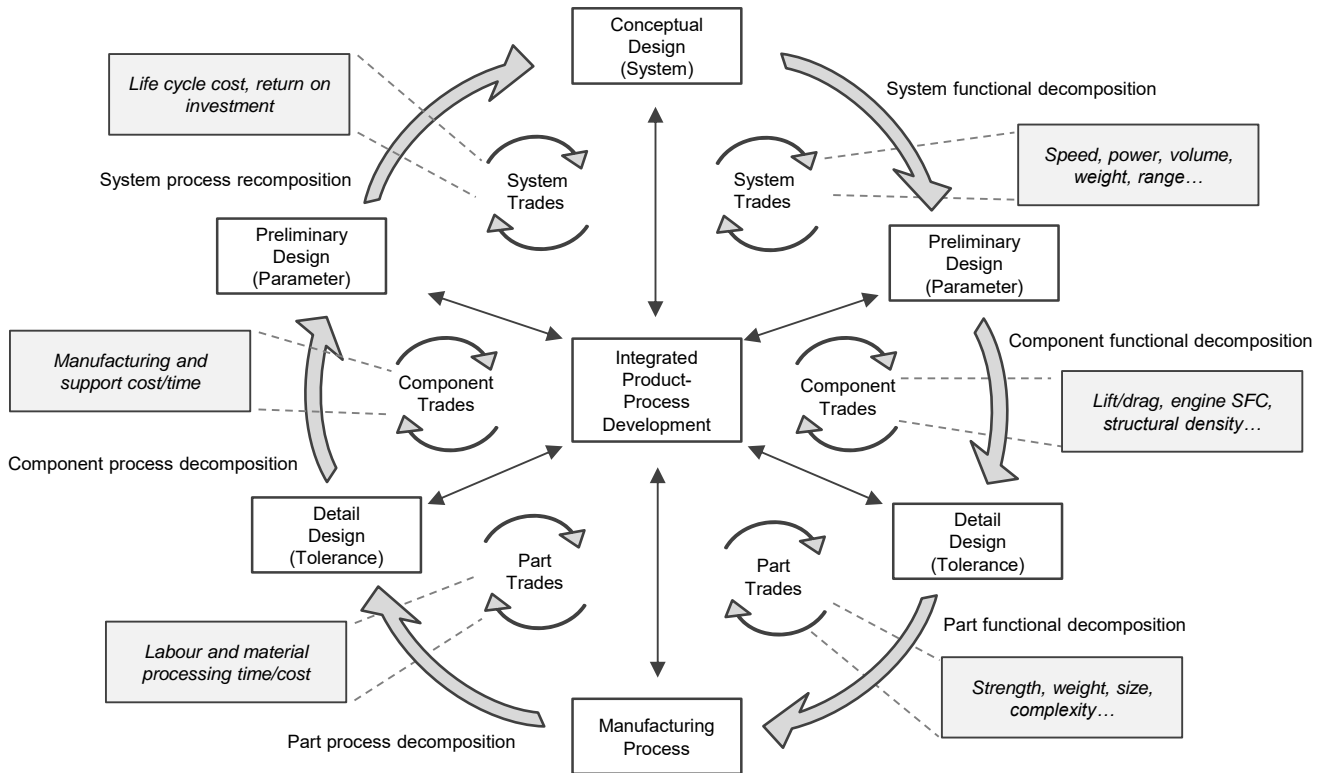
**Figure 2-17: Classification of DFAM approach according to Kumke et al. (2016) (recreated)**

Since DFAM in essence addresses the entire product development cycle, a suitable point of reference can be considered as the established general procedure of systematic development and design according to VDI 2221: *Systematic approach to the development and design of technical systems and products*, from the Verein Deutscher Ingenieure (VDI) (VDI, 1993; Kumke et al., 2016). However, a main shortcoming of current DFAM frameworks has been identified as a lack of integration with reference to design and manufacturing process phases, as well as integration of multiple disciplines throughout the process phases from idea to detailed design as prescribed in VDI 2221, namely clarification and definition of the problem, conceptual design, embodiment design, and detail design (VDI, 1993; Krehmer et al., 2009; Kumke et al., 2016; Zaman et al., 2018).

Whereas frameworks have been proposed for the integration of product development phases, such as material, process, and machine selection with early design stages, published literature on the integration of AM, or more specifically LPBF, with other disciplines is sparse. A promising approach to draw analogies from is offered by the Integrated Product/Process Development (IPPD) management method which aims to systematically integrate different disciplines throughout the entire product life cycle (Schrage, 1999; Oyesola et al., 2019). The generic IPPD methodology is shown in Figure 2-18(a). Four key elements namely, Systems Engineering Methods (SE), Quality Engineering Methods (QE), Top Down Decision Support (T3DS), and Computer Integrated Environment (CIE), form an umbrella under which three main columns of sub-elements are presented. The system to be developed is decomposed (top down) on the right hand side under SE, and recomposed (bottom up) under the QE on the left hand side. The SE and QE elements feed into the TD3S process where trade-offs are evaluated in a CIE. The trade-off process flow in the presented context of rotorcraft design is presented in Figure 2-18(b) with the right half representing the decomposition from Conceptual Design to Detail Design and the recomposition from Manufacturing Process to the System (Schrage, 1999). For this study the focus is shifted towards the right-hand side of Figure 2-18(b) for enhancing part functionality and subsequently the costing and return on investment aspects



(a)



(b)

**Figure 2-18: IPPD with (a) the generic methodology and (b) the hierarchical trade-off assessment process flow, (recreated from Schrage, 1999)**

Zaman et al. (2018) proposed an IPPD framework for resource selection to integrate material, process, and machine selection during the conceptual and embodiment design stages. It is based on a summary of the potentials offered by AM and the factors that need to be considered in order to achieve them. Figure 2-19 presents this summary with AM potentials in the inner circle and factors for obtaining these potentials in the outer circle.

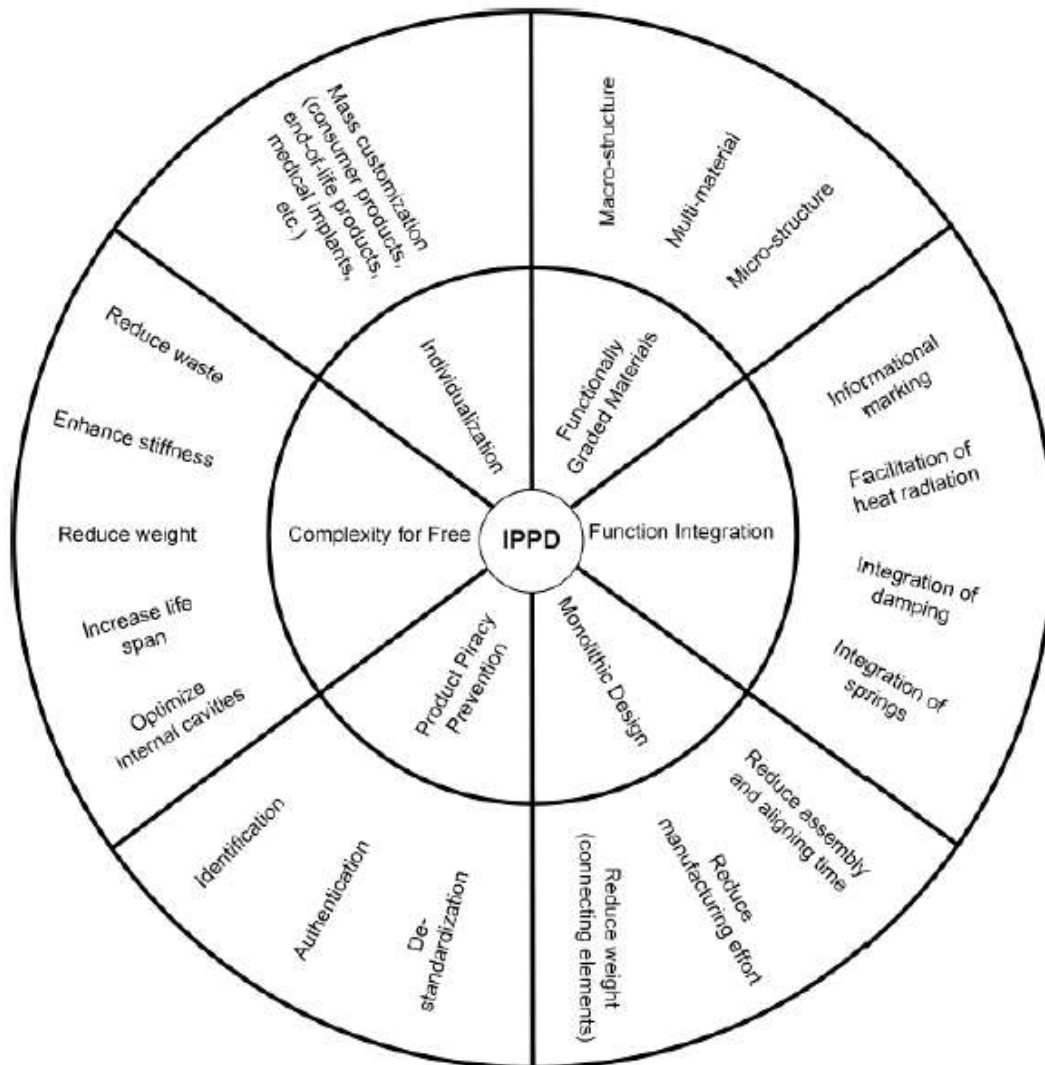


**Figure 2-19: IPPD with AM potentials and factors to achieve them (Zaman et al., 2018)**

The framework is presented in Figure 2-20. Respective decision areas are indicated with the shaded boxes. Decisions were guided by axioms and multi criteria decision making (MCDM) tools such as Analytical Hierarchy Process (AHP). AHP is a particularly useful MCDM tool in the manufacturing sector since it allows for the incorporation of both subjective and objective attributes in the decision making process (Emrouznejad & Marra, 2017).

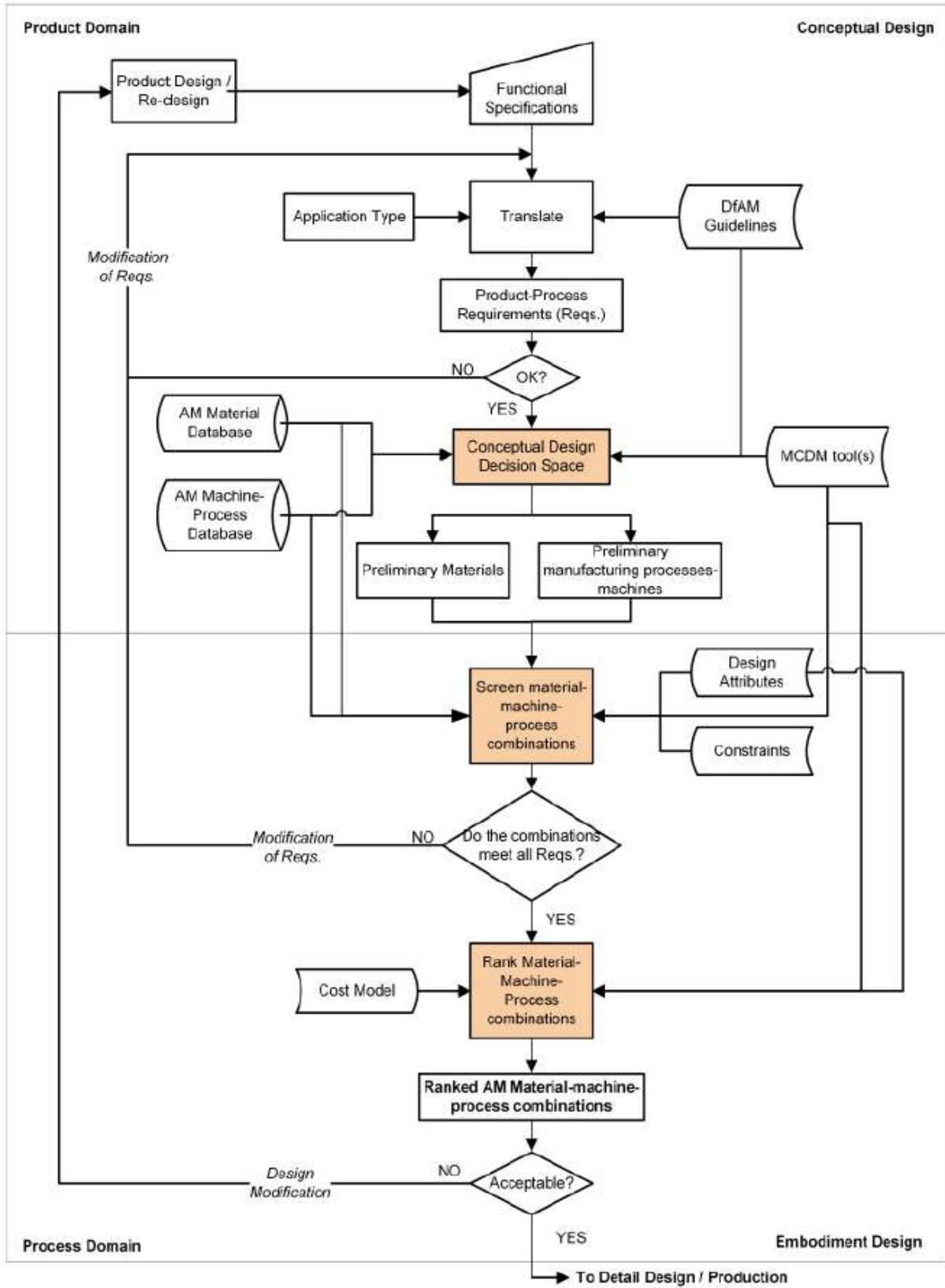
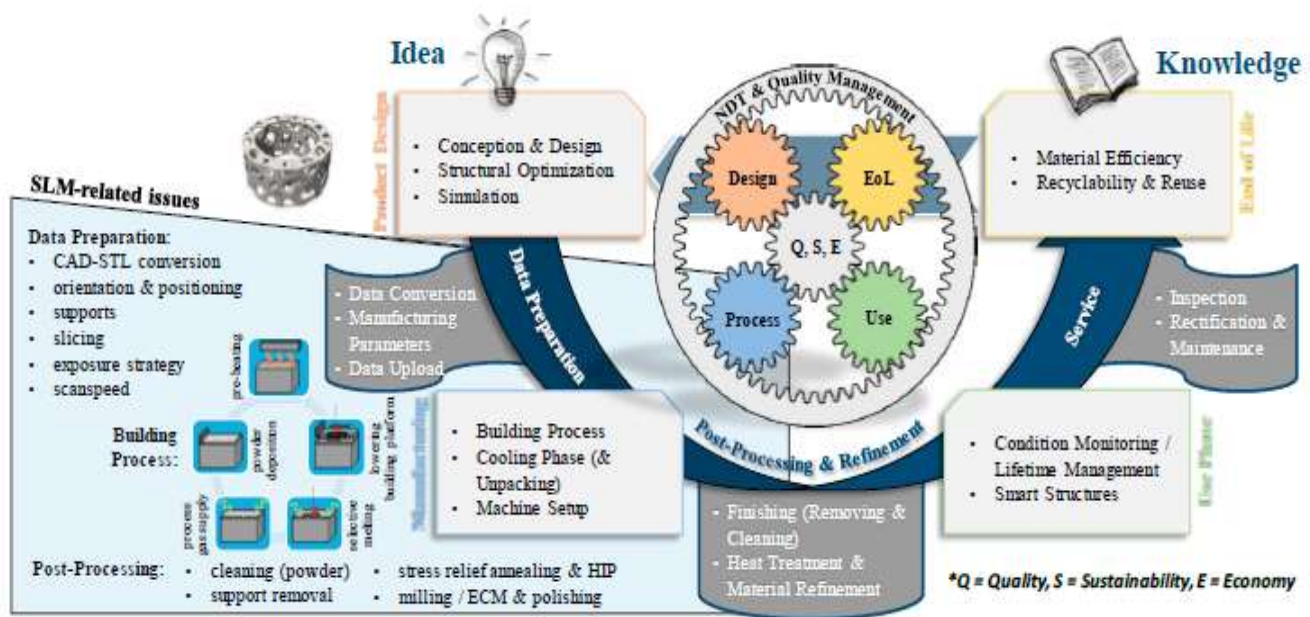


Figure 2-20: Integrated design oriented framework for resource selection in AM (Zaman et al., 2018)

Renjith et al. (2020) proposed a framework to aid designers and product developers with the early integration of AM capabilities by combining Axiomatic Design (AD) and Theory of Inventive Problem Solving (TRIZ). The design problem is decomposed into functional requirements through AD and design parameters for satisfying the functional requirements are determined through TRIZ. An AM capabilities database is then used to find the appropriate AM capability for the respective design parameters to satisfy the functional requirement. The framework was demonstrated with the case of redesign for a housing cover (consisting of a cover, gasket, and threaded socket) (Renjith et al., 2020).

Kaspar et al. (2019) proposed an integrated AM development framework that emphasises the importance of integrating downstream processes such as post-processing and NDT (non-destructive testing) into early stages of product development (Figure 2-21). It aims at aiding both experienced and inexperienced engineers to consider details regarding the manufacturing, post-processing, and quality control processes from the beginning in order to guide the design of parts. To demonstrate the integration of downstream processes, their framework was applied to the theoretical design of a multi-material rotor shaft and turbine blade assembly (Kaspar et al., 2019).



**Figure 2-21: Integrated AM product development framework with focus on post processing and quality management (Kaspar et al., 2019)**

In reference to Kumke et al. (2016), this framework considers DFAM in both the broad and strict sense, however it is limited to mostly the design stages within the engineering product development process

and does not specifically incorporate different disciplines. Nevertheless, the holistic approach provides the potential user with a more focused overview of the multitude of various processes and the details that require consideration when developing products and process chains centred on AM, specifically LPBF (referred to as SLM in Figure 2-21). This aids in defining restrictions for conceptual design and thus rendering the solution space more manageable than an open canvas approach, especially regarding the design freedom offered by PBF AM processes. Furthermore, by elucidating the details of downstream processes early in the design phases, potential users obtain an idea of the challenges and opportunities in integrating AM into conventional process chains, which is highlighted as a major organisational obstacle towards further industrialisation of AM (Kaspar et al., 2019).

Kim et al. (2015) adopted a systems engineering approach for the conceptualisation of information management system architecture for the digital information generated throughout the AM process chain. In their work, the process chain is divided into eight “phases”, part geometry/design, raw/tessellated data, tessellated 3D model, build file, machine data, fabricated part, finished part, and validated part. The framework is coupled both to the main generic phases within the AM chain as well as to supporting factors such as standards, methods, techniques, hardware, and software. This is not unlike that of the Integrated AM product development from Kaspar et al. (2019) in Figure 2-21, however, the focus is not so much on part realisation as on management and systematic integration of the information resulting from the different phases of the process chain. The importance of multidisciplinary issues is highlighted within a layer termed “Interoperability” and while it is emphasised for its importance in information flow and transparency, it is not concretised with specific details or application cases (Kim et al., 2015).

A set-based approach, termed Integrated Product and Production Engineering (IPPE) for the integration of design, process selection, and material selection has also been proposed, with the high-level overview of the framework presented in Figure 2-22 (Stoffels et al., 2018). The three areas of consideration are Product Definition, Production Definition, and Material Definition, each sharing four phases, Specification Phase, Concept Phase, Component / Detailed Phase, System Integration Phase, each with its respective detail. It is emphasised that integration of processes and methods are required on a deeper level than merely the integration of organizational units. In their framework, the results of each of the individual domains are evaluated together in the integrated phases. This allows for consideration of all requirements as well as the interactions between the individual domains (product,

process, and material) with the aim of converging to an appropriate solution. Kaspar et al. (2018) demonstrated this approach for a comparative assessment in terms of technical, economic and ecological criteria, of AM to conventional manufacturing methods in the early phases of concept development.

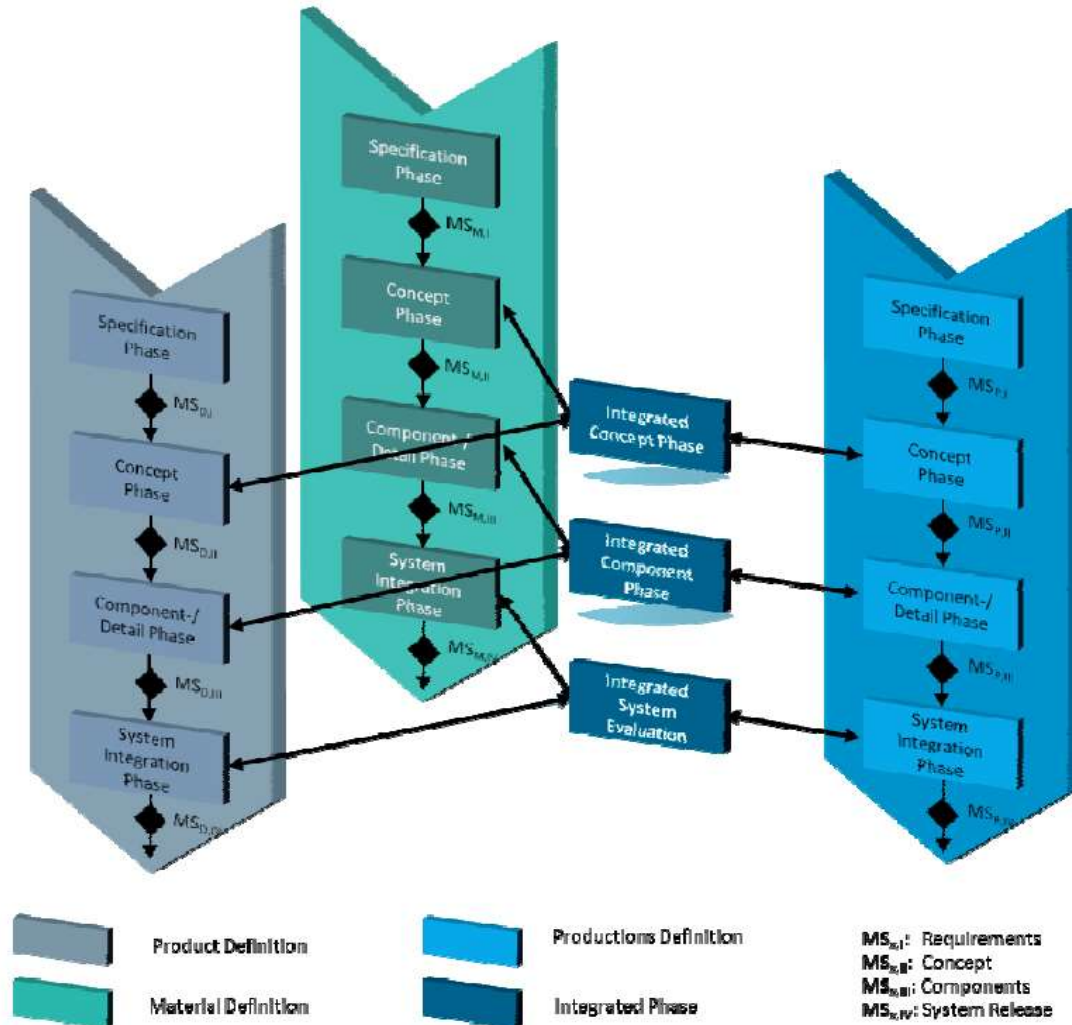
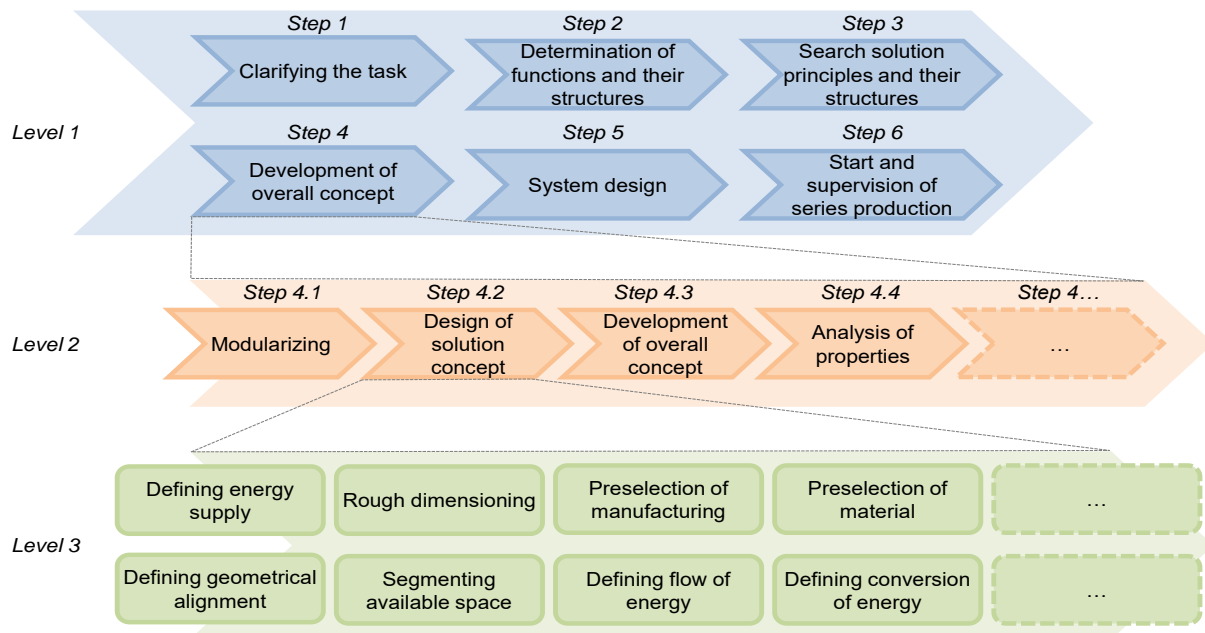


Figure 2-22: Overview of IPPE Framework (Stoffels et al., 2018)

Whereas the preceding frameworks aim at integrating AM into the product development and manufacturing process chains, a focus on the integration of LPBF with detailed aspects of different disciplines does not yet appear to be formalised. Nonetheless, in the seeming dearth of interdisciplinary frameworks aimed specifically at LPBF for drug delivery applications, analogies can be drawn to frameworks aimed at integrating different organisational entities within a product or process development cycle for deriving the framework for this study.

Krehmer et al. (2009) presented a process model developed through extensive research collaboration (FORFLOW) by four universities in order to guide a multidisciplinary product development process. The general design of their FORFLOW-process is presented in Figure 2-23. It contains three levels, each containing a number of steps. The first prescribes the six main steps to be executed in a recommended order with more detailed steps in Level 2 for each step in Level 1. Level 3 contains all the steps required, to satisfy the respective step in Level 2. These steps are situation specific with regards to both their details and execution order. It is based on an integrative approach for systems with high complexity and identifies the following challenges, “integration of mechatronic aspects”, “situation-specific process planning”, “integration of design iterations”, “integration of lessons learned”, “supporting aspects of Design for X (DFX)”, “support of CAx-aspects”, “multi-level safeguarding” and “integration of simultaneous and concurrent engineering”. This model specifically highlights two important aspects, the documentation of lessons learned from iterations, regarding them as learning opportunities for improvement rather having than an exclusively negative impact on project time and cost, and the parameterisation of a search space to aid engineers in the finding of relevant information, especially in early development phases when they do not necessarily know what they are searching for. Here, the search space refers to organisational data, but this can be extrapolated to information search within literature. Thus, the question becomes how to reduce the time spent in finding information when the “knowledge does not yet exist” and the search space is exploratory.



**Figure 2-23: Integrated design oriented framework for resource selection in AM (recreated from Krehmer et al., 2009)**

This framework, however, seems to mostly consider conventional manufacturing and assembly processes with an emphasis on mechatronic systems embedded in modern products. The integrative approach, aiming at different disciplines, both technical and organisational, serves as a strong foundation, based on established theories (V-Modell XT, process models from Pahl and Beitz (1988), and VDI guidelines), which can be incorporated in the derivation of the framework in this study (VDI, 1993; Broy & Rausch, 2005).

Eigner et al. (2016) presented an interdisciplinary framework to integrate information and data of different disciplines for the development of cybertronic (mechatronic system which interfaces with computer software in order to automate its behaviour based on data collected and communication with other systems) systems termed the mecPro<sup>2</sup> model framework. Derivation of the framework considered, among other, discipline specific frameworks from mechanical design, systems engineering, and software development from which they concluded that typically frameworks share four main phases termed RFLP, requirements, function, logical system element (principle solutions and preliminary layouts), and physical element (definite layouts and product documentation). The abstract structure of the level based framework is presented in Figure 2-24.

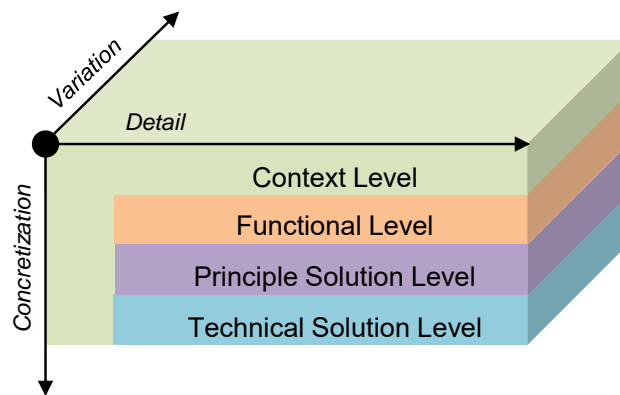


**Figure 2-24: General structure of level based mecPro<sup>2</sup> model framework (recreated from Eigner et al., 2016)**

The “Detail” axis refers to the gathering of information without limiting the solution space. When further detailing without concretization is not possible, a transition is made to a deeper level of the framework on the “Concretization” axis. The “Variation” axis indicates that concretization of a solution should not progress without the evaluation of alternatives. The context level refers to the specific

boundaries within which the system is analysed. The functional level aims at a solution-neutral description of the required functionality within the specific context. The principle solution level indicates the investigation of technical aspects which could enable the functionality. In this level, solution variants should be evaluated both individually with regards to a specific function as well its capability for integration with function structures within the specified context. The technical solution level dictates the full concretization of the solution (Eigner et al., 2016).

Whereas the previous models address integration of different disciplines or organisational entities, the positioning of additive manufacturing knowledge (AMK) is not specifically addressed. Laverne et al. (2017) proposed a model for the integration of AMK in the conceptual and embodiment design phases. The aim in their work was to improve the creativity and innovation potential of the solution space through reducing restrictive thoughts and self-censorship within designers during the early development stages. In view of this a Design with X (DWX) perspective was linked with a DFAM perspective. The final model is presented in Figure 2-25 with the DWX component bordered by the red dashed line and the DFAM component bordered by the blue dashed line. The diamond shapes represent divergence (widening from left to right) and convergence (narrowing from left to right) both within the individual processes and the overall model. The DWX approach aids to widen the solution space for originality and innovation in concept generation whereas the DFAM approach provides necessary guidelines for convergence towards manufacturable designs (Laverne et al., 2017). A series of experiments performed with both experienced and inexperienced AM users elucidated the requirements regarding the timing, media, and content with which to introduce AMK as the introduction of too much AMK too early not only quickly becomes overwhelming, but it can also restrict the width of the divergence process within the initial solution search space. This combination of DWX and DFAM with the timed introduction of AMK is termed by Laverne et al. (2017) as Design with Additive Manufacturing (DWAM).

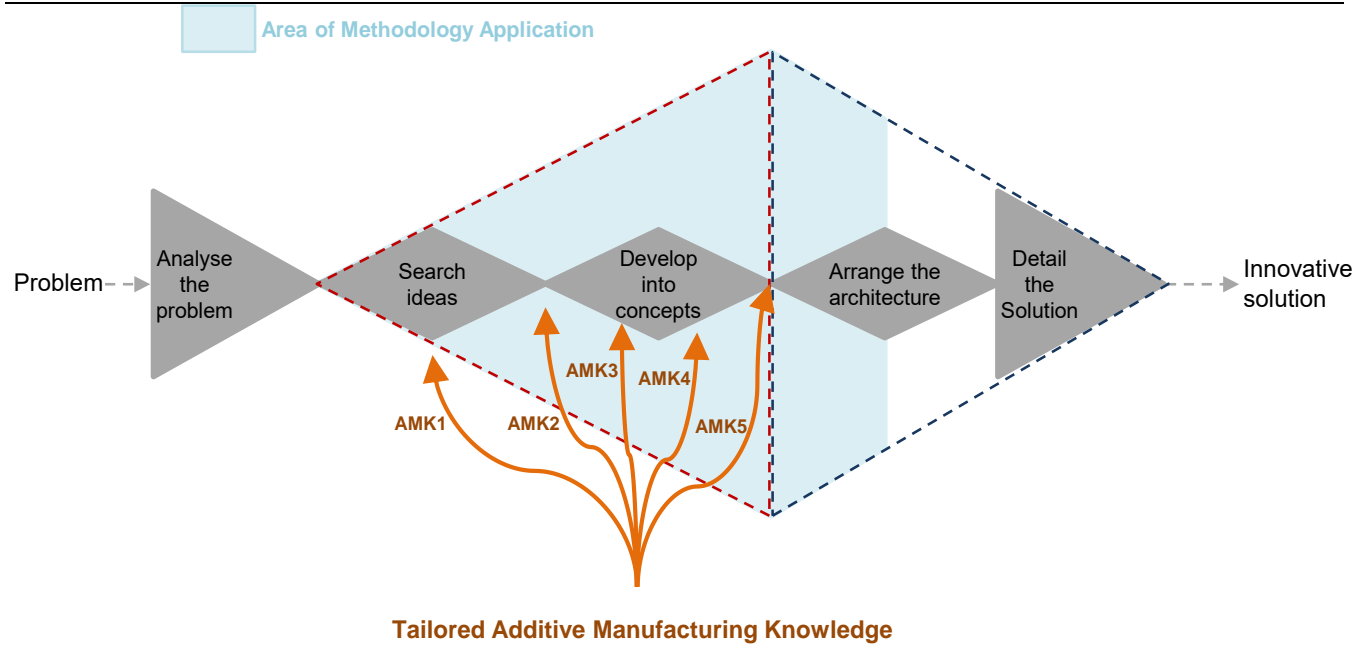


**Figure 2-25: DWAM model for conceptual and embodiment design phases (recreated from Laverne et al., 2017)**

Building on the DWAM framework, Segonds (2018) proposed a five-step modular framework termed Design by Additive Manufacturing (DBAM), presented in Figure 2-26. This framework integrates DWAM (which integrates DWX and DFX) with Creativity through Additive Manufacturing (CTAM) to promote innovative solutions (Rias et al., 2016).

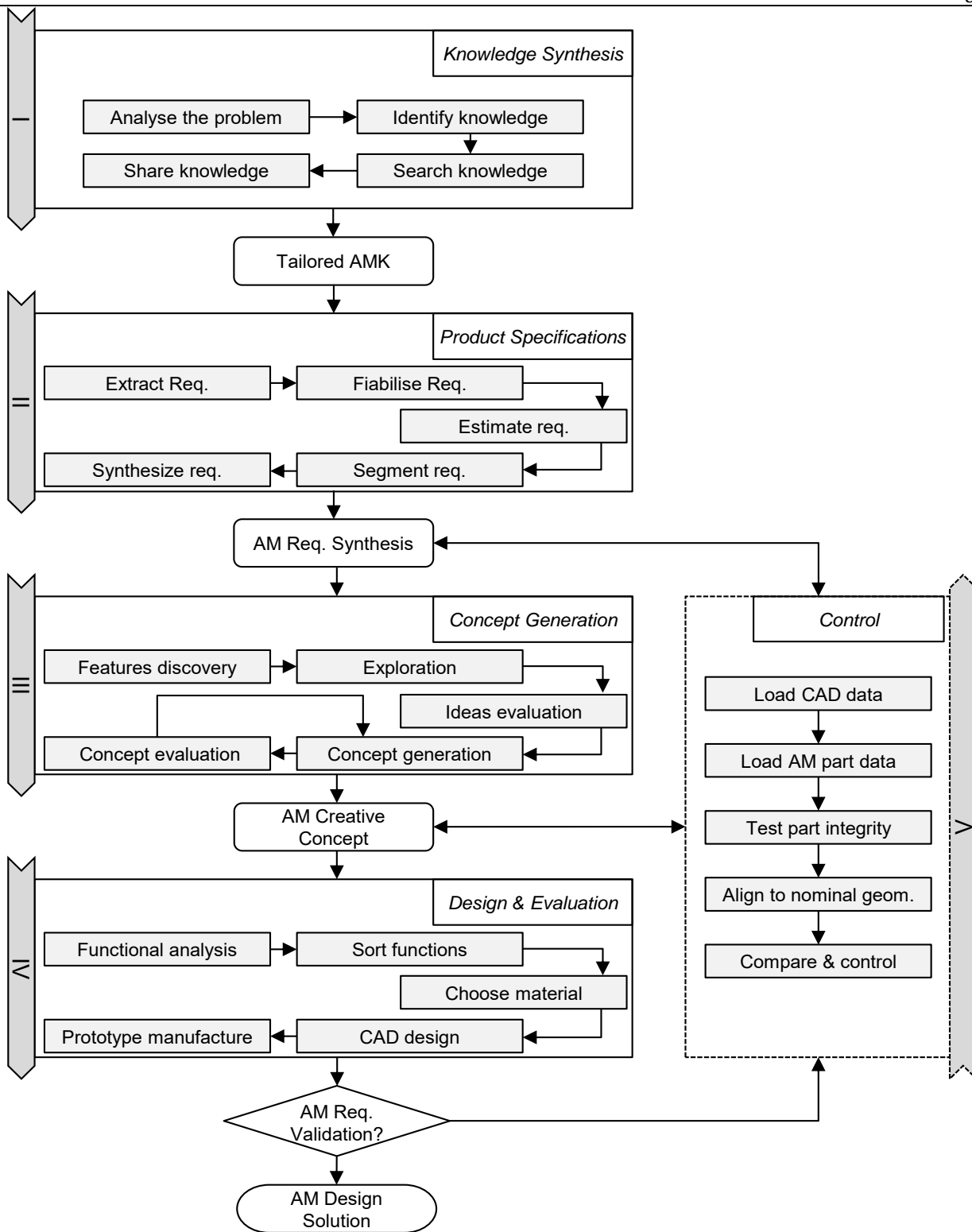


**Figure 2-26: DBAM framework for enhancing innovation (recreated from Segonds, 2018)**

DBAM aims to address three main shortcomings of existing DFAM, DWAM and CTAM frameworks as identified by Segonds (2018) namely, lack of integration with established frameworks, lack of

standardisation due to fragmented and independent development of DFAM, DWAM and CTAM frameworks, and a lack of attention to the creative phases. It is divided into 5 main steps, *Knowledge Synthesis*, *Product Specification*, *Concept Generation*, *Design and Evaluation*, and *Control*, each with a number of sub-steps including iterative processes where applicable. In the *Knowledge Synthesis* step the aim is to study and apply the identified required knowledge related to the product and the AM process. The *Product Specification* phase strives to precisely define the product through specifying the requirements. During *Concept Generation* the DBAM framework encourages the use of CTAM methods as presented by Rias *et al.* (2016). The *Design and Evaluation* step ensures the generated concept is AM feasible and here specific DFAM guidelines (DFAM in the strict sense according to Kumke *et al.* (2016)) and optimisation methods should amount to the fabrication of the physical prototype. The control step is intended for quality assurance and data capturing during design and manufacturing. The DBAM framework has been demonstrated with an optronic part. Through utilisation of the framework a component consisting of 5 parts and performing 16 functions has been consolidated to a single part performing 20 functions (Segonds, 2018). In relation to the DBAM framework, this study aims to build further on the concept by specifically aiming at integrating paradigms of different frameworks towards an effective, but generalizable LPBF-centred framework for enabling drug delivery.

The frameworks discussed above form a basis from which the high level framework for this study was derived. The reviewed frameworks, together with the identified established methods for conventional design and manufacturing processes, were used as a theoretical base from which the framework for the application case of this study was derived.

## 2.5 Conclusion

Four main areas related to the interdisciplinary problem solving in the application of LPBF for enabling local drug delivery from cementless hip stems were addressed in this chapter. Issues regarding infection in THA were discussed. The importance of addressing the problem of infection was emphasised by providing an overview of its devastating effects on the patient's quality of life as well as on the medical and financial resources required for its treatment. To gain a basic understanding of the infection process and the current treatment procedures, microbial infection and specifically biofilm formation were discussed, providing information on why established PJI can be such a challenge to eradicate. A need exist for the development of novel drug delivery strategies that can be used both in treatment and prophylaxis applications.

Secondly, local drug delivery strategies in clinical use as well strategies in development were briefly reviewed. It was demonstrated that a large research gap currently exists between the development of local drug delivery strategies based on external conditioning of the implant surface and the development of strategies focusing on the utilisation of internal reservoirs. This gap can be addressed by the application of LPBF for the fabrication of implants with internal reservoirs.

Thirdly, the LPBF process was reviewed in the context of processing Ti6Al4V ELI which is used to manufacture cementless hip stems. Several process parameters exist that affects part quality produced with LPBF, with many of these parameters hard to control. Therefore the main user controllable parameters were identified as laser power, scanning speed, and hatch spacing. A criterion often used that consolidates these parameters is the VED. When approached with caution, due to its aliasing and simplified nature, this criterion can provide valuable insights regarding the effects of the main process parameters to resulting part density. Specifically, the use of VED in attempts to optimise process parameters with respect to resulting part porosity has received much focus in research. Tailoring of the LPBF process parameters to induce porosity for the production of permeable structures however, is an identified area with little publically available research data. This study therefore contributes to the literature by developing a process window within which permeable structures can be produced in Ti6Al4V ELI through LPBF. Although the LPBF technology allows for great design freedom, process and machine specific limitations do exist and need to be respected to ensure a manufacturable design. This study contributes to the application cases of LPBF by demonstrating how one of these limitations could be overcome to enable the direct integration of permeable and dense components with an in-process assembly method.

Fourthly, to build a theoretical base for the derivation of an LPBF-centred interdisciplinary problem solving framework for the application case of this study, selected frameworks from literature were reviewed. These frameworks span across different disciplines and application areas namely, established design and product development methods, AM and MAM specific, IPPD, IPPE, and multidisciplinary product development in the context of mechatronic systems. This study contributes to the literature by building on these frameworks to derive a new interdisciplinary LPBF-centred framework for enabling drug delivery from cementless hip stems.

### 3. High-Level LPBF-Centred Interdisciplinary Framework

The developed framework consists of three parts namely, an overall procedural approach for interdisciplinary problem solving, a perspective from which the problem solving process was approached, and tools for ensuring integrated solution concepts. The framework highlights the importance of structured LPBF knowledge for integrated conceptual and embodiment design phases to foster creativity and innovation. To derive the high-level framework, analogies were drawn to the existing frameworks discussed in Section 2.4 in the abstract domain and concretised with regards to the specifics of the application case in this study.

#### 3.1 Positioning of Framework Application within Product Life Cycle Phases

The application area of the framework in this study mainly focuses on the prototyping stages of a traditional product life cycle (PLC), indicated with the dashed line in Figure 3-1. Although the framework is intended to be sufficiently generic for tailoring to different applications, in this study it mainly concerns the design and prototype manufacturing phases. The positioning in Figure 3-1 therefore marks the boundaries of the scope for application of the developed framework in this study within the context a traditional PLC representation (Chen et al., 2009; Ali et al., 2019).

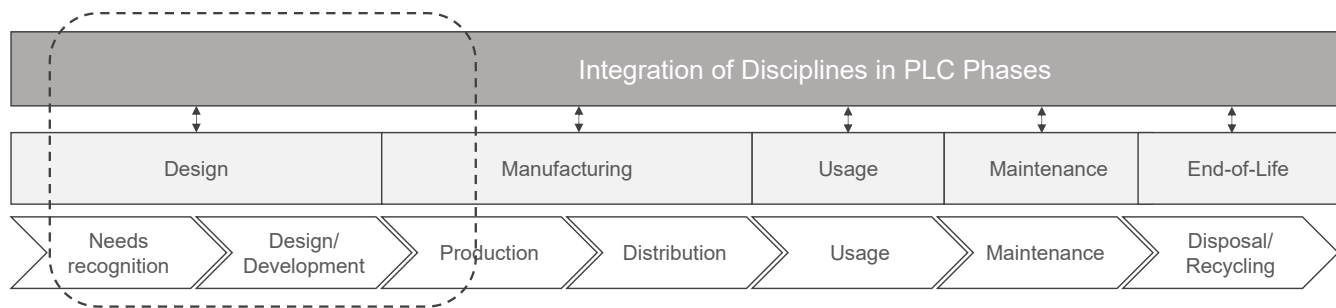


**Figure 3-1: Positioning of framework (indicated with dashed line) within PLC phases, (adapted from Chen et al., 2009; Ali et al., 2019)**

Since the framework falls within the design and manufacturing phases of the PLC, the approach is mainly focused on a theoretical background within these areas as discussed in Section 2.4. The main areas requiring an LPBF-centred interdisciplinary integration were identified based on the overall problem of bacterial colonisation of medical implant surfaces and the concept of local drug delivery through utilising the bulk of the implant itself as a reservoir. These areas also derive from the structure of the literature reviewed in Chapter 2. The areas are, pathogen, drug, drug delivery vehicle, LPBF process, LPBF materials, post processing, and design constraints. These areas form the main thematic

elements of the framework which are to be integrated through the perspective of an LPBF knowledge base, since this is the main generative component for physical prototype realisation.

### **3.2 High-Level Framework**

The entire framework consists of three parts, an overall interdisciplinary problem solving framework, an LPBF-centred perspective, and tools for ensuring integrated solution concepts. The high-level interdisciplinary problem solving framework for developing an integrated LPBF process chain for drug delivery is presented in Figure 3-2. The framework, with its structure based on the VDI 2221 (1993), consists of five levels, each with the aim of an integrated outcome for input to the following level.

In the first level, an overall problem is identified. This problem is decomposed in the second level into partial problems according to the disciplines involved and structured to ensure an understanding of the various aspects and required knowledge areas of the problem. The expected communication requirements between the partial problem areas should also be defined. In the third level, the partial problems are detailed into single problems. An essential factor within this level is the maintaining of communication between single problems within a partial problem as well as between the partial problems across all discipline specific areas. For example, details regarding a drug and drug delivery vehicle need to communicate not only in relation to each other and pathogen to ensure activity of the released drug molecules, but also with geometry and material of the reservoir to be manufactured. Thus the outcome of this level in the form of single solutions should also bear consensus before proceeding to the recomposition of the individual problem solutions towards an eventual overall solution. The partial solution recomposition takes place in the fourth level. Here possible interlayer iterations may be necessary, as insights obtained during individual and partial solutions may reveal that an effective integrated understanding of the partial problems was not adequately achieved during the second level. If consensus on the partial solutions is reached, the overall solution can be assembled from the partial solutions in the final layer and evaluated for its efficacy. Again here, interlayer iterations may occur which would indicate that the overall problem identified is not solved, and thus need to be redefined.

This systematic process is generic for application regarding the problem complexity. That is, for complex problems, the tool could also be applied within partial problems to further decompose them within a certain identified discipline. When a problem is decomposed into its most basic form as a single problem, the dashed levels are redundant and can collapse to directly go from overall problem to overall solution.

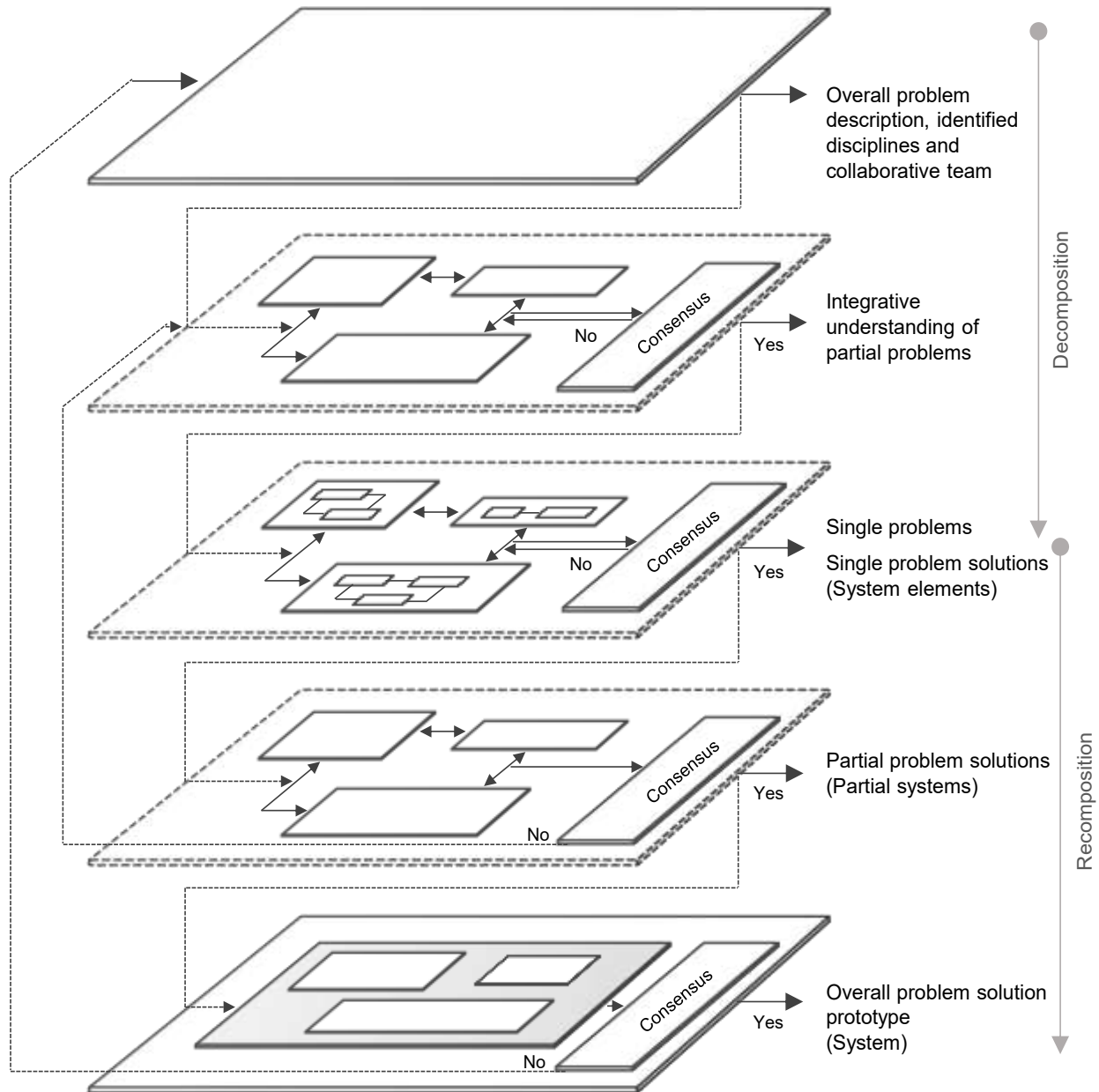


**Figure 3-2: High level overall interdisciplinary problem solving framework**

In the context of this study, it is important that the perspective of integration be rooted within the LPBF process. This aims to aid in exploiting the potential benefits of LPBF while avoiding unrealistic solution concepts. To graphically present this perspective in Figure 3-3, satellites representing discipline specific knowledge areas are arranged around an LPBF knowledge base for integration (under the 'Perspective' heading in the centre of Figure 3-3).

For the specific application of this study, the main high-level disciplines identified are Microbiology, Polymer Science, and Manufacturing Engineering. Albeit Manufacturing Engineering in the context of LPBF can be regarded as multidisciplinary with regards to the four identified satellite areas, LPBF process and machine, materials, post processing, and geometry, it is regarded here as a single high-level discipline for simplicity. The satellite areas are positioned to intersect with the LPBF-centred process chain. This indicates that certain ‘knowledge packages’ are required from each of the satellite areas and each of the satellite areas requires a certain LPBF ‘knowledge package’. Communication takes place both to and from each of the contributing satellite areas and relevant knowledge is consolidated for decision making in the integrative space in the centre.

Building on the overall framework and perspectives, high level systematic tools are derived from the IPPD trade-offs representation (Figure 2-18(b)) and the DWAM and DBAM knowledge package proposition (Figure 2-25 and Figure 2-26). The aims of these tools are to ensure effective integration and to promote creativity and innovation during the project. These tools are indicated under the “Integrated Solution Concepts” heading in Figure 3-3.

The entire high-level framework in Figure 3-3 is thus structured as three main parts, an overall problem solving procedure which guides the user with process steps, a perspective approach which emphasises the need for integrated knowledge packages from a LPBF-centred view, and tools to aid in creativity and innovation through the beneficiation of trade-offs and structured integrated knowledge packages.

The IPPD-based trade-off and integration potentials tool (refer Figure 2-18) is presented in Figure 3-4. The right hand side represents the processes related to the decomposition of the problem into single problems and the left hand side represents the processes of recomposition of solutions towards an overall solution. The arrow connecting “Overall Solution” and “Problem Definition” represents the evaluation of the solution in terms of the actual problem defined. The addition of integration potentials within each of the five levels of the overall problem solving framework is intended to strengthen interdisciplinary communication, collaborative work and skills development, and creativity and innovation. For example, active collaboration between parties during testing phases could lead to more efficient utilisation of in-house resources (example presented in Section 4.2), which might otherwise be overlooked due to insufficient communication.

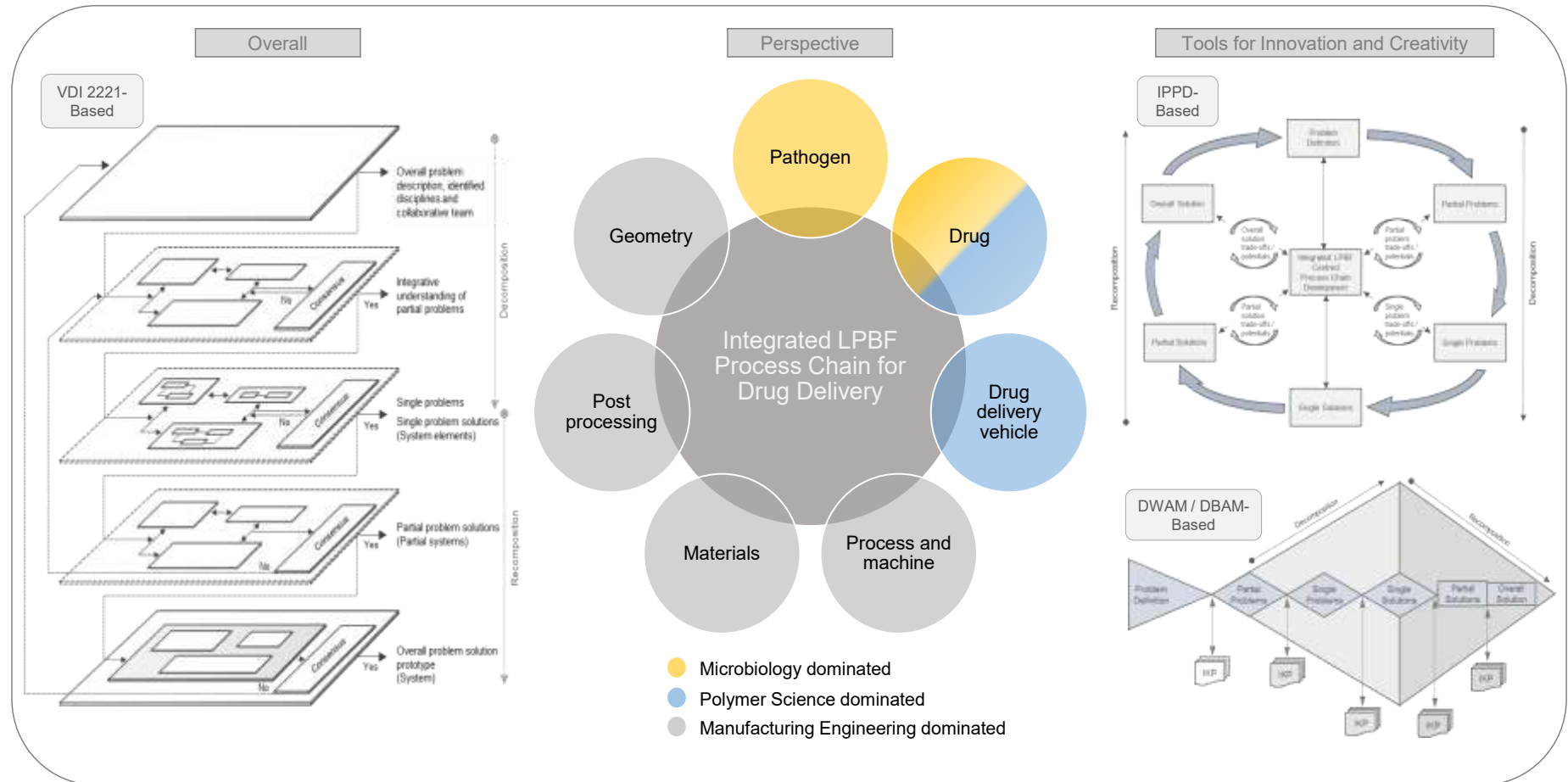


**Figure 3-3: High-level interdisciplinary framework for developing an integrated LPBF process chain for drug delivery**

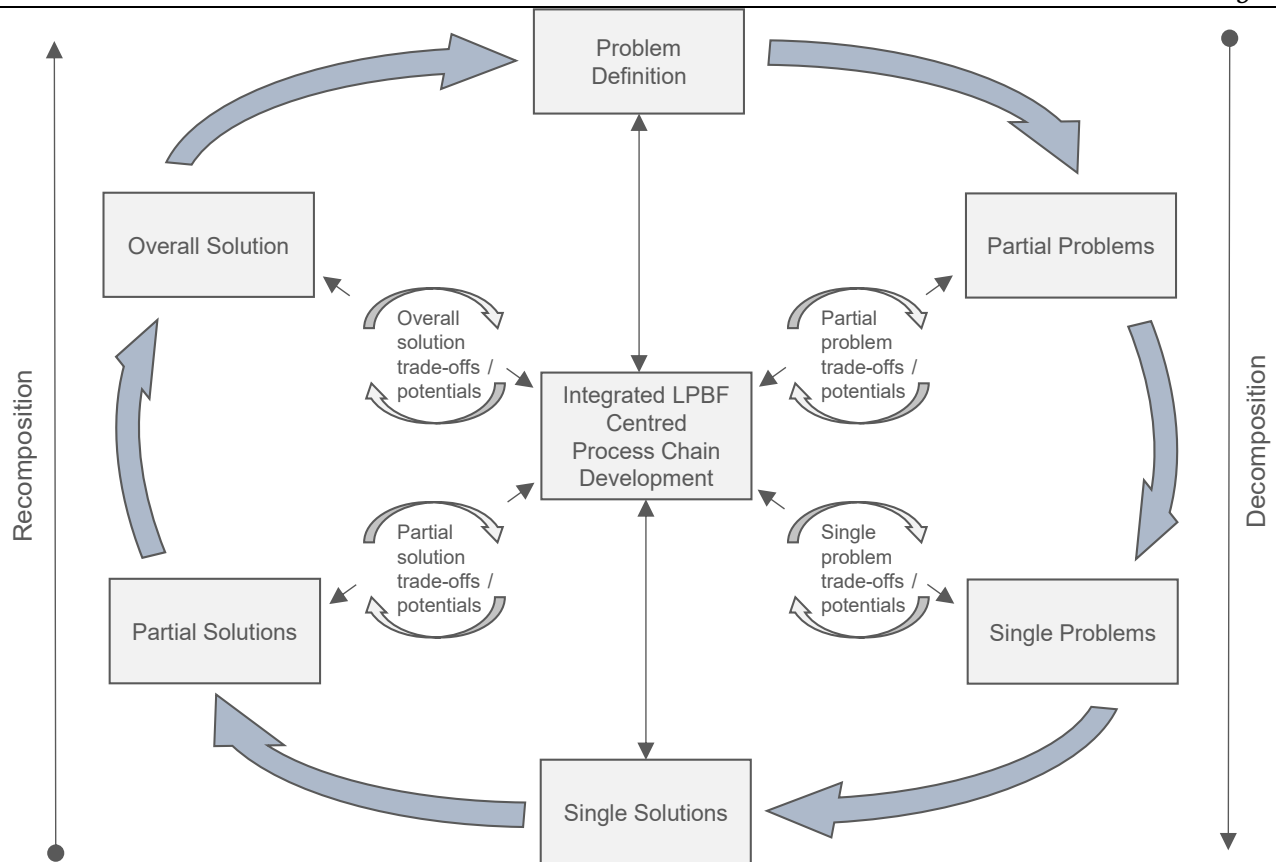


**Figure 3-4: Systematic procedure for integrative decomposition and recomposition of problems and solutions**

For the trade-offs and potentials to be identified and evaluated, a certain amount of knowledge is required from each of the satellite disciplines in Figure 3-3 and each of the satellite disciplines requires a certain amount of LPBF knowledge. This is demonstrated in the DWAM/DBAM-based (refer Figure 2-25) tool in Figure 3-5. The triangular shapes represent divergent processes when widening from left to right and convergent processes when narrowing from left to right. The five levels of the overall framework are represented here as a linear process, each encompassing divergent and convergent phases. The required knowledge for each phase, termed Integrated Knowledge Package (IKP) is indicated with the external input arrows. Also indicated in the tool is the changeover point from an overall divergent (decomposition) to a convergent (recomposition) process. The IKPs are ideally intended to streamline the processes within the five levels by, amongst others, provide users with sensible boundaries within the solution space regarding the different disciplines while aiming to avoid restrictive thoughts which may reduce the creativity and innovation within the divergent processes. This is also a bidirectional communication process, as not all the interactions, trade-offs, or potentials could necessarily be determined beforehand, especially in the case of an LPBF-centred approach where

historical data and a general knowledge database is limited. Subsequently, when new knowledge is generated during the problem solving process it is communicated to the IKPs.

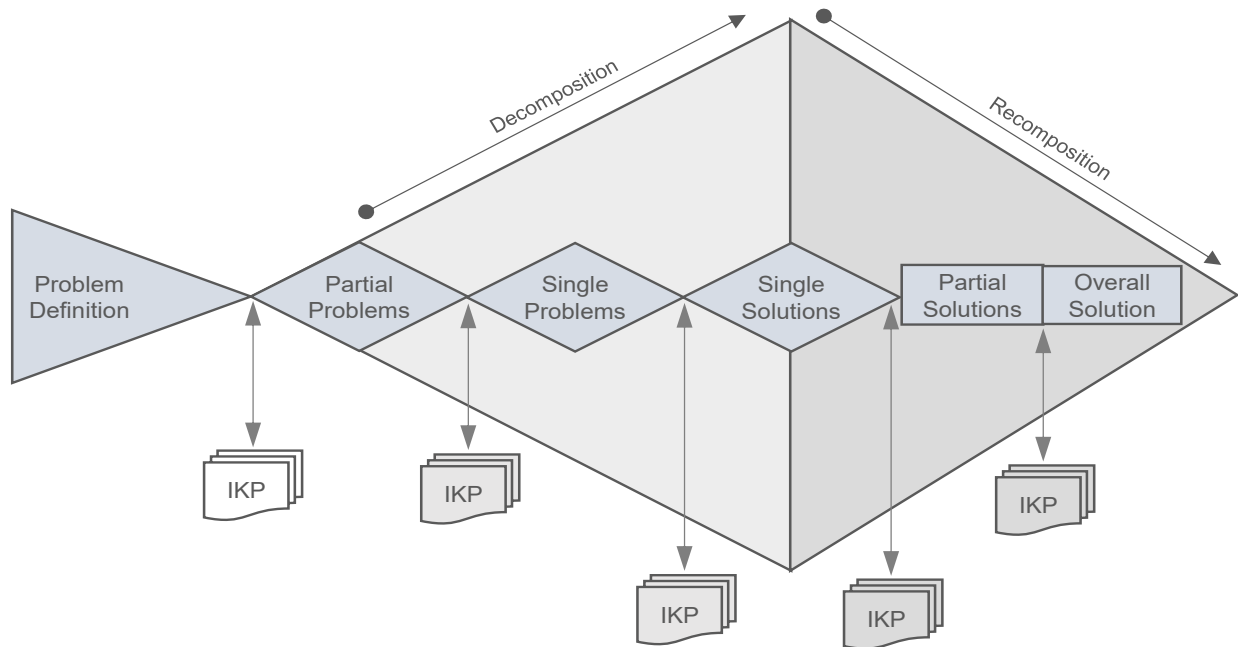


**Figure 3-5: Interaction of integrated knowledge packages with divergent and convergent processes during problem decomposition and recombination**

As indicated in Figure 3-5, IKP's should be available at the required time points during the problem solving process. In order to optimise the content of each IKP, extensive experimentation and iterations are required which is beyond the scope of this study. Rather, the focus in this study is on the early identification of the different knowledge areas which would form part of IKPs. It is argued that for an integrated process chain development, a basic understanding of each IKP should be shared by the involved parties.

The identified knowledge areas, based on the literature reviewed in Chapter 2, is presented in Table 3-1 with respect to the three main identified disciplines in Figure 3-3. In view of the paucity of historical data for the application of this study, it could be expected that optimised IKPs would not be structured from the outset. Therefore, an emphasized component during iterations is the necessity of data capturing regarding lessons learned and improved IKP structuring. For example, in Chapter 7 it is shown that LPBF can be used to induce different levels of porosity in Ti6Al4V ELI thin wall components and subsequently release vancomycin with different diffusion profiles. This can be regarded as the generation of an IKP regarding material, LPBF process, drug formulation, and drug release profile.

**Table 3-1: Summary of Identified disciplines, satellite topic, and required knowledge areas for process integrated LPBF-centred process chain development**

Identified Discipline	Satellite Topic	Required Knowledge Areas
Microbiology	Pathogen	<ul style="list-style-type: none"> <li>• Size and key morphological features</li> <li>• Minimum inhibitory concentration for selected drug</li> <li>• Adhesion to surfaces and biofilm formation</li> </ul>
Microbiology / Polymer Science	Drug	<ul style="list-style-type: none"> <li>• Target pathogen</li> <li>• Molecular weight</li> <li>• Chemical structure</li> <li>• Physical properties</li> <li>• Chemical properties</li> <li>• Stability</li> <li>• Antimicrobial activity</li> </ul>
Polymer Science	Drug delivery vehicle	<ul style="list-style-type: none"> <li>• Material</li> <li>• Drug compatibility</li> <li>• Biocompatibility</li> <li>• Biodegradability</li> <li>• Polymerisation reaction (temperature)</li> <li>• Preparation techniques</li> <li>• State</li> <li>• Size</li> <li>• Morphology</li> <li>• Drug release profile</li> </ul>
Manufacturing Engineering	Process and machine	<ul style="list-style-type: none"> <li>• Build envelope</li> <li>• Build chamber properties</li> <li>• Laser properties and parameters</li> <li>• Powder bed properties and parameters</li> <li>• Powder coater properties and parameters</li> <li>• Machine properties and parameters</li> </ul>
	Materials	<ul style="list-style-type: none"> <li>• Biocompatibility</li> <li>• Melting and solidification properties</li> <li>• Relevant material properties</li> </ul>
	Post processing	<ul style="list-style-type: none"> <li>• Post process details</li> <li>• Jigs and fixtures</li> <li>• Effects on relevant material properties</li> </ul>
	Geometry	<ul style="list-style-type: none"> <li>• Project defined constraints (organisational)</li> <li>• Manufacturability</li> <li>• Post processing</li> <li>• Accuracy</li> <li>• Effects on drug release</li> <li>• Effects on relevant material properties</li> </ul>

### 3.3 Project Problem Breakdown Structure

To generate a roadmap for the experimental investigations of this study, the problem was broken down according to the high-level framework in Figure 3-2. This problem breakdown structure is presented in Figure 3-6 below. Main responsible collaborative parties are indicated by first listing where applicable (e.g. MB/IE indicates that MB was the main responsible party for a given problem). The dashed border surrounding the respective single problems under the partial problem “Drug formulation” indicates that they were executed independently of the development of the cementless implant demonstrator. As presented in Chapter 4, these dashed single problems resulted in an independent demonstrator for an alternative sustained release formulation for vancomycin.

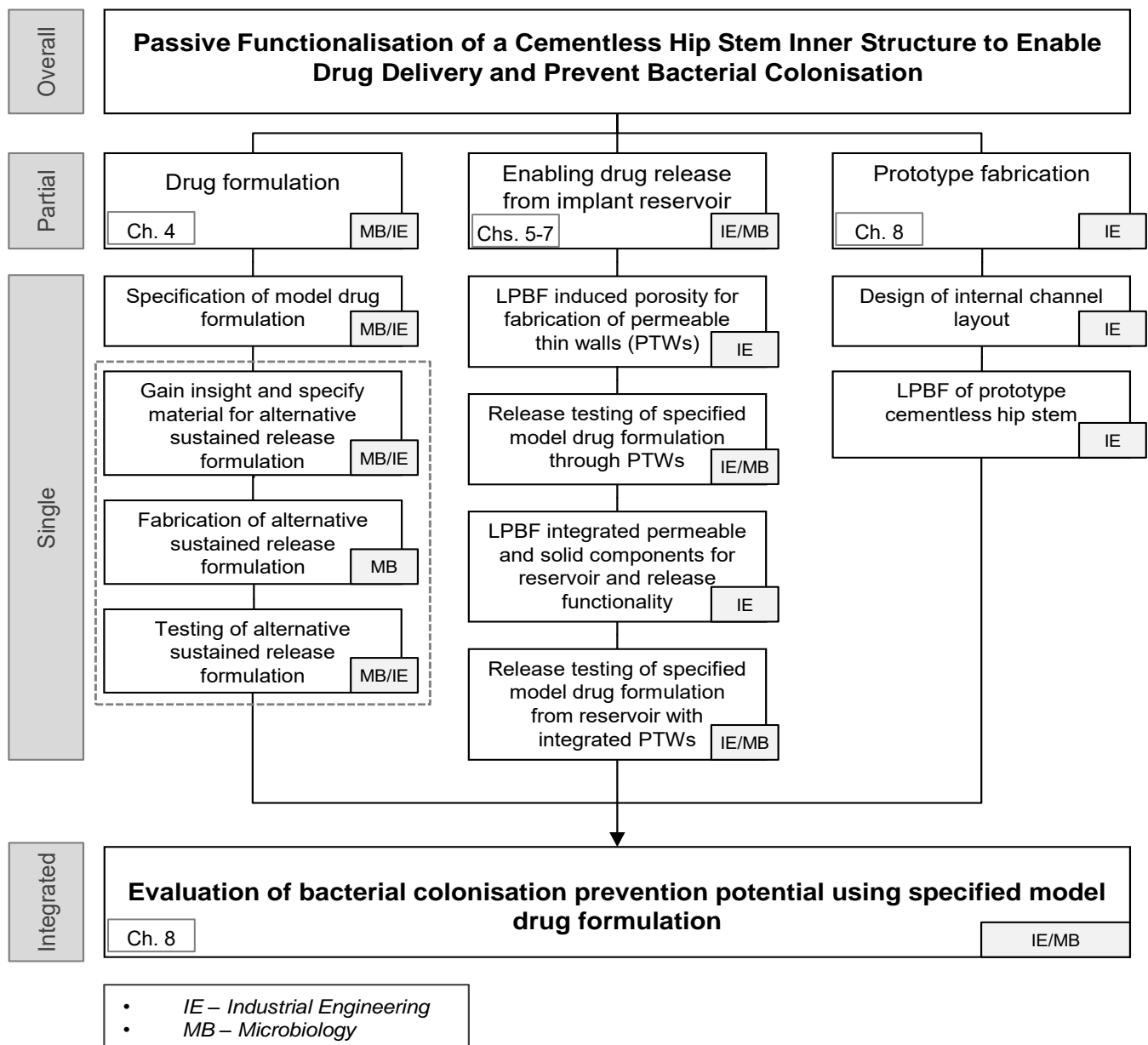


Figure 3-6: Problem breakdown structure

## 4. Sustained Release Vancomycin Drug Formulation

This chapter addresses the partial problem “Drug formulation” from Figure 3-6, focusing on the single problems within the dashed border for the development of a sustained release vancomycin drug formulation. It demonstrates an option for loading vancomycin into a cementless implant for sustained release. The work was executed collaboratively according to Figure 3-6 and published as a standalone research paper (Booyesen et al., 2019). Insight was gained for materials selection and procurement followed by fabrication of a sustained release formulation, and release testing. The first part relied on the study of available literature and the second part on effective collaboration to develop a customised setup for release testing.

### 4.1 Gaining Insight for Formulation Material Selection

Insight for material selection was gained through the execution of two tasks. A literature study was performed on the use of biodegradable polymers for the encapsulation of vancomycin. It was found that PLGA is an FDA approved polymer available in different grades which can be specified to tailor the biodegradation rate and subsequent drug release profile. Secondly, a qualitative understanding of the polymer erosion and drug release process was gained through a stochastic simulation adopted from literature (Göpferich, 1997).

#### 4.1.1 Sustained Vancomycin Release Formulation

Vancomycin is a hydrophilic glycopeptide antibiotic produced by the species *Streptomyces orientalis* (Bryskier & Veyssier, 2005). It is targeted against resistant Gram-positive bacterial infections, especially MRSA (Mascaretti, 2003). The molecular structure of vancomycin is presented in Figure 4-1. Due to its chromophores (for example the aromatic carbon rings and carbonyl groups), the molecule can be detected and quantified with UV absorption methods.

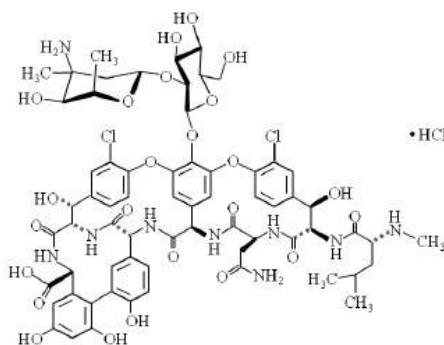
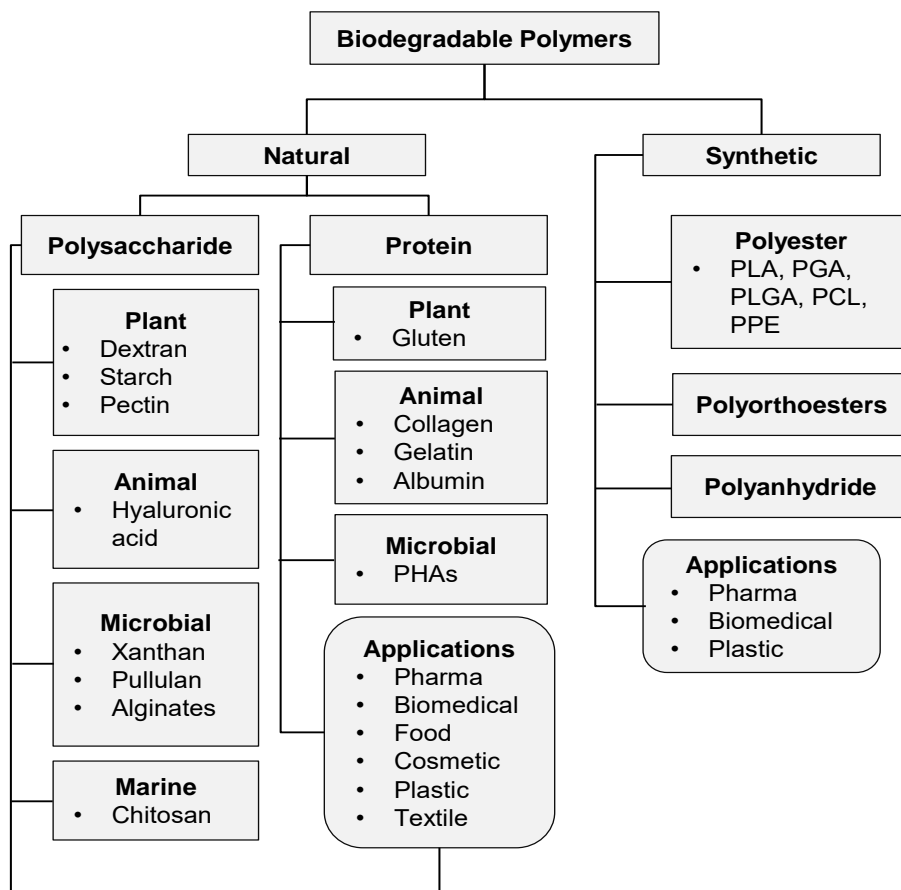


Figure 4-1: Vancomycin molecule 2D representation

A functional, clinically approved alternative for sustained drug release is encapsulation of the drug into polymer micro- or nanoparticles (Prajapati et al., 2015). Such a formulation can be suspended in a fluid medium and injected into the reservoir structure within the implant (Wang et al., 2011). Biodegradability is regarded of high importance, especially as it delivers the entire drug load during degradation, eliminates the risk of carrier toxicity, and does not necessitate removal surgery. Figure 4-2 shows a classification of the various biodegradable polymers used for drug delivery.



**Figure 4-2: Biodegradable polymers for drug delivery (recreated from Prajapati et al., 2015)**

Depending on several factors, drug release can vary from hours to months (Hachicha et al., 2006; Sayin et al., 2006). These factors include, among other, the polymer composition and structure, crystallinity, its molecular weight, hydrophilicity and other chemical properties related to both polymer and drug, and drug distribution (Freiberg & Zhu, 2004). Selection of polymer for vancomycin encapsulation is therefore no trivial task. An initial screening from the lists presented in the reviews of Prajapati et al. (2015) and Song et al. (2018) was performed based on whether the material is approved by the FDA for drug delivery. The list is presented in Table 4-1.

**Table 4-1: FDA approved biodegradable polymers for drug release (Prajapati et al., 2015; Song et al., 2018)**

Natural	Synthetic
Starch	PLGA
Dextran	PLA
Alginate	PGA
Pectin	PEG
Collagen	PELA
Gelatin	PCL
Fibrin	Polyanhydride
Hyaluronic acid	Polyurethane
Silk	Polyphosphazenes
Polyhydroxyalkanoates	
Albumin	

A serious disadvantage of natural biodegradable polymers is difficulty in controlling the degradation rate whereas synthetic biodegradable polymers can be modified for a wide range of mechanical and degradation properties (Song et al., 2018). An important example on the control offered by synthetic polymers is the ability to alter the initial burst release and maintain a steady sustained release of the remainder of the drug. Burst release of drug is generally attributed to accumulation of drugs at the surface and near the surface of the micro- or nanoparticles (Freiberg & Zhu, 2004).

Consider the drug release profiles in Figure 4-3. Both represent the *in vitro* release of vancomycin from a PLGA microparticulate formulation, however, the grades of the PLGA (lactic acid to glycolic ratio and average molecular weight), preparation method, resulting particle size, and drug loading conditions differ. Both studies evaluated the release over 30 days, but significantly different profiles can be observed. A high burst release (> 30% of loaded vancomycin over 24 hours) can be observed in Figure 4-3(a) with complete release at ~20 days. In comparison, the formulation in Figure 4-3(b) had a well suppressed burst release and loaded drug was not yet all released at 30 days. With the possibility of combining an antibiotic intraosseous injection or HA gel coating as prophylaxis, it is argued that for treatment of PJI the focus should be on reducing in burst release and aim for steady sustained release of vancomycin to either prevent or treat PJI from susceptible organisms.

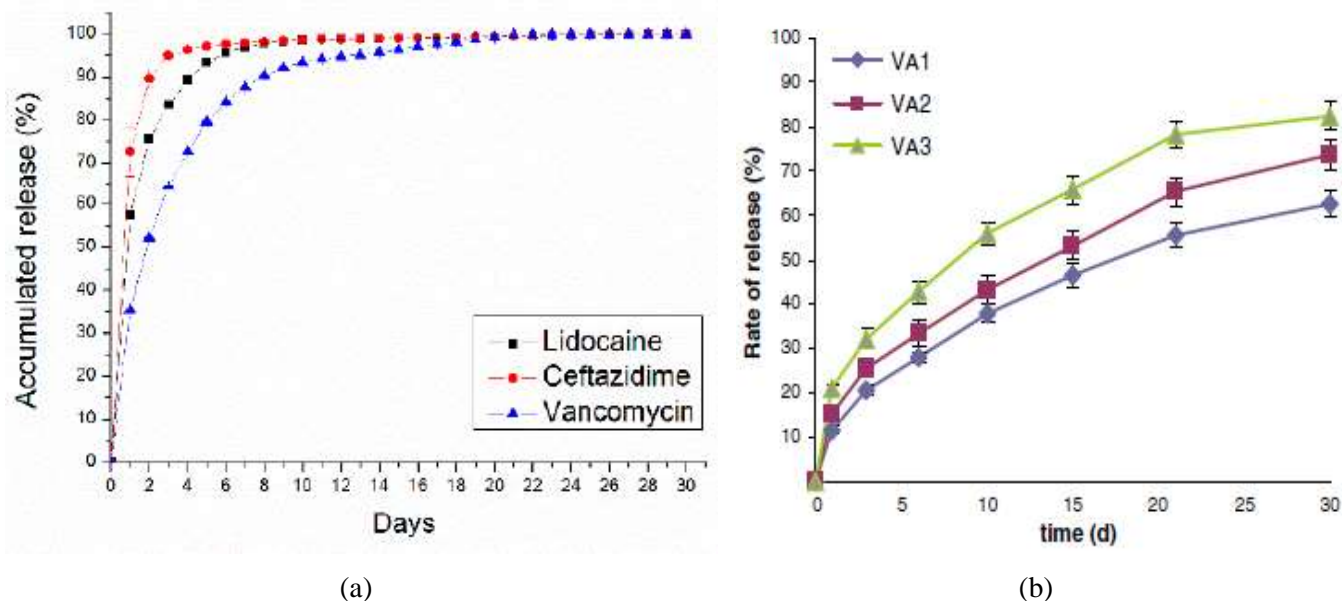


**Figure 4-3: PLGA encapsulated vancomycin microparticulate formulations with (a) showing burst release (PLGA 50:50, 33,000 Da) (Hsu et al., 2018) and (b) showing sustained release with a suppressed burst release (PLGA 75:25, 30,000) (Wang et al., 2011))**

Using the list in Table 4-1 as a point of departure, a literature search has been performed using the Scopus database. The objective was to compile a list of peer reviewed publications that encapsulated vancomycin in micro- or nanoparticles prepared from FDA approved biodegradable polymers. The search string was as follows, “TITLE-ABS-KEY(“*POLYMER*” AND (“nanoparticles” OR “microparticles” OR “microspheres”) AND “vancomycin” AND NOT “chitosan”)”. For each search the word “*POLYMER*” was replaced with the name of the respective polymer including alternative spellings or naming conventions (for example “poly(lactic acid)” and “poly lactide” for PLA) where relevant. The command “AND NOT “chitosan”” was included to clarify the search results since chitosan is not FDA approved for micro- or nanoparticulate drug formulations and several publications report on hybridising an FDA approved biodegradable polymer with chitosan (Hu et al., 2013; Li et al., 2017). The resulting list is included in Table B-1 in Appendix B.

Figure 4-4 visualises the relative number of relevant publications found per biodegradable polymer. It is clear that for the encapsulation of vancomycin the vast majority of available literature involved PLGA. Furthermore, PLGA dominates a list of commercial biodegradable microspheres presented in a review by Prajapati et al. (2015). Given the available historical data, the current market dominance, and the objective of material selection rather than investigation or development, PLGA is identified as a suitable material for encapsulation and sustained delivery of vancomycin.

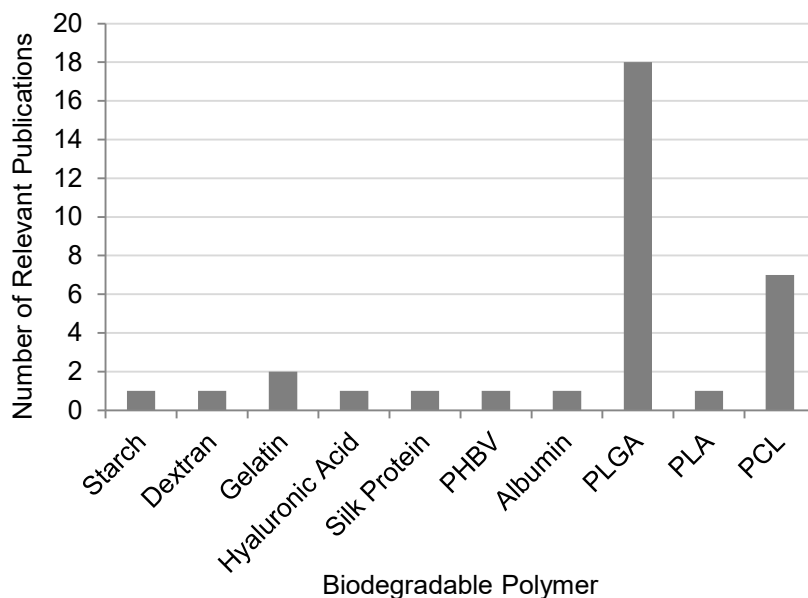


**Figure 4-4: Number of relevant publications of biodegradable polymers from Scopus search**

PLGA is available in a wide range of grades. This entails the PLA:PGA ratio, average molecular weight or inherent viscosity, and the polymer chain end chemistry (carboxylic acid or ester terminated). All these factors significantly influence the biodegradation and release behaviour. These factors are all identified as important for consideration during further material specification for vancomycin delivery within the framework (Kapoor et al., 2015).

#### 4.1.2 Gaining Insight into PLGA Erosion and Drug Release

PLGA is a biodegradable aliphatic copolymer consisting of adjustable ratios of PLA, usually in an equal ratio of the poly D-lactic acid (PDLA) and poly L-lactic acid (PLLA) enantiomers, and PGA (Makadia & Siegel, 2011). The structure of the polymer is shown in Figure 4-5. Commercial variations typically offer either a carboxylic acid or methyl ester end group, indicated by the R in Figure 4-5.

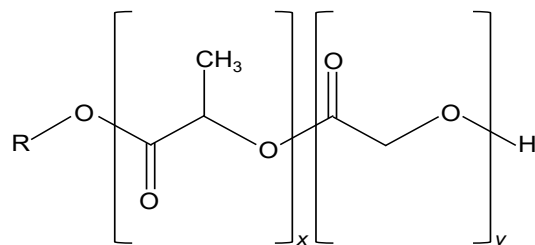


**Figure 4-5: PLGA structure (recreated from Makadia & Siegel, 2011)**

PLGA undergoes bulk erosion in aqueous environments through random hydrolysis of ester linkages along the polymer backbone (Makadia & Siegel, 2011). This means that degradation happens heterogeneously throughout the polymer and the process can be divided into a sequence of four steps (Lanao et al., 2013). First the polymer is hydrated as water enters through the amorphous regions and disrupts the hydrogen bonds and van der Waals forces, leading to a decrease in the glass transition temperature. Second is the initial degradation which involves the cleavage of covalent bonds, decreasing the molecular weight of the polymer. Third is the continuous degradation, autocatalysed through carboxylic acid end groups, resulting in mass loss by extensive cleavage of the backbone and subsequent loss of structural integrity. Fourth is solubilisation where remains (fragments) are further cleaved into molecules that are soluble in the aqueous environment (Lanao et al., 2013; Gentile et al., 2014). The end products of PLGA degradation are lactic acid and glycolic acid Figure 4-6 which are processed through metabolic routes and excreted as carbon dioxide and water.

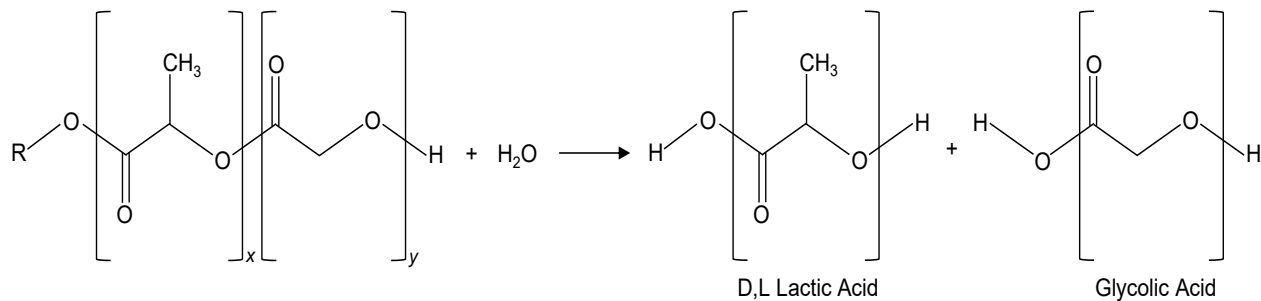


**Figure 4-6: Hydrolysis of PLGA (recreated from Makadia & Siegel, 2011)**

The objective of this section is to develop a basic understanding of the PLGA bulk erosion and drug release mechanism through a stochastic simulation approach according to that of (Göpferich, 1997). The stochastic model was implemented in *MATLAB*, with the algorithm code provided in Appendix B. For simplicity, the model currently does not take polymer swelling into account. It distinguishes between polymer degradation, loss in molecular weight due to hydrolysis of the ester linkages, and polymer erosion, mass loss due to diffusion of degradation products out of the polymer matrix. It is further based on the assumption that degradation necessarily precedes erosion, and that erosion can only proceed by an open pathway to the polymer surface.

A two dimensional (2D) computational grid Figure 4-7 is initialised which represents the polymer matrix. The grid size can be altered by specifying different values for the number of elements in the x ( $nx$ ) and y ( $ny$ ) directions.

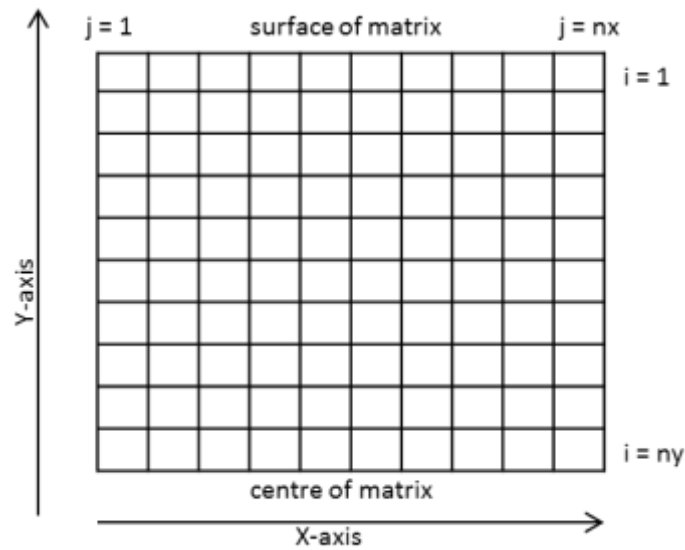


**Figure 4-7: 2D computational grid for simulation of PLGA bulk erosion and drug release**

In Figure 4-7, a periodic boundary condition exists on the x-axis,

$$\begin{array}{l} x_{i,0} = x_{i,nx} \\ x_{i,nx+1} = x_{i,1} \end{array} \left| \begin{array}{l} 1 \leq i \leq ny \end{array} \right. \quad (4-1)$$

and a reflective boundary condition is imposed on the y-axis.

$$y_{ny+1,j} = y_{ny,j} \left| \begin{array}{l} 1 \leq j \leq nx \end{array} \right. \quad (4-2)$$

Each element (subsequently referred to as pixels) represents a part of the polymer matrix and, utilising a greyscale colour map, can be in one of three states, intact (black pixel = 0), degraded (grey pixel = 0.5), or eroded (white pixel = 1), that is.

$$\begin{array}{l} \text{Intact} \\ \text{Degraded} \\ \text{Eroded} \end{array} \quad \begin{array}{l} x_{i,j} = 0 \\ x_{i,j} = 0.5 \\ x_{i,j} = 1 \end{array} \left| \begin{array}{l} 1 \leq i \leq ny \\ 1 \leq j \leq nx \end{array} \right. \quad (4-3)$$

Described above is the effective erosion and drug release matrix. Other matrices are initialised and utilised which communicates and control erosion and drug release processes from the effective matrix. These are the polymer state, pixel lifetime, and drug distribution matrices. Interactions between the matrices are presented in the schematic below. An additional matrix (not shown in Figure 4-8) is also created for visualisation purposes which represents the complete state of the starting polymer matrix with respect to crystalline (black), amorphous (grey), and drug (white) pixels.

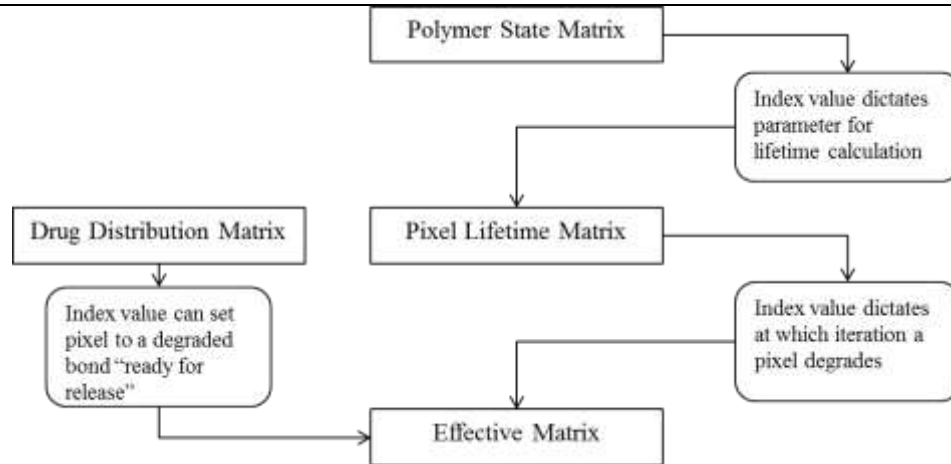


**Figure 4-8: Schematic of communication between matrices**

First a polymer state matrix is initialised where the indices represent amorphous or crystalline regions. Whether a pixel is crystalline or amorphous is determined by a Bernoulli trial in which the probability of success is the user specified percentage of the polymer matrix expected to have a crystalline structure (Wang et al., 2007).

Once the polymer state is determined, the lifetime for each pixel is determined. It is assumed that degradation arrival times follow a Poisson process and is calculated according to Equation 4-4 below derived by (Göpferich, 1997),

$$t_{i,j} = \frac{1}{\lambda_{i,j} \ln(n^2)} \ln(1 - \epsilon) \quad (4-4)$$

where  $\lambda_{i,j}$  is the degradation rate constant for pixel  $i,j$ ,  $n$  is the number of pixels in either x- or y-direction for a square grid, and  $\epsilon$  is a random variable distributed between 0 and 1 which represents the probability that a pixel erodes within the respective time interval (Göpferich, 1997). When the iteration time step  $t_{i,j}$  is reached, the corresponding pixel degrades and turns grey in the effective matrix, unless the pixel is already eroded, in which case it remains white.

The drug distribution matrix is initiated according to Bernoulli trials where the probability of success is the fraction of drug loading within the polymer matrix. Pixels that represent drugs are set to grey in the effective matrix. If a path to the surface exists, the pixel is eroded, which in this case represents release of the drug, and said pixel turns white.

Currently, the model is in a generic format with regards to the required parameters that would need to be determined empirically in order to tailor the model for a specific PLGA grade. These parameters include the ratio of crystalline to amorphous structure, arrival rate ( $\lambda$ ) of bond hydrolysis for the respective structures, and the fraction of drug loading. The model currently allows for changing any of these parameter settings. The following example aims to demonstrate the simulation program with parameter values set to obtain typical profiles witnessed in literature (Makadia & Siegel, 2011).

Firstly, the program uses Bernoulli trials to populate the computational grid (300 x 300 pixels) with either crystalline, amorphous, or drug pixels (Figure 4-9). This figure can be used as reference to trace back the identity of uneroded pixels at the end of an execution scenario.

Starting Polymer State: Crystalline (black), Amorphous (grey), and Drug (white)

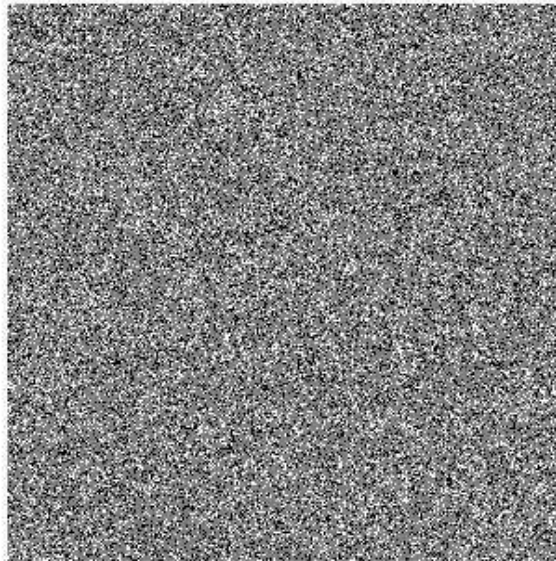


**Figure 4-9: Output matrix of the starting polymer matrix**

Based on this matrix, the polymer matrix for erosion, presented in Figure 4-10(a) is created. Since drug pixels are assumed to be able to erode on contact with a path leading to the surface, they act as already degraded bonds. Black pixels indicate intact bonds and grey pixels degraded bonds. A black pixel (intact bond) first needs to turn grey (degraded bond) before it can turn white (erode out of matrix). The eroded and degraded bonds are represented in Figure 4-10(b).

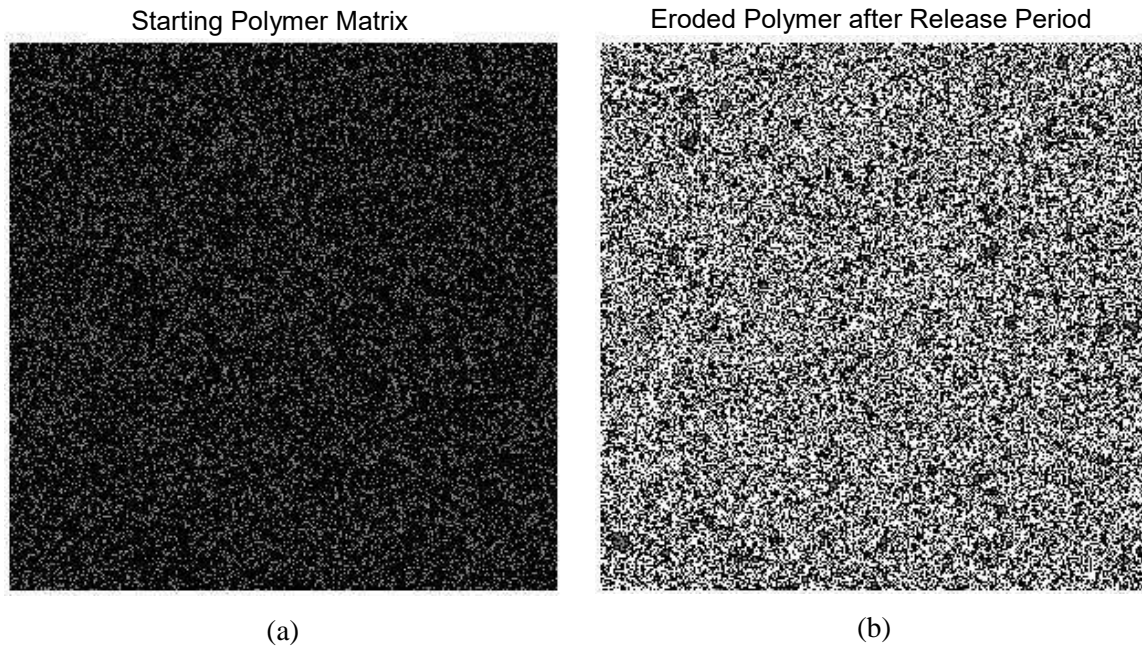


**Figure 4-10: Pixel matrices representing (a) polymer state at initiation of program and (b) polymer state after program execution**

In order to trace back the drug pixels to the original distribution, the program outputs both scenarios as figures during execution of the program. Represented by the two matrices in Figure 4-11 below are the distributions of the drug pixels before (Figure 4-11(a)) and after (Figure 4-11(b)) execution of the program.

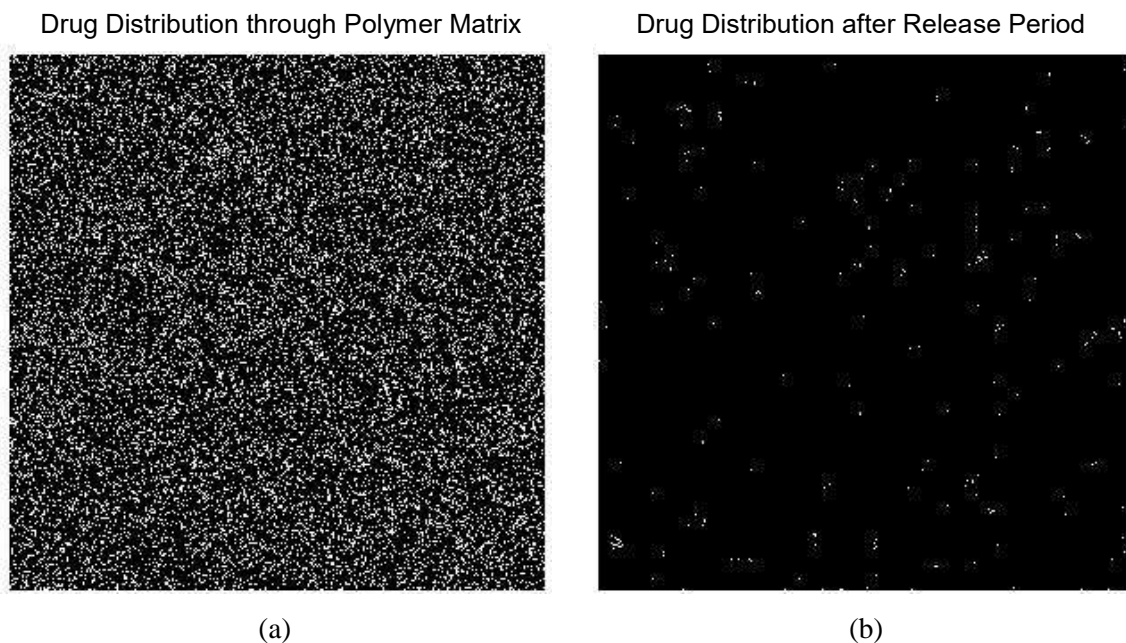


**Figure 4-11: Simulated drug distribution (a) at the start of the program and (b) at the end of the program**

The resulting degradation and erosion profiles as the average of three executions from the current program are presented in Figure 4-12(a) along with the output from that of Göpferich (1997) (Figure 4-12(b) and (c)). Users can specify the amount of times the program should loop. The resulting general profile from the *MATLAB* code appears to be in close agreement with that of Göpferich (1997). The degradation profile begins at  $1 - \text{Probability}(\text{drug pixel})$  since the drug pixels are assumed to behave as already degraded bonds.

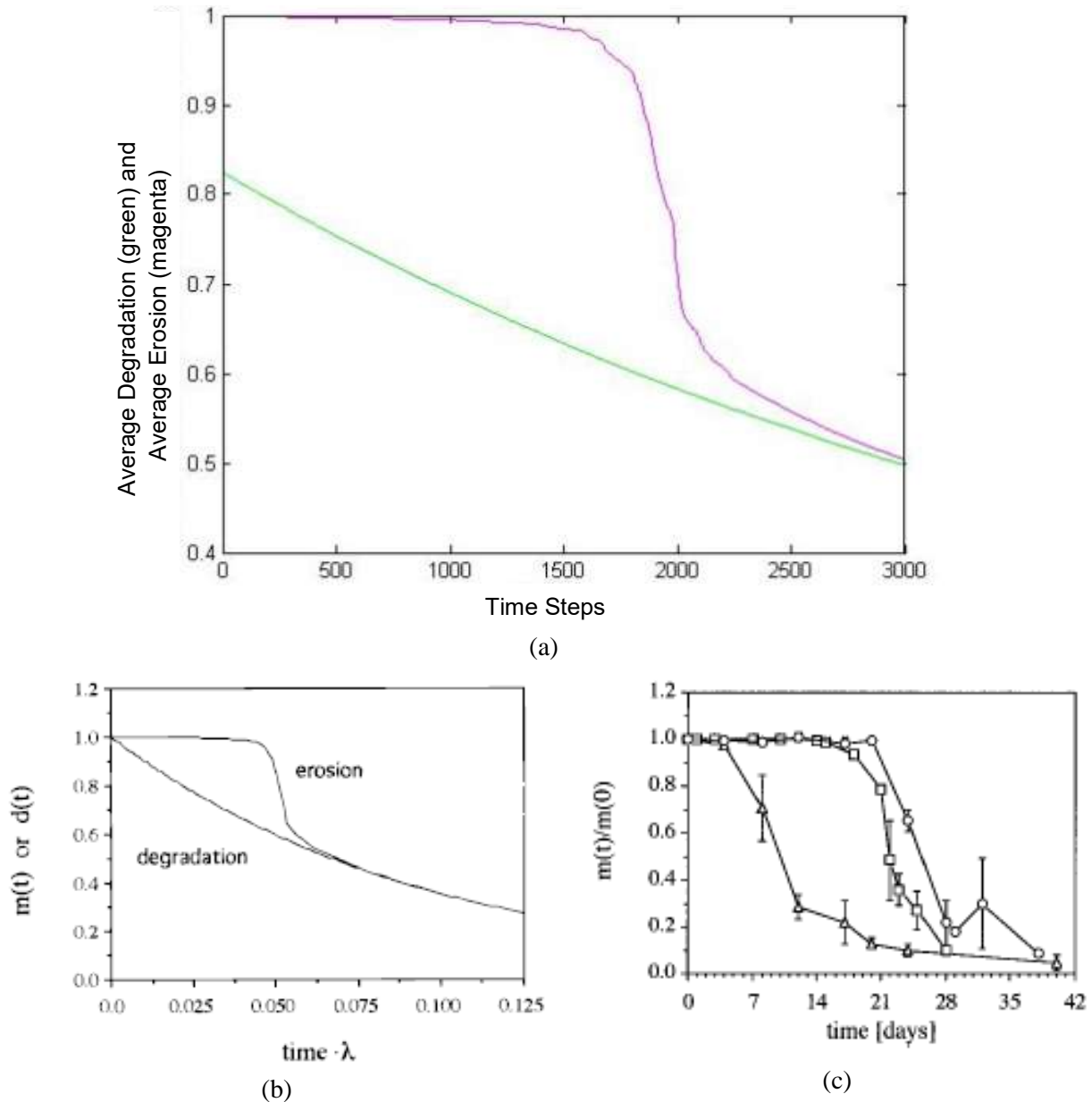


**Figure 4-12: Degradation and erosion profiles of (a) simulation program, (b) from the simulation of Göpferich (1997), and (c) experimentally obtained mass loss profile for Resomer RG 502H (triangles), Resomer RG 504H (squares), and Resomer RG 502 (circles) (Göpferich, 1997)**

The erosion profile indicates a percolation threshold effect in bulk erosion. An underlying condition for bulk erosion is that the dissolution medium penetrates into the matrix faster than the degradation products can diffuse out (Makadia & Siegel, 2011). Several tiny paths for erosion thus develop all at once, which lead up to a critical point that when reached, causes large amounts of degraded bonds to erode all at once. It is reported in literature that this can occur on smaller scales during the bulk erosion process (Duvvuri et al., 2006; Ramchandani & Robinson, 1998), and the stochastic nature of the program manages to capture these random occurrences as shown in Figure 4-13. The encircled area indicates a period in the program where pixels had not yet a connected erosion path which, when coming to existence, creates small erosion bursts within the overall mass erosion.

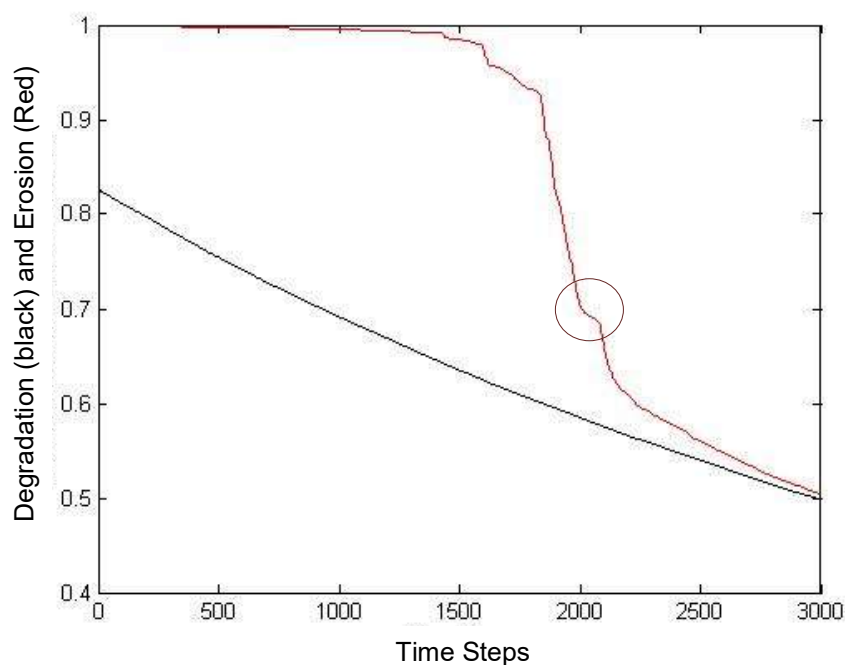
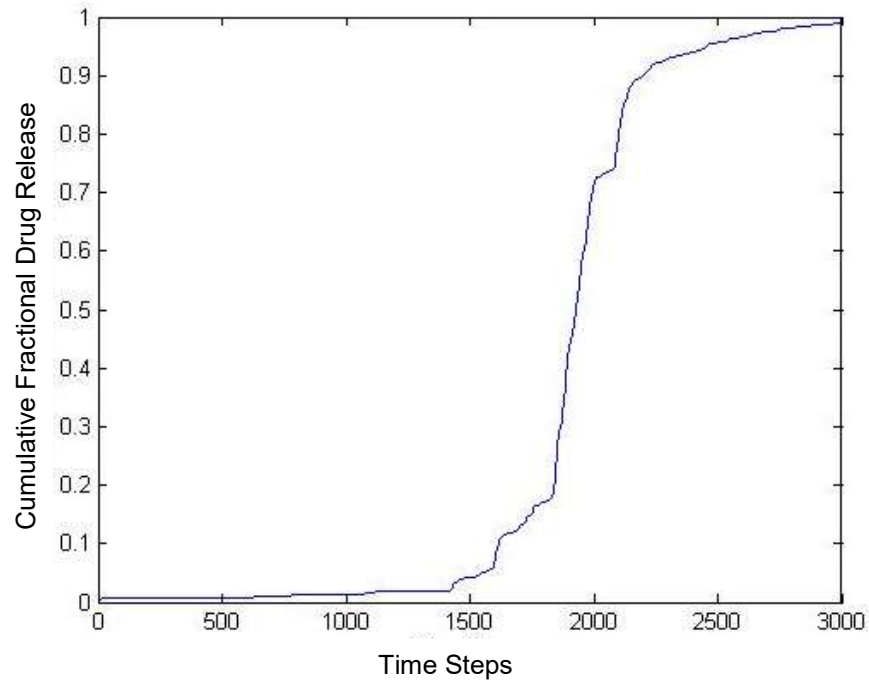
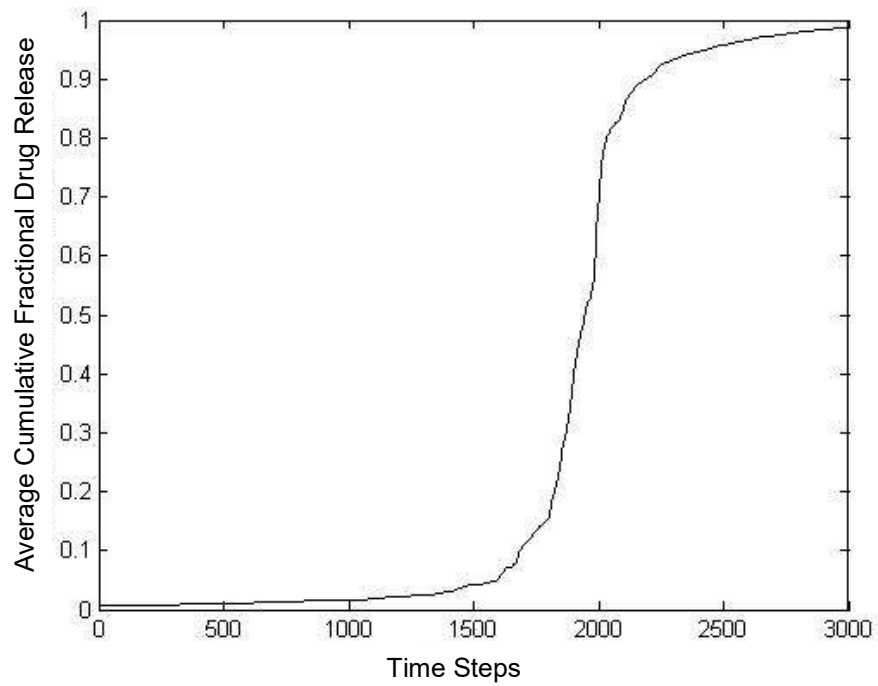


**Figure 4-13: Degradation (black) and erosion (red) from a single program execution**

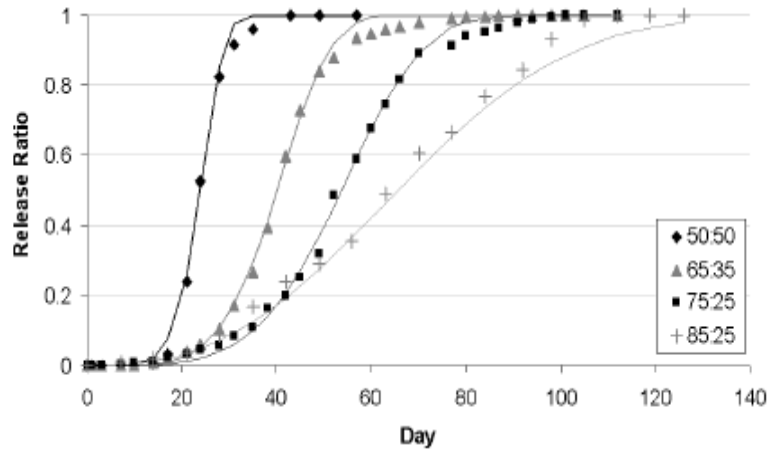
Resulting drug release profiles from the simulation are presented in Figure 4-14(a) and (b). A typical sigmoidal profile can be observed which is often reported for drug release from PLGA matrices without any additives. This is demonstrated with the profiles reported by (Amann et al., 2010) in Figure 4-14(c) and by (Duvvuri et al., 2006) in Figure 4-14(d). Degradation and Release profiles can however be difficult to accurately predict due to the relatively large amount of possible variables, all adding complexity to the process. These include copolymer composition, average molecular weight of the chains, crystallinity and glass transition temperature, and autocatalytic effects due to locally reduced pH levels caused by the acidic degradation products of PLGA.



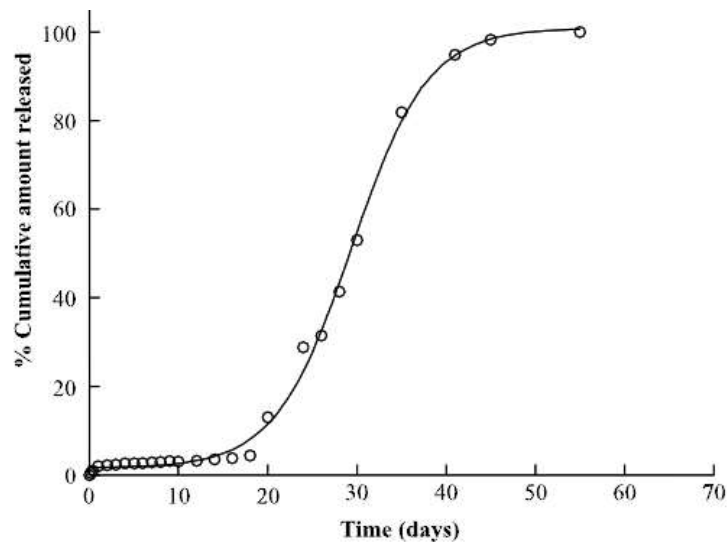
(a)



(b)



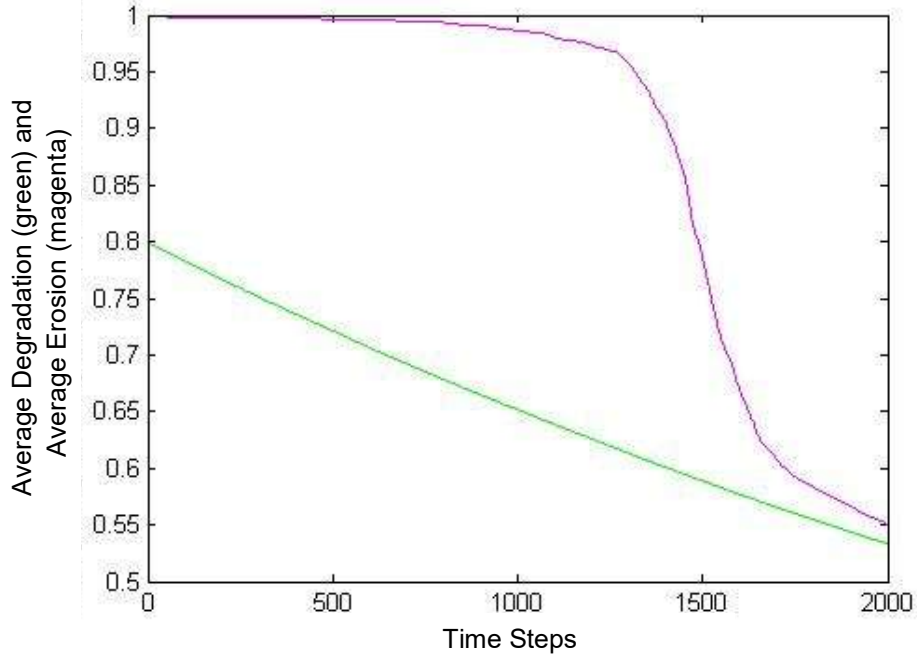
(c)



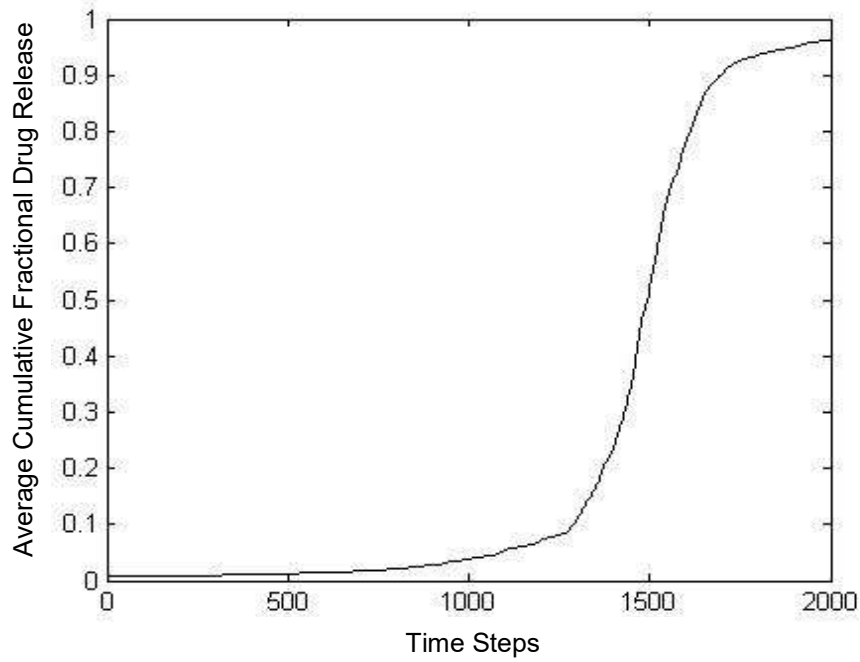
(d)

**Figure 4-14: Drug release profile from (a) single program execution, (b) average of three executions, (c) modelled release profiles in literature (key indicates lactic acid to glycolic acid ratio) (Amann et al., 2010), (d) cumulative release profile of ganciclovir from Resomer RG 502H in literature (Duvvuri et al., 2006)**

A useful result of the model is that it can also give an indication of the effect of drug-polymer ratio on time shifts in reaching the percolation threshold. This is demonstrated in Figure 4-15, the average of 5 program executions where the probability of a pixel being a drug is varied between 0.2 (Figure 4-15(a) and (b)) and 0.35 (Figure 4-15(c) and (d)). When taken into consideration that, if drug molecules can readily diffuse out of the matrix instead of first degrading into smaller parts, it is likely that the higher the drug loading, the quicker the percolation threshold will be reached and subsequently mass erosion occurs. This, however, needs to be substantiated with further empirical evidence, but is outside the scope of this study.



(a)



(b)

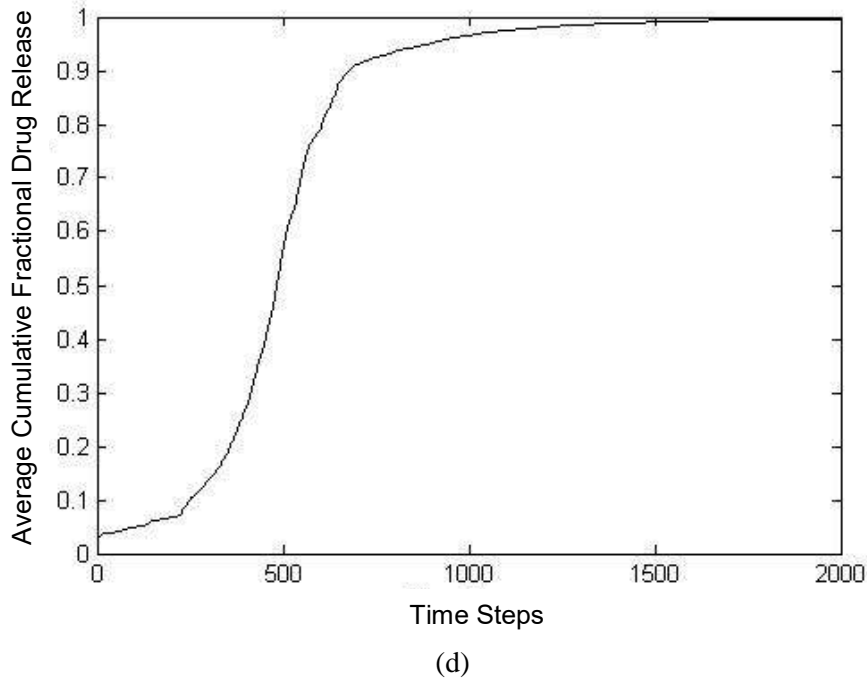
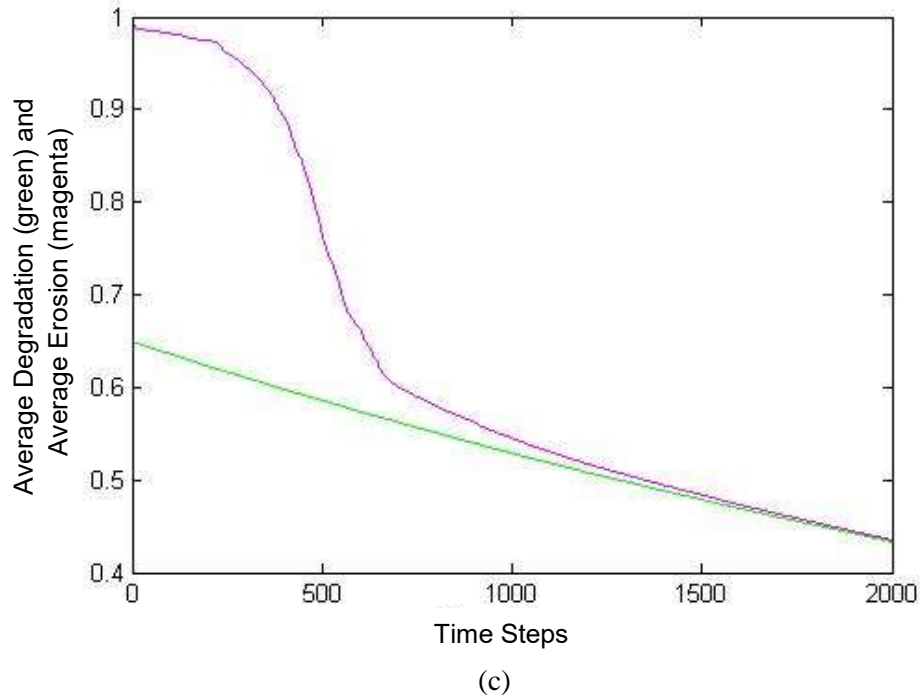


**Figure 4-15: Average degradation and erosion (a), average cumulative fractional drug release (b) for a drug probability of 0.2, and average degradation and erosion (c) with average cumulative fractional drug release (d) for a drug probability of 0.35**

Although simplifications in the model most likely impart several causes of inaccuracies, the basic profile holds well when compared to literature where PLGA without further modifications has been used. At this point it is concluded that the model reasonably captures the bulk erosion and drug release process in a simplified form. The model can be further developed and adapted to a specific employed formulation by empirical refinement of the model parameters. From here the model can be improved through incorporation of specialised function modules such as polymer swelling and time or geometry dependent degradation behaviour, thereby defining the lifetime of pixels as a function of time and space within the computational grid. Nevertheless it aids in providing a basic level of insight to the non-polymer scientist within the context of the interdisciplinary framework into the expected erosion and drug release profiles resulting from encapsulation of a drug in PLGA.

#### ***4.2 Vancomycin Encapsulated Nanoparticles Preparation and Release Testing***

Fabrication of vancomycin encapsulation PLGA nanoparticles was performed by the Department of Microbiology using an electrospraying preparation method (Figure 3-6). The experimental details regarding the preparation and testing of the nanoparticles can be found in Booysen et al. (2019). Resomer RG 753 H PLGA was procured from Evonik Nutrition & Care GmbH for nanoparticle preparation. Material selection was mainly based on the properties of the polymer regarding vancomycin release profiles reported in literature (Wang et al., 2011). The properties are lactic acid to glycolic acid ratio of 75:25, inherent viscosity of 0.32-0.44 dl/g which corresponds to a molecular weight of roughly 30,000 – 35,000 Da, and non-end capped (carboxylic acid terminated). A field emission scanning electron microscope (FE-SEM) image of the PLGA nanoparticles with encapsulated vancomycin is presented in Figure 4-16. The mean size of the nanoparticles is 247 nm with a polydispersity index (PI) of 0.385. The relatively high PI can possibly be related to the electrospraying setup and specifically the flow rate of polymer solution to the spray nozzle (Booyesen et al., 2019).

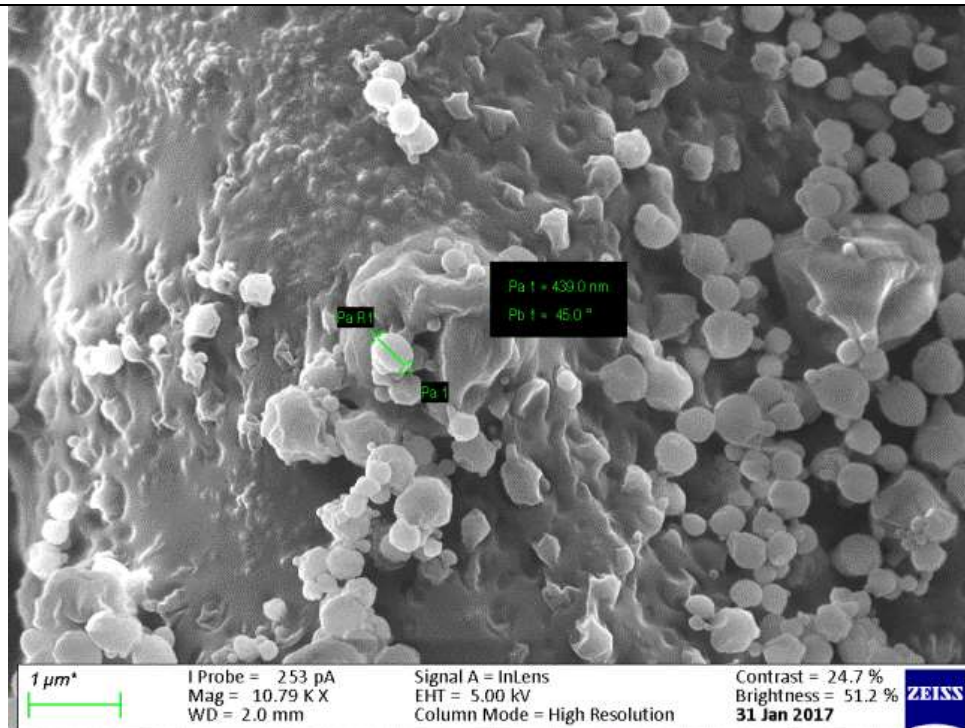


**Figure 4-16: FE-SEM image of vancomycin encapsulated PLGA nanoparticles**

A customised setup was required for release testing of the nanoparticles. Challenges involved the size of the nanoparticles and the requirement for simultaneous release testing of several batches which enhances testing efficiency. These challenges were addressed through a collaborative effort in which a tailored solution was developed using the design freedom within AM. A custom diffusion cell was designed using *Autodesk PowerSHAPE* and manufactured with a commercial fused deposition modelling (FDM) Zortrax M200 3D-printer (Figure 4-17). The diffusion cell (Figure 4-17(a)) consisted of a press fit assembly of three parts: (1) a frame to fit a 5 kDa molecular weight cut off polyethersulfone membrane for the donor reservoir, (2) a foot piece to fix the frame to the buffer reservoir with space for a magnetic stirrer bar to enable continuous agitation of the buffer medium, and (3) an acceptor reservoir. The assembly (Figure 4-17(b)) was closed off with a cap to reduce evaporation (Figure 4-17(c)). Vancomycin release sampling and analysis details can be found in Booyesen et al. (2019).

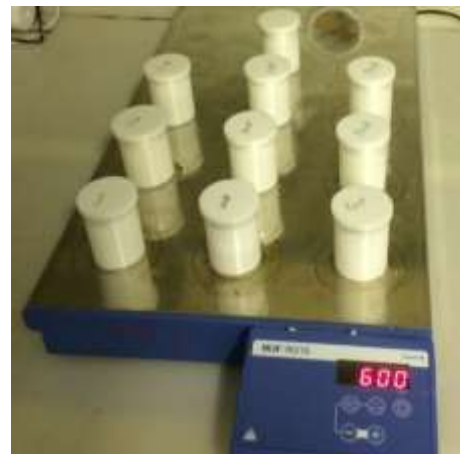
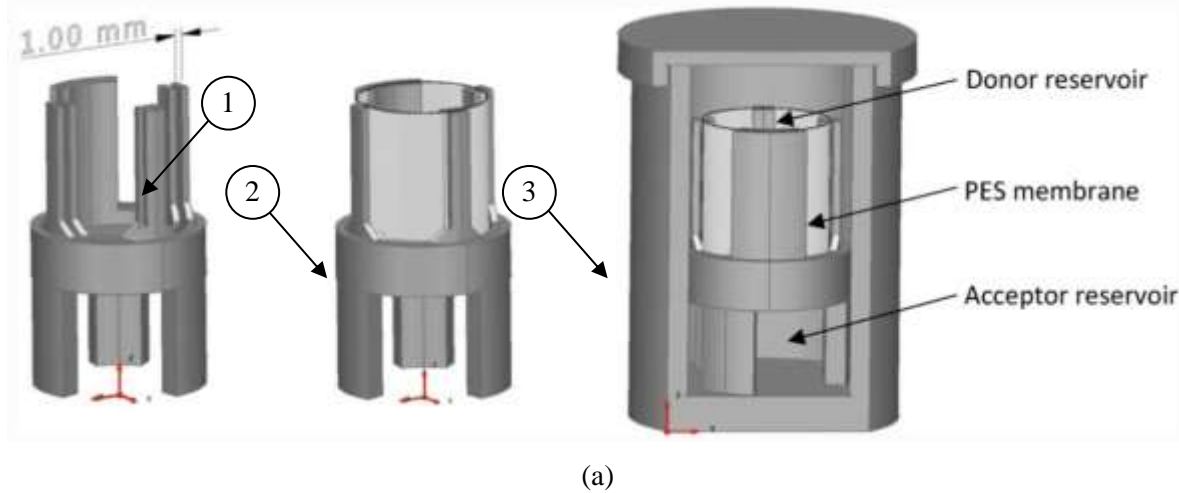


**Figure 4-17: Custom made diffusion cell with (a) CAD model (adapted from Booyesen et al., 2019), (b) assembled cell, and (c) diffusion cells in release testing with magnetic stirring at 600 rpm**

The vancomycin release profile from PLGA nanoparticles is presented in Figure 4-18. Release was monitored for a period of 240 h and effective vancomycin concentrations ( $5 \mu\text{g/mL}$ ) were detected after 24 h. Importantly, no significant burst release was observed, which confirms the selection of a suitable PLGA grade for the objective of steady sustained release. Furthermore, after 10 days, 50% of the total vancomycin content was released, which indicates that the formulation can sustain vancomycin release. An important finding was a reduction effect of vancomycin encapsulation on the MIC against both *S. aureus* Xen 36 (MSSA) and *S. aureus* Xen 31 (MRSA). PLGA encapsulated vancomycin had an MIC of  $1 \mu\text{g/mL}$  for both strains of *S. aureus* whereas the MIC of free vancomycin was found to be  $3 \mu\text{g/mL}$  for *S. aureus* Xen 36 and  $5 \mu\text{g/mL}$  for *S. aureus* Xen 31.

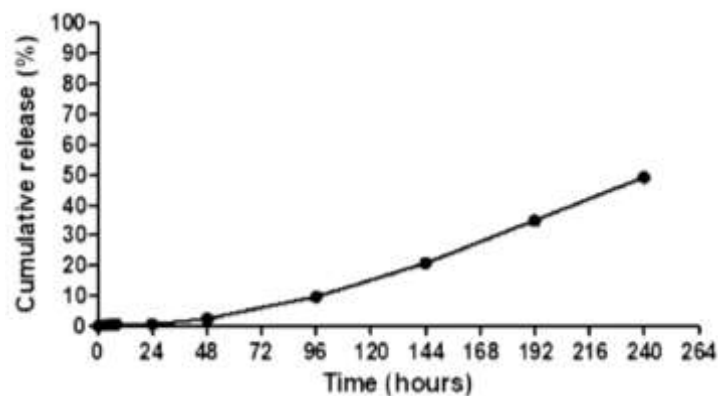


Figure 4-18: Vancomycin release profile from PLGA nanoparticles (Booyesen et al., 2019)

### 4.3 Conclusion

This chapter addressed the single problems for developing a demonstrator formulation for the sustained release of vancomycin. Based on the results, the following conclusions were made:

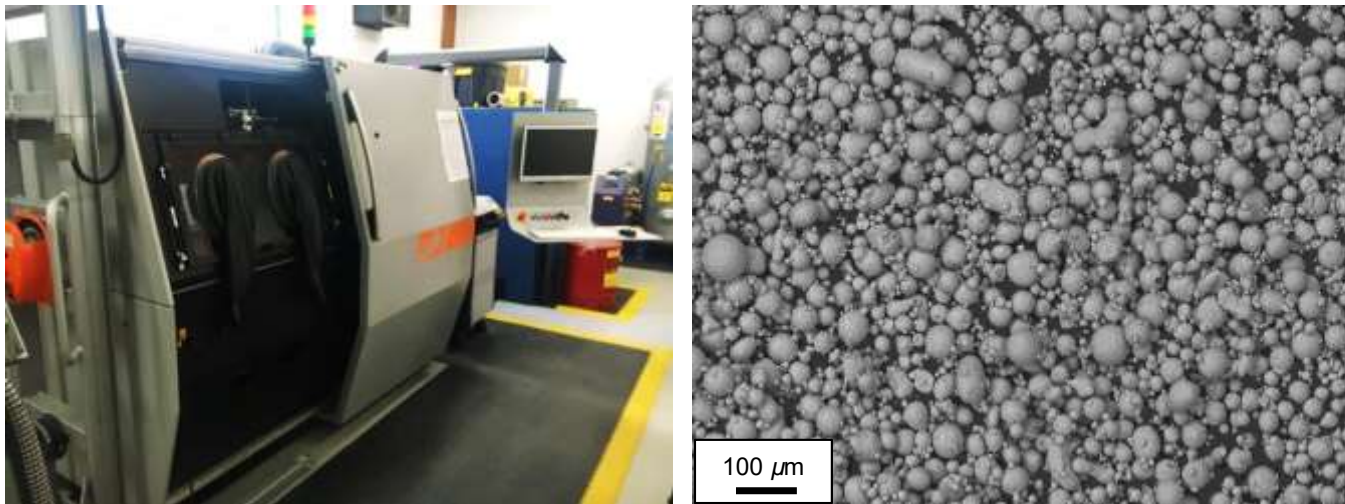
- PLGA was identified to be the most frequently used clinically approved polymer for sustained release
- A simplified stochastic model has been implemented in *MATLAB* to aid non-polymer scientists in gaining an understanding of the polymer bulk erosion and drug release process
- Trade-offs regarding the PLGA grade and effects on erosion need to be carefully studied in order to select a grade which offers the appropriate potentials for the application
- Vancomycin can be encapsulated in PLGA through an electrospraying process to yield vancomycin encapsulated PLGA nanoparticles
- An IKP was generated through interdisciplinary collaboration within the single problems through the development of a custom experimental setup for vancomycin release testing
- Release of vancomycin can be sustained for at least 240 h by a PLGA nanoparticle formulation while suppressing a significant burst release
- Encapsulation of vancomycin in PLGA reduced the MIC against both *S. aureus* Xen 36 and Xen 31, thereby reducing the total amount of vancomycin required to maintain antimicrobial efficacy
- An IKP on the release considers the fact that therapeutic vancomycin concentrations was reached after 24 h and therefore immediate prophylactic availability of vancomycin released locally through a cementless hip stem should also be investigated using a low viscosity formulation in which vancomycin has high solubility, for example an aqueous vancomycin solution

## 5. Inducing Porosity in LPBF for Drug Release

A study was performed to identify the effects of the key process parameters namely, laser power, scanning speed, and hatch spacing, on the resulting relative porosity within Ti6Al4V ELI cylindrical specimens. It represents a point of departure in the decomposition process within the overall framework for the partial problem of “Enabling drug release from implant reservoir”. The screening study provided insight into the effects of these LPBF process parameters from the in-house available *M2 cusing* LPBF machine from Concept Laser GmbH. IKPs generated in this chapter were implemented in subsequent experimental designs regarding the production of components with induced porosity for drug delivery from a cementless hip stem.

### 5.1 LPBF Machine and Material

Unless otherwise specified, all titanium alloy parts within this study were fabricated using an *M2 cusing* system (Concept Laser GmbH, Lichtenfels, Germany) (Figure 5-1(a)), fitted with a 200 W ytterbium fiber laser emitting at 1070 nm wavelength. Gas atomized Ti6Al4V ELI powder (TLS Technik GmbH & Co, Bitterfeld-Wolfen, Germany) (Figure 5-1(b)) with a particle size distribution of  $d_{10} = 25.51 \mu\text{m}$ ,  $d_{50} = 37.63 \mu\text{m}$ , and  $d_{90} = 50.47 \mu\text{m}$  and chemical composition as reported on the official certificate of analysis is presented in Table 5-1 were used.



(a) (b)  
**Figure 5-1: (a) LPBF machine and (b) Ti6Al4V ELI powder**

**Table 5-1: Chemical composition of the Ti6Al4V ELI powder (wt%)**

	Ti	Al	V	Fe	O	C	N	H	Y	Other each	Other total
<b>TLS</b>	Balance	6.34	3.94	0.25	0.082	0.006	0.006	0.001	n/a	n/a	n/a
<b>ASTM F3001 (max)</b>	Balance	6.5	4.5	0.25	0.13	0.08	0.05	0.012	0.005	0.1	0.4

The build chamber was flooded with argon gas prior to the building process to maintain an inert atmosphere (oxygen content < 0.1%) and reduce the risk of oxidation. The laser scanning strategy was kept constant as the default island pattern throughout all experiments (Figure 5-2). Briefly, the 2D layer is divided into islands of 5 x 5 mm resulting in a chessboard-like pattern (Figure 5-2(a)). The islands are exposed in a random order. Each island is filled with vectors alternating in direction and neighbouring islands are oriented with their fill vectors perpendicular to each other (Figure 5-2(b)). To reduce compounding effects of exposing vectors directly on top of each other, each subsequent layer the island pattern is moved by 1 mm in both the x- and y-direction (Figure 5-2(c)) (Carter et al., 2014). The entire pattern was built at a rotation of 45°.

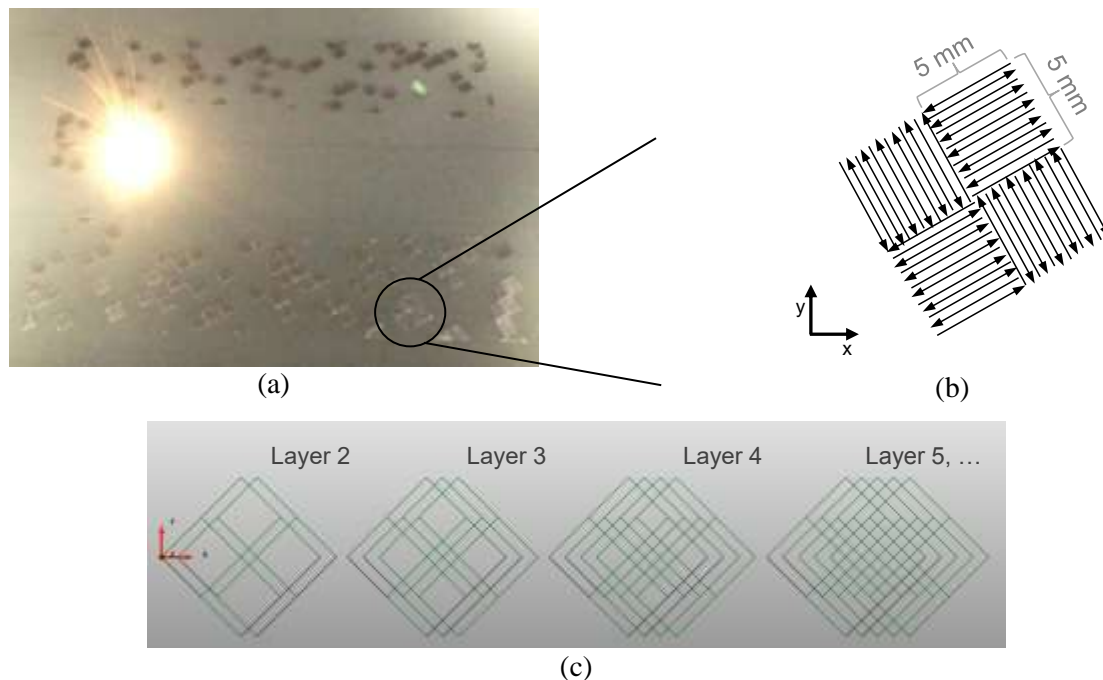


**Figure 5-2: Default island scanning strategy with (a) a layer being exposed inside the building chamber, (b) a schematic of the islands and fill vector directions, and (c) a schematic of the pattern shift between subsequent layers**

## 5.2 Influence of Key Parameters - Experimental Setup and Design

### 5.2.1 Process Parameter Variation

The values of the parameters were varied according to a DoE approach with a spherical central composite design (CCD) with star points at a distance of  $\pm\sqrt{k}$  ( $k$  is the number of factors) at a level of significance ( $\alpha$ ) of 0.05, using *Design Expert* (Statease) statistical software. Three centre points were included as well as an extra point which represents the machine manufacturer's default parameters for Ti6Al4V ELI, which are 100 W laser power, 600 mm.s<sup>-1</sup> scanning speed, 0.7 $d$   $\mu$ m hatch spacing, where  $d$  is the aperture which is specified in the control software as 150  $\mu$ m, yielding a default hatch spacing of 105  $\mu$ m. The layer thickness was kept constant at 30  $\mu$ m. The manufacturer specified parameters are henceforth referred to as 'default parameters'. The CCD parameter variations are presented in Table 5-2.

**Table 5-2: Spherical CCD DoE investigation of influences of key parameters on part porosity**

Run ID	Laser Power (W)	Scanning (mm.s <sup>-1</sup> )	Speed ( $\mu$ m)	Hatch Spacing ( $\mu$ m)	VED (J.mm <sup>-3</sup> )	Relative Porosity (%)
1	80	1215		130.95	16.76	5.35
2	122.5	825		105	47.14	0.28
3	80	435		79.05	77.55	0.78
4	165	435		79.05	159.95	1.28
5	80	1215		79.05	27.76	2.58
6	165	435		130.95	96.55	0.89
7	165	1215		79.05	57.26	0.18
8	196.11	825		105	75.46	0.46
9	122.5	825		105	47.14	0.44
10	122.5	825		60.05	82.42	0.28
11	122.5	825		105	47.14	0.30
12	122.5	825		149.95	33.01	0.53
13	48.89	825		105	18.81	1.52
14	122.5	435		130.95	46.81	0.28
15	122.5	1500.5		105	25.92	1.24
16	165	1215		130.95	34.57	0.92
17	122.5	149.5		105	260.13	0.72
18*	100	600		105	52.91	0.26

\* Manufacturer specified default parameter set

### 5.2.2 Relative Porosity Measurement

Relative porosity of cylindrical specimens was analysed non-destructively at the computed tomography (CT) unit of the Central Analytical Facilities (CAF) at SU. A General Electric *Phoenix VTOMAX L240* micro computed tomography ( $\mu$ CT) machine was used with standardised data acquisition parameters as specified by du Plessis *et al.* (2017). The scan resolution was set to a voxel size of 20  $\mu$ m. Porosity analysis was performed by the CAF CT-unit using *VGStudio Max 2.1* (Volume Graphics). Received CT data were reviewed, and images created using the viewer version of the analysis software, *myVGL*.

### 5.3 Influence of Key Parameters - Results and Discussion

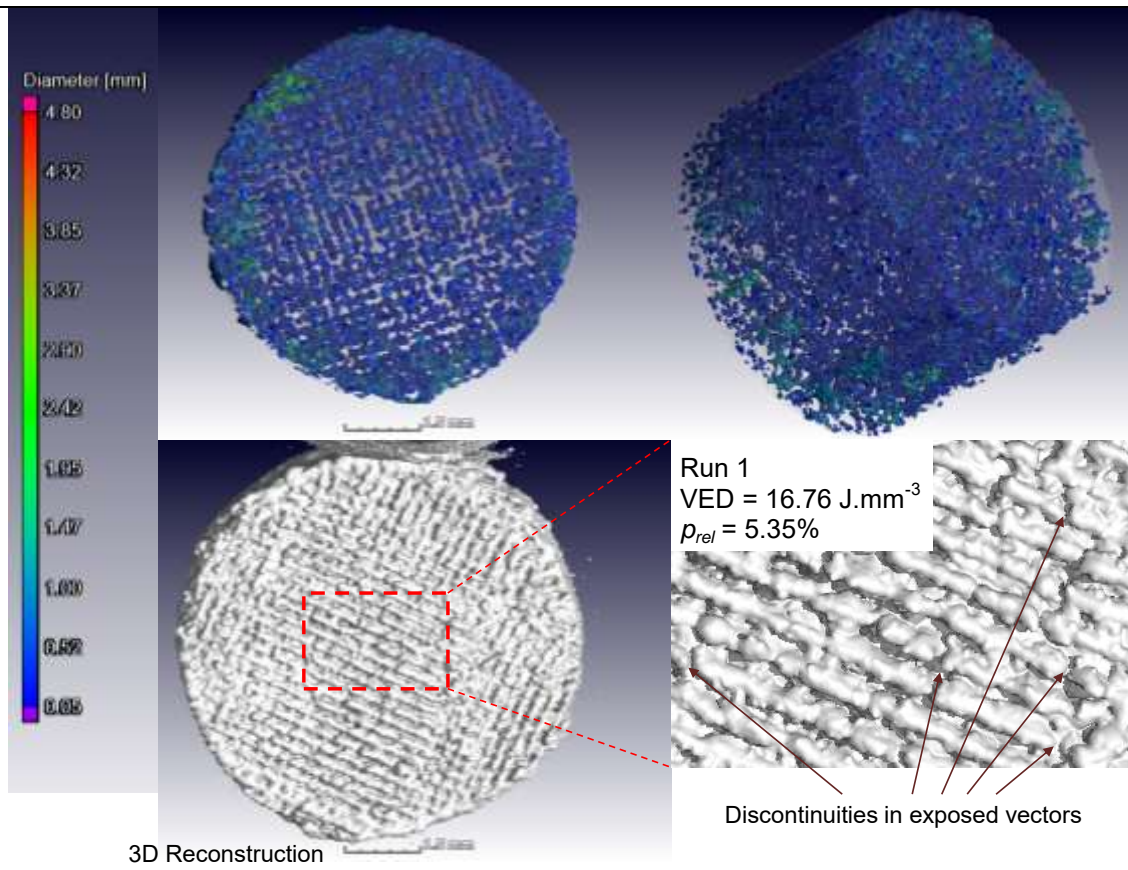
The fabricated specimens are presented in Figure 5-3. Obtained relative porosity ( $p_{rel}$ ) values are included in Table 5-2 (refer Section 5.2.1 above).



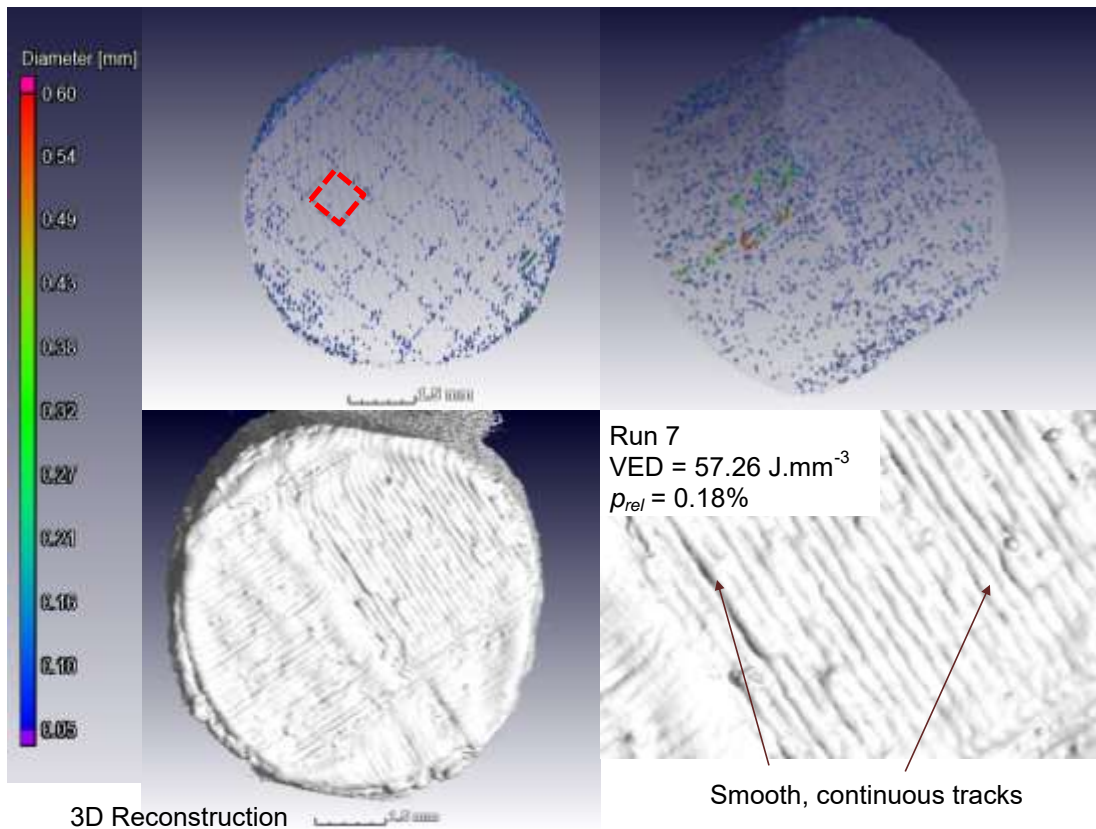
**Figure 5-3: Cylindrical specimens for porosity measurement**

Three dimensional reconstructions of the porosity from the  $\mu$ CT analyses for selected runs 1, 4, and 7 are presented in Figure 5-4 with the reconstructions from the other runs available in Figure C-1 in Appendix C. The selected runs represent each of the three melting zones as identified in Section 2.3.4, which are insufficient energy input (Run1 in Figure 5-4(a)), stable melting (Run 7 in Figure 5-4(b)), and excessive energy input (Figure 5-4(c)).

Large pores, irregular in shape with some interconnectivity, can be seen in Figure 5-4(a). The total relative porosity was the highest for this run with 5.35%. The observations are typical for porosity which results from insufficient melting of the metal powder due to a lack of energy input per unit volume per unit time (Kasperovich *et al.*, 2016; Mierzejewska, 2019). In the bottom right of Figure 5-4(a), an enlarged area of the exposed vectors is presented. Several discontinuities in the scan vectors can be identified confirming insufficient energy input to maintain a stable melt pool for the formation of continuous tracks.



(a)



(b)

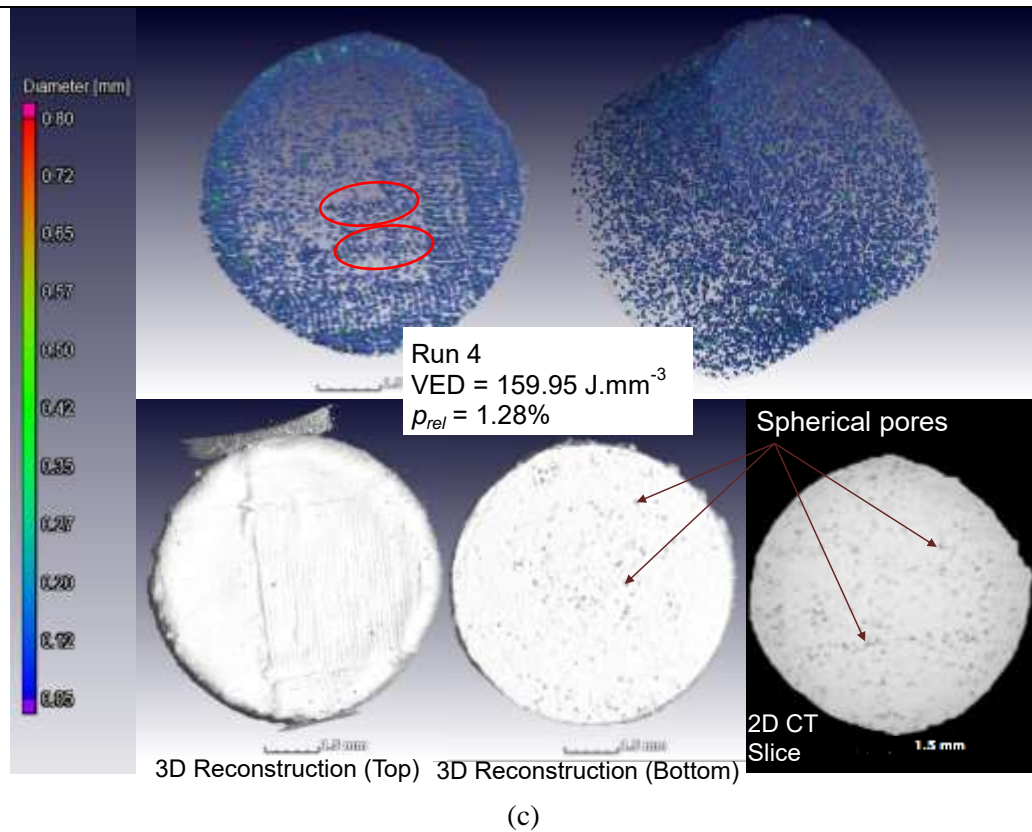


**Figure 5-4: Porosity from  $\mu$ CT analyses for (a) Run 1, (b) Run 7, and (c) Run 4**

The observed discontinuities appear at random within the exposed vectors. The default island scanning strategy and interlayer islands position shift (Figure 5-2) promotes the spatial randomisation of these discontinuities. This is corroborated by the relatively even distribution of the pores throughout the entire specimen volume and pores do not appear to be concentrated in certain areas. This is an important observation regarding the induction of porosity for permeability. A spatially independent distribution of process induced pores throughout the specimen volume simplifies design and LPBF building setup aspects (for the specific LPBF machine in question) with regard to potential effects on pore distribution as a result of part geometry and build orientation.

Figure 5-4(b) presents the run with the least porosity (0.18%). From the enlarged area on the bottom right, it can be observed that the exposed vectors are characterised by smooth, continuous tracks. It is likely that a stable melt pool was formed and the main cause of porosity is unlikely to be strongly related to the values of the investigated process parameters. It would be more likely to originate from the laser exposure pattern and control system (Hagedorn-Hansen et al., 2017). For example, with the default scanning strategy the 5 x 5 mm islands are shifted 1 mm in the x- and y-directions after each layer (Figure 5-2). These 1 x 1 mm layer shifts are clearly visible in Figure 5-4(b) (indicated with red

dashed square). It is also evident that when observing the distribution of the pores throughout the reconstructed specimen volumes that exceptionally few pores were detected in the volumes contained within this shift pattern. This supports that the pores were more likely a result of the scanning strategy than unstable melting due to the laser processing parameters. Even though these pores are relatively small (yielding a relative porosity of 0.18%), it should be noted as a hard-to-control factor specifically for the default scanning strategy of the LPBF system in question that contributes to total part porosity.

Figure 5-4(c) presents a case of excessive energy input. The smaller overall pore sizes and near spherical morphology is corroborated by the literature which relates these pores mainly to the effects of gaseous artefacts produced by the high temperatures reached during processing (Gong et al., 2014). The spherical morphology can be observed in the bottom view of the 3D reconstructed view as well as the 2D CT slice in the bottom right of Figure 5-4(c). The pores are distributed more evenly throughout the specimen volume. An effect related to the scanning pattern can however be identified with pores concentrated on the apexes (shape of apex visible in Figure 5-9(b)) of the exposed vectors (example encircled). At these apexes the laser slows down and accelerates, increasing the dwell time. This in turn increases the effective input energy density and subsequently the maximum temperature reached in these areas (Martin et al., 2019).

Prior to DoE model fitting analysis, the data were explored with the compilation of a correlation matrix and scatter plots. The correlation matrix, presented in Table 5-3, is a useful tool in exploring the influences of independent variables on the response within the obtained data. Correlation magnitude and direction are indicated with the colour of the corresponding cell with darker colours representing stronger correlation. Positive correlation is indicated with red shades and negative correlation with purple shades.

**Table 5-3: Correlation matrix for relative porosity investigation input factors and responses**

	Run ID	$P$ (W)	$v$ (mm.s <sup>-1</sup> )	$h$ (μm)	$p_{rel}$ (%)	VED (J.mm <sup>-3</sup> )
Run ID	1.000	-0.038	-0.076	0.261	-0.417	0.115
$P$ (W)	-0.038	1.000	0.020	0.000	-0.371	0.310
$v$ (mm.s <sup>-1</sup> )	-0.076	0.020	1.000	0.000	0.370	-0.696
$h$ (μm)	0.261	0.00	0.00	1.000	0.160	-0.234
$p_{rel}$ (%)	-0.417	-0.371	0.370	0.160	1.000	-0.220
VED (J.mm <sup>-3</sup> )	0.115	0.310	-0.696	-0.234	-0.220	1.000

From Table 5-3 it can be observed that the relative porosity is negatively correlated with laser power, positively correlated with scan speed, and slightly positive correlated with hatch spacing. Furthermore, the correlation of relative porosity with hatch spacing is less than half of that with laser power and scanning speed. The resulting porosity is negatively correlated with VED, suggesting that pores resulting from insufficient energy input have a larger total effect than pores resulting from excessive energy input. This is in accordance with the images in Figure 5-4 and Figure 2-15 (Mierzejewska, 2019). Within the range of values investigated for the variables, it is also evident that scanning speed had the largest influence on the resulting input VED, which is not unexpected given the relatively large range compared to that of laser power and hatch spacing.

The obtained relative porosity data ranged from 0.18 – 5.35%. Figure 5-5 presents a plot of relative porosity against applied VED. A similar plot for relative porosity versus VED has been reported in literature by Hassanin et al. (2016) for LPBF of Ti6Al4V, although the ranges for the variables that were investigated differ. This entails a reduction in relative porosity with increasing VED up to a certain range (around  $57.26 \text{ J.mm}^{-3}$ ) within which the relative porosity reached a minimum. Beyond this range, the relative porosity increased with further increase in applied VED. This trend is typically observed for the transitions from insufficient melting, to full melting, to overheating (Gong et al., 2014; Hassanin et al., 2016; Kasperovich et al., 2016). These transitions are also reflected by the difference in visible pore morphology in the 2D CT-scan slices included in Figure 5-5 for Runs 1, 7, and 17. Although a similar spike in porosity to that of Run 4 (VED of  $\sim 160 \text{ J.mm}^{-3}$ ) compared to Run 17 (VED  $\sim 260 \text{ J.mm}^{-3}$ ) has been reported by Hassanin et al (2016) where VEDs of 142.86 and  $200 \text{ J.mm}^{-3}$  resulted in relative porosities of 0.76 and 0.34 % respectively, potential reasons for this were not discussed. A potential reason could be the increase in effective VED at the scan track turning point. Figure 5-6 presents an estimate on the effective VED as the laser decelerates. In both studies, the lower static VED resulted in a higher effective VED at the scan track apex. The higher laser power and lower hatch spacing of Run 4 (165 W,  $80 \mu\text{m}$ ) to that of Run 17 (123 W,  $105 \mu\text{m}$ ) thus resulted in a higher localised effective VED at the apex of the scan track which may have led to a higher concentration of pores observed at these locations (Figure 5-4c) (Run 17 3D reconstruction available in Appendix C) which contributed to a higher overall relative porosity (Martin et al., 2019).

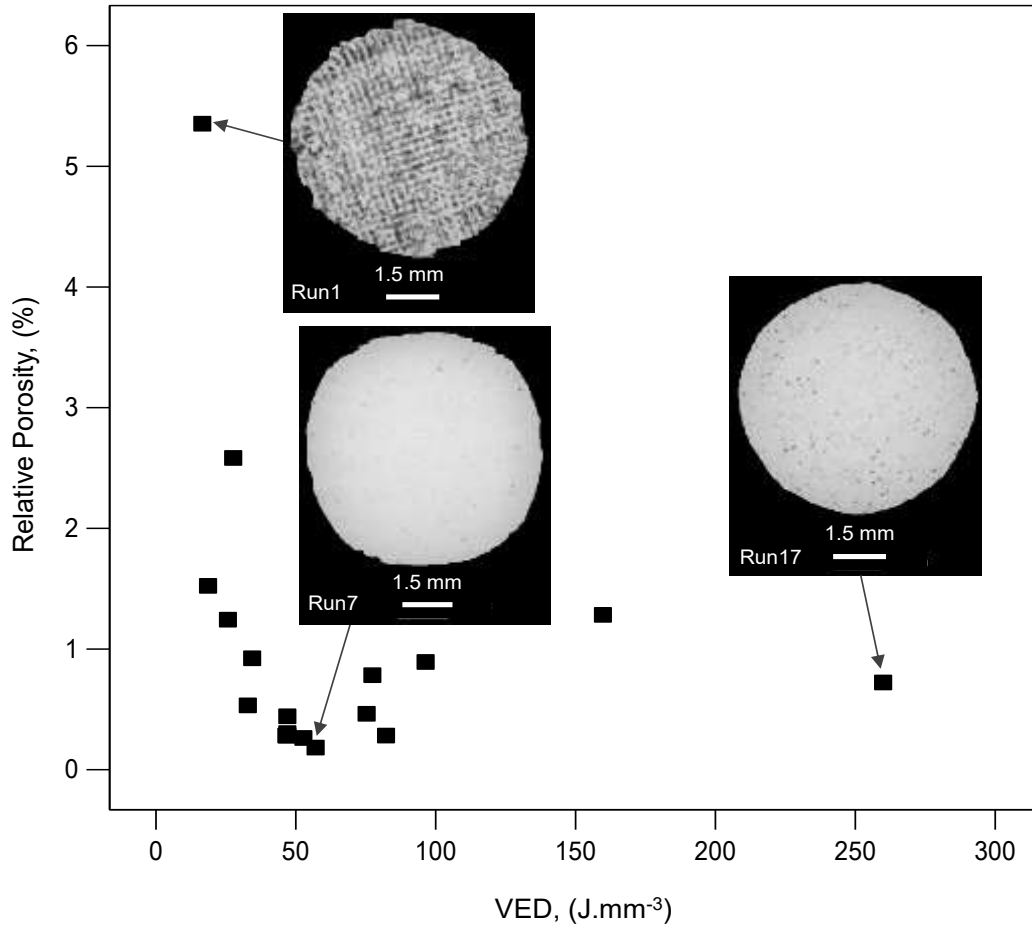


**Figure 5-5: Scatter plot of the relation of relative porosity to the input VED**

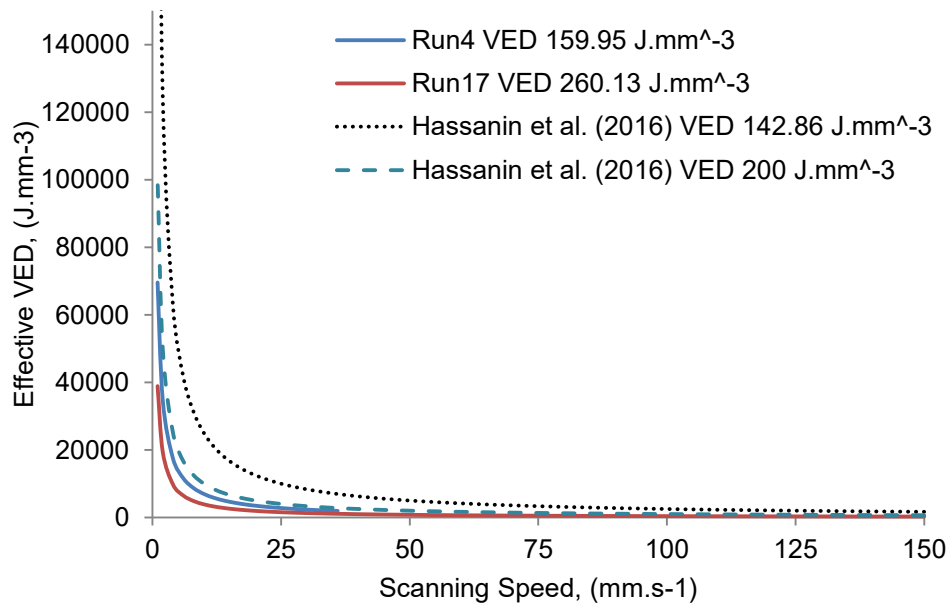
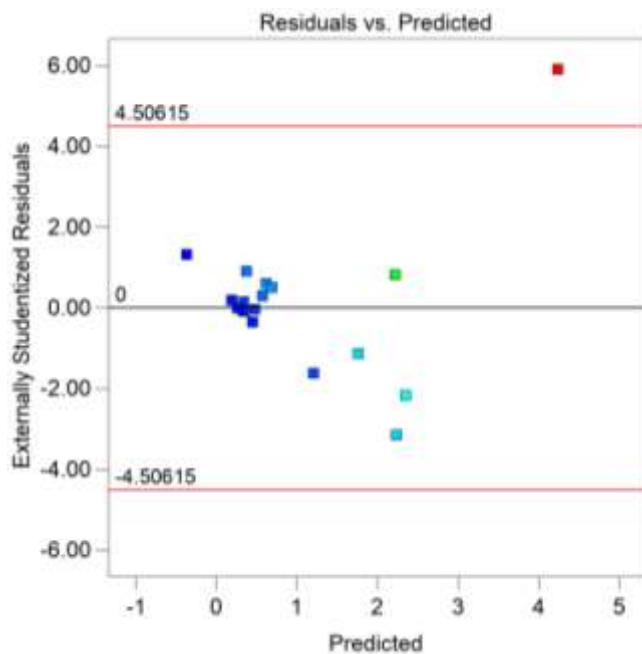


**Figure 5-6: Estimated effective VED at scan track apex**

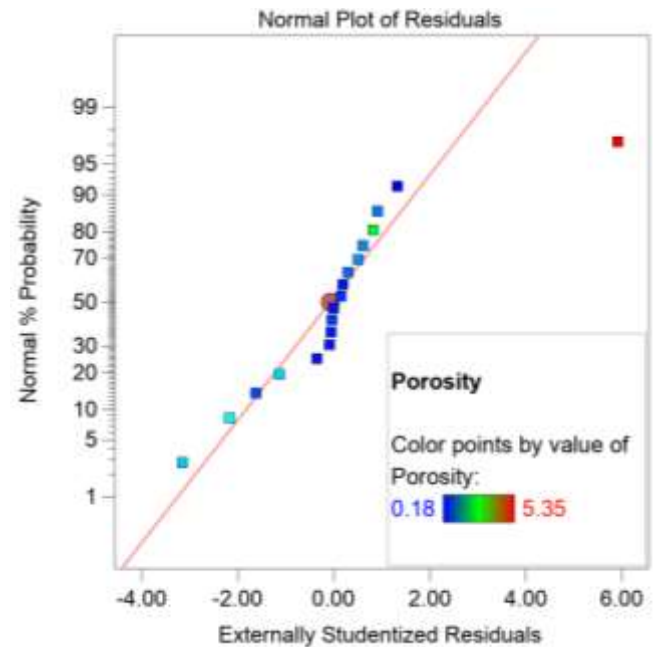
The correlation matrix (Table 5-3) suggests that the individual factors investigated, within the respective ranges, are not equal in their influence on the resulting relative porosity and further processing of the data is required. However, the ratio of the maximum to the minimum porosity is 29.72, which is greater than 10, and thus indicates that the data may need to be transformed in order to perform a multiple linear regression analysis (Stat-Ease, 2020). The software diagnostics detected that the residuals were not normally distributed and suggested a natural log transformation.

The residuals for untransformed data were detected to be a function of the magnitude of the predicted value, presented in Figure 5-7(a). The normal plot of the residuals for the untransformed data (Figure 5-7(b)) confirmed this departure from the normality assumption, which underlines the Analysis of Variance (ANOVA) analysis method (Montgomery & Runger, 2007). Transformation of the data with the natural logarithm removed the observed trend in the residuals (Figure 5-7(c)) and imparted linearity to the residuals along the normal plot of residuals (Figure 5-7(d)). Therefore, the subsequent analysis for this data set in *Design Expert* was performed with the application of a natural logarithm transformation to the data.

A quadratic model was fitted to the transformed data with coefficients estimated by multiple linear regression analysis (Myers & Montgomery, 2002). The general form of the three factor quadratic model is presented in Equation 5-1 with the ANOVA output for model significance presented in Table 5-4.



(a)



(b)

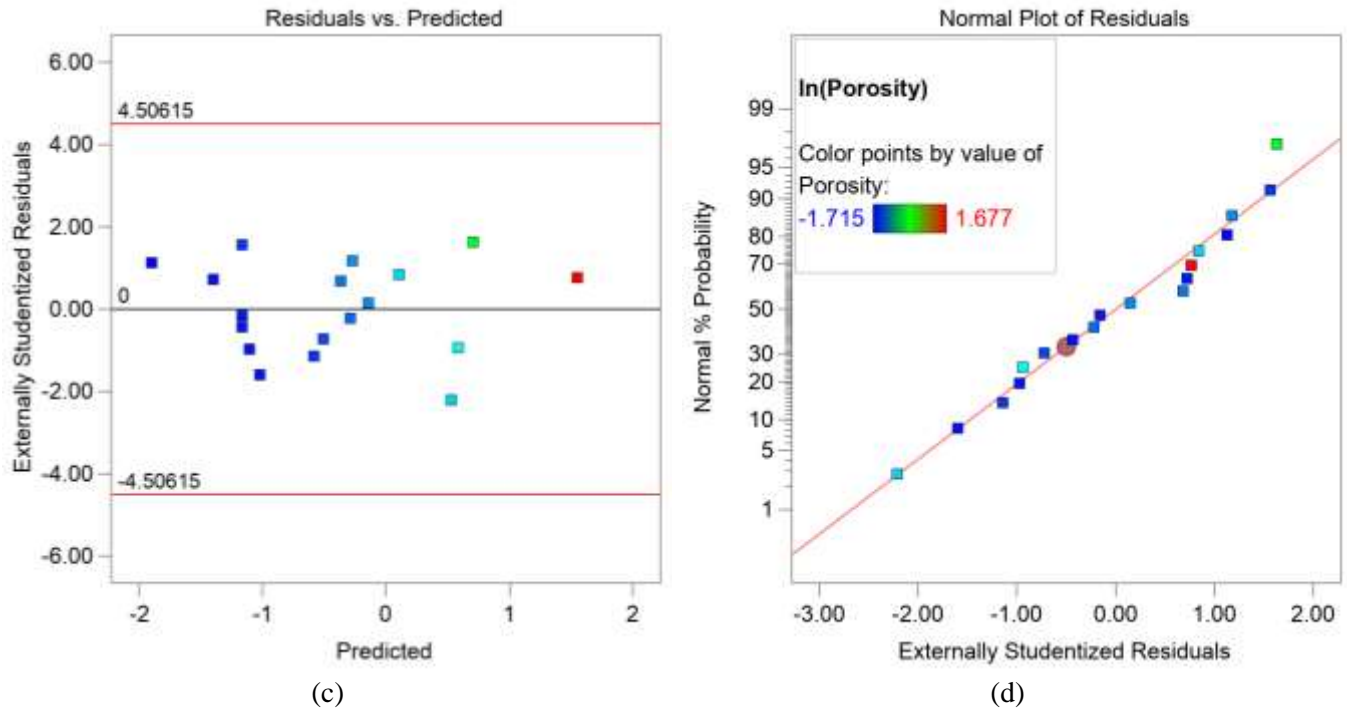


Figure 5-7: Diagnostic plots for (a-b) raw data and (c-d) transformed data

$$\ln(Y) = \beta_0 + \beta_1 X_1 + \beta_2 X_2 + \beta_3 X_3 + \beta_{11} X_1^2 + \beta_{22} X_2^2 + \beta_{33} X_3^2 \quad (5-1)$$

$$+ \beta_{12} X_1 X_2 + \beta_{13} X_1 X_3 + \beta_{23} X_2 X_3$$

Table 5-4: ANOVA results for quadratic model of the effects of laser power, scanning speed, and hatch spacing on the relative porosity

Source	Sum of Squares	df	Mean Square	F-value	P-value
<i>Model</i>	13.10	9	1.46	18.55	0.0002
A-Laser Power	1.61	1	1.61	20.54	0.0019
B-Scanning Speed	0.7923	1	0.7923	10.09	0.0131
C-Hatch Spacing	0.3084	1	0.3084	3.93	0.0827
AB	4.77	1	4.77	60.77	<0.0001
AC	0.3055	1	0.3055	3.89	0.0840
BC	1.76	1	1.76	22.38	0.0015
A <sup>2</sup>	1.95	1	1.95	24.90	0.0011
B <sup>2</sup>	2.37	1	2.37	30.16	0.0006
C <sup>2</sup>	0.2380	1	0.2380	3.03	0.1198
<i>Lack of Fit</i>	0.5093	6	0.0849	1.43	0.4663

The low P-value in the first row indicates that the model is significant. This is also supported by the non-significant lack of fit of the model and the adjusted  $R^2$  value of 0.903. The analysis is described here in reference to the objective of identifying the significance of the factors, within their respective investigated ranges, on the resulting porosity. More detailed diagnostic and surface plots are presented in Figure C-3 in Appendix C. The P-values in Table 5-4 indicate that laser power and scanning speed are both significant factors in the model, with their interaction (AB) of particularly high significance. Hatch spacing is detected as a borderline insignificant factor. Furthermore, the interaction of hatch spacing with laser power (AC) is also not detected as significant, but the interaction of hatch spacing and scanning speed (BC) is detected as significant. When initially only considering the single factors and their respective F- and P-values from the ANOVA significance test, it is suggested that laser power is the most important factor, followed by scanning speed, and then hatch spacing, subject to the investigated ranges.

The model equation is presented in both coded and actual factors in Table 5-5. In coded form, the fitted equation is useful for evaluating the relative impact of individual factors on the response by comparison of their coefficients. The equation in terms of the actual factors can be applied for predictions about the response for the given levels of each of the factors.

**Table 5-5: Equation of the fitted quadratic empirical model in terms of coded and actual**

Equation in terms of coded factors	Equation in terms of actual factors
$\begin{aligned} \text{Ln}(p_{rel}) = & \\ & - 1.16 \\ & - 0.337 \times A \\ & + 0.236 \times B \\ & + 0.148 \times C \\ & - 0.769 \times AB \\ & + 0.195 \times AC \\ & + 0.469 \times BC \\ & + 0.388 \times A^2 \\ & + 0.428 \times B^2 \\ & + 0.134 \times C^2 \end{aligned}$	$\begin{aligned} \text{Ln}(p_{rel}) = & \\ & 7.64 \\ & - 0.041 \times P \\ & - 3.2 \times 10^{-3} \times v \\ & - 0.096 \times h \\ & - 4.6 \times 10^{-5} \times P \times v \\ & + 1.8 \times 10^{-4} \times P \times h \\ & + 4.6 \times 10^{-5} \times v \times h \\ & + 2.2 \times 10^{-4} \times P^2 \\ & + 2.8 \times 10^{-6} \times v^2 \\ & + 2.0 \times 10^{-4} \times h^2 \end{aligned}$

From the coded equation, when only regarding the single factor terms (A, B, and C) it is apparent that laser power (A) has the greatest effect, followed by scanning speed (B) and, then the hatch spacing (C). Overall, however, the interaction factor of laser power and scanning speed has the greatest influence, nearly double that of any interaction with hatch spacing. From this initial analysis regarding the

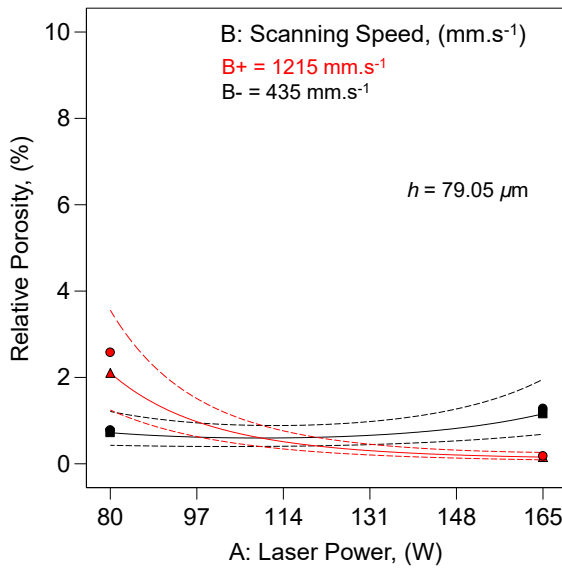
ANOVA and coded model equation, it thus appear that the effects of laser power and scanning speed, as well as their interaction, on the relative porosity dominates that of hatch spacing within the investigated ranges for the respective process parameters.

Figure 5-8 presents the two factor interaction plots, with the third factor stationary at its high and low level. For scanning speed at its low level (black line) and hatch spacing at both its high and low levels (Figure 5-8(a) and (b)), the porosity increased with increasing laser power. This can be attributed to the effects of excessive energy input on the resulting porosity as the laser power exceeds a certain threshold leading to excessive energy input (Yang et al., 2016). However, for the high level of scanning speed, an increase in laser power reduced the porosity at both low and high hatch spacing. The effect however, is more pronounced at high hatch spacing. Increasing the laser power increases the input VED, and increasing the hatch spacing decreases the VED.

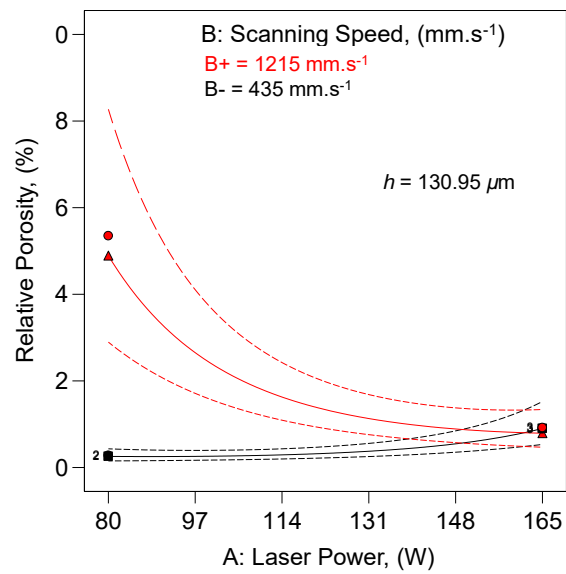
Furthermore, when substituting hatch spacing and layer thickness from the VED equation with laser spot size to consider an area energy density ( $\text{J.mm}^{-2}$ ) (AED), the scan track width is affected by the applied AED. Lowering the AED below a certain threshold significantly reduces the scan track width (Yang et al., 2016). Subsequently, the hatch spacing required to ensure overlapping of scan tracks becomes smaller. The pronounced increase in porosity at high hatch spacing and scanning speed with decreasing laser power in Figure 5-8(b) therefore encompasses a combination of effects related to melt pool formation, stability, and dimensions. To counter these effects, a significant increase in laser power is required to cause sufficient melting and overlapping of scan tracks. This is in accordance with previous observations (Figure 5-4 and Figure 5-5) which demonstrates the transition from insufficient melting and scan track discontinuities to stable melting and smooth scan tracks.

In Figure 5-8(c) and (d) it can be observed that, although the confidence interval bands interact, no significant interaction is present in the data for laser power and hatch spacing. At the low level of scanning speed (Figure 5-8(c)), the trends of resulting relative porosity for both high and low hatch spacing are similar with high hatch spacing consistently yielding a lower porosity across the full investigated range of laser power. This indicates that the low level of scanning speed ( $435 \text{ mm.s}^{-1}$ ) required both a decrease in laser power and an increase in hatch spacing to reduce the VED and subsequent excessive energy input effects on the relative porosity. For the high level of scanning speed the opposite was observed. Thus, at the high level of scanning speed ( $1215 \text{ mm.s}^{-1}$ ) both an increase in laser power and decrease in hatch spacing was required to counter the effects of insufficient energy input.

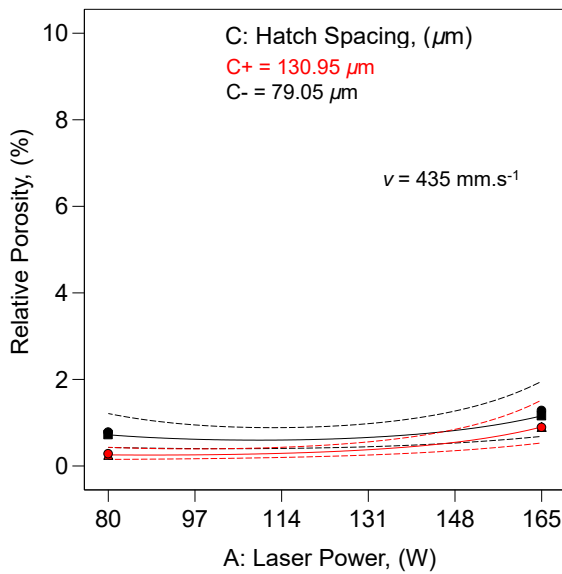
Although the interaction for scanning speed and hatch spacing has been detected as significant in the ANOVA (Figure 5-8 (e) and (f)), the interaction plots follow the same general trends with regards to the effects on relative porosity. The direction of the curves seem to depend more on the value of laser power, which governs whether porosity is increased or decreased with scanning speed rather than the hatch spacing value (except for the case at low laser power and high scanning speed as discussed above). This is especially visible in Figure 5-8(f), where the plots largely overlap within the confidence bands as well as following the same general trend for both high and low values of hatch spacing.



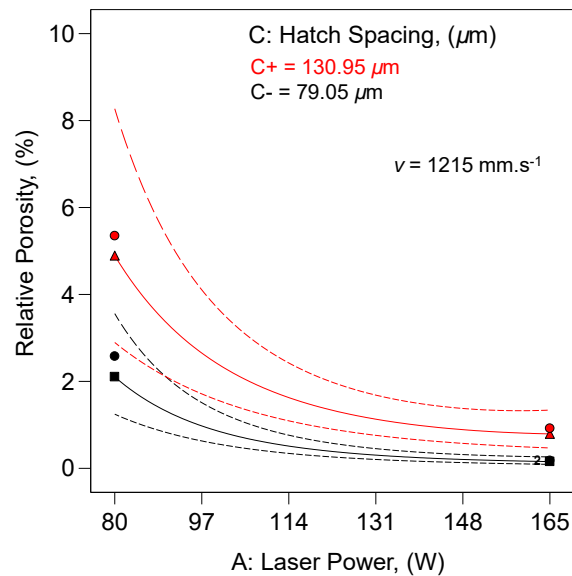
(a)



(b)



(c)



(d)

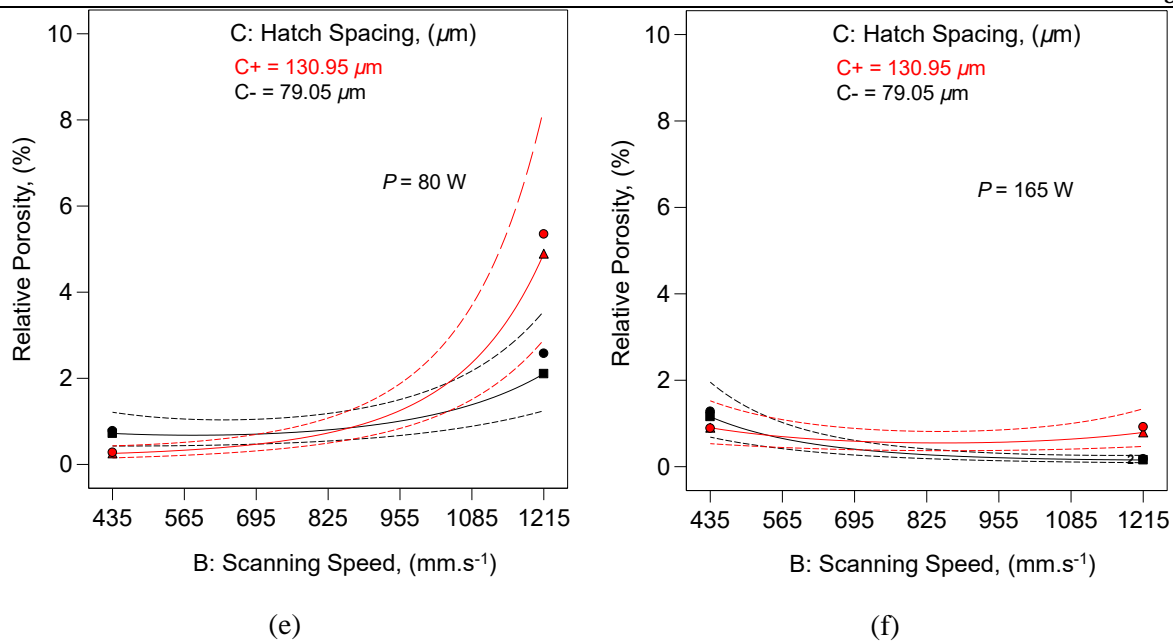


**Figure 5-8: Two factor interaction plots with high and low variations for third factor with (a-b) laser power and scanning speed, (c-d) laser power and hatch spacing, and (e-f) scanning speed and hatch spacing**

This decreased effect of hatch spacing on the relative porosity compared to the effects of laser power and scanning speed appears inconsistent with reported literature, where hatch spacing is typically reported to be a significant factor regarding the porosity of LPBF-produced components (Hassanin et al., 2016). In line with the problem solving framework developed throughout this study, this indicates a requirement for further diagnostics into possible causes. When examining the exposed vectors, a phenomenon in the laser exposure path control of the LPBF equipment hardware was identified that could contribute to the reduced effect of hatch spacing on the porosity.

The observation is presented at various magnifications in Figure 5-9. An entire island with adjacent islands visible is presented in Figure 5-9(a). The ridge like appearance is exaggerated due to this scanning artefact which is visible in Figure 5-9(b). In all four islands at this junction it is clear that the vector positioning is not according to expectation and potentially leads to a contribution in porosity. At higher magnification in Figure 5-9(c), the measured distance between the centres of adjacent scan vectors is twice that of the set hatch spacing distance of 105  $\mu\text{m}$ . Further diagnostics revealed that the distance between odd numbered vectors, for example the 1<sup>st</sup>, 3<sup>rd</sup>, 5<sup>th</sup>, ... seemed to be positioned correctly, but the even numbered vectors move in and out of phase with regards to their required position as the schematic in Figure 5-9(d) indicates.

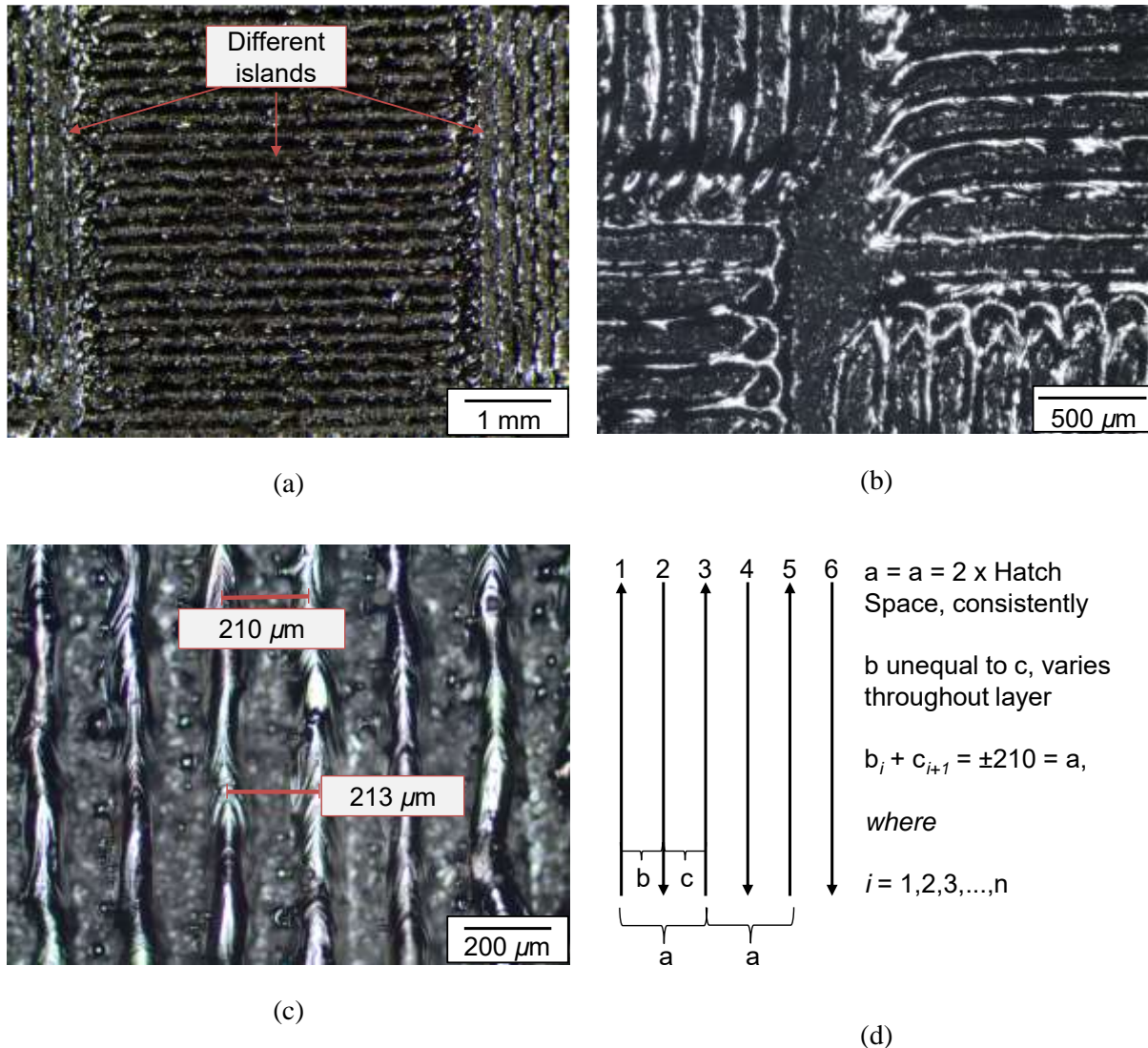


**Figure 5-9: Detected laser exposure issue on machine with regards to positioning of scan vectors with (a) the entire island visible, (b) a junction of four islands with perpendicularly alternating island fill vector directions, (c) measurements showing the positioning to be double the hatch spacing, and (d) schematic describing the observations of the phenomenon**

It was also observed that this error does not occur consistently throughout or within each layer and is therefore hard to monitor or detect *in situ*. In the 3D reconstructions from the CT data, this irregularity could be positively identified on the top surface in 14 of the 18 runs. To demonstrate that this positioning issue did not occur consistently throughout the part volume, Figure 5-10 presents the top and bottom surface of the specimen produced with Run1. On the top surface the laser positioning irregularity is identifiable, whereas on the bottom surface the tracks appear to be aligned correctly. Measurements were made directly from the 3D reconstructions using *Image J*.

The apparent randomness of occurrence could therefore be a source of the noise within the hatch spacing variable, rendering it a borderline insignificant factor with regards to porosity within the screening experiment. In view of this unpredictable scanning irregularity combined with the lack of significance of the effect of hatch spacing on the relative porosity within the data of this pilot study, it was decided to fix hatch spacing as a constant at the default value of  $105\ \mu\text{m}$  in all subsequent experimental work and focus on laser power and scanning speed as independent variables.

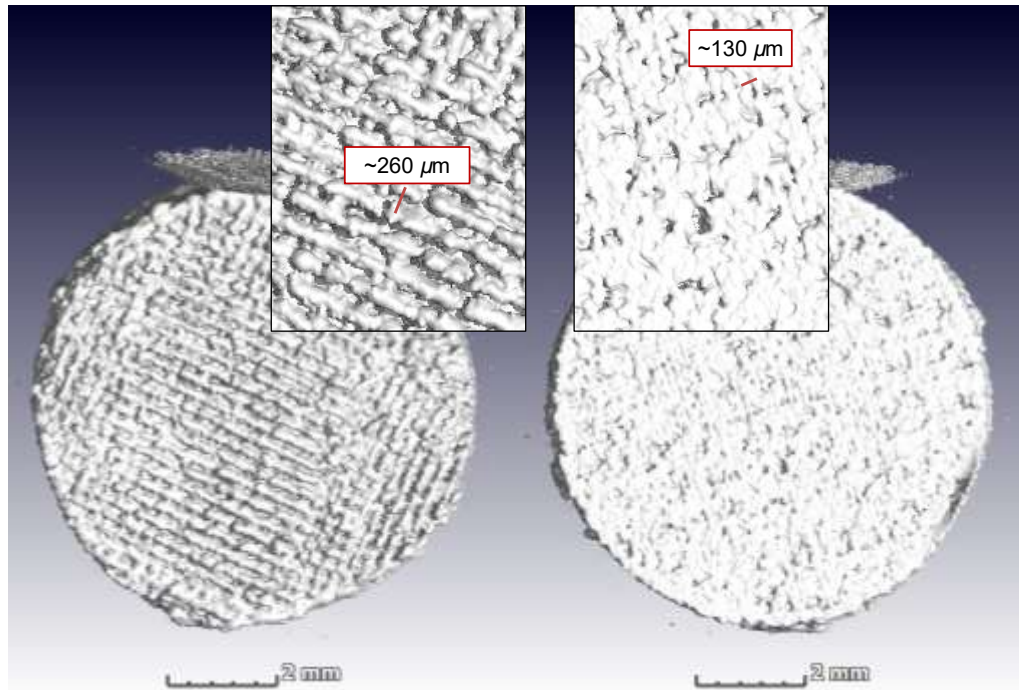


**Figure 5-10: 3D reconstructions for Run1 with top (left) revealing exposure irregularity and bottom (right) revealing correct laser positioning**

For the application of the framework, this knowledge would be added to the integration section of “Process and Machine”. It emphasizes that expected functionality of the LPBF hardware should not be assumed outright. The range of LPBF machines on the market is also expanding and new models of existing machines and software as well as hardware and software updates, are released periodically. It is therefore important to study the specific machine and process combination beforehand, as insights gained in this stage through screening tests can streamline the design and resource requirements of subsequent investigations.

## 5.4 Permeable Thin Walls for Vancomycin Release Screening

### 5.4.1 Fabrication of Thin Wall Specimens

The next step was an investigation into the feasibility of creating permeable structures by inducing porosity through the variation of laser power and scanning speed. For this purpose, 10 x 10 x 0.4 mm thin walls were built with different settings for laser power and scanning speed. As stated above, the hatch spacing setting was maintained constant at 105  $\mu\text{m}$ , and layer thickness was kept constant at 30  $\mu\text{m}$ . The different parameter sets are presented in Table 5-6. Values for process parameters were selected to reflect a wide range of VED in order to assess whether vancomycin permeable structures can be produced by either insufficient energy input or overheating. The thickness of 400  $\mu\text{m}$  was selected to ensure that more than one scan vector would be required, whilst maintaining a thickness close to the build minimum wall thickness, which has been determined both in-house and in literature to be in the range of 150 – 200  $\mu\text{m}$  (Abele et al., 2015) for the respective machine. By applying more than one scan vector, the porosity should be such that there is sufficient interconnectivity between pores in order to allow drug transport.

**Table 5-6: Process parameter settings for induced porosity screening**

Run ID	Laser Power (W)	Scanning Speed ( $\text{mm}\cdot\text{s}^{-1}$ )	VED ( $\text{J}\cdot\text{mm}^{-3}$ )	Selected (Y/N)
1	40	150	84.66	N
2	40	600	21.16	Y
3	40	1100	11.54	Y
4	100	150	211.64	N
5	100	600	52.91	N
6	100	1100	28.86	Y
7	180	200	285.71	N
8	180	600	95.24	N
9	180	1100	51.95	Y

A qualitative screening of manufactured thin walls was done by evaluating whether light could pass through the structures. The samples were placed on a light source and observed through an Olympus SX7B optical microscope. Elimination was done conservatively and where for example, it was not clear whether light passing through or a reflection was observed; the samples were included for vancomycin release screening. Selected parameter sets are indicated in Table 5-6.

### 5.4.2 Experimental Setup and Design

For vancomycin release screening of the thin walls built with the identified parameter sets, diffusion wells were custom designed and 3D-printed on an UPBox FDM machine from acrylonitrile butadiene styrene (ABS) filament. Prior to introduction of the thin walls, all wells were monitored for leakages for at least 24 hours and no leakages were detected. Permeable walls were introduced and meticulously sealed off using a commercial silicone sealant appropriate for use with both metals and polymers. The assembled wells for parameter set 6 are presented in Figure 5-11.



**Figure 5-11: Custom 3D-printed diffusion wells for vancomycin release screening of parameter set 6**

Unless otherwise stated all materials used were of analytical grade. On the numbered side of the thin wall 1 mL of a 2 mg/mL solution of vancomycin (Sigma Aldrich) in distilled water was placed and on the other side a buffer of 1 mL distilled water. Since the objective here was only to screen for vancomycin transport, a 25  $\mu$ L sample was taken from the buffer side at 0, 15, 30, 45, and 60 min. Regarding the short duration of the experiment and the solubility of vancomycin in water of greater than 100 mg/mL, a buffer of 1 mL was regarded as an adequate sink for the objective of the experiment. Furthermore, a 60 min test duration was specified as, ideally, drugs should be available at the target site as soon as possible after administration. Vancomycin concentration was determined by the Microbiology Department with a bicinchoninic acid (BCA) assay. For the standard curve, a dilution series of 0, 25, 125, 250, 500, 750, 1000, 1500, 2000  $\mu$ g/mL was added in duplicate to each sampling time point. A volume of 200  $\mu$ L BCA working solution (Thermo Scientific) was added to each sample and vortexed to ensure a homogenous solution. Plates were incubated at 37  $^{\circ}$ C for 30 min before loading into the microtiter plate reader and absorbance was read at a wavelength 562 nm. Parameter sets were analysed in triplicate (Figure 5-11).

### 5.4.3 Experimental Results

The standard curves for each of the plates corresponding to the sampling time points of 0, 15, 30, 45, and 60 min are available in Appendix C (Figure C-4). All curves show a linear correlation of the measured absorbance with the full dilution series of vancomycin standard concentrations and  $R^2$  values greater than 0.994. The measured vancomycin concentrations for samples in the screening experiment are presented in Figure 5-12. It can be observed from the release curves that Runs 2 and 3 allowed for vancomycin transport with detectable signals starting after 15 min. Runs 6 and 9 did not allow passive diffusion of vancomycin within the 60 min screening period. This indicates a potential cut-off for diffusive vancomycin transport in the zone of 21.16 (Run 2) and 28.86  $\text{J}\cdot\text{mm}^{-3}$  (Run 6). Nevertheless, the release curves provided evidence that Ti6Al4V ELI permeable thin walls (PTWs) can be fabricated with the LPBF process using appropriate process parameter settings.

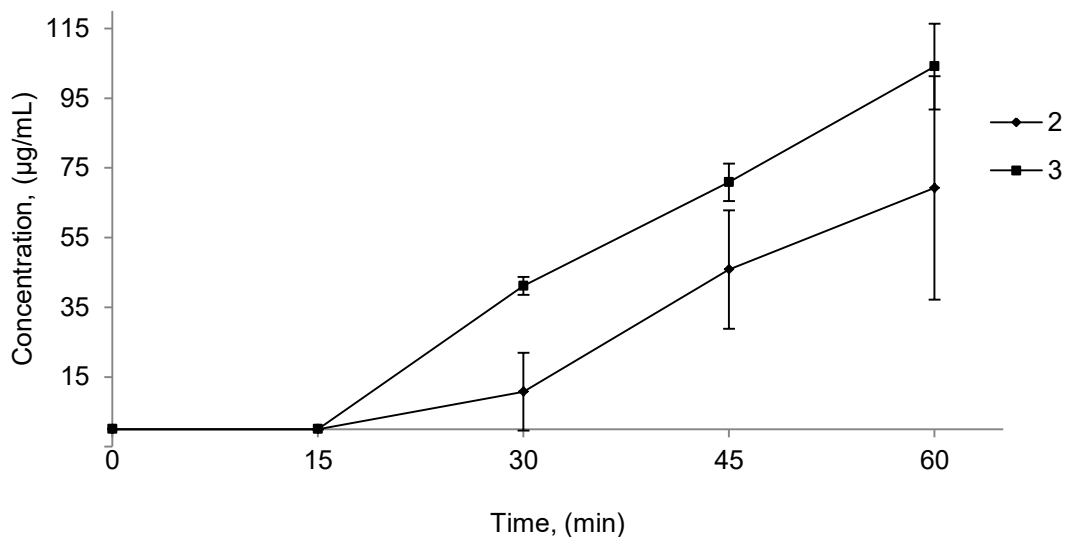


**Figure 5-12: Vancomycin diffusion screening across LPBF Ti6Al4V ELI thin walls**

To qualitatively visualise the diffusion, a blue dye was introduced to distilled water in the reservoir side of a diffusion well containing a PTW built with parameter set 3. This is presented in Figure 5-13. It is important to note that the diffusion appears uniform across the PTW and not concentrated at a specific area. This implies that pores are distributed throughout the structure and not concentrated in one area of the PTW. This corroborates the relatively even distribution of pores resulting from insufficient energy input as identified in Figure 5-4(a).

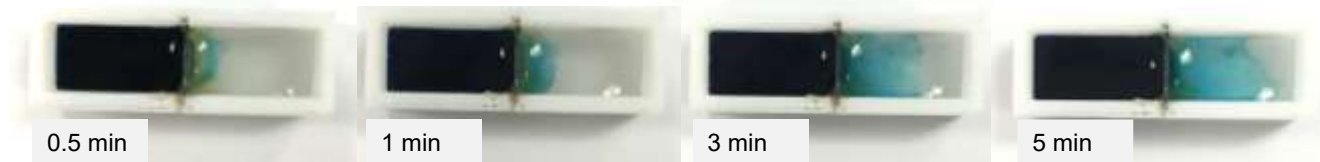


**Figure 5-13: Qualitative representation of blue dye diffusion through PTWs**

### 5.5 Conclusion

This chapter presented screening experiments regarding the application of the LPBF process for inducing porosity into Ti6Al4V ELI components to enable the fabrication of PTWs across which vancomycin can be transported by passive diffusion. From the above discussed investigations the following conclusions were made:

- Pores induced through insufficient energy input were larger and irregular in shape than pores produced with excessive energy input
- Overall, VED is a useful DoE criterion to identify different processing regimes and relate them to the type of resulting porosity, however, VED should be utilised with care as it does not account for the complex physics of the melting process which, among other, influences the melt pool dimensions and resulting scan track profile (Bertoli et al., 2017)
- Within the investigated ranges, laser power and scanning speed were identified as the main process parameters affecting the porosity with hatch spacing borderline insignificant
- The importance of studying the specific LPBF machine for use is underlined, as results suggested that both the scanning strategy (inclusive of layer exposure pattern and exposure pattern interlayer shift) as well as the laser positioning control system contributed to the total porosity
- 400  $\mu\text{m}$  PTWs were successfully fabricated for screening of vancomycin permeability through passive diffusion
- Porosity resulting from insufficient energy input allowed vancomycin transport whereas porosity from excessive energy input was not sufficient to allow passage of light
- A potential cut-off zone for VED to produce PTWs which allow transportation of vancomycin was identified between 21.16 and 28.86  $\text{J}\cdot\text{mm}^{-3}$
- Based on these screening results, a more detailed investigation is presented in the next two chapters regarding the production of PTWs for vancomycin release with VEDs below the identified cut-off limit of  $\sim 29 \text{ J}\cdot\text{mm}^{-3}$ .

## 6. Tailored Drug Release with LPBF-Produced PTWs – Experimental Setup and Design

This chapter presents the experimental setup and design for an investigation into the LPBF of integrated Ti6Al4V ELI PTWs for controlled drug delivery of vancomycin from an aqueous solution. The study was done in two main stages. Firstly, the fabrication of 400  $\mu\text{m}$  PTWs for vancomycin release with differing laser power and scanning speeds, based on the identified VED limits from the screening study in the previous chapter. Secondly, the part consolidation capability of LPBF was utilised for the fabrication of integrated PTW and dense reservoir samples. Vancomycin release from the integrated reservoirs and, importantly, the resulting antimicrobial efficacy were evaluated.

### 6.1 PTWs

The experimental study roadmap for investigating tailored vancomycin release through LPBF-produced PTWs is presented in Figure 6-1. The roadmap entails three main phases namely Part Fabrication, Part Inspection, and Antimicrobial Efficacy. The PTWs (400  $\mu\text{m}$  in thickness) were fabricated with differing values of laser power and scanning speed, followed by investigations into the wettability, relative porosity, vancomycin release and antimicrobial activity against *S. aureus* Xen 36.

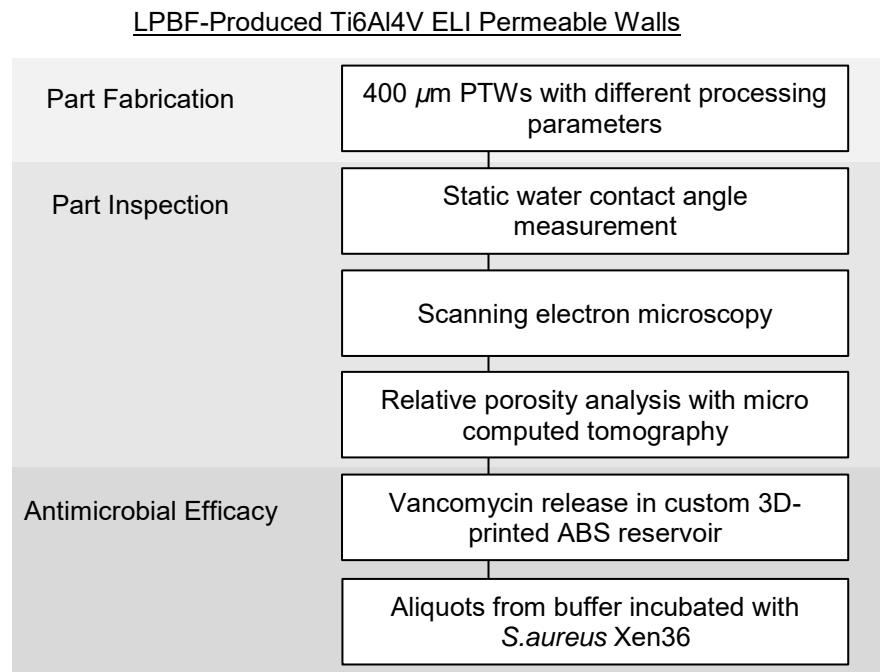


**Figure 6-1: PTW experimental study roadmap**

### 6.1.1 Part Fabrication

Thin walled parts, 10 mm x 10 mm x 0.4 mm, were designed using *Autodesk PowerSHAPE*. To enable in-process assembly of the parts the PTW component was oversized to create an interference with the support frame (Figure 6-2). The current machine software restricts the allocation of different process parameters to different regions within a part volume. Therefore, parts were kept as separate sliced files and loaded individually to the machine software which allowed the allocation of different process parameters. This oversizing of components and subsequent interference of their geometries in space allows for the possibility of in-process assembly of components built with different process parameters through essentially a re-melt at the interfering regions. Build files were created with *Magics 15.0*.

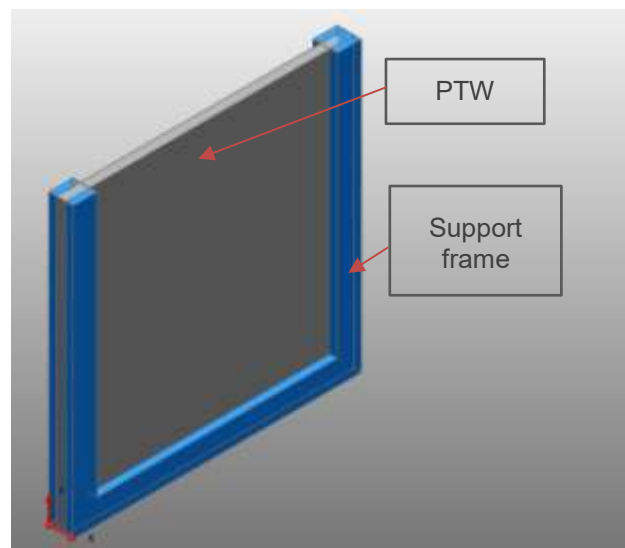


**Figure 6-2: PTW and support frame showing interference of geometries**

The process parameters laser power and scanning speed were specified as the independent test variables with hatch spacing and layer thickness kept respectively at the manufacturer default values of 0.105 mm and 0.03 mm. The effects of laser power and scanning speed on the release of vancomycin from an aqueous solution were investigated by means of a face centred cubic (FCC) response surface DoE. The experimental design encompassed two factors, each with three levels. The DoE was set up using *Design Expert* statistical software. Augmentation of the DoE involved the duplication of all design points, adding a third centre point, and the addition of a previously in-house identified point which yielded a high level of porosity (PS-10 in Table 6-1).

**Table 6-1: Parameter variation DoE for production of PTWs**

Parameter Set	Laser Power (W)	Scanning Speed (mm.s <sup>-1</sup> )	VED (J.mm <sup>-3</sup> )
PS-1	50	800	19.84
PS-2	30	1200	7.94
PS-3	50	1600	9.92
PS-4	30	800	11.91
PS-5	70	800	27.78
PS-6	70	1600	13.89
PS-7	50	1200	13.23
PS-8	30	1600	5.95
PS-9	70	1200	18.52
PS-10	40	1000	12.70

Parts were built directly onto the building plate with a 1 mm machining allowance in the z-direction for part removal with w-EDM. The non-permeable features were built with LPBF machine manufacturer's default parameters, 100 W laser power and 600 mm.s<sup>-1</sup> scanning speed. After removal from the building plate, the fabricated parts were cleaned by sonication in acetone, ethanol and distilled water for 15 min, respectively.

## 6.1.2 Part Inspection

### 6.1.2.1 Water Contact Angle

The static water contact angles of the fabricated PTWs were evaluated with the sessile drop method (ASTM International, 2013). Images were obtained with a Smile 400 tool presetting and measuring machine from Zoller Inc. For reference, two non-permeable surfaces were included in as-built vertical (ABV) and mechanically polished (MP) condition respectively. Mechanical polishing was done according to standard guidelines to obtain a mirror finish by sequential grinding with SiC paper of 600, 800, and 1200 grit size, followed by polishing with 9  $\mu\text{m}$  diamond suspension and 0.04  $\mu\text{m}$  colloidal silica respectively (Struers, 2016).

The physical setup involved configuration of a custom jig (Figure 6-3(a)) with which the specimen was set at a distance of  $2.999 \pm 0.003$  mm from the drop source (Figure 6-3(b)) which was within specification according to ASTM D7334-08 (ASTM International, 2013). The volume of the water droplet was determined by depositing a single droplet on a PTW and weighing the specimen on an analytical balance. Mass measurements of the distilled water droplet were converted to volume using a

density of  $1 \text{ g}\cdot\text{cm}^{-3}$ . The mass measurements are presented in Table 6-2. The water droplet volume was estimated as  $3.48 \pm 0.16 \mu\text{L}$  which allows for the spherical assumption (Extrand & Moon, 2010). A droplet was deposited in three different locations on the specimen surface and the measured contact angles averaged. During the entire test the environment was climate-controlled at 21-22 °C. Images were taken at a minimum of 10 s after deposition to allow the droplet to stabilise.

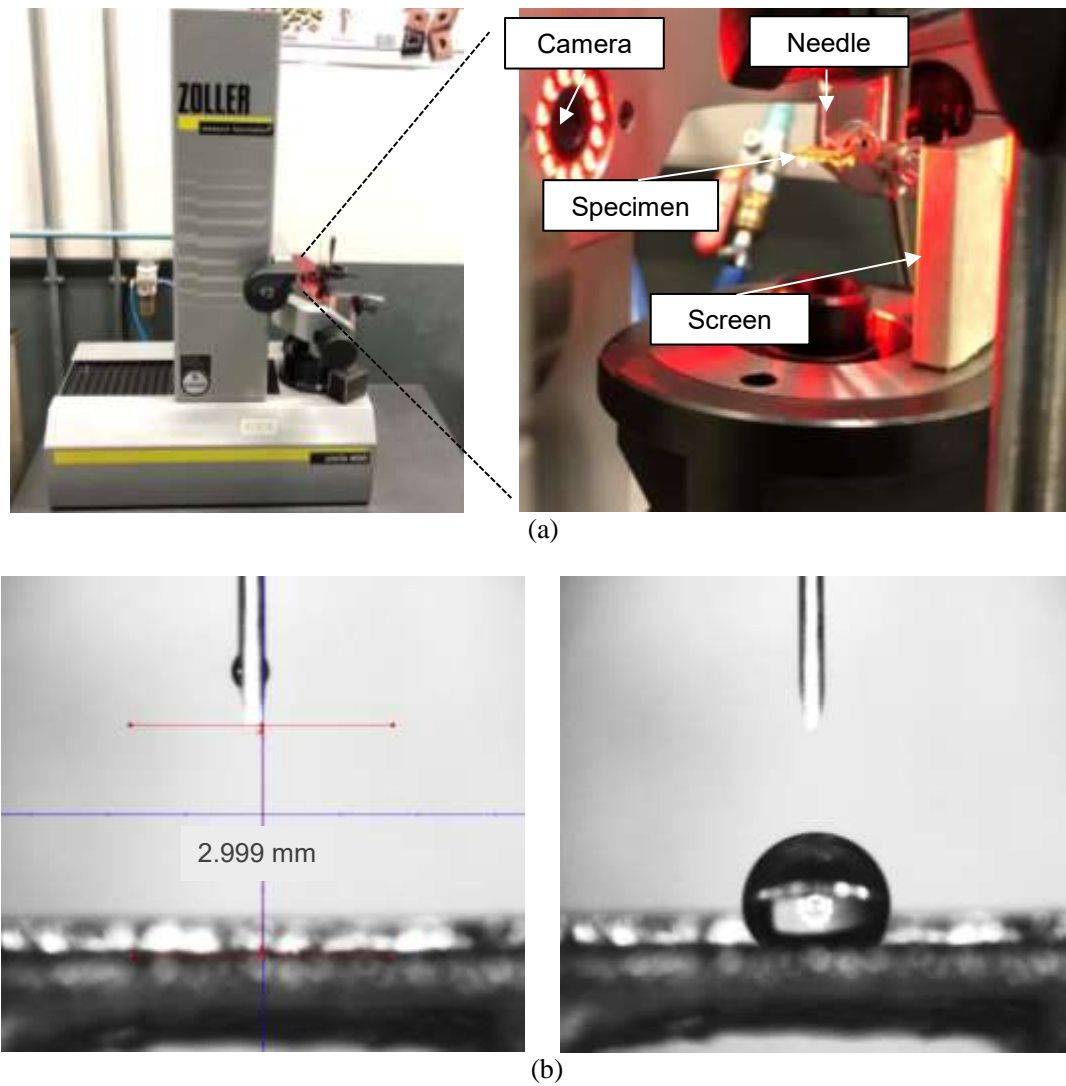
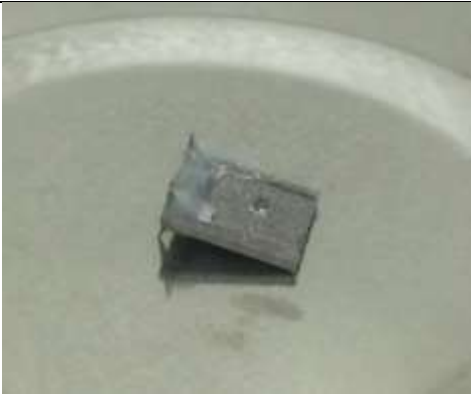


**Figure 6-3: Static water contact angle measurement experimental setup with (a) the physical configuration, and (b) image example**

**Table 6-2: Mass measurement of water droplet on PTW**

Measurement Number	Mass (mg)
1	3.57
2	3.45
3	3.73
4	3.47
5	3.23
6	3.44
Average $\pm$ Standard Deviation	$3.48 \pm 0.16$



Contact angles were measured in the *ImageJ* software environment using a *Contact Angle* plugin (Brugnara, 2006). To obtain the contact angle, images were adjusted for brightness and contrast to identify the contact line of the droplet and PTW as well as the droplet profile. Five points on the droplet profile were then specified as input to the contact angle plugin (Figure 6-4(a)). The points are used to generate a best fit circle and ellipse with tangents running through the three phase contact line (Figure 6-4(b))

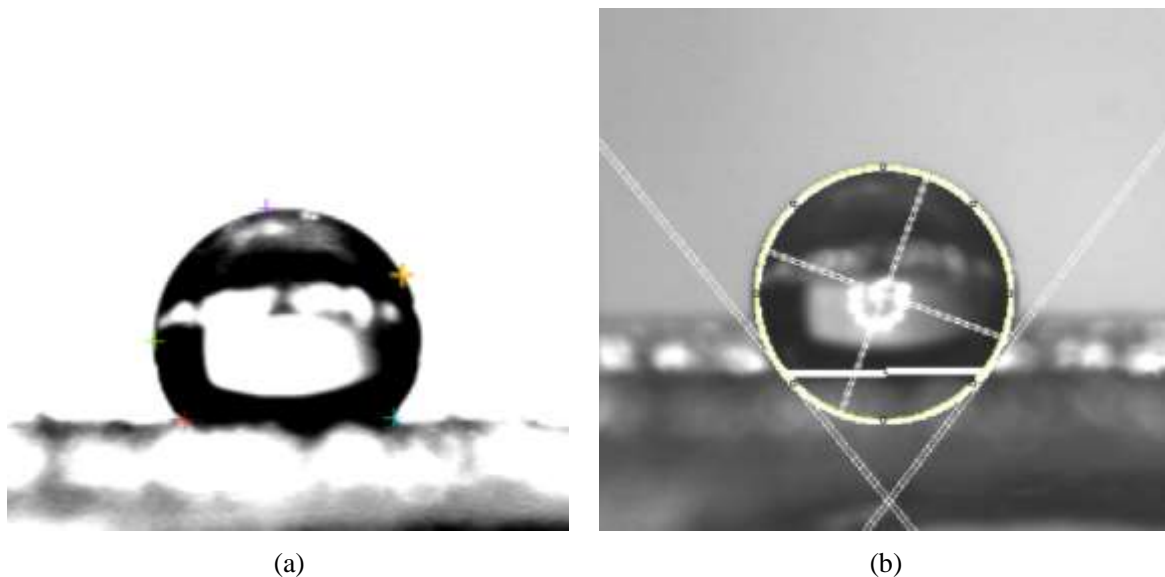


**Figure 6-4: Contact angle measurement procedure using *Image J* and *Contact Angle* plugin showing (a) the image adjustment and points selection and (b) the best fit output**

### 6.1.2.2 Surface Roughness

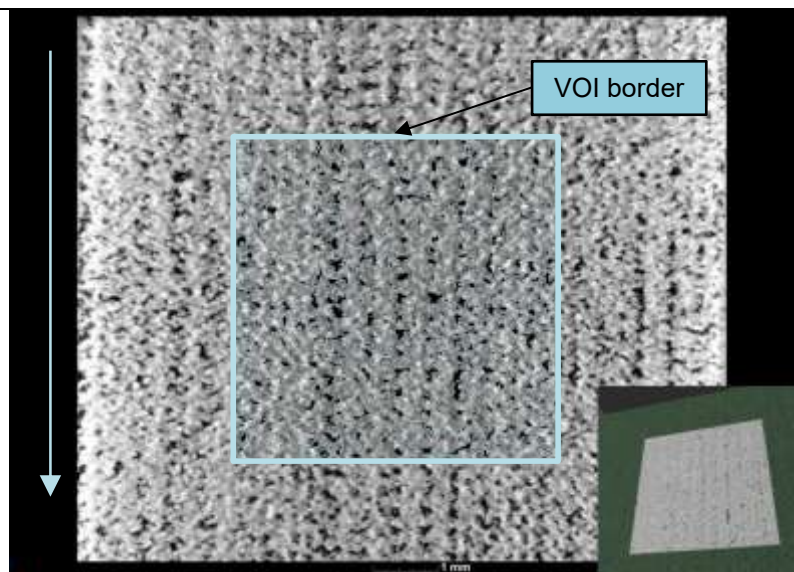
Reported surface roughness measurements were all obtained using a portable MarSurf PS10 tactile perthometer. Where applicable, the mean surface roughness,  $Ra$ , and five-point mean peak to valley height,  $Rz$ , were recorded for three profiles on the respective specimen, traced in the building direction.

### 6.1.2.3 Relative Porosity

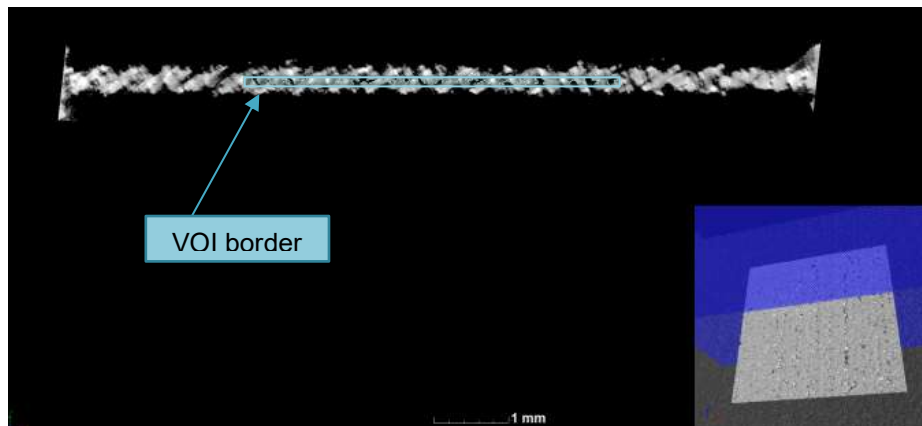
PTW surfaces were qualitatively observed with a Zeiss MERLIN FE-SEM at the Electron Microscopy unit of the CAF at SU. PTW specimens were fixed on aluminium stubs using conductive carbon tape. A beam potential of 5 kV was used.

The relative porosity of the PTW structures was evaluated non-destructively with  $\mu$ CT using a General Electric Nanotom S and a custom method developed by the CT-Scanner unit of CAF at SU. System parameters for scanning and data acquisition were specified according to the standard guidelines as published by the CT-Scanner unit (Du Plessis et al., 2017). The X-ray parameters were a potential of 140 kV, a current of 40  $\mu$ A, copper beam filtration of 1.5 mm, and an exposure time of 0.5 s. Scans were performed at a voxel size resolution of 5  $\mu$ m. 3D reconstructions and porosity analysis were done using *VGStudioMax 3.1* software. Similar to the screening experiment in Chapter 5, the relative porosity percentage was calculated as the total sum of pore volume to the total bulk part volume.

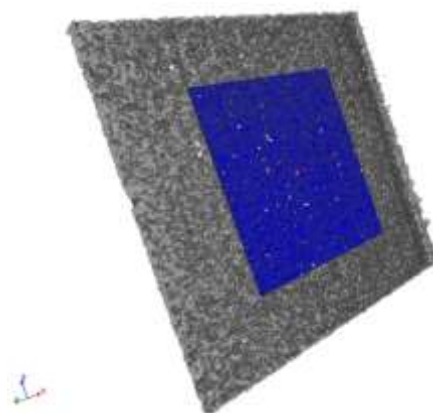
To avoid difficulties in the porosity detection algorithm which is based on the grayscale values of an image, a volume of interest (VOI) within the part volume was specified. A 5 x 5 x 0.1 mm VOI was identified for each part in the centre of the CT reconstruction. The specified VOI is presented in Figure 6-5. The build direction is indicated in Figure 6-5(a) by the downwards arrow. The VOI border is indicated in the x-z plane in Figure 6-5(a), in the x-y plane in Figure 6-5(b), and the VOI contained within the 3D reconstruction is presented in Figure 6-5(c). To evaluate the repeatability of PTW relative porosity, three samples at the DoE centre point, and two samples at each of the highest and lowest energy densities were analysed. An additional sample in the DoE range was randomly selected to account for possible large deviations in repeatability between the extreme design points and the centre point.



(a)



(b)



(c)

**Figure 6-5: Specification of 5 mm x 5 mm x 0.1 mm VOI with (a) 2D view in x-z plane, (b) 2D view in x-y plane, and (c) 3D VOI view**

### 6.1.3 Antimicrobial Efficacy

#### 6.1.3.1 Vancomycin Release through PTWs

In order to investigate the release of vancomycin through the PTWs, release cells were custom designed and 3D-printed from ABS polymer using a commercial FDM machine (Figure 6-6). The cells contained a 1 mL reservoir and a 7 mL buffer. The PTW parts were fixed in place to separate the reservoir and buffer and sealed (Figure 6-6(a)). The release cell assemblies were monitored for any leakages over a period of 48 h. To standardise the area in contact with antibiotic solution, the reservoir side of each PTW was covered with a polyvinyl chloride (PVC) mask (Figure 6-6(b)) and sealed to yield a contact area of  $24.72 \pm 0.17 \text{ mm}^2$  (Table D-1, Appendix D).

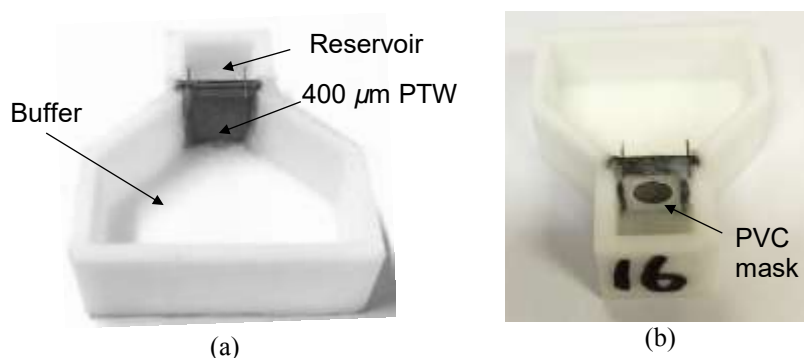


**Figure 6-6: Photographs of PTWs assembled in ABS custom made diffusion wells (a) showing the buffer side of the PTW and (b) showing the reservoir side of the PTW**

The reservoir was filled with 1 mL of vancomycin solution at a concentration of 1 mg/mL. The buffer side contained 7 mL of sterile phosphate buffered saline (PBS) (pH 7.4) solution. Release cells were then incubated at 12 h at 37°C. Sampling times were 1, 3, 6, and 12 h. At each sampling point 1.5 mL was extracted from the buffer and the removed volume was replaced with fresh PBS solution. Samples were homogenised by vortex. Aliquots of 200 μL were filtered using 0.22 μm polyvinylidene fluoride (PVDF) syringe filters and injected into autosampler vial inserts. The vancomycin concentration within each aliquot was quantified using a Waters Synapt G2 QTOF reversed-phase ultra-high performance liquid chromatography (RP-UHPLC) machine at the LC-MS unit of CAF at SU. The RP-UHPLC was fitted with a Hypersil GOLD C<sub>18</sub> column. An injection volume of 2 μL was used, and ultraviolet absorbance was detected at a wavelength of 280 nm. The mobile phase consisted of deionized (DI) water and acetonitrile (AcN) containing 0.1% formic acid respectively. A gradient elution protocol was adapted from literature and is presented in Table 6-3 (Baranowska et al., 2010).

**Table 6-3: Mobile phase elution protocol for RP-UHPLC**

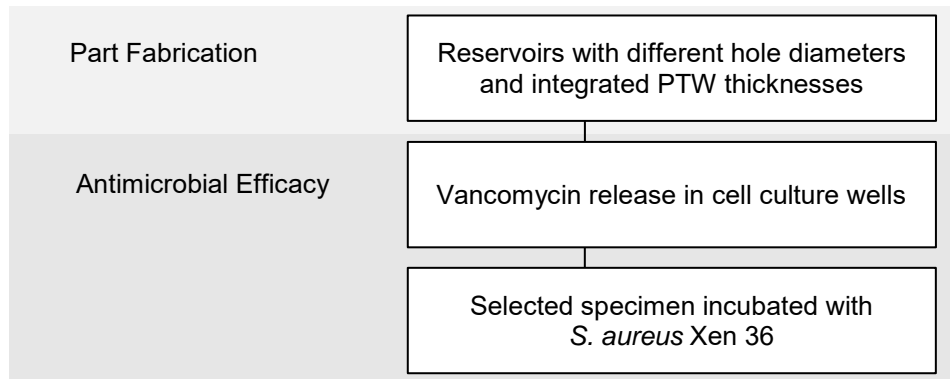
Time (min)	0.1% Formic Acid	AcN with 0.1% Formic Acid
0.00	100.0	0.0
0.50	100.0	0.0
2.50	75.0	25.0
3.00	10.0	90.0
4.00	100.0	0.0
5.00	100.0	0.0

### 6.1.3.2 Activity of Released Vancomycin

Antimicrobial tests were prepared by the Department of Microbiology at SU. Release cells were rinsed with double-distilled water, prepared with a milli-Q system. The reservoir side was filled with 1 mL of vancomycin at a concentration of 1 mg/mL and the buffer side contained 3 mL of sterile PBS (pH 7.4). At time points 0 h, 5 h and 18 h, 1 mL samples were taken from the buffer and replaced with fresh PBS. Antimicrobial activity of the samples was evaluated with an agar-well diffusion assay. Brain heart infusion (BHI) agar (1% w/v) was seeded with an overnight (18 h) culture of *S. aureus* Xen 36 (1 %, v/v). Wells of 5 mm in diameter were made into the solidified agar using a sterile glass pasteur pipette. An aliquot volume of 100  $\mu$ L from each of the samples was introduced into a well. Plates were then incubated for 18 hours at 37 °C.

## 6.2 Integrated Reservoir Specimens

The experimental study outline for investigating the fabrication and vancomycin release of LPBF-produced reservoirs with integrated PTWs is presented in Figure 6-7. Whereas part of the focus for the experiment outlined in Section in 6.1 was to investigate the effects of LPBF process parameters on vancomycin release, the main objective here was to integrate PTWs and investigate the effect of geometry on vancomycin release. The identified geometry for investigation was limited to the size of the channel opening, referred as hole diameter, and the thickness of the integrated PTW. It entailed two main phases namely Part Fabrication and Antimicrobial Efficacy.

LPBF-Produced Ti6Al4V ELI Integrated Reservoir Specimens**Figure 6-7: Integrated reservoir specimens study layout****6.2.1 Part Fabrication**

Integrated PTW reservoir specimens were design using *Autodesk PowerSHAPE*. The reservoir consisted of a cuboid volume of 10 x 10 x 12 mm with a circular drug release opening (dark grey parts in Figure 6-8) varying between 2 and 8 mm and an integrated PTW varying in thickness from 0.4 – 1.5 mm. Similar as before, the PTW was sufficiently oversized in all dimensions to ensure interference with the dense reservoir and subsequent assembly due to remelting at the interference zones of the part volumes. Examples of selected design variants are presented in Figure 6-8. A treatment with a 2 mm hole and 0.4 mm PTW is shown in Figure 6-8(a), a 5 mm hole 0.95 mm PTW in Figure 6-8(b), an 8 mm hole and 1.5 mm PTW in Figure 6-8(c), and a fabricated specimen with 5 mm hole and 0.95 mm PTW in Figure 6-8(d).

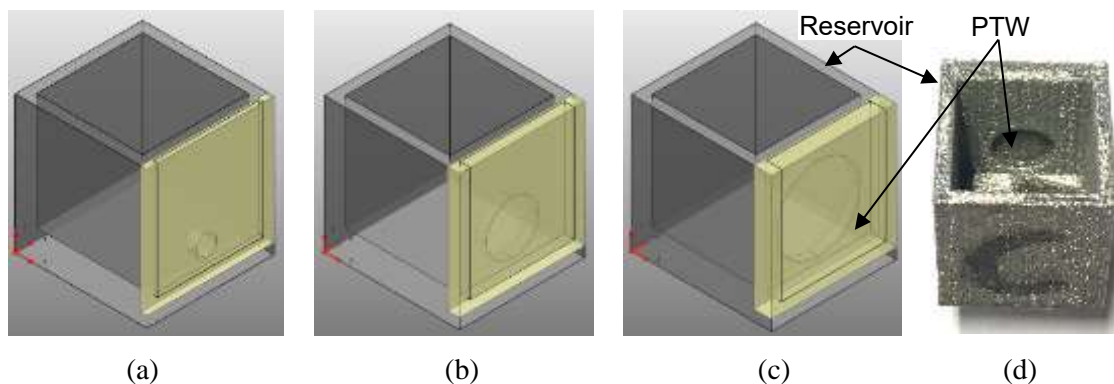


**Figure 6-8: Examples of integrated reservoir specimen design variations with (a) 2 mm hole and 0.4 mm PTW, (b) 5 mm hole and 0.95 mm PTW, (c) 8 mm hole and 1.5 mm PTW, and (d) fabricated specimen with 5 mm hole and 0.95 mm PTW**

According to the LPBF machine manufacturer's guidelines, holes or channels built parallel to the build plate should not be not smaller than 2 mm in diameter to avoid collapse and not greater than 8 mm in diameter to ensure reasonable geometrical accuracy and avoid caving in of the overhanging material without the use of support structures. These values are at the limits of the specified machine capability, and therefore a FCC DoE was selected. The treatment combinations are presented in Table 6-4, 'F' refers to factorial point, 'A' to axial point, and 'C' to centre point. All dense parts of the reservoir were built with default parameters and the PTWs with PS-10 as defined in Table 6-1.

**Table 6-4: Design parameter variation for production of integrated reservoir specimens**

Sample Name	Hole Diameter (mm)	PTW Thickness (mm)
1F	2.0	0.40
2F	8.0	0.40
3F	2.0	1.50
4F	8.0	1.50
1A	5.0	0.40
2A	2.0	0.95
3A	8.0	0.95
4A	5.0	1.50
C	5.0	0.95

## 6.2.2 Antimicrobial Efficacy

### 6.2.2.1 Vancomycin Release from Integrated Reservoirs

The integrated reservoir specimens were loaded with 1 mL of 1 mg/mL vancomycin and placed in the wells of a 12 multiwell cell culture plate, with each well containing 2.5 mL sterile PBS (Figure 6-9). The plates were incubated at 37°C for a total of 24 hours. At each of the specified time points, 1, 3, 6, 12, and 24 hrs, samples were taken from the PBS buffer and the integrated reservoir specimens were transferred to a fresh 2.5 mL PBS buffer in a clean cell culture well. The order of sampling and transfer of integrated reservoir specimens to fresh PBS buffers were randomised at all times.

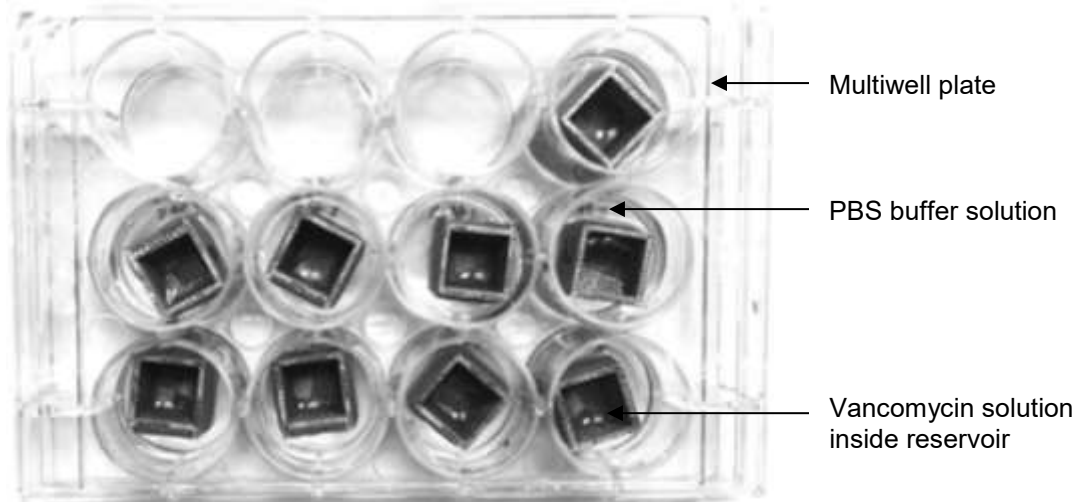


**Figure 6-9: Photographic representation of experimental setup for vancomycin release from integrated reservoir specimens**

Vancomycin concentrations in the buffers were quantified at the Department of Microbiology with reversed-phase high performance liquid chromatography (RP-HPLC) on a Finnigan Surveyor Plus system using a Hypersil GOLD C<sub>18</sub> column. Samples were filtered using 0.22  $\mu\text{m}$  PVDF syringe filters and injected into autosampler vials. For RP-HPLC analysis an injection volume of 20  $\mu\text{L}$  was used. Ultraviolet absorbance detection was done at a wavelength of 254 nm using a Surveyor UV/Vis Plus detector. The mobile phase consisted of DI water and AcN containing 0.1% trifluoroacetic acid (TFA) respectively. The gradient elution protocol used has been developed previously in-house and is presented in Table 6-5 (Bezuidenhout et al., 2015). Standard vancomycin concentrations for the calibration curve were 0, 5, 20, 62.5, and 125  $\mu\text{g}/\text{mL}$ .

**Table 6-5: Mobile phase elution protocol for RP-HPLC**

Time (min)	0.1% TFA	AcN with 0.1% TFA	Elution type
0.0-1.0	95.0	5.0	Isocratic
1.0-5.0	95.0 – 0.0	5.0 – 100.0	Linear gradient
5.0-6.0	0.0	100.0	Isocratic
6.0-11.0	0.0 – 95.0	100.0 – 5.0	Linear gradient
12.00	95.0	5.0	Isocratic

---

**6.2.2.2 *S. aureus* Xen 36 Colonisation Prevention Potential**

The surface colonisation prevention potential tests were prepared by the Department of Microbiology at SU. The integrated reservoir specimens were sterilized by soaking them in 70% ethanol (v/v) for 15 min after which the ethanol was left to evaporate. A 300  $\mu$ L overnight culture of *S. aureus* Xen 36 was inoculated in 30 mL melted 1% w/v BHI agar (cooled to 40 °C) for an *S. aureus* concentration of 1% v/v. The agar solution was then swirled and plated out. Integrated reservoir specimens were then fixed in the agar. The reservoirs were filled with 0.7 mL of 1 mg/mL vancomycin. Incubation of the plates was done at 37 °C for 18 h. Clear zones surrounding the titanium block would be indicative of effective release of vancomycin and successful prevention of surface colonisation.

## 7. Tailored Drug Release with LPBF-Produced PTWs – Results and Discussion

This chapter presents the main part of the results to the partial problem of “Enabling drug delivery from implant reservoir” within the overall problem breakdown structure as presented in Figure 3-6. Investigation of the PTWs can be regarded as problem decomposition where insight is gained for the establishment of an LPBF process window within which permeable structures can be produced for passive diffusion of vancomycin from an aqueous solution. The integrated reservoir specimens thereafter represent a recombination phase where in-process assemblies representing potential drug release location of an eventual demonstrator prototype were evaluated. The IKPs which resulted from this work were implemented in the design of the demonstrator cementless hip stem prototype.

### 7.1 PTWs

#### 7.1.1 Fabricated PTWs Part Inspection

The as-built in-process assembled PTWs and support frames on the LPBF building plate are presented in Figure 7-1. Two parameter sets, PS-2 ( $VED = 7.94 \text{ J.mm}^{-3}$ ) and PS-8 ( $VED = 5.95 \text{ J.mm}^{-3}$ ) did not build and one set, PS-4 ( $VED = 11.91 \text{ J.mm}^{-3}$ ) resulted in fragmented parts. An example of a non-built and of a fragmented PTW is indicated with dashed ellipses in Figure 7-1.



**Figure 7-1: As-built PTWs within support frame on build plate**

Subsequently, these parameter sets, all involving a laser power of 30 W, were excluded from further analyses. However, PS-3 ( $VED = 9.92 \text{ J.mm}^{-3}$ ) resulted in a successful build but had a laser power of 50 W. This means parts with higher VED but lower laser power failed to build. It implies that at certain processing boundaries the laser power alone may have a greater effect on melt pool stability than the combination of laser power and scanning speed. Successful builds were obtained with PS-10 ( $VED = 12.70 \text{ J.mm}^{-3}$ ,  $P = 40 \text{ W}$ ). Therefore, considering the investigated range of scanning speed, a lower

boundary between 30 and 40 W can be inferred for the required laser power to cause intermittent melting of the Ti6Al4V ELI powder.

### 7.1.1.1 Water contact angle

Selected images of the droplets on specimens are presented in Figure 7-2. The static contact angle on the reference dense specimens, ABV and MP, indicates that the bulk of the LPBF Ti6Al4V ELI is hydrophilic. For implant applications, hydrophilic surfaces are preferred as this reduces bacterial adhesion through hydrophobic effects. The averages of contact angles on 400  $\mu\text{m}$  PTWs, however, are all in the range of 114 – 127° and thus consistently indicative of hydrophobic surfaces. However, after using water for pre-wetting of the 400  $\mu\text{m}$  PTWs, water droplets were no longer repelled.

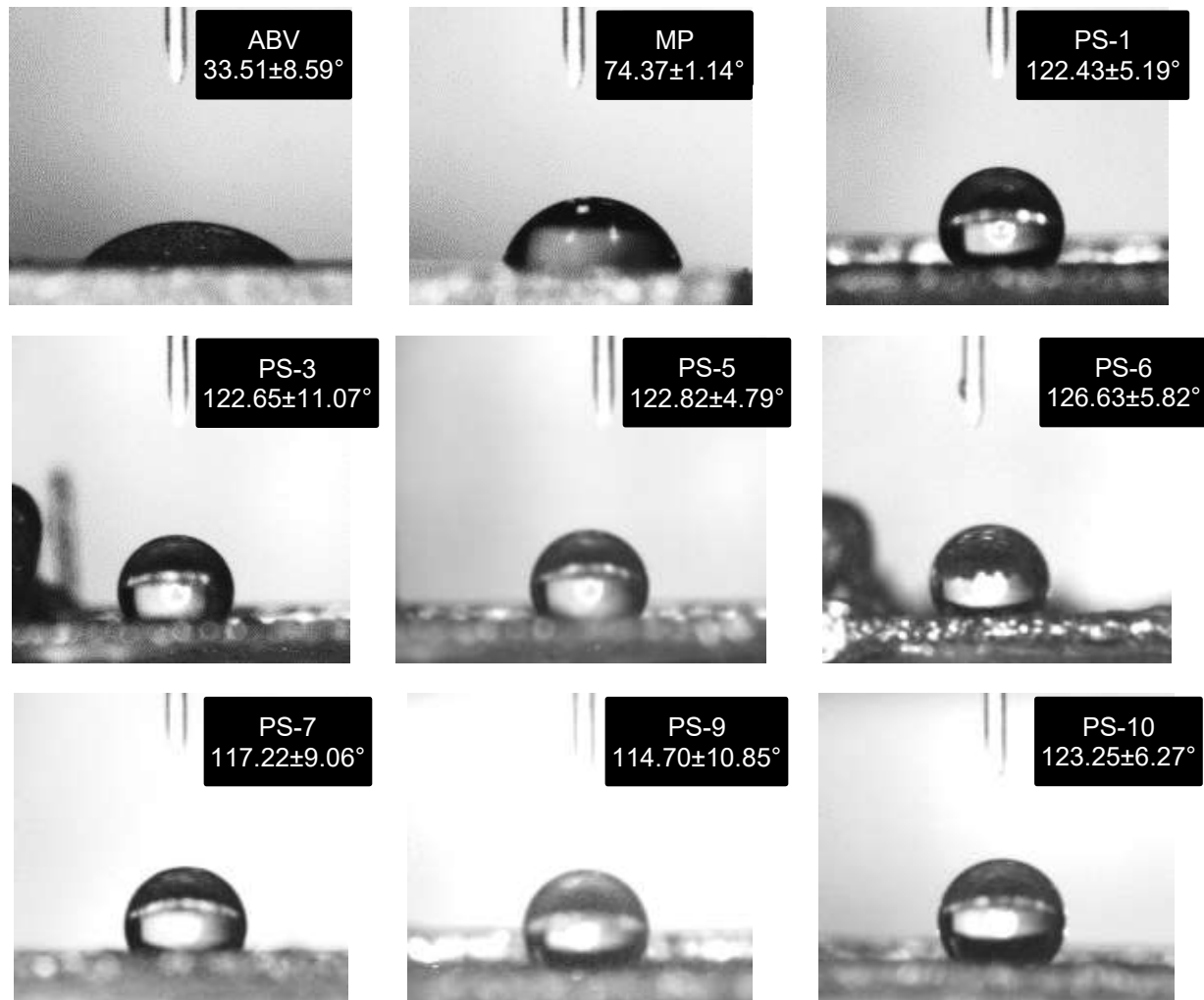
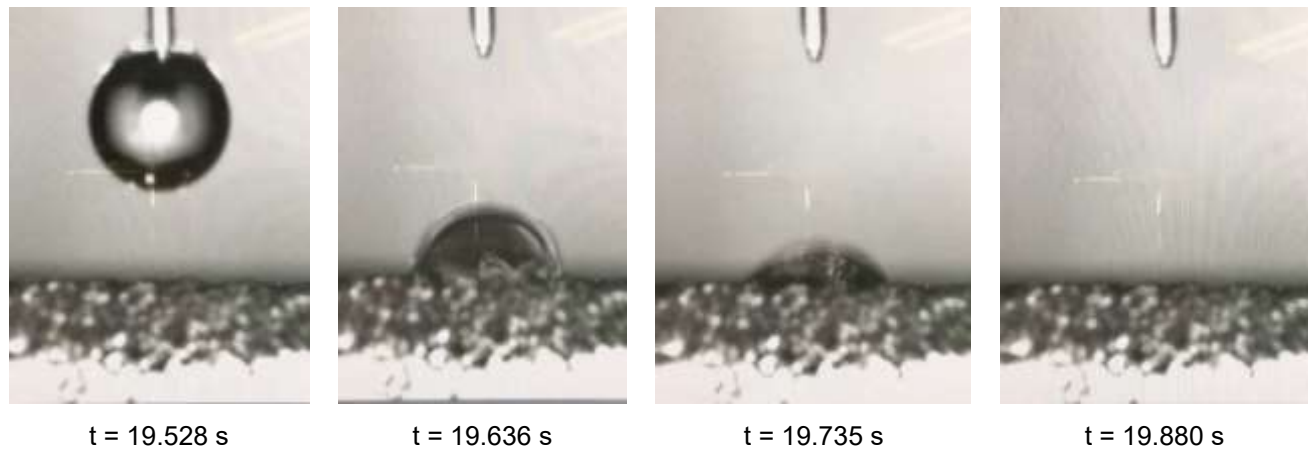


Figure 7-2: Static water contact angles on reference and 400  $\mu\text{m}$  PTW specimens

In contrast to this, the 950  $\mu\text{m}$  PTW imbibed a water droplet within  $222 \pm 50.41$  ms. A time series of screen shots of the water droplet imbibed into the 950  $\mu\text{m}$  PTW is presented in Figure 7-3. Video frames before surface contact and after imbibition were identified using a commercially available digital audio workstation software. The wetting behavior is therefore influenced by the thickness of the porous structure. Similar observations have been reported for macroporous anodised aluminium oxide layers, but reasons for the wetting transition based on thickness were stated as unclear and residual electrolyte in the thicker porous structure was suspected (Buijnsters, et al., 2013).



**Figure 7-3: Image frames for creation of a time series of water droplet imbibed into 950  $\mu\text{m}$  thick permeable wall fabricated with PS-10**

The Young equation for theoretically describing the contact angle,  $\theta$ , of a droplet on an ideal, smooth surface is,

$$\cos\theta_{\text{Young}}\gamma_{lv} = \gamma_{sv} - \gamma_{sl} \quad (7-1)$$

where  $\gamma_{lv}$ ,  $\gamma_{sv}$ , and  $\gamma_{sl}$  denotes the liquid-vapour, solid-vapour, and solid-liquid interfacial tensions respectively (Rupp et al., 2014). This is schematically presented in Figure 7-4(a). However, the ideal nature of the model does not account for real surfaces. Two theories developed more than 70 years ago aim to describe the contact angle on a rough surface. In the Wenzel wetting model (Figure 7-4(b)), a water droplet interacts with the full surface profile. The measurable Wenzel contact angle,  $\theta_w$ , is expressed by,

$$\cos\theta_w = r_w \cos\theta_{\text{Young}} \quad (7-2)$$

where  $r_w$  is a roughness parameter which relates the actual surface area to the projected surface area and is therefore greater than one. Considering the hydrophilic nature of the ABV specimen which had a mean surface roughness,  $Ra$ , of  $(8.382 \pm 1.01 \mu\text{m})$ , and the  $Ra$  of the PS-10 PTWs ( $16.70 \pm 1.18 \mu\text{m}$ ), it is unlikely that the contact angles for the PTWs could be accounted for by the Wenzel wetting model. This is because the contact angle on the ABV specimen is significantly lower than that of the MP specimen and if this trend is assumed to be indicative with regards to surface roughness, according to the Wenzel model the increase in roughness of the PTW should further decrease the contact angle (Rupp et al., 2014).

Cassie and Baxter (1944) described a situation where the water droplet interacts with a heterogeneous surface comprising both the rough solid material and air (Figure 7-4(c)) (Lembach et al., 2010). In this case, the measurable contact angle,  $\theta_c$  is described by,

$$\cos\theta_c = f\cos\theta_{\text{Young}} + f - 1 \quad (7-3)$$

where  $f$  is the area fraction of the solid that is in contact with the droplet. According to Rupp et al. (2014), high contact angles on microrough blasted and acid-etched titanium surfaces are likely to be a result of the Cassie-Baxter state. Whereas this may account for the apparent large contact angles on the  $400 \mu\text{m}$  PTWs it does not explain the transition to rapid imbibition with an increase in PTW thickness.

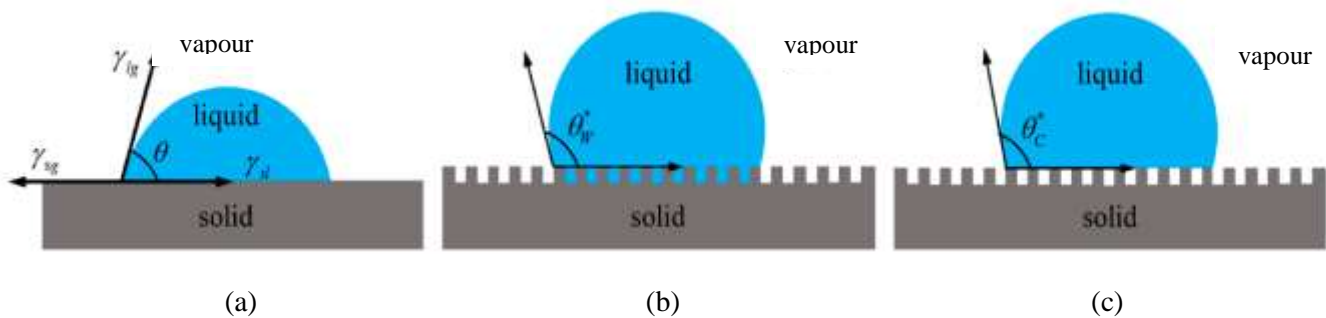


**Figure 7-4: Schematic of models for wetting with (a) the Young model, (b) the Wenzel model, and (c) the Cassie-Baxter model (Han et al., 2019)**

The transition suggests that the increase in PTW thickness essentially alters the physical classification from a hydrophobic surface to a hydrophilic complex porous volume with capillary action sufficiently large to act as a wicking medium for water. Furthermore, Bico et al. (2002) showed that imbibition takes place if the contact angle is below a certain critical contact angle,  $\theta_{crit}$ , define by,

$$\cos\theta_{crit} = \frac{1 - \phi_s}{r_W - \phi_s} \quad (7-4)$$

where  $\phi_s$  is called the emerged fraction of solid, in other words, the part of the surface which is above the film level. As the thickness of the PTW increases, the effective surface area and subsequently  $r_W$  increases. For sufficiently thick porous materials  $r_W \rightarrow \infty$  which means that  $\cos\theta_{crit} \rightarrow 0$  and therefore  $\theta_{crit} \rightarrow \pi/2$  or  $90^\circ$  which is also the criterion for capillary rise (Bico et al., 2002). In Figure 7-3 it can qualitatively be observed that upon contact with the  $950 \mu\text{m}$  PTW the apparent contact angle is less than  $90^\circ$  indicating that this condition for imbibition was met. The mechanistic aspects of imbibition and spreading of droplets on dry porous layers is complex and beyond the scope of this study (Starov et al., 2002). Nonetheless, these observations are particularly highlighted as an avenue for further research into LPBF for fabrication of integrated permeable components where wicking properties are required such as, among other, heat pipe sections, tissue engineering structures, and smart drug delivery applications.

### 7.1.1.2 Relative Porosity

A summary of the relative porosities for the fabricated  $400 \mu\text{m}$  PTWs is presented in Table 7-1. Parameter sets that yielded non-build or fragmented parts are excluded (PS-2, PS-4, and PS-8). For the fabricated PTWs the relative porosities varied from 33.62% (range = 0.81%) at the lowest VED of  $9.92 \text{ J}\cdot\text{mm}^{-3}$  to 2.73% (range = 1.37%) at the highest VED of  $27.78 \text{ J}\cdot\text{mm}^{-3}$ . This constitutes a tailorable range of more than a factor ten. The mean surface roughness of the PTWs is consistently higher for all parameter sets than that produced with the default parameters. This is likely due to the ragged textures resulting from intermittent melting and the partial sintering of powder particles forming agglomerates on the surface visible on the FE-SEM images of the PTW surfaces in the bottom left of Figure 7-5.

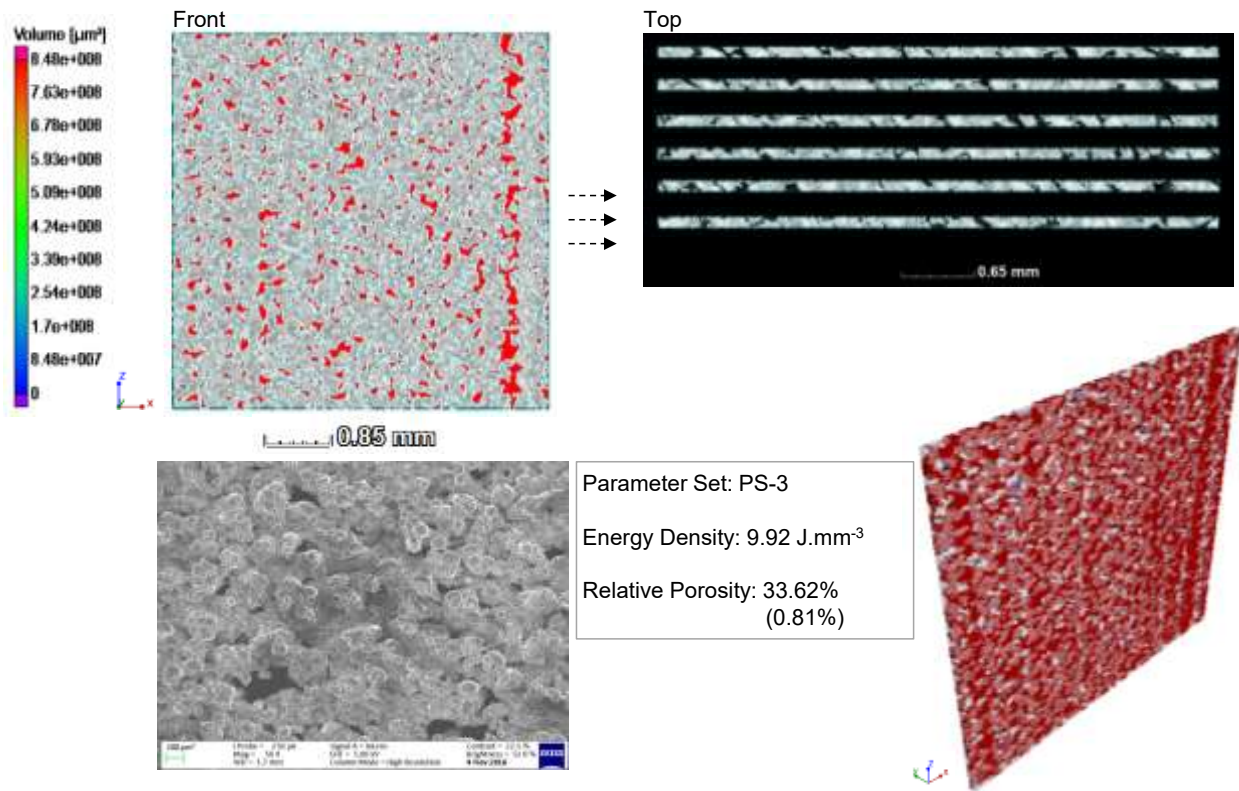
**Table 7-1: Summary of fabricated  $400 \mu\text{m}$  PTWs**

Parameter Set	$P$ (W)	$v$ ( $\text{mm}\cdot\text{s}^{-1}$ )	VED ( $\text{J}\cdot\text{mm}^{-3}$ )	$Ra$ ( $\mu\text{m}$ )	$P_{ret}$ (%)	
PS-1	50	800	19.84	$15.08 \pm 1.38$	17.37	15.24
PS-3	50	1600	9.92	$16.88 \pm 1.57$	34.02	33.21
PS-5	70	800	27.78	$12.35 \pm 1.01$	3.41	2.04
PS-6	70	1600	13.89	$19.78 \pm 3.42$	21.17	
PS-7	50	1200	13.23	$18.30 \pm 3.06$	28.01	26.66 26.87
PS-9	70	1200	18.52	$16.94 \pm 1.39$	12.27	
PS-10	40	1000	12.70	$16.70 \pm 1.18$	26.74	

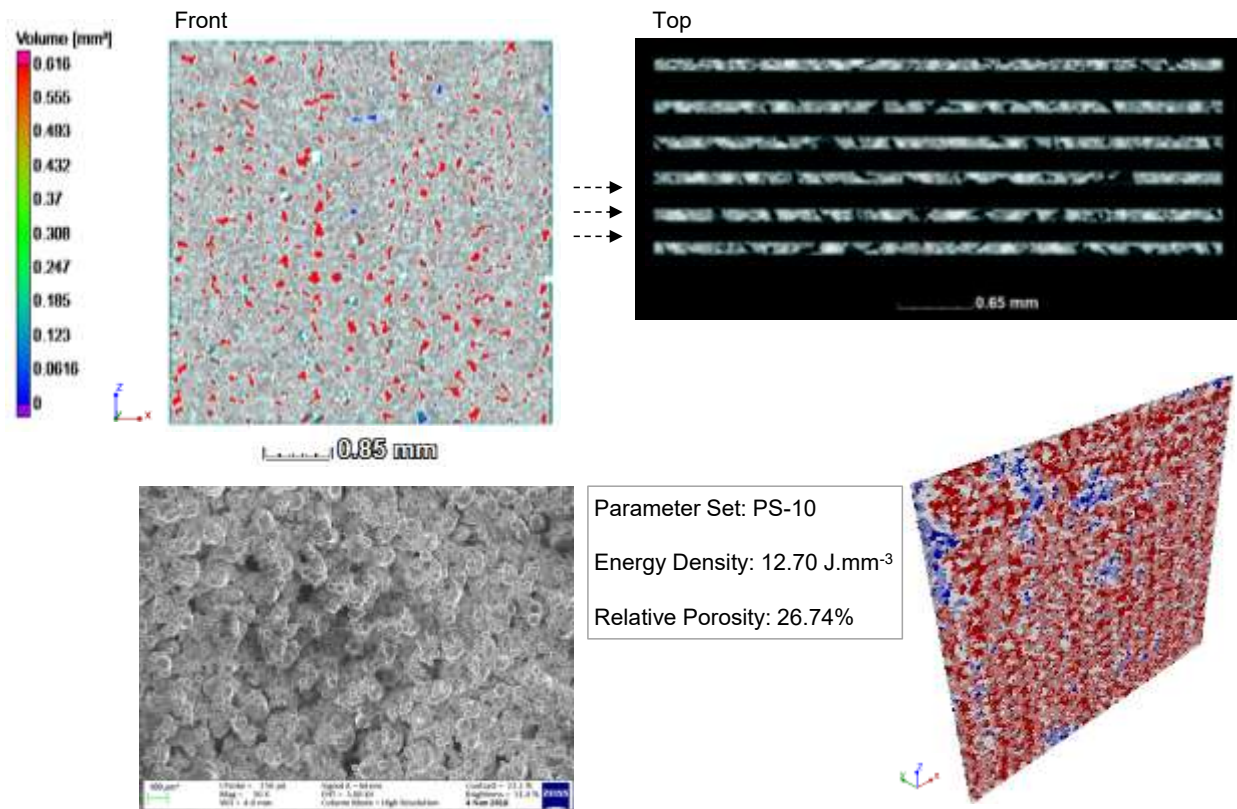
The relative porosity results for the PTWs are presented in Figure 7-5. The “Front” view (top left) depicts a section in the x-z plane through the centre of the VOI (at a depth of 0.05 mm in the y-direction). The “Top” view represents six lateral sections (x-y plane) spaced 1 mm apart in the z-direction. A 3D reconstruction showing the pore distribution throughout the VOI is presented in the bottom right. PTWs are arranged in order of increasing VED applied. PTWs analysed for repeatability evaluation are presented in Appendix D (Figure D-1).

From the reconstructions of the  $\mu$ CT scans, pores can be observed to be evenly distributed throughout the VOI. This suggests intermittent melting during the LPBF process to yield parts with pores dispersed throughout and not centred within a certain number of layers. The enabling factor is, arguably, the fabrication of layers with a defect factor which subsequently extends through the entire part height. This can be observed in the “Top” view images, especially for Figures 7-5 (a) – (d) and (f), where through-pores in the VOI are not confined within a single section, but can be observed in multiple sections taken throughout the entire height of the PTW VOI. In Figure 7-5 (e) less through pores can be observed with nearly none in Figure 7-5 (g). Figure 7-5 therefore visualises that, generally, as the VED decreased, the pores became more interconnected to the point where nearly one large interconnected pore has been obtained (Figure 7-5(a)).

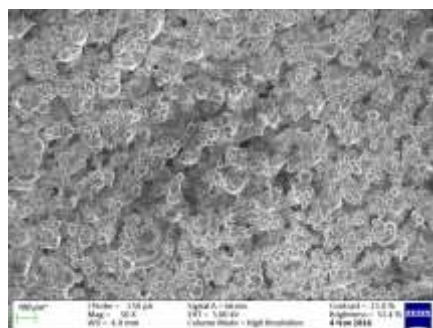
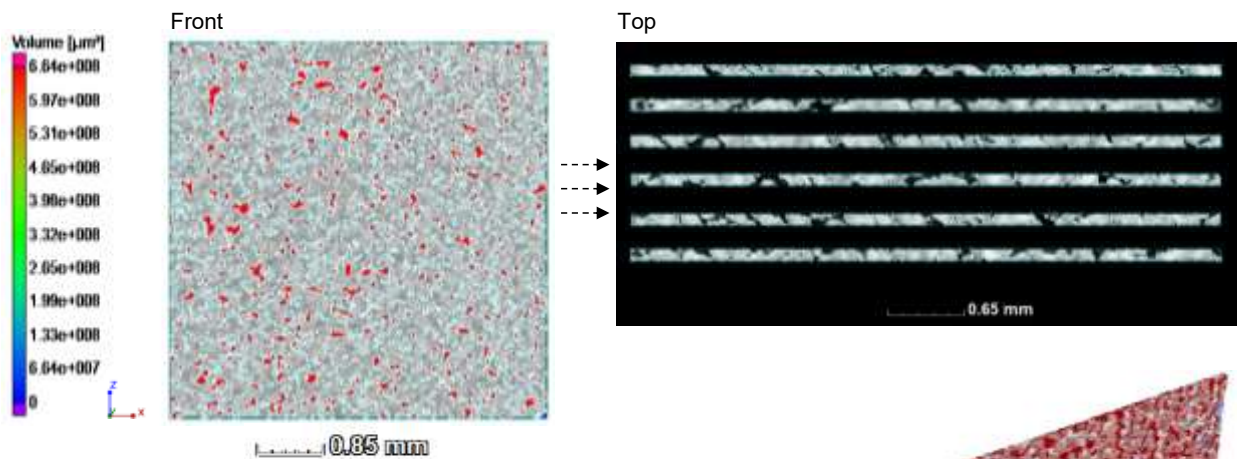
The intermittent melting of the metal powder resulted in short lengths of fused molten powder material. For the part to be built successfully, sufficient bonding is required between layers. The molten material sections within each layer should therefore sufficiently overlap with that of the preceding layer to establish sufficient bonding. However, when the energy input was too low, adequate bonding between successive layers was not achieved. Consequently, the parts were fragmented. Whereas interconnectivity of pores is essential for generating a path through the PTW structure for diffusion, it is, however, not recommended to work at the minimum VED boundary as this risks part fragmentation.



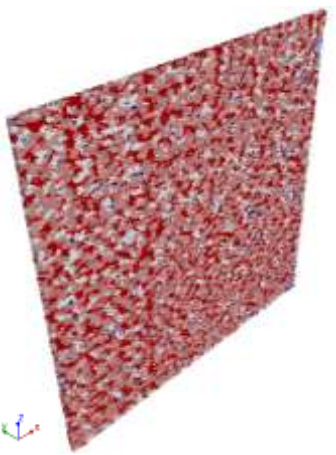
(a)



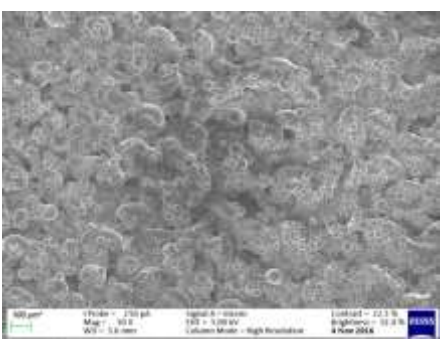
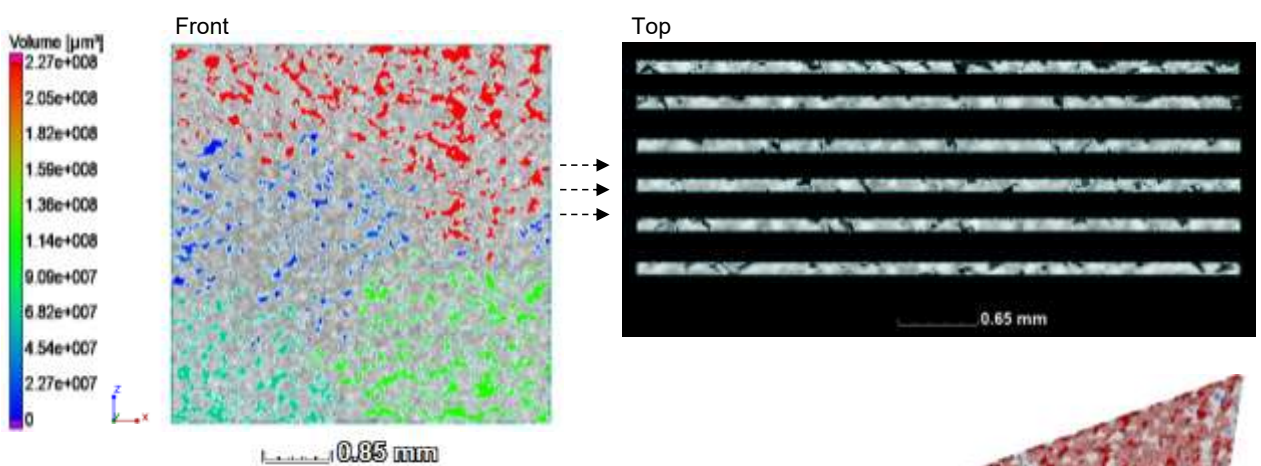
(b)



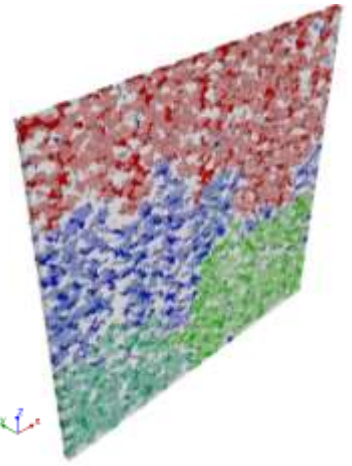
Parameter Set: PS-7  
Energy Density: 13.23 J.mm<sup>-3</sup>  
Relative Porosity: 27.18 ± 0.73%



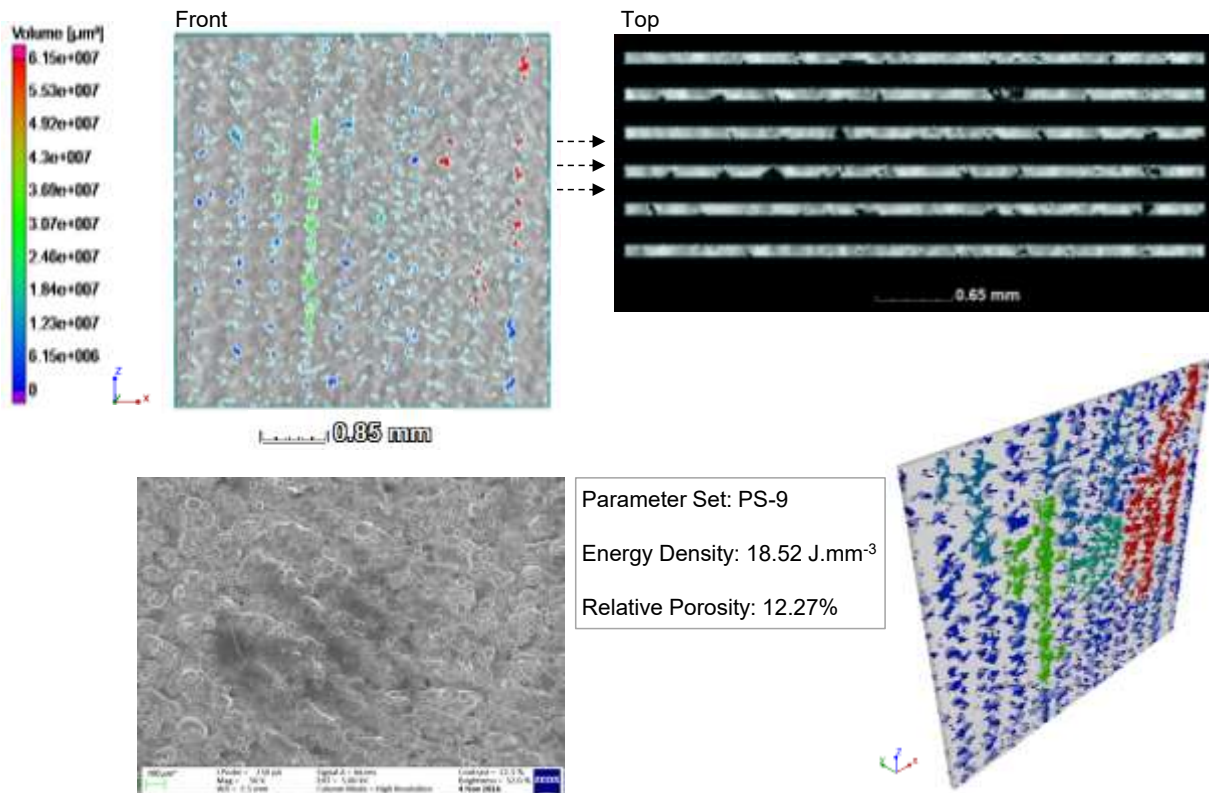
(c)



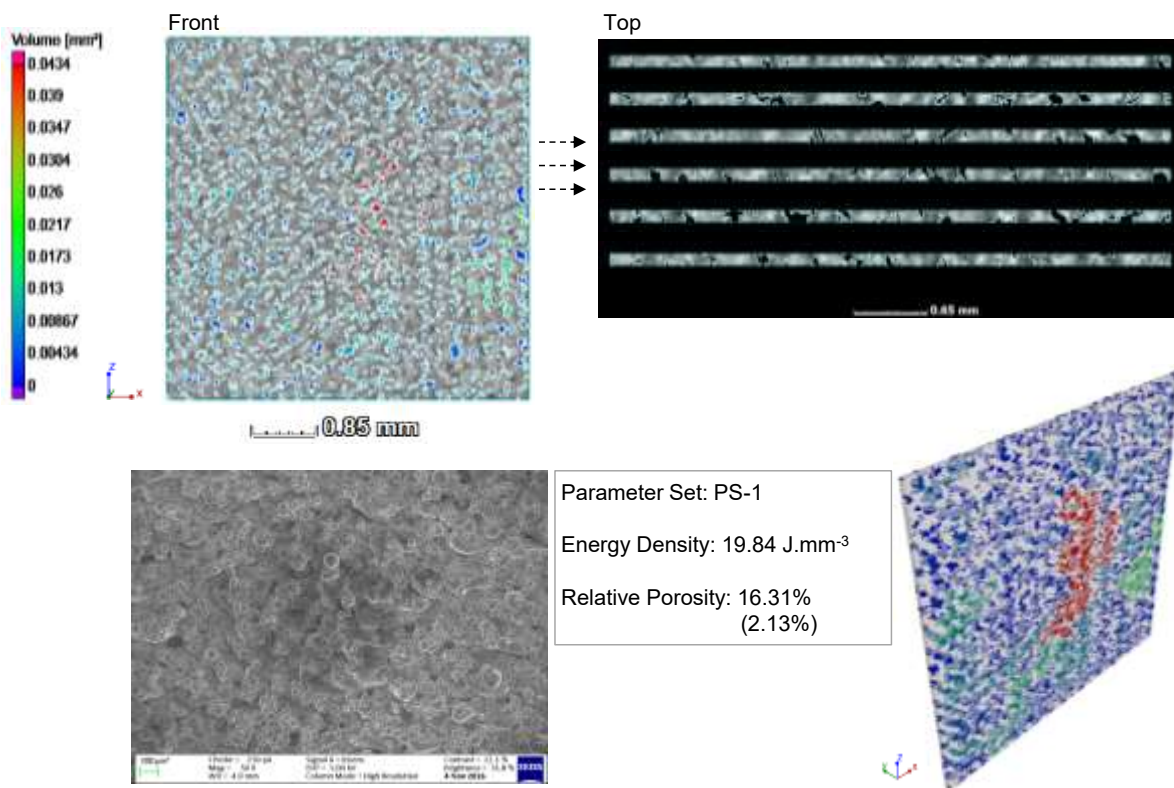
Parameter Set: PS-6  
Energy Density: 13.89 J.mm<sup>-3</sup>  
Relative Porosity: 21.17%



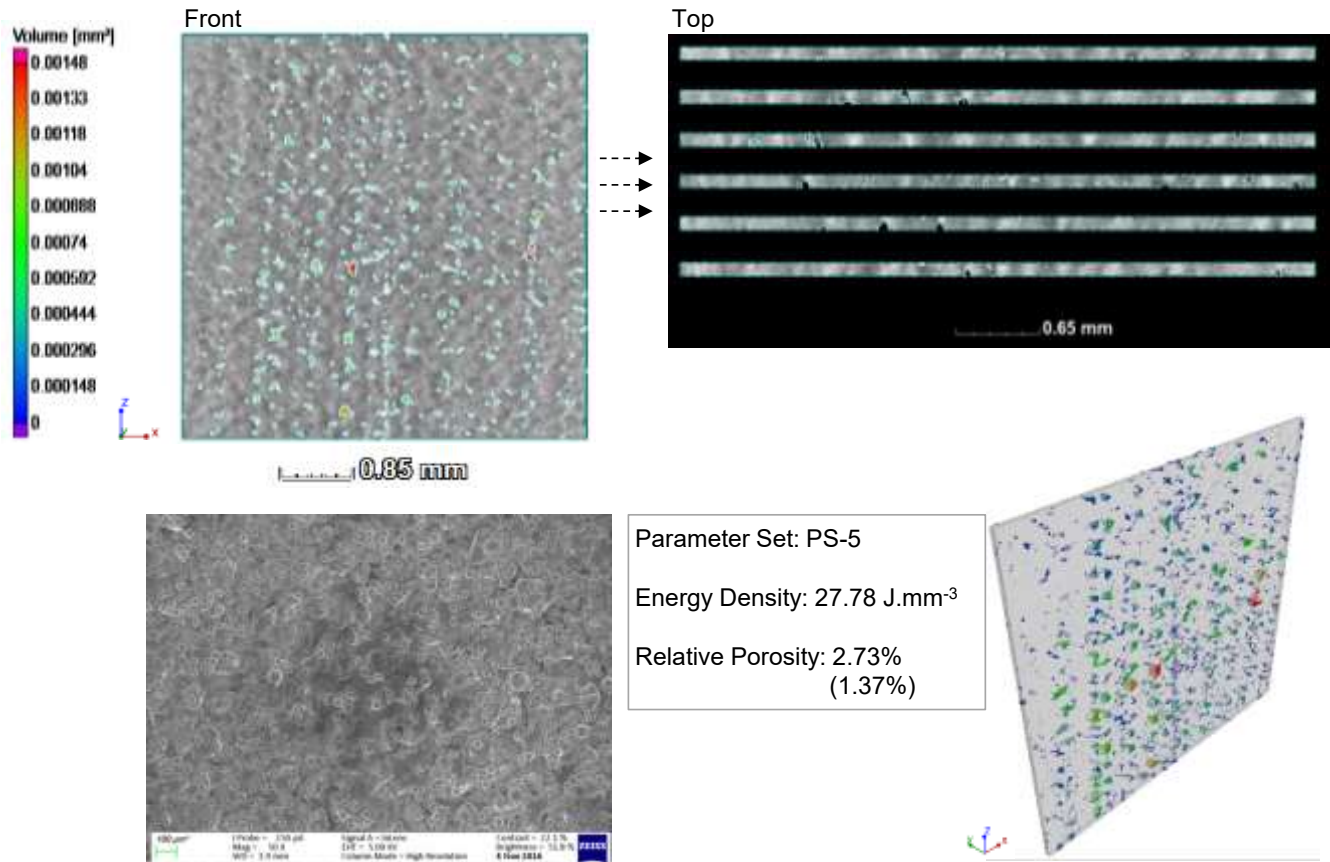
(d)



(e)



(f)



(g)

**Figure 7-5: Relative porosities with FE-SEM images of the front surfaces for 400 μm PTW samples in order of ascending VED with (a) PS-3, (b) PS-10, (c) PS-7, (d) PS-6, (e) PS-9, (f) PS-1, and (g) PS-5**

The relationship of obtained relative porosities to input VED is presented in Figure 7-6. For the investigated range of VED, relative porosity values can be simplified to follow a negative linear trend ( $R^2 = 0.931$ ).

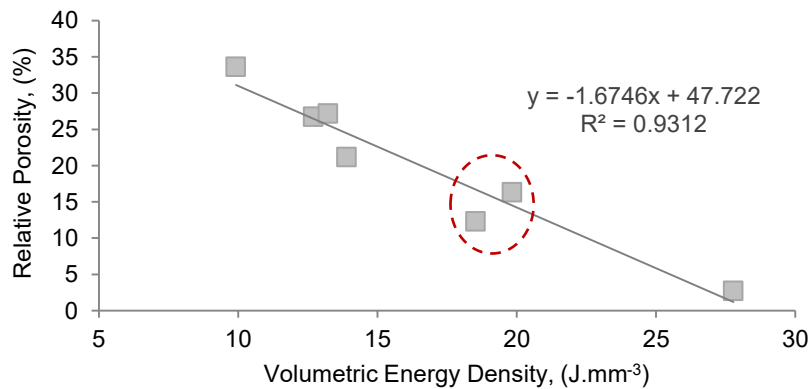


**Figure 7-6: Scatter plot of obtained relative porosity for different input VED**

Considering that the VED range investigated was specifically selected for intermittent melting, the trend in Figure 7-6 fits well with trends reported elsewhere for the insufficient energy input report as well as that of Figure 5-5 (Abele et al., 2015; Hassanin et al., 2016). The dashed circle regards PS-1 (Figure 7-5(f),  $19.84 \text{ J.mm}^{-3}$ , 16.31%) and PS-9 (Figure 7-5(e),  $18.52 \text{ J.mm}^{-3}$ , 12.27%). Although PS-1 has a slightly larger VED, a substantially higher porosity than that of PS-9 was obtained. Moreover, in the “Top” view images of Figures 7-5(e) and (f) more through-pores for the VOI can be observed for PS-1. Due to the range of PS-1 relative porosity measurements, 2.13%, and the standard deviation for the centre point PS-7, 0.73%, the inherent variation of the process is unlikely to account for this observation. From the screening experiment in Section 5.3 laser power was identified as the main factor affecting the relative porosity. The laser power for PS-1 and PS-9 was 50 W and 70 W respectively. This increase in laser power could account for the marginally higher level of powder particle fusion, decreasing the number of  $\mu\text{CT}$  detected through pores. This is reflected in the obtained vancomycin release profiles which are further discussed in the next section. Nevertheless, these results present a process window, within which parts can be produced from nearly dense to highly porous.

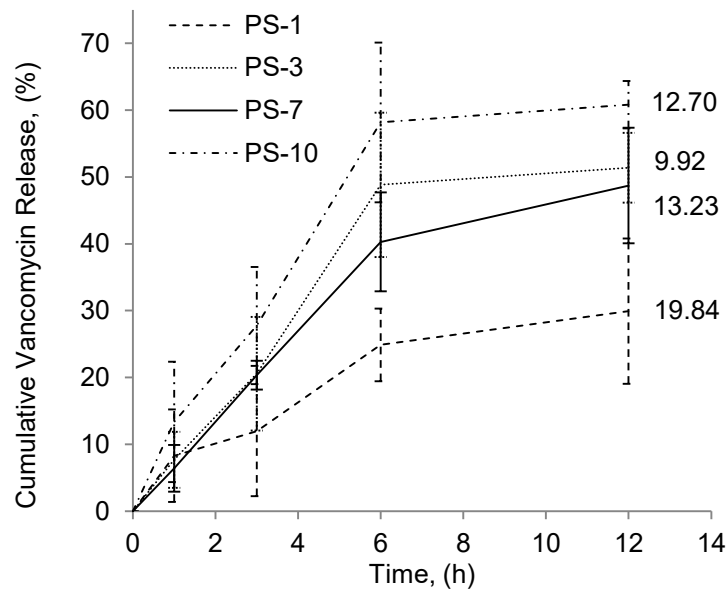
### 7.1.2 Vancomycin Release Testing

The RP-UHPLC vancomycin calibration curve had a  $R^2$ -value of greater 0.999 and is presented in Appendix D (Figure D-2). Vancomycin concentration in the buffer at sampling times could thus be accurately determined up to the maximum selected standard concentration of  $250 \mu\text{g/mL}$ .

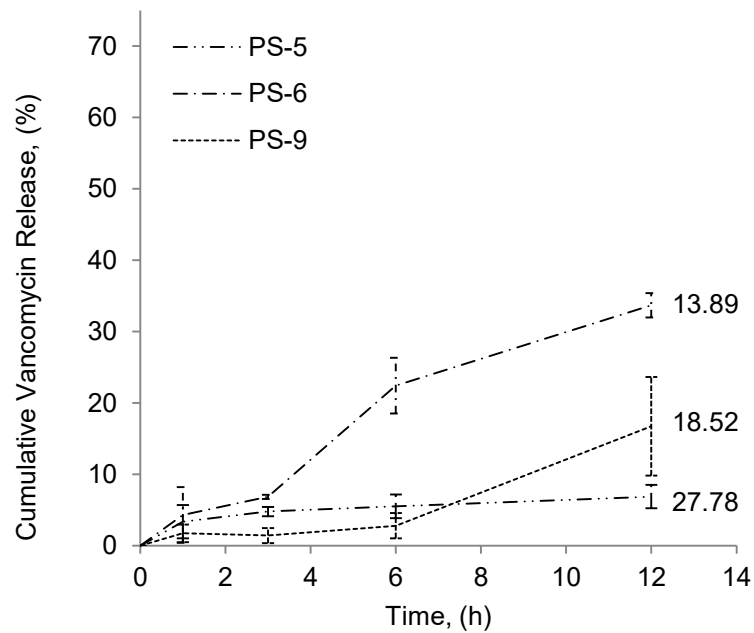
The cumulative mass of vancomycin removed from the release cell at each sampling point during the test duration was determined using the following equation,

$$M_b = (C_n \times V_b) + \sum_{i=0}^{n-1} (C_i \times V_{s,i}) \quad \text{for } n = 1, \dots, \text{number of sampling points} \quad (7-5)$$

with  $M_b$  the total mass of drug released in the buffer ( $\mu\text{g}$ ),  $C_n$  the measured concentration at sampling point  $n$  ( $\mu\text{g/mL}$ ),  $V_b$  the buffer volume (mL),  $C_i$  the concentration measured at the previous sampling point ( $\mu\text{g/mL}$ ), and  $V_{s,i}$  the sampling volume at the previous sampling point (mL). The average cumulative vancomycin release percentages are presented in Figure 7-7. In order to ease reading of the graphs, the profiles have been divided according to the applied laser power, with 50 W and less in Figure 7-7(a) and 70 W in Figure 7-7(b).



(a)



(b)

**Figure 7-7: Average vancomycin release profiles across PTWs with (a) the process parameter sets with laser power of 40 and 50 W, and (b) the process parameter sets with laser power of 70 W. Error bars represent the Standard Deviation ( $n = 3$ ) for PS-7 and the Range ( $n = 2$ ) for all other parameter sets. The VED ( $\text{J}\cdot\text{mm}^{-3}$ ) values are indicated at the end of the profiles (adapted from Bezuidenhout et al., 2018)**

The release profiles generally correlate negatively with applied VED. However, some exceptions can be observed similar to that of Section 7.1.1. The quickest release rates were observed for PS-3, PS-7, and PS-10 which corresponds to the parameter sets with the highest porosities and through-pores in the investigated VOI. The vancomycin release profile for these parameter sets are similar and resemble a near-free diffusion profile. A constraint diffusion profile can be observed for PS-1 and PS-6 with heavily constraint to little release for PS-9 and PS-5 (Jeon et al., 2012). Therefore, decreasing the VED to below a threshold of  $13.23 \text{ J.mm}^{-3}$  while maintaining a laser power of 50 W, led to the generation of sufficient pore interconnectivity that did not significantly inhibit vancomycin transport. This is corroborated by the “Top” view images in Figure 7-5. Conversely, a greater difference between the profiles of PS-6 and PS-7 was observed, even though the VED differed by only  $0.66 \text{ J.mm}^{-3}$ . The laser power, however, differed by 20 W, reflecting the significance of the effects of laser power further investigated below. The difference in release profiles demonstrates the application opportunity of LPBF to induce porosity for PTWs which resulted in different rates of drug diffusion across the structures. Currently, this work appears to be the only publically available results on this specific application (Bezuidenhout et al., 2018).

The correlation matrix for the cumulative vancomycin release percentage in the buffer at 12 hours, ( $M_b/M_{\infty}/t = 12$ ) to the input variables laser power,  $P$ , and scanning speed,  $v$ , is presented in Table 7-2. The colour coding of the matrix is the same as that used in Table 5-3.

**Table 7-2: Correlation matrix for cumulative vancomycin release after 12 hours to laser power and scanning speed**

	Run ID	$P$ (W)	$v$ ( $\text{mm.s}^{-1}$ )	$M_b/M_{\infty}/t = 12$ (%)
Run ID	1.000	0.095	-0.031	-0.283
$P$ (W)	0.095	1.000	0.131	-0.800
$v$ ( $\text{mm.s}^{-1}$ )	-0.031	0.131	1.000	0.342
$M_b/M_{\infty}/t = 12$ (%)	-0.283	-0.800	0.342	1.000

From Table 7-2 it can be observed that  $M_b/M_{\infty}/t = 12$  is strongly negative correlated with  $P$ , and moderately positive correlated with  $v$ . This reflects the effects of  $P$  and  $v$  on porosity as identified both in the screening experiments and in Figure 7-5, albeit here the effect is more pronounced as the ranges of the process parameters are limited to a range of interest identified through the preceding screening experiments.

To statistically analyse the effects of laser power and scanning speed within the investigated ranges on vancomycin release through PTWs, a two-factor interaction (2FI) model was fitted according to the standard equation below. The ANOVA output for fitting of the 2FI model is presented in Table 7-3.

$$Y = \beta_0 + \beta_1 X_1 + \beta_2 X_2 + \beta_{12} X_1 X_2 \quad (7-6)$$

**Table 7-3: ANOVA for fitted 2FI model**

Source	Sum of Squares	df	Mean Square	F-value	P-value
<i>Model</i>	4599.90	3	1533.30	42.28	< 0.0001
A-Laser Power	3557.52	1	3557.52	98.10	< 0.0001
B-Scanning Speed	303.17	1	303.17	8.36	0.0161
AB	150.03	1	150.03	4.14	0.0693
<i>Lack of Fit</i>	26.6	3	8.87	0.1847	0.9035

The low P-value in the first row indicates that the model is significant. This is also supported by the non-significant lack of fit of the model and an adjusted  $R^2$  value of 0.905. Model fitting and diagnostic plots are presented in Figure D-3 in Appendix D. The model equation is provided in Table 7-4.

**Table 7-4: Equation of the fitted 2FI empirical model in terms of coded and actual**

Equation in terms of coded factors	Equation in terms of actual factors
$M_b/M_{\infty} _{t=12} =$ $+ 40.29$ $- 21.15 \quad \times A$ $+ 7.09 \quad \times B$ $+ 6.29 \quad \times AB$	$M_b/M_{\infty} _{t=12} =$ $165.73581$ $- 2.66759 \quad \times P$ $- 0.039919 \quad \times v$ $+ 0.001048 \quad \times P \times v$

The 3D response surface plot is presented in Figure 7-8(a) with the associated interaction plot in Figure 7-8(b). For the purpose of graphic representation and the discussion which follows, the ‘Laser Power’ axis was adjusted to descend away from the intersection with the ‘Scanning Speed’ axis.

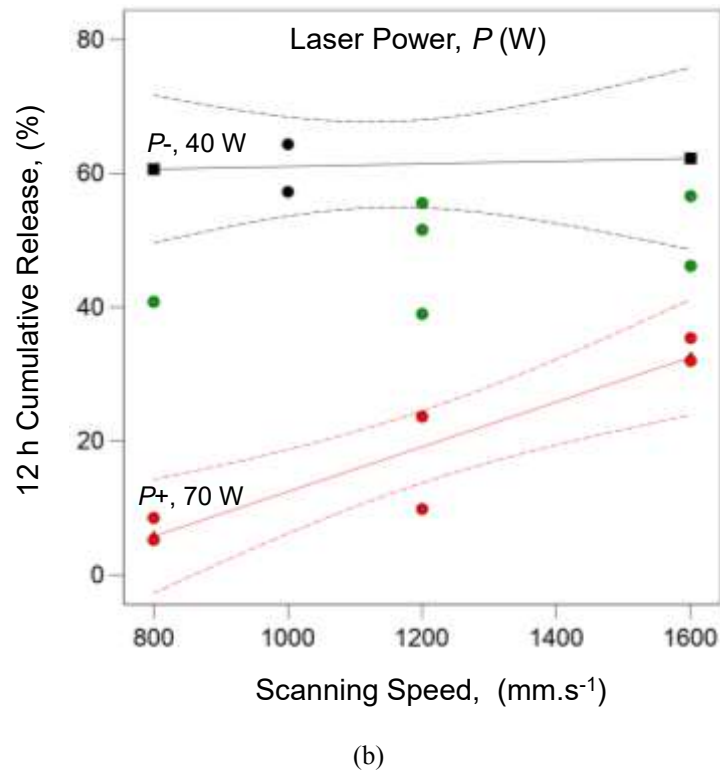
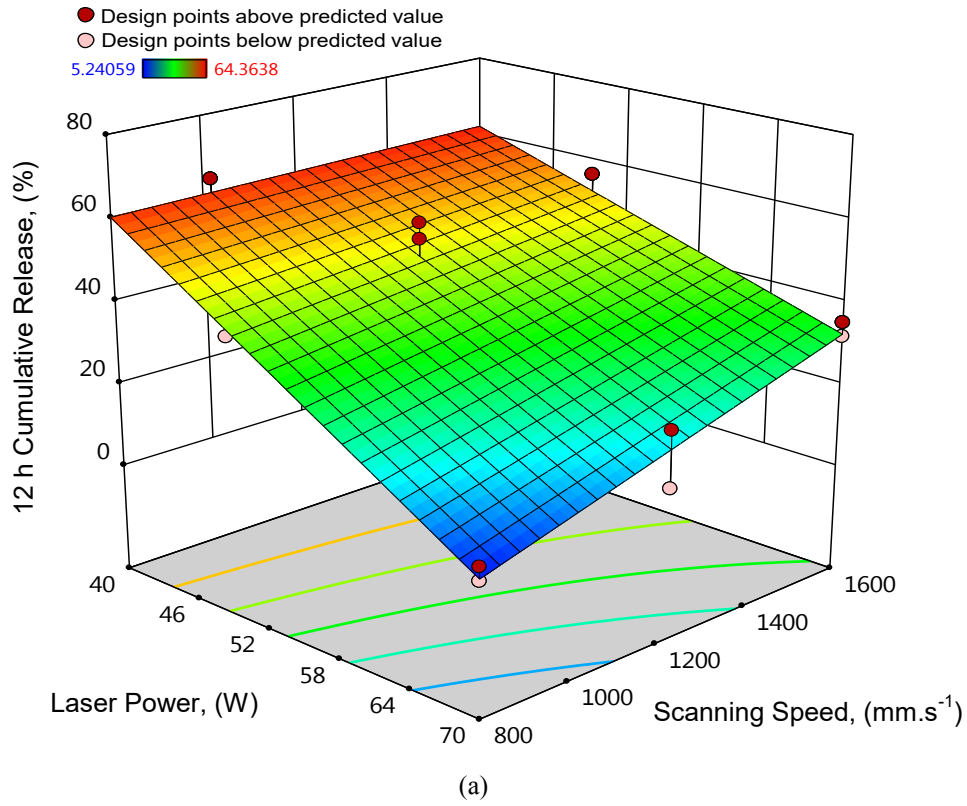
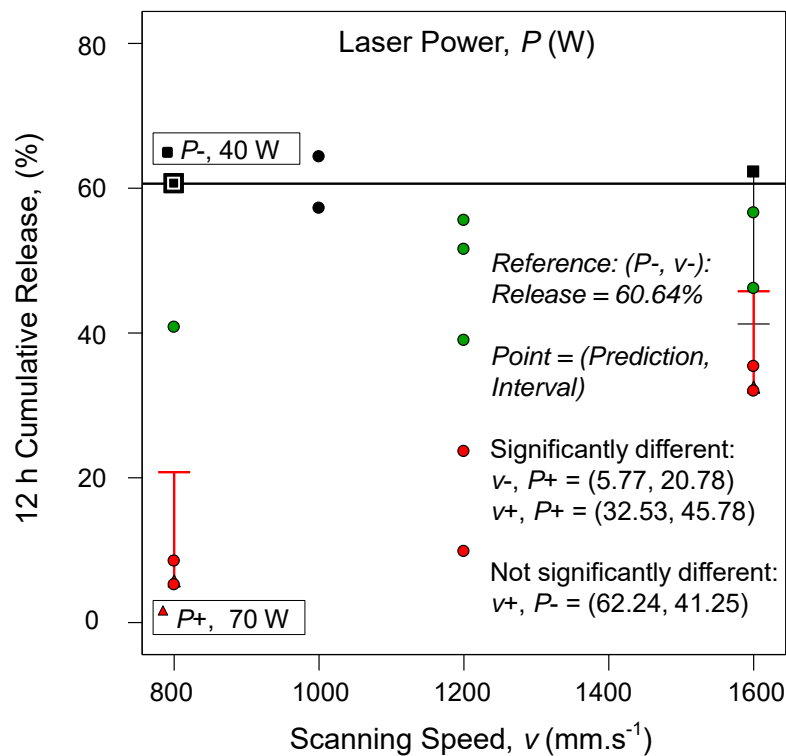
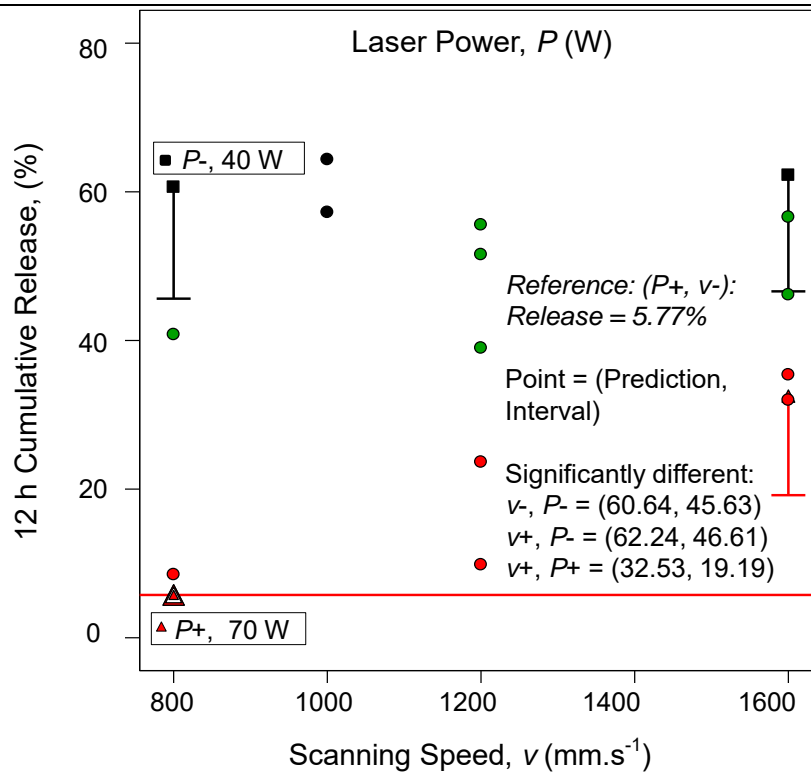


**Figure 7-8: Effect of process parameters on vancomycin release with (a) response surface of two factor interaction model and (b) interaction effects plot (adapted from Bezuidenhout et al., 2018)**

Both of the factors have been identified to exert a significant influence on the vancomycin release. Laser power was detected as the main significant factor with a P-value of  $< 0.0001$  in comparison to scanning speed which has a P-value of 0.0161. The interaction of the factors was detected as borderline insignificant (P-value = 0.0693). From the response surface and interaction plots, however, it is clear that the effect of scanning speed depended on the corresponding laser power. This is consistent with the observations in Figures 7-5 and 7-6. A near-zero gradient can be observed for the low level of laser power (40 W) over the full investigated range of scanning speed. This suggests that over the range investigated of scanning speed, it is likely that a laser power of 40 W would lead to structures that do not inhibit free diffusion of vancomycin from an aqueous solution. However, a significant increase in the 12 h cumulative vancomycin release percentage is observed at a high laser power (70 W) as the scanning speed increased and the VED decreased. For a laser power of 70 W, little vancomycin was released after 12 h (6.88%) at  $800 \text{ mm}\cdot\text{s}^{-1}$  whereas at  $1600 \text{ mm}\cdot\text{s}^{-1}$  a vancomycin release of 33.70% was recorded. It supports the argument that laser power is the main factor at lower processing boundaries for PTWs. Figure 7-9 presents a pairwise comparison performed using *Design Expert* software. A horizontal reference line is constructed for a selected design point with the least significant difference lines generated vertically.



(a)

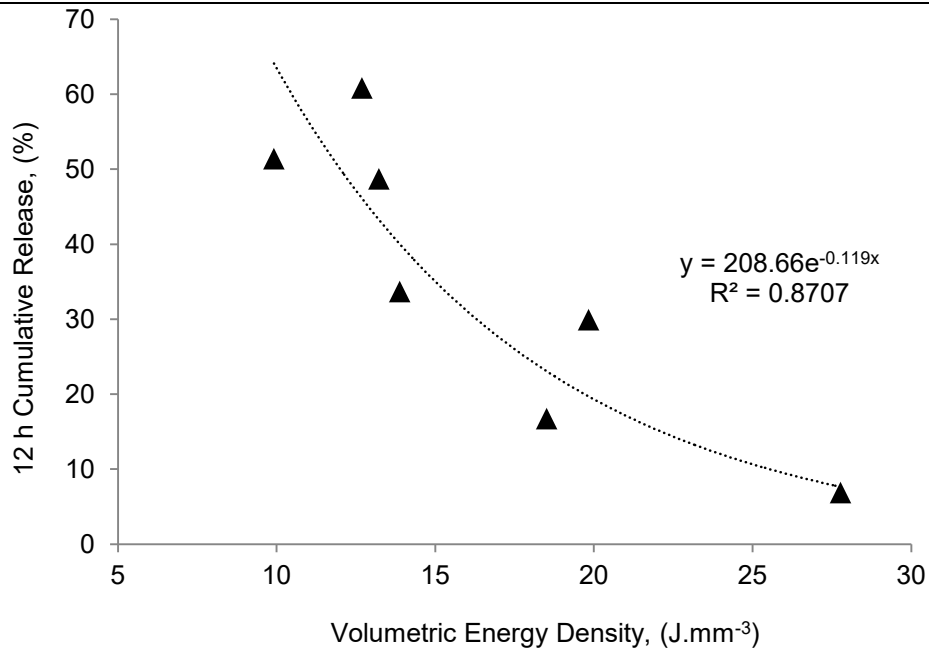


(b)

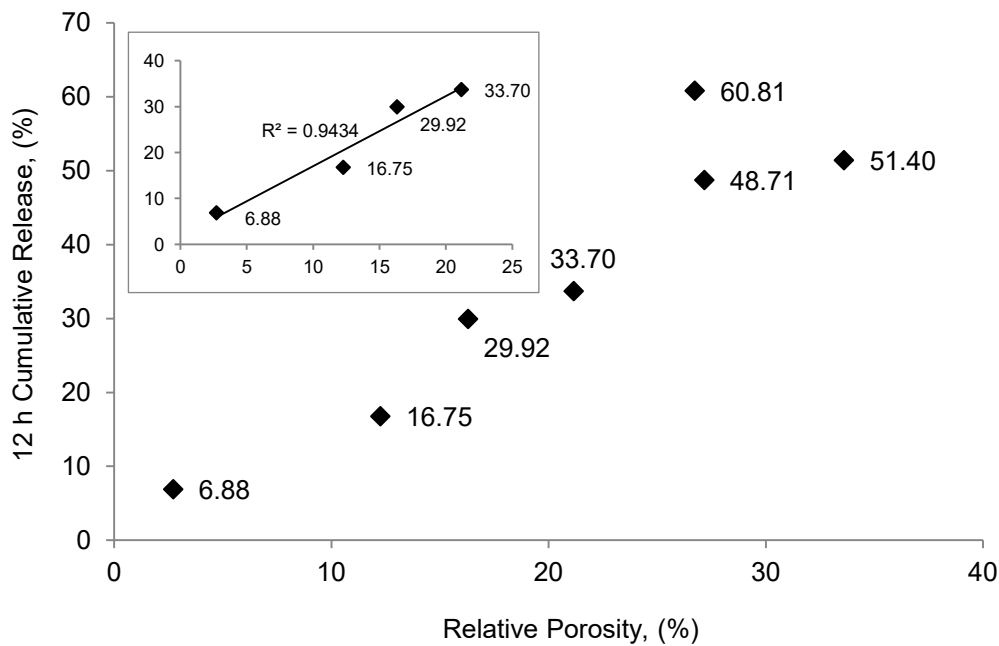
**Figure 7-9: Pairwise comparison on predictions for (a) low scanning speed and low laser power and (b) low scanning speed and high laser power (adapted from Bezuidenhout et al., 2018)**

Figure 7-9(a) statistically supports the observation that scanning speed did not exhibit a significant influence with the laser power at the low setting (black-coloured data points). When the laser power was at the high setting (red-coloured data points), Figure 7-9(b) demonstrates that the 12 h cumulative release percentages were significantly different from that of the reference point for all other extreme design points.

The relation of VED on cumulative release percentage after 12 hours is shown in Figure 7-10(a). Cumulative vancomycin release revealed a decrease with an exponential trend ( $R^2 = 0.871$ ) as VED was increased. This can be attributed to the reduction of pore size, pore interconnectivity and number of through pores in the PTWs as the VED was increased. Figure 7-10(b) presents the relation of relative porosity on the cumulative release percentage after 12 h of incubation. Initially the trend is highly linear ( $R^2 = 0.9434$ , inset in Figure 7-10(b)), but deviates from linearity beyond a relative porosity above 21.17% and a VED of  $13.89 \text{ J}\cdot\text{mm}^{-3}$ . It is therefore possible that around this point structures were obtained with an interconnected porosity which altered the vancomycin release profile from constraint to near-free diffusion.



(a)



(b)

**Figure 7-10: Graphic representation of (a) investigated volumetric energy density and 12 h cumulative release percentage and (b) relative porosity to 12 h cumulative vancomycin release percentage (adapted from Bezuidenhout et al., 2018)**

### 7.1.3 Activity of Released Vancomycin

The antimicrobial activity of vancomycin released through PTWs produced with PS-10, evaluated against *S. aureus* Xen 36 (MSSA) in duplicate is presented in Figure 7-11. Zones of inhibition (ZOIs) around the wells containing vancomycin indicate the area where effective concentrations of vancomycin were present. The observed vancomycin activity correlates with the release graphs. Effective vancomycin concentrations were released within 5 h and maintained for at least 18 h.

The average and standard deviation of the diameters of the ZOIs were determined with *Image J* software to be  $12.29 \pm 0.96$  mm at 5 h and  $12.88 \pm 0.60$  mm at 18 h, based on five measurements for each of the ZOIs at 5 and 18 h from Figure 7-11. The released vancomycin can therefore be considered to retain its antimicrobial activity after diffusing through the PTWs, that is, the interaction with LPBF-produced Ti6Al4V ELI did not cause the vancomycin molecule (Figure 4-1) to degrade. Furthermore, the resistance to wetting as indicated by the static water contact angle measurements (Section 7.1.1.1) did not restrict vancomycin from transport across the PTW to reach an effective antimicrobial concentration in the buffer.

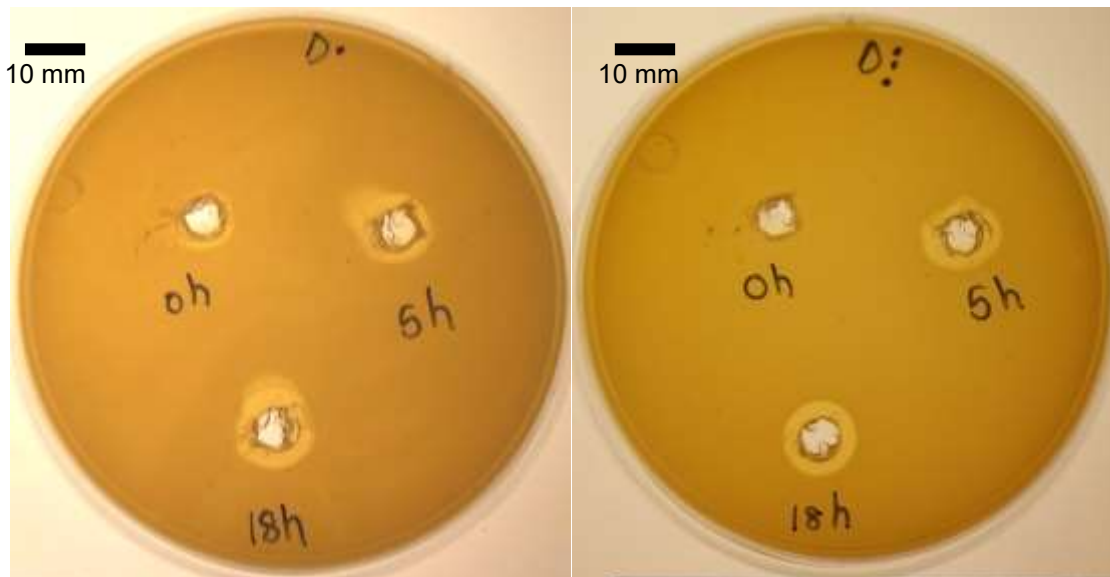


**Figure 7-11: Activity against *S. aureus* Xen 36 of vancomycin released through PTWs produced with PS-10 for different time points (0, 5, and 18 h) as indicated on the petri dishes (adapted from Bezuidenhout et al., 2018)**

## 7.2 Integrated Reservoir Specimens

### 7.2.1 Fabricated Integrated Reservoir Specimens

Reservoir specimens with integrated PTWs built with PS-10 and the in-process assembly method are presented in the as-built state on the LPBF building plate in Figure 7-12 (encircled with the dashed line). All specimens were fabricated successfully and no cracked or fractured PTWs were observed.

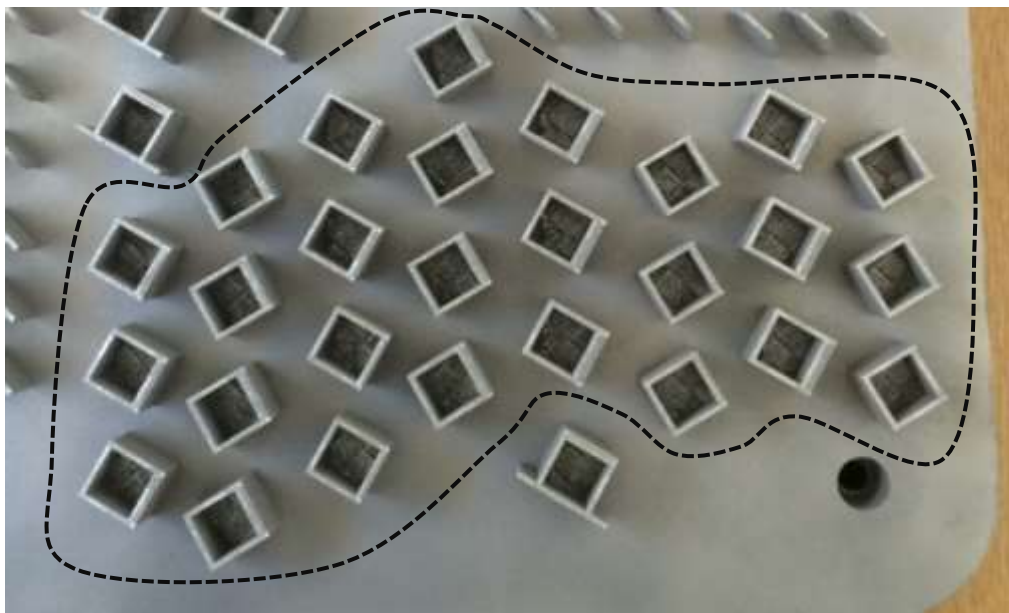
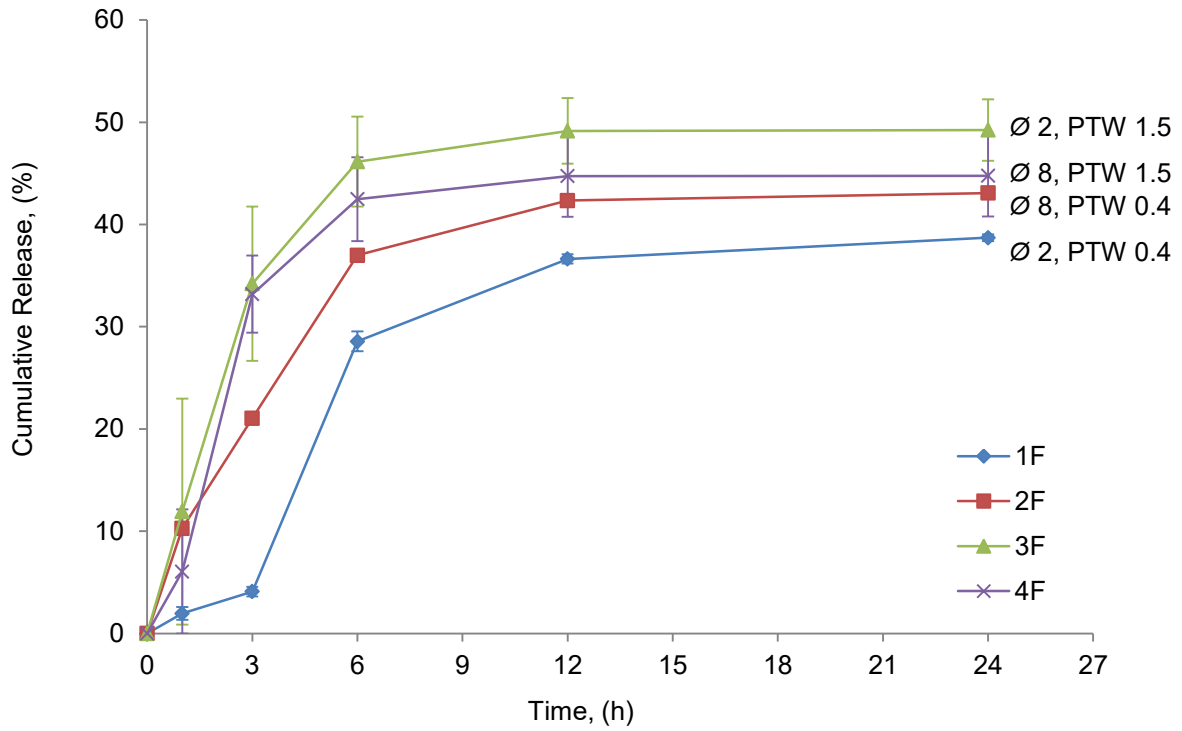


**Figure 7-12: LPBF-produced integrated reservoir specimens (encircled)**

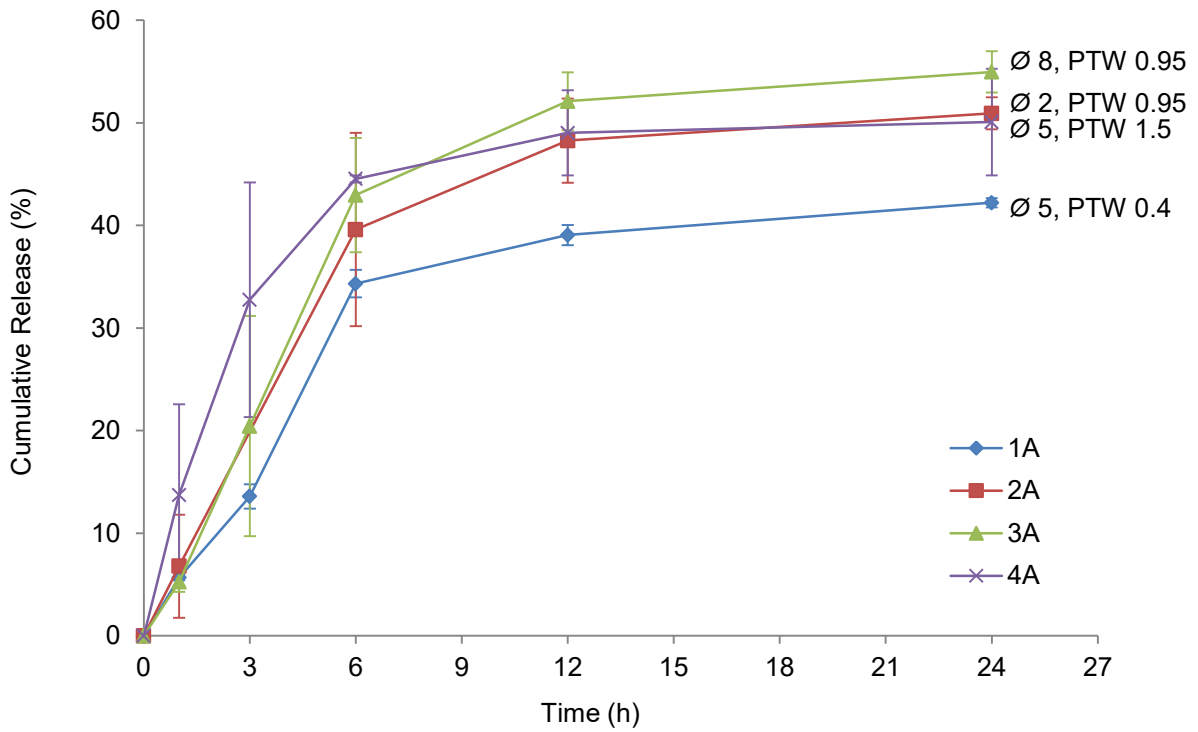
### 7.2.2 Vancomycin Release Testing

The RP-HPLC vancomycin calibration curve had a  $R^2$ -value of 0.987 (Figure D-4, Appendix D). Vancomycin concentration in the buffer at sampling times could thus be determined with reasonable accuracy up to the maximum selected standard concentration of  $125 \mu\text{g/mL}$ . Since the entire buffer was replaced at each sampling point, no correction equation was required as was the case for the vancomycin release results presented in Section 7.1.2 for the case of the PTWs (Equation 7-5).

The average cumulative vancomycin release profiles for the integrated reservoir specimens are presented in Figure 7-13. For deconvolution of the representation, curves have been split into the factorial DoE points (Figure 7-13(a)), axial DoE points (Figure 7-13(b)), and the centre point (Figure 7-13(c)). Similar to Figure 7-7, error bars in Figures 7-13 (a) and (b) represent the range ( $n = 2$ ) and error bars in Figure 7-13(c) represent the standard deviation ( $n = 3$ ) for the centre point treatment.



(a)



(b)

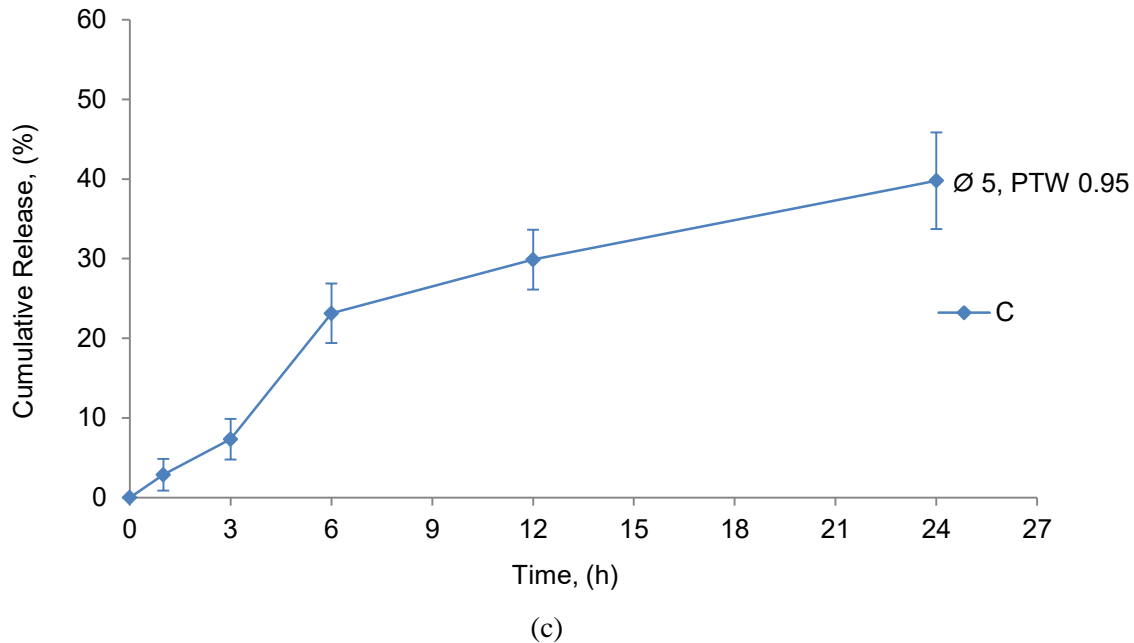


**Figure 7-13: Average vancomycin release profiles from integrated reservoir specimens for (a) the factorial points (error bars represent the range,  $n = 2$ ), (b) the axial points (error bars represent the range,  $n = 2$ ), and (c) the centre point (error bars represent standard deviation,  $n = 3$ . The hole diameter,  $\varnothing$  (mm), and PTW thickness (mm) values are indicated at the end of the profiles.**

The effect of PTW thickness at the low level of hole diameter (2 mm) is pronounced (profiles *1F* and *3F* in Figure 7-13(a) and *2A* in Figure 7-13(b)). A significantly quicker release was observed through a PTW thickness of 1.5 mm than through a 0.4 mm PTW. This is consistent with the wettability tests presented in Section 7.1.1.1. The lagging phase of *1F* ( $< 3$  h) can potentially be accounted for by the time required to displace the air according to the initial Cassie-Baxter like wetting of the dry 0.4 mm PTW. Once the air has been displaced the release rate drastically increased. This implies that a percolation type threshold existed where the increased surface free energy of the PTW during wetting exceeded the energy required to overcome the surface tension of the aqueous vancomycin solution (Bico et al., 2002). Subsequently the PTW was rapidly penetrated by the liquid solution leading to the observed increase in vancomycin transport rate.

For diameters 5 mm and 8 mm the observations were different. Vancomycin release profiles for the 8 mm hole diameter (*2F*, *3A*, and *4F* in order of increasing PTW thickness) appear similar. The contact area for wetting is thus likely to be large enough at a diameter of 8 mm to quickly overcome the apparent hydrophobicity of the 0.4 mm PTW. Furthermore, the effects of the investigated PTW thicknesses on the release profile were not significant for the 8 mm hole diameter. For 5 mm hole

diameter, however, a similar effect to that of the 2 mm hole was observed between the profiles for PTW thickness of 0.4 and 1.5 mm respectively (1A and 4A). However, the lowest release rate was observed for a PTW thickness of 0.95 mm. The reason for this is not clear. A lag phase can be observed, but considering the rapid imbibition observed during the contact angle test (Figure 7-3), this lag phase cannot directly be attributed to a resistance to wetting and further research into the transport processes within the PTW is required. Nevertheless, it imparts a desirable property for local drug delivery leading to a more near-zero order release profile

Furthermore, when considering all the release series represented in Figure 7-13 from a DoE perspective, it is not directly evident whether significant effects exist between from the DoE treatments. This is corroborated by the result that a meaningful model fit in *Design Expert* software could not be obtained when evaluating the cumulative percentage of drug released at each sampling time point respectively. It can, however be observed that differences did occur in the diffusional release rates, especially during the first 6 hours of the experiment. To investigate this further, the release data was modelled according to a first order diffusive mass transfer model derived by (Lin et al., 2009). Briefly, the change of molar flux with time can be expressed as,

$$\frac{dN_A}{dt} = k_1 A (C_{Ae} - C_A) \quad (7-7)$$

Where  $k_1$  is a mass transfer coefficient incorporating the diffusivity and thickness of the diffusion layer,  $A$  is the surface area for the mass transfer process,  $C_A$  and  $C_{Ae}$  is the concentration in the buffer at time  $t$  and an equilibrium concentration respectively. With regards to  $C_{Ae}$  it is important to respect the limitations of the study such as release time and environmental influences which could unintentionally have influences on the diffusion process. When considering a constant volume, as is the case in this study,  $dN_A = V dC_A$ , Equation 7-7 can be rewritten as,

$$\frac{dC_A}{dt} = k_1 \frac{A}{V} (C_{Ae} - C_A) \quad (7-8)$$

Equation 7-8 strongly reflects the Noyes-Whitney equation as expressed by Costa and Lobo (2001) for drug release from a dosage with constant area under sink conditions,

$$\frac{dC_A}{dt} = k_2(C_{Ae} - C_A) \quad (7-9)$$

where  $k_2$  represents a volumetric mass transfer coefficient (Lin et al., 2009). Integrating Equation 7-9 with the initial conditions,  $C_A = 0$  at  $t = 0$  and  $C_A = C_A$  at  $t = t$  yields,

$$C_A = C_{Ae} [1 - e^{-k_2 t}] \quad (7-10)$$

which can be expressed in terms of release percentage as,

$$R = R_e [1 - e^{-k_2 t}] \quad (7-11)$$

where  $R$  and  $R_e$  represents the cumulative percentage drug released into the buffer at time  $t$  and at equilibrium respectively (Lin et al., 2009). Model parameters were estimated with *MSExcel Solver* using nonlinear least squares fit (Brown, 2001). The nonlinear coefficient of fit  $R^2$  was computed according to Equation 7-12 below (Brown, 2001)

$$R^2 = 1 - \frac{\sum(y - y_{fit})^2}{\sum(y - y_{mean})^2} \quad (7-12)$$

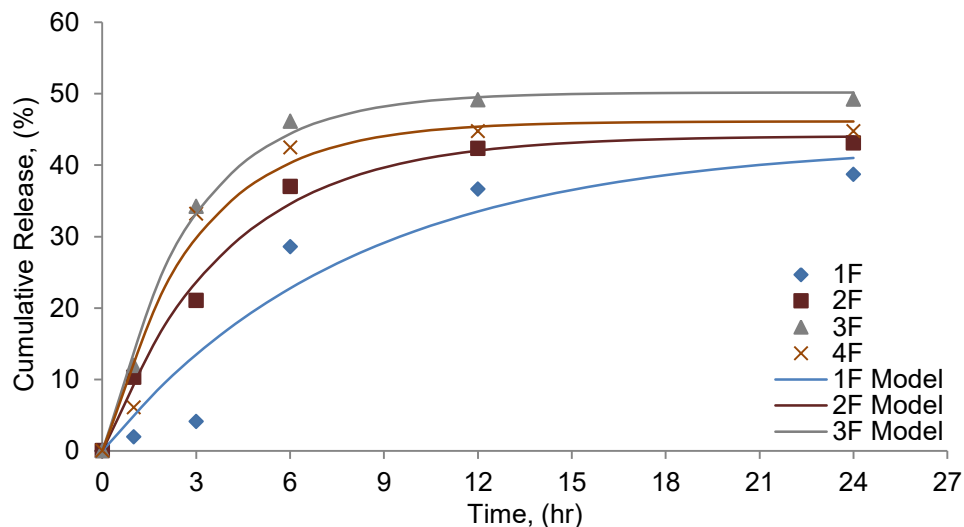
The resulting model parameters are presented in Table 7-5. With the exception of treatment *IF* all treatments show a high coefficient  $> 0.95$  of correlation with the first order model. This is mainly due to the lag phase that can be observed for treatment *IF* in Figure 7-13(a). After this lag phase however, the release follows a typical diffusion profile. Furthermore, as the interest is in sustaining drug release, the interest is in lower values of  $k_2$ , with treatment C exhibiting the lowest value and therefore the slowest mass transport of vancomycin across the PTW. Treatment C is also promising for its trend of continued release at 24 h rather than presenting a plateau as do most of the other treatments in Figure 7-13.

The fitted models are plotted with continuous lines to the observed data points for the DoE treatments in Figure 7-14. Again, the plots have been split according to the DoE factorial points (Figure 7-14(a)), axial points (Figure 7-14(b)), and centre point (Figure 7-14(c)). It is evident that the release profile can be described well by this first order model. For the factorial treatments in Figure 7-14(a), the profiles are clearly distinguished and closely correlate with the value of  $k_2$  with regards to the relative rates of

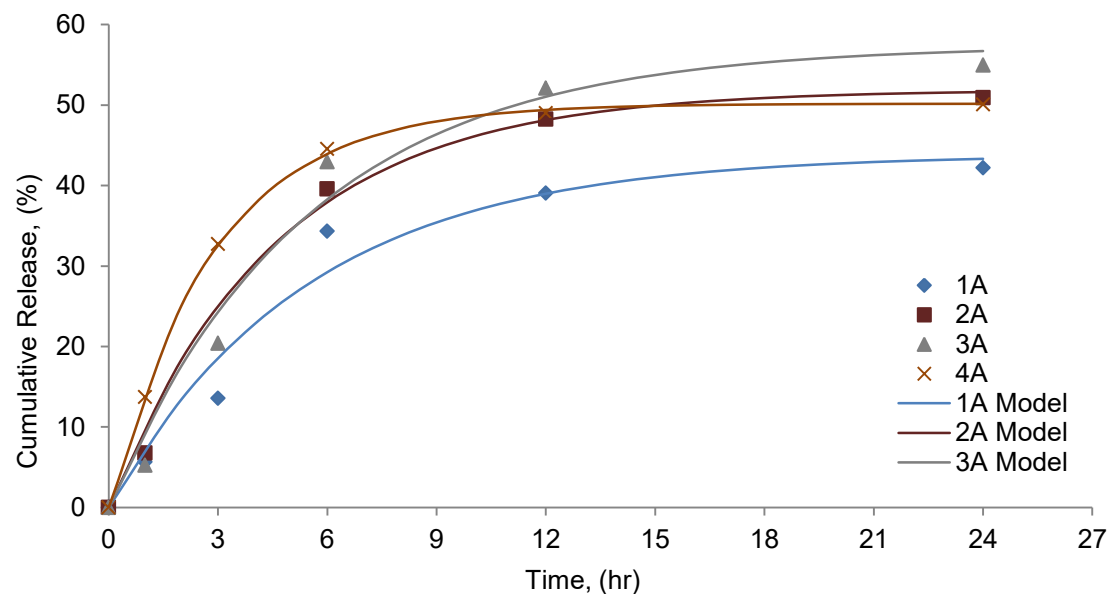
vancomycin release. That is, a higher  $k_2$  indicates faster release. For the axial points, this is not the case. The profiles are not all clearly distinguished and can be observed to cross each other as a result of diffusion rate and a subsequent plateau effect. This is also reflected by the larger range of parameter  $R_e$  for the axial points (43.86 – 57.42) compared to that of the factorial points (43.17 – 50.18). Since  $R_e$  can essentially be regarded as a scaling parameter, it is important to consider also this parameter for the axial points. It can therefore be seen that although treatments 1A and 3A have similar mass transfer coefficients, the difference in  $R_e$  yields the total cumulative release to differ considerably. For treatments 2A and 4A having similar  $R_e$ , the difference in release profile can be predicted by the mass transfer coefficient  $k_2$  from which it could be expected that treatment 4A will have a quicker diffusion rate, as is confirmed in the data.

**Table 7-5: Model parameters for vancomycin release profiles from integrated reservoir specimens**

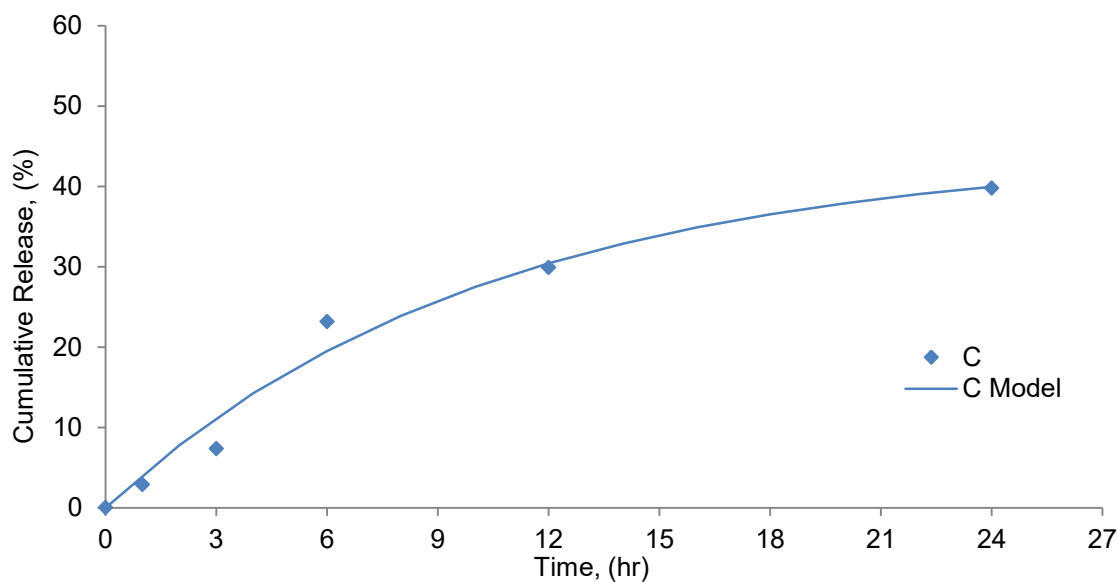
Treatment	$R_e$	$k_2$	$R^2$
1F	43.17	0.1248	0.8874
2F	44.09	0.2554	0.9916
3F	50.18	0.3598	0.9925
4F	46.13	0.3446	0.9586
1A	43.86	0.1830	0.9638
2A	51.89	0.2187	0.9930
3A	57.42	0.1831	0.9768
4A	50.17	0.3472	0.9992
C	44.27	0.0969	0.9753



(a)



(b)



(c)

**Figure 7-14: Fit of model to the average experimental data for (a) the factorial points ( $n = 2$ ), (b) the axial points ( $n = 2$ ), and (c) the centre point ( $n = 3$ )**

As mentioned above, treatment C offered the most sustained release profile, slightly constraining the diffusion process. This is clearly correlated with treatment C having the lowest  $k_2$  parameter of 0.0969. Therefore, treatment C was identified for antimicrobial efficacy testing against *S. aureus* Xen 36 to evaluate the colonisation prevention potential of the strategy of delivering vancomycin locally through an in-process LPBF-assembled PTW integrated reservoir.

### 7.2.3 Colonisation Prevention Potential

The antimicrobial activity of vancomycin released from the integrated reservoir specimens produced with DoE treatment 'C' is presented in Figure 7-15. Specimens were removed from the solidified agar to improve visibility of the inhibition zones. The locations of the surface with the PTW are indicated by the arrows in Figure 7-15. All three specimens tested prevented *S. aureus* Xen 36 from reaching the surface containing the PTW. This is the surface of interest as bacterial colonisation should be prevented on the surfaces which contain the PTWs. The concept evaluated here of utilising LPBF to produce reservoirs with in-process integrated PTWs for local delivery of vancomycin offers the possibility of effective drug release as well as potential for colonisation prevention of implant surfaces by a vancomycin susceptible *S. aureus* species.

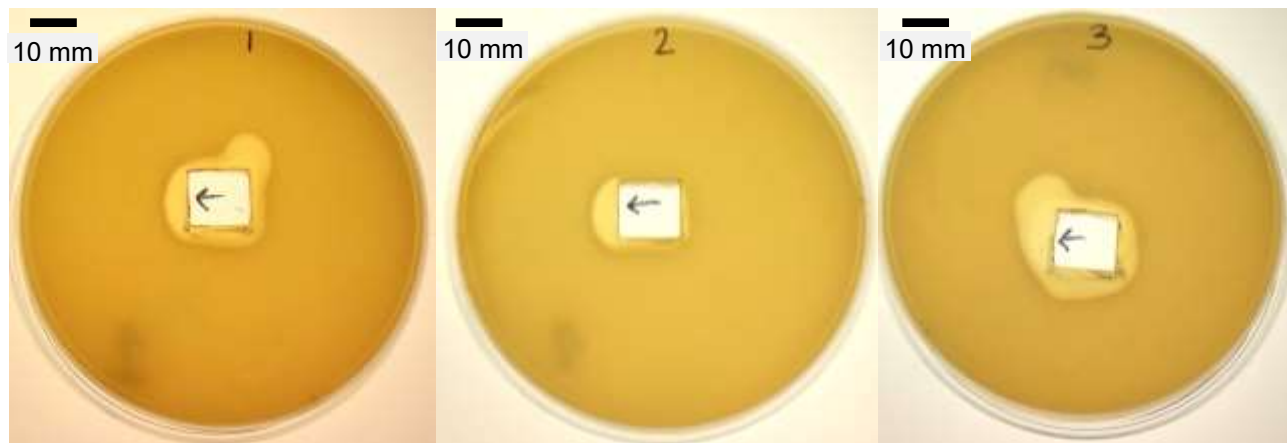


**Figure 7-15: Inhibition zones showing effective prevention of colonisation of the surface where the integrated PTW is situated (indicated with arrows) for integrated reservoir specimens with DoE treatment 'C' (adapted from Bezuidenhout et al., 2018)**

### 7.3 Conclusion

This chapter presented the results from the investigation into the LPBF of integrated Ti6Al4V ELI PTWs for controlled drug delivery of vancomycin from an aqueous solution. A method was presented for local drug delivery from Ti6Al4V ELI reservoirs with integrated PTWs by utilising LPBF technology with a specific emphasis on part consolidation and inducing porosity through tailored settings of laser power and scanning speed.

For the 400  $\mu\text{m}$  PTWs investigation, test specimens were fabricated with different sets of process parameters. Failed builds or fragmented parts were obtained at a laser power of 30 W. At a laser power of 40 W, the effect of scanning on the resulting porosity is predicted to not significantly alter the

expected vancomycin release for at least 12 h. A lower boundary was thereby identified for laser power where PTWs could be produced considering the investigated range of scanning speed. The drug release profile could be altered from constraint to near-free diffusion. It is likely related to the intermittent melting occurring at a low laser power (and VEDs below 13,89 J/mm<sup>3</sup>). This constitutes a process window for the respective process parameters within which PTWs were produced. Main findings to incorporate into the framework are concluded as follows:

- Permeable features were assembled to dense parts in-process with LPBF by oversizing their dimensions and fabricating each feature as a distinct part.
- Dry PTWs can be tailored from hydrophobic to hydrophilic by either increasing the PTW thickness or by pre-wetting.
- A range of interconnected porosity can be induced in LPBF-produced Ti6Al4V ELI through adjustment of the process parameters within the identified insufficient energy input range.
- Vancomycin was released from an aqueous solution introduced in parts containing PTWs. Different release profiles were obtained, offering an alternative drug delivery strategy through the utilisation of the implant rather than a temporary spacer. Vancomycin transported across LPBF-produced Ti6Al4V ELI PTWs retained antimicrobial activity against *S. aureus* Xen 36.
- Cumulative vancomycin released across 400  $\mu\text{m}$  PTW revealed a linear relation to a relative porosity of up to 21.17%, after which deviations from linearity were observed.
- VED should be utilised cautiously as an indicator for the prediction of relative porosity and vancomycin release. This is due to the observation that at the low processing boundary within the investigated range, laser power became the main factor. Laser power also played a pivotal role in the resulting pore size and interconnectivity (Figure 7-5).

For the integrated reservoirs investigation, test specimens were produced with PS-10 to evaluate possible effects of geometry in the form of channel opening diameter and PTW thickness on vancomycin release. The main implications are summarised as follows:

- By utilising the method developed it is possible to successfully manufacture reservoirs with different hole sizes and integrated PTW thicknesses within the investigated ranges.

- 
- For a 2 mm channel opening, the release can be altered by the PTW hydrophobicity. The effect is dependent on the hole diameter. A trade-off and potential exist here to tailor the desired release to the intended application.
  - Although differences in the resulting release profiles can be observed, a convincing statistical model describing the significance of the factors is not readily obtainable from the measured data. The rate of release however can be quantified with a first order diffusional mass transfer coefficient. Based on this, the centre point (hole diameter of 5 mm and PTW thickness of 0.95 mm) offered the best release profile within the investigated DoE treatments for the intended application.
  - For larger diameter holes, a measure of freedom towards design decisions for the channel opening diameter and PTW thickness can thus be transferred to the framework with regard for the limitations imparted by the investigated ranges of these two geometric factors.
  - Within the investigated range and within reason unless confirmation experiments are to be executed, it is therefore possible to prioritise other aspects that may arise such as compression strength and certain requirements for post processing operations above a strict prescription on channel opening diameter and PTW thickness.
  - For the purposes of this study it is advised to not depart significantly from the centre point treatment 'C' and generally the trends indicate that a thicker structure (data limited up to 1.5 mm) accelerates vancomycin release. The reasons for this are likely to be in physicochemical interactions and elucidation of these mechanistic aspects is outside of the scope of this study, but emphasised as an important avenue for future research.
  - With the variety of available LPBF systems, it should be noted that the results were obtained with the specific applied LPBF system and environmental conditions.

## 8. Implant Internal Structure Functionalisation

This chapter presents the design, manufacture and antibacterial efficacy testing of the demonstrator prototype. It addresses the partial problem of “Prototype fabrication” which is largely a recombination process relying on the output of the preceding partial problems. The antibacterial efficacy of the demonstrator prototype is subsequently the evaluation of the functionality of an overall solution. A functional demonstrator confirms that a prototype overall solution has been achieved for the overall problem within the defined scope.

### 8.1 Internal Channel Layout Design

The process flow of the internal channel layout is shown Figure 8-1. Bullet points indicate the main considerations at each process step. The following sections in this chapter systematically discuss each of the steps listed and their corresponding considerations.

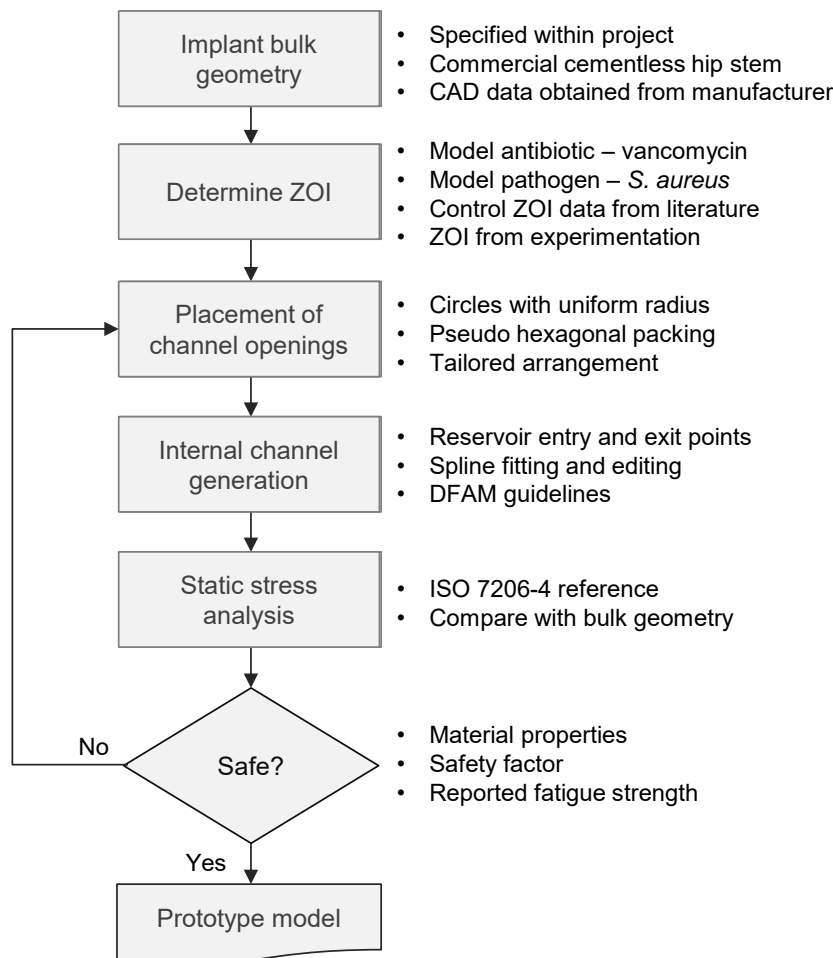


Figure 8-1: Prototype model design and fabrication process flow

### 8.1.1 Implant Bulk Geometry and ZOI parameters

The bulk geometry of the implant body belongs to that of a commercial implant manufacturer, of which the details are protected for confidentiality reasons. The main argument influencing the design approach is that the external surface of the hip stem can be covered with an arrangement of circles, uniform in radius, which represents the ZOI of vancomycin against vancomycin susceptible *S. aureus* strains. Together with the results from Section 7.2.3, Table 8-1 has been compiled which lists a number of reported ZOIs for vancomycin susceptible *S. aureus*. From the control data in Table 8-1 a value of 15 mm is identified for the working diameter of the ZOI. The value, 15 mm, represents the lower limit of the control data and is thus a conservative approach.

**Table 8-1: ZOIs reported for vancomycin as positive control against *S. aureus* strains**

Reference	Strain	ZOI (mm)	Std Dev (mm)	Utilisation
(Hannan et al., 2008)	ATCC 25923	21.31	0.79	Positive control
	UHS Imm 12	19.91	0.38	
	UHS Imm 25	20.86	0.62	
	AFIP 23845	20.66	0.99	
	AFIP 2079	20.66	0.77	
	AFIP 26763	21.85	0.17	
	AFIP 23807	19.88	0.21	
	AFIP 23197	20.53	0.44	
	AFIP 21089	21.9	0.48	
	AFIP 23804	20.36	0.74	
(Gibbons et al., 2002)	XU212	18	n/a	Positive control
(Chandrasekaran et al., 2008)	n/a	17-21	n/a	Positive control
(Pesewu et al., 2008)	UELSHB 102	20	n/a	
	UELSHB 103	22	n/a	
(Mojab et al., 2008)	ATCC 33591	17	n/a	Positive control
(Abdallah et al., 2009)	ATCC 25923	17.8	1	Positive control
	MRSA-1	18.0	1	
	MRSA-2	17.6	0.8	
	MRSA-3	18.3	0.8	
	MRSA-4	17.6	0.8	
	MRSA-5	20.0	0.5	
	MRSA-6	21.8	1.3	
	MRSA-N32064	17.8	0.9	
(Percival et al., 2011)	MRSA non-spec	17.9	0.9	
(Chan et al., 2014)	ATCC 33591	21.0	0.0	Positive control
	Clinical Isolate	20.2	0.3	
	Clinical Isolate	18.5	0.5	
(Basri et al., 2014)	ATCC 33591	18.0	0.0	Positive control
(Saiful et al., 2011)	ATCC 33591	18.83	n/a	Positive control
(Arullappan et al., 2009)	Various Isolates	16.0-22.0		Positive control
(Alshaibani et al., 2016)	ATCC 43300	18.0		Positive control

(Junaidah et al., 2015)	ATCC 49476	16.0	Positive control
	ATCC 43300	15.0	
	ATCC 33591	15.0	

### 8.1.2 Placement of Channel Openings

Circles of constant diameter representing the 15 mm ZOI were patterned according to a hexagonal arrangement, the densest packing possible. However, as could be expected, a hexagonal packing did not perfectly fall within the contours of the implant (Figure 8-2(a)) and what is termed here a ‘pseudo-hexagonal’ packing arrangement was subsequently implemented using *PowerSHAPE*. Firstly, a position was located where the tessellated centre points yielded circles that just cover the immediate zone of the implant surface (Figure 8-2(b)).

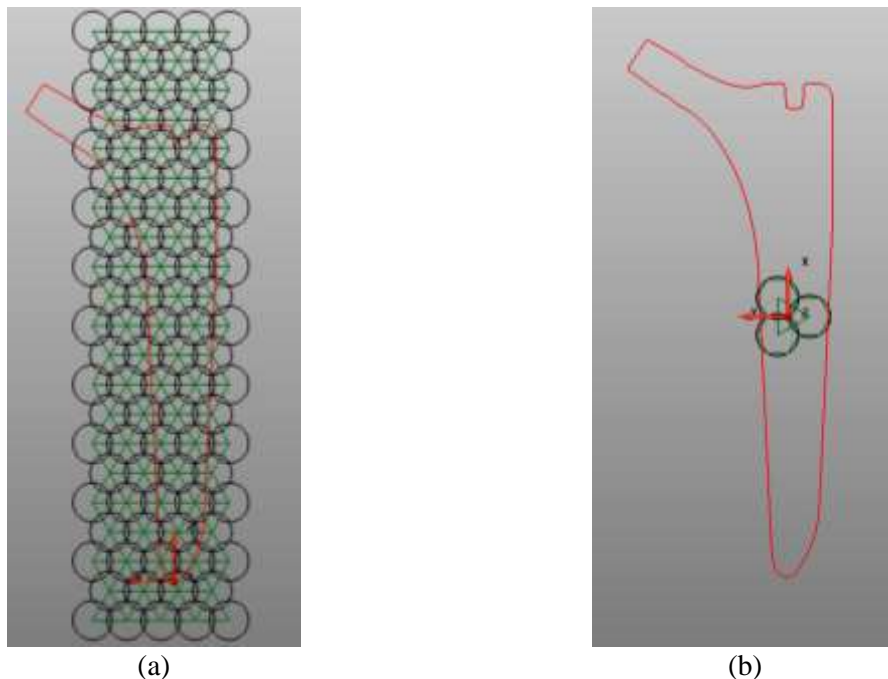


**Figure 8-2: Channel opening placement approach with (a) full hexagonal arrangement over implant profile and (b) starting point identification for pseudo-hexagonal packing**

From the intersection point of the three starting circles, indicated with the coordinate system in Figure 8-2(b), half the distance between a vertical line running through this intersection point and the implant profile, and the distance between the centre points of vertically oriented intersecting circles (the vertical side of the green triangle in Figure 8-2(b)) were utilised as pattern generation for the circle centre points (Figure 8-3(a)). Circles were placed manually for the proximal part (three circle diagonals), with the circles on the medial and lateral sides completely ensuring ZOI surface coverage in 3D space (Figure 8-3(a)-(c)).

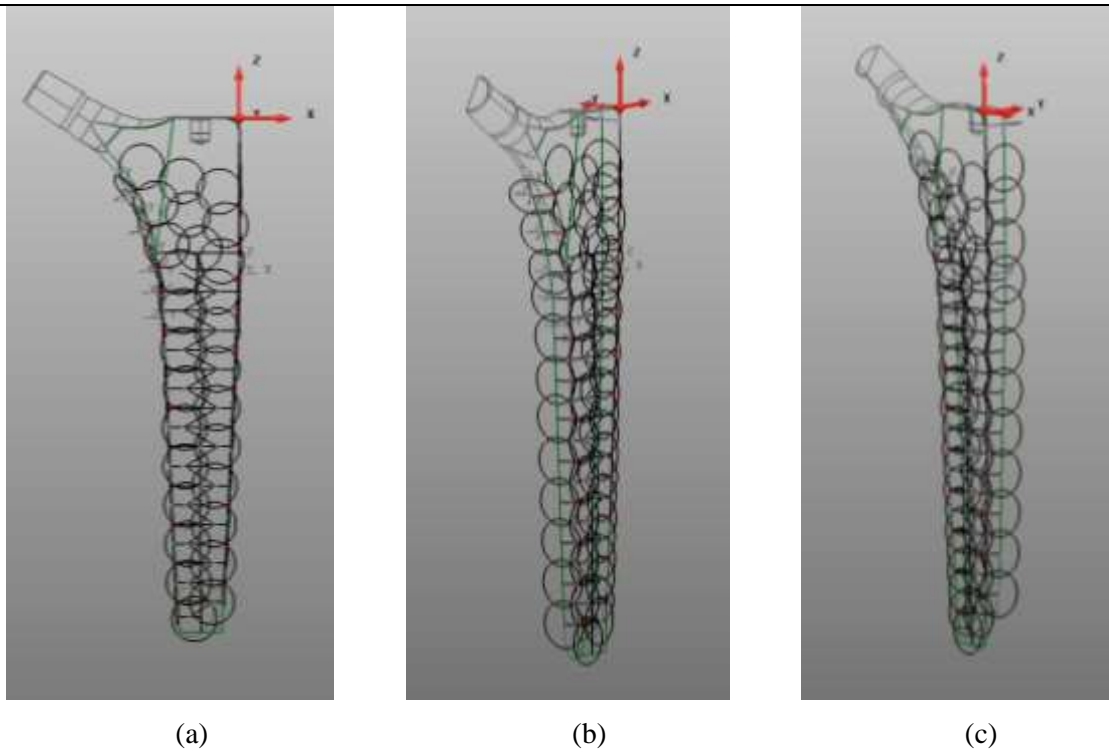


**Figure 8-3: Pseudo-hexagonal circle packing with (a) placement of channel openings on anterior surface (b) on the medial and anterior surfaces and (c) on the lateral and anterior surfaces**

### 8.1.3 Internal Channel Generation

Once channel opening positions have been established, it needed to be configured how the drug formulation will reach these release points. This led to many possibilities and possible channel layouts. With the main selection criteria being simplicity and maintaining a solid core within the stem for strength, the channel layout development for the prototype is presented in Figure 8-4. First a spline was fitted to the selected channel fill pattern and manually edited to fit inside the margin lines set for maintaining a wall thickness of 3 mm (based on conformal cooling channel designs (Armillotta et al., 2014) (Figure 8-4(a))). Therefore, at the channel openings, situated at the apices (which represent exit points) of the smoothed spline (Figure 8-4(b) and (c)), the effective margin is  $3 - (0.5 \times \text{channel diameter})$  mm. The remaining margin is thus the distance from an exit point of the channel to the surface. To avoid the channel running into itself, the maximum constant profile diameter was found to be  $\pm 2.5$  mm (Figure 8-4(d)). It was also ensured that the channel remained within the internal margin on the medial-lateral sides of the stem (Figure 8-4(e)).

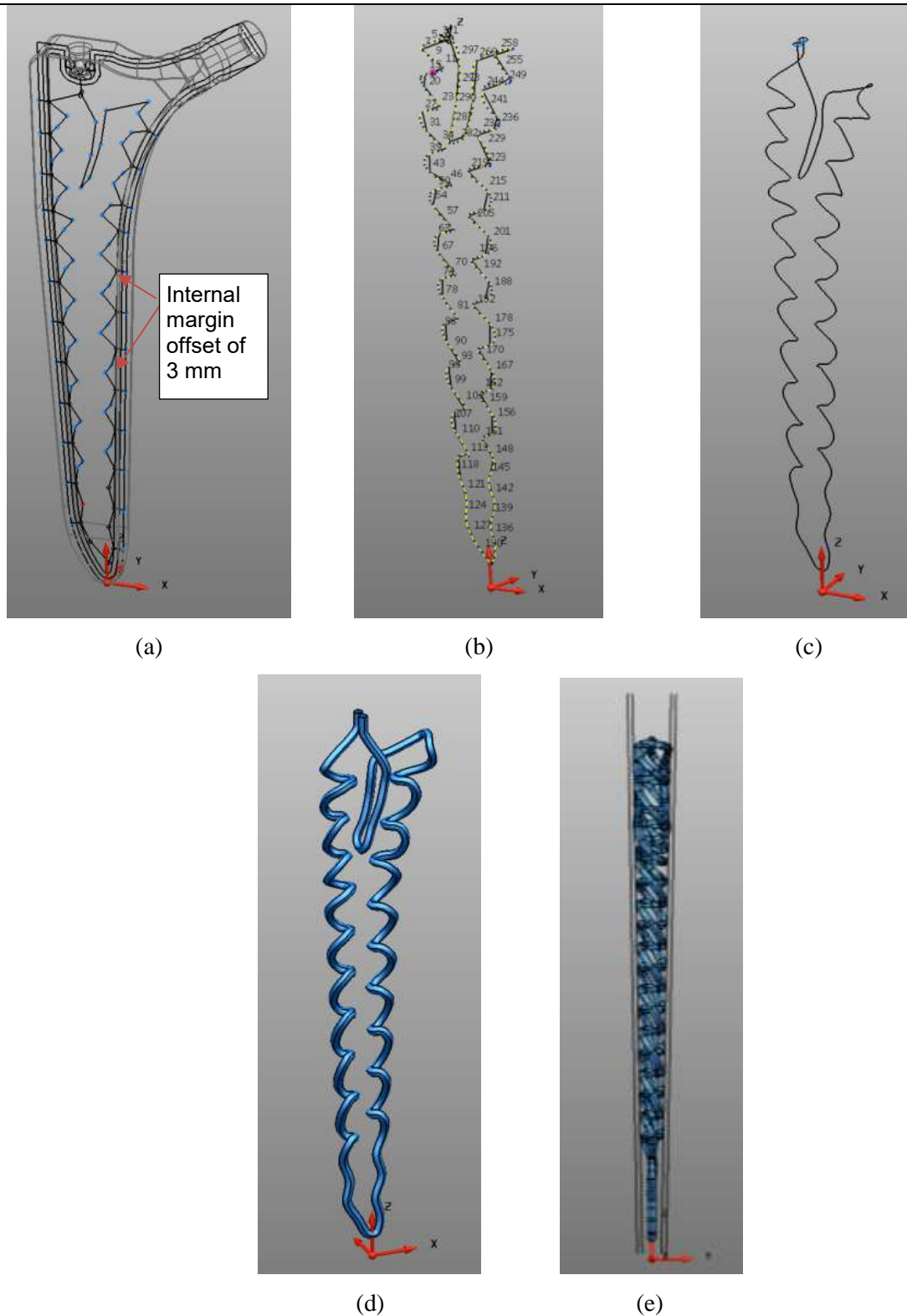


**Figure 8-4: Internal channel layout with (a) anterior-posterior view of channel fill variant, (b) reprinted spline, (c) smoothed spline with entry and exit points, (d) channel of constant 2.5 mm diameter, (e) medial-lateral view**

The *PowerSHAPE* software operates largely with Boolean operations for trimming, cutting, combining, or splitting solid models. Subsequently, the surface channel model was converted to a solid and ensured to be watertight. A cutter insert was then designed for the channel openings. A cutter was placed at each of the channel opening points and moved inwards to interfere with the stem perpendicular to its own work plane situated at the respective channel opening. This allowed control over the orientation of the curves leading into the margin and to the surface of the implant. Figure 8-5(a) shows the channel (converted to a solid for Boolean operations) with cutter inserts (cutter insert with dimensions showed in breakout image). The channel with cutters was then Boolean subtracted from the implant body, yielding the stem with integrated channel and openings (Figure 8-5(b)). The internal channel is designed with loading and extraction points in the recess where the surgeon impacts the implant during insertion (Figure 8-5). Utilising this area for channel main entry and exit theoretically provides the opportunity for reinforcing the existing drug, or extraction, rinsing, and loading of a different drug with minimally invasive procedures.

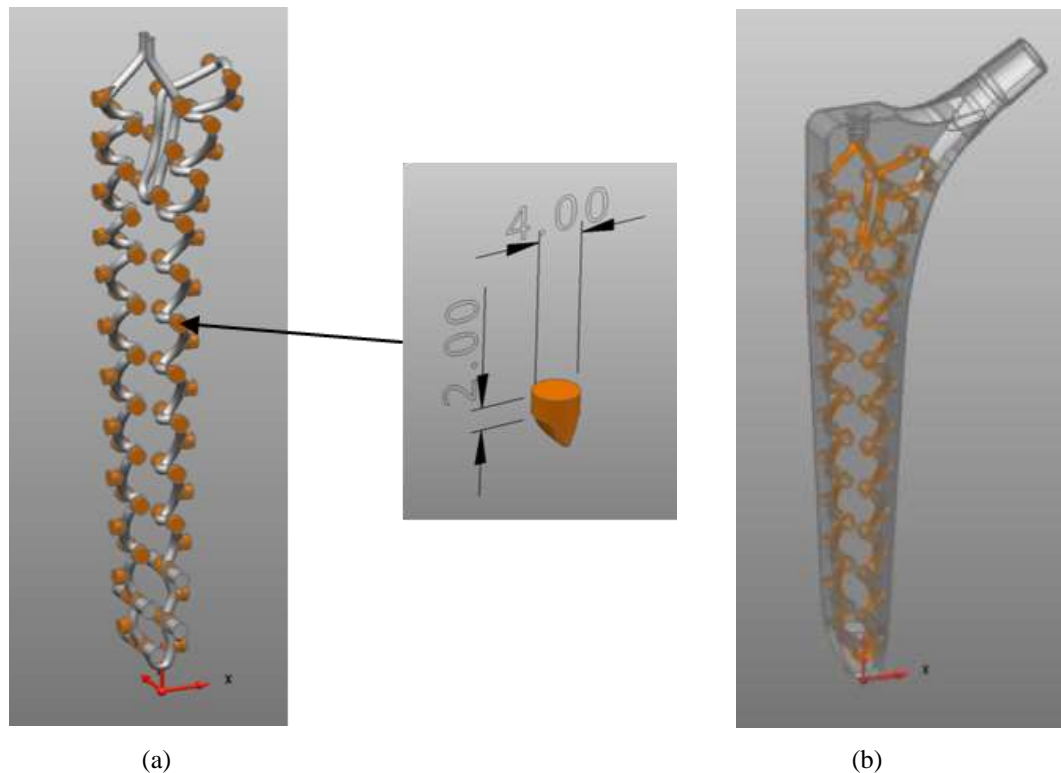
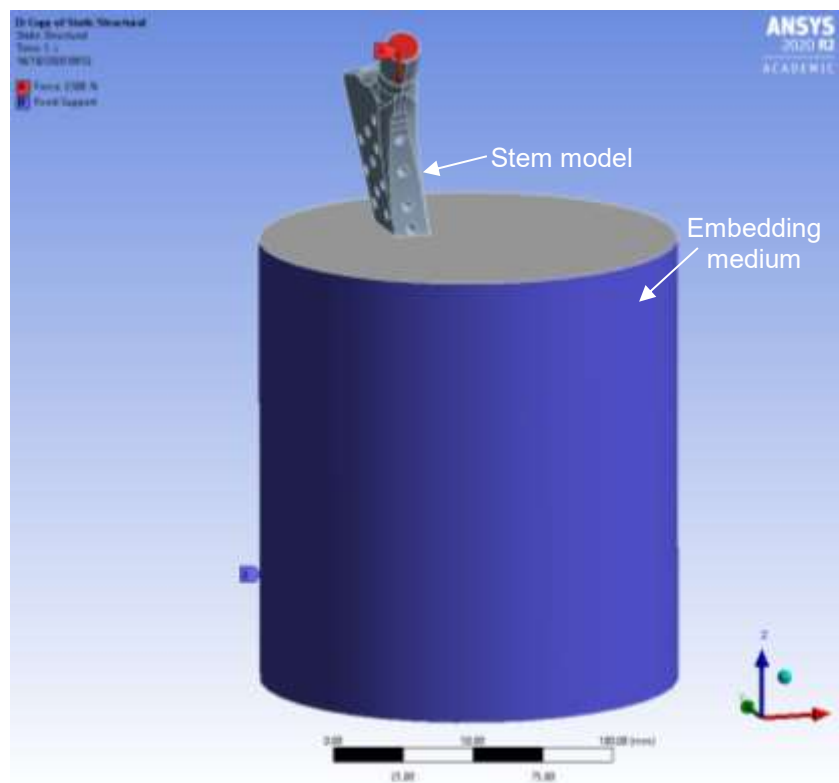


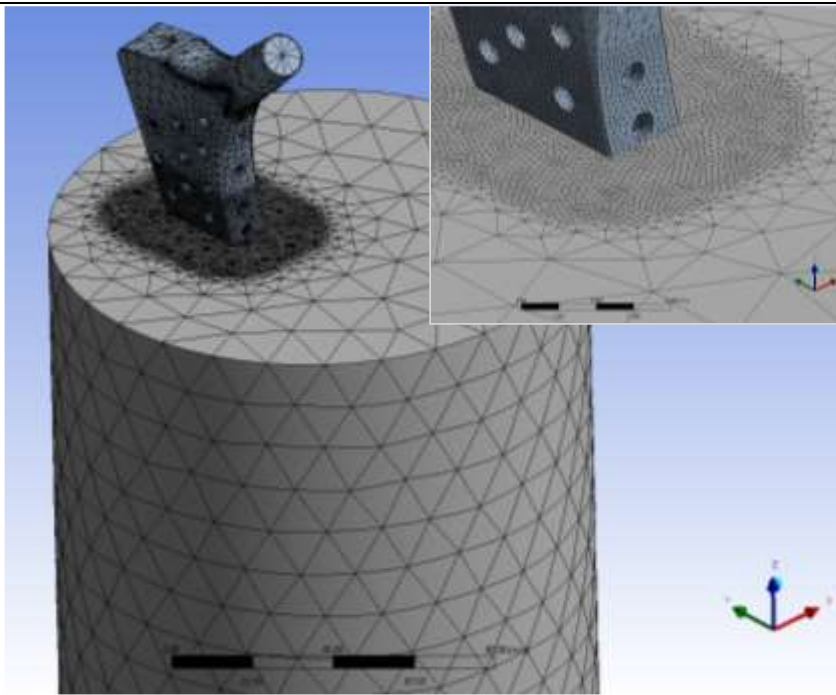
**Figure 8-5: Internal channel generation in hip stem with (a) channel solid model and cutter inserts and (b) hip stem solid model with internal channel**

### 8.1.4 Static Stress Analysis Simulation

The stem design was evaluated with a static stress analysis in *ANSYS 2020 R2* according to the orientation, load, and boundary conditions specified for fatigue testing in ISO 7206-4 – Orientation of specimen under test – Implant with no anteversion (ISO 7206-4:2002(E), 2002). Use of this international standard for static stress analysis was also regarded as a standardisation approach for design evaluations within the larger collaborative Intelligent Implants project. The orientation and load case applied to the cementless stem with internal channel model is presented in Figure 8-6(a). A load of 2.3 kN is applied to the face in contact with the femoral head in the negative z-direction (Ploeg et al., 2009) and the outer surfaces of the embedding medium are fixed. The tetrahedral (Tet10 elements) mesh is presented in Figure 8-6(b). Mesh refinement at the contact regions included reduction of element size and matching of the nodes of contacting elements between the two bodies (inset in Figure 8-6(b)). The resulting mesh consisted of 419,380 nodes and 267,485 elements. The material properties used for the stem model and the embedding medium are presented in Table 8-2.



(a)



(b)

**Figure 8-6: Prototype hip stem static stress analysis setup with (a) orientation, load, and boundary conditions of model and (b) mesh setup in ANSYS 2020 R2 with inset showing nodes matching at contact surfaces**

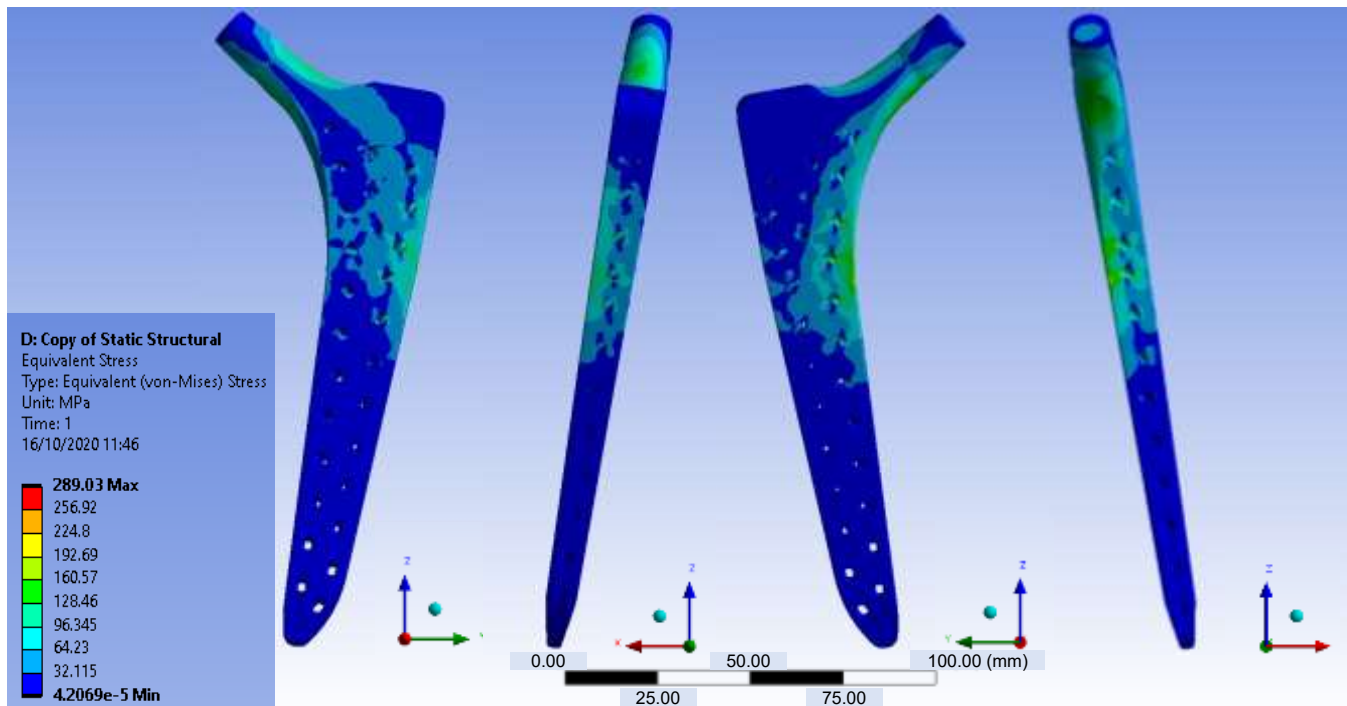
**Table 8-2: Material properties used in the static stress analysis simulation**

Material Reference	Property	Value
Ti6Al4V ELI	Density ( $\text{kg.m}^{-3}$ )	4430
(ASTM International, 2013)	Elastic modulus (GPa)	104.8
(Bari & Arjunan, 2019)	Poisson's ratio	0.32
(Hocking et al., 2019)	Tensile yield strength (MPa)	795
	Tensile ultimate strength (MPa)	860
	Compressive yield strength (MPa)	825
Embedding medium	Elastic modulus (GPa)	4.5
(ISO 7206-4:2002(E), 2002)	Poisson's ratio	0.35
(Kurtz et al., 2001)	Tensile ultimate strength (MPa)	35.3
(Lee, 2005)	Compressive ultimate strength	93.0

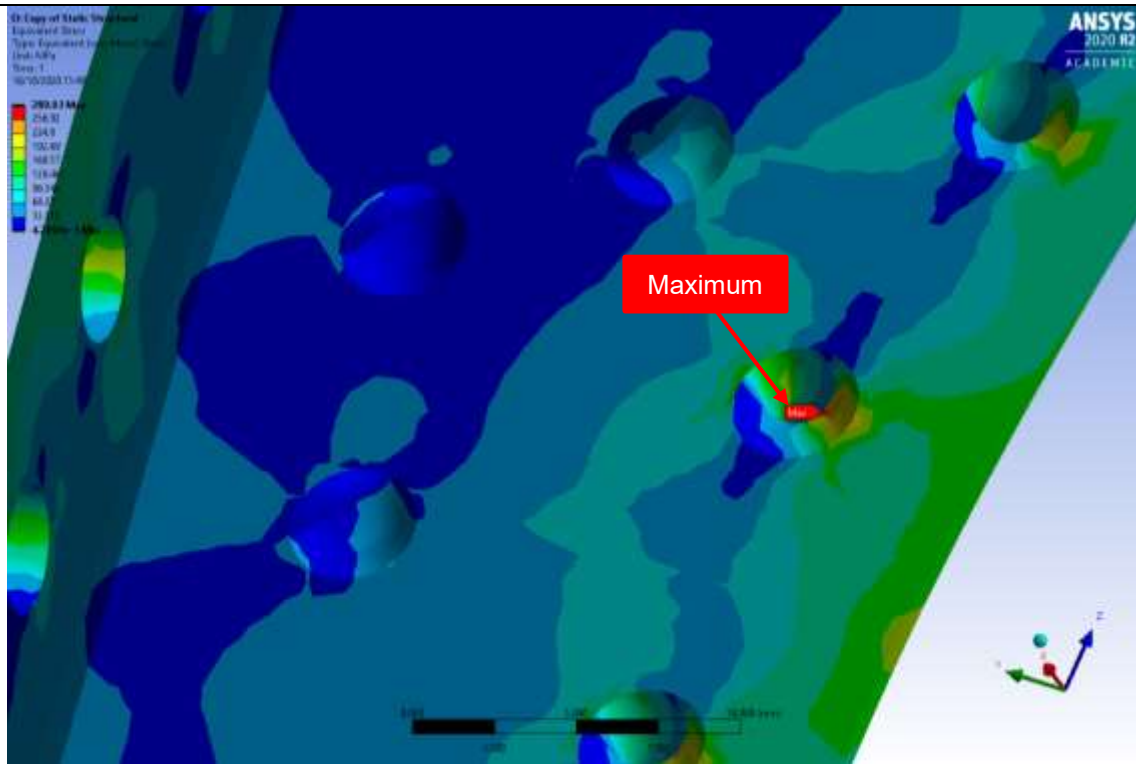
The von Mises equivalent stress and total deformation distributions resulting from the simulation are presented in Figure 8-7. The maximum von Mises equivalent stress (Figure 8-7(a)) is approximated as

289.03 MPa (compared to 156.97 MPa of the solid stem reference presented in Figure F2 in Appendix F), which is safely below the yield strength of wrought Ti6Al4V ELI, the benchmark material (795 MPa used as reference) as well as reported fatigue strengths for post processed LPBF-produced Ti6Al4V ELI (Li et al., 2016). Initial inspection of the simulation results revealed a possible concern regarding the current design which is the location of the areas of maximum simulated stress, visible in Figure 8-7(b).

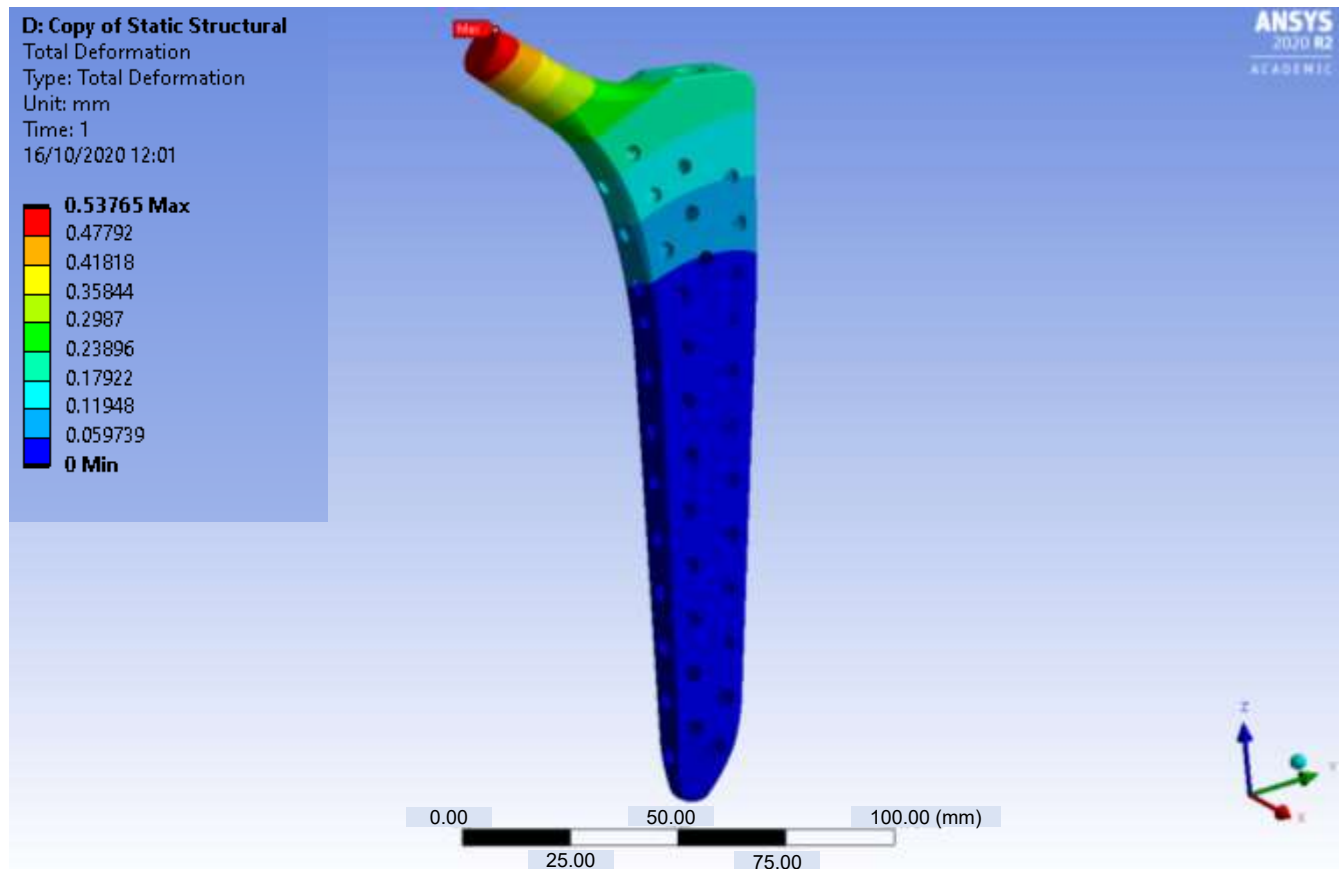
However, when regarding the total deformation in Figure 8-7(c), it can be observed that the simulated deformation in areas of maximum stress is low, in the range 0 – 0.06 mm (Figure 8-7(d)). Furthermore, the overall maximum total deformation is 0.54 mm, situated at the same site of that of the reference stem, which has a maximum simulated deformation of 0.45 mm (Figure F2 in Appendix F). The deformation distribution contours of the two stems are highly similar, suggesting that no large deformations are introduced to the stem with the internal channel design. Considering the simulation results with regard to the maximum stress and deformation distributions, the current design is deemed safe as a proof of concept with reference to the properties of wrought Ti6Al4V ELI. As stated previously, this study assumes that comparable properties can be obtained for LPBF-produced Ti6Al4V ELI and detailed investigations into the mechanical behaviour are outside of the scope.



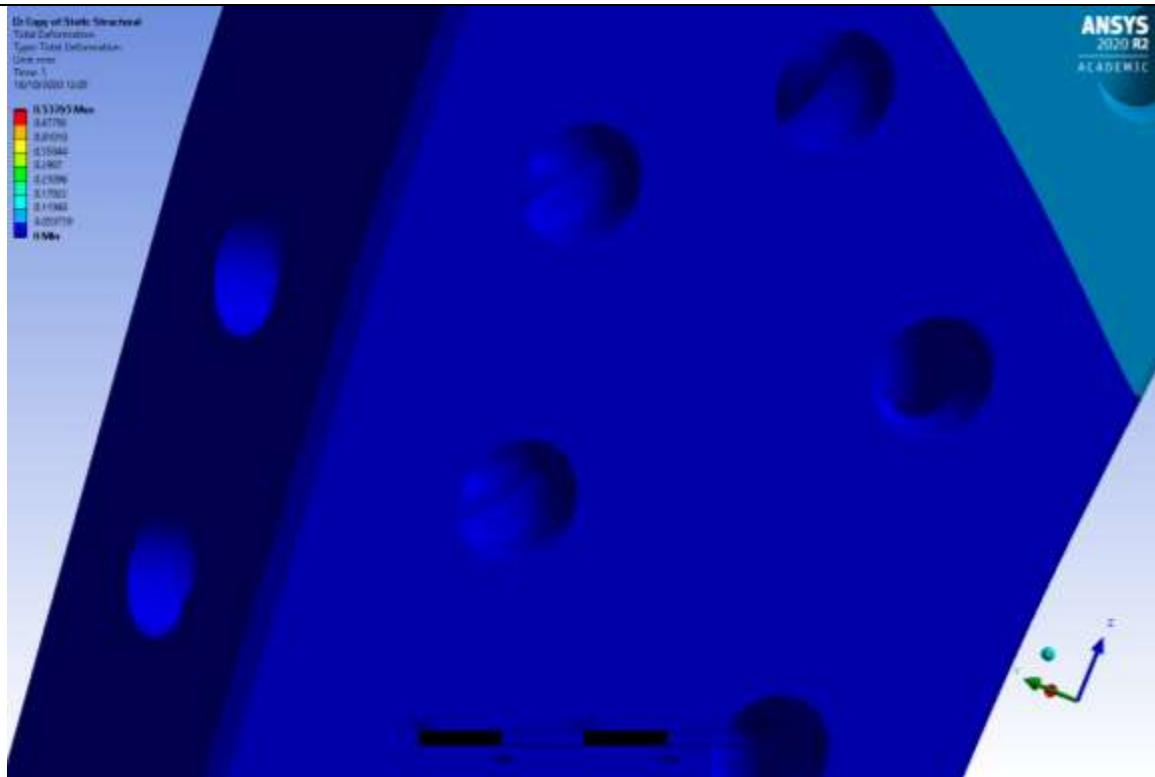
(a)



(b)



(c)



(d)

**Figure 8-7: Selected static stress analysis results with (a) full prototype model view, (b) view of maximum stress areas, and (c) total deformation approximation, and (d) zoomed view of total deformation in maximum von Mises equivalent stress area**

## 8.2 Implant Prototype Manufacture

### 8.2.1 First Iteration Prototype Fabrication

To produce an in-process assembly of the implant prototype with permeable structures, oversized discs of 1 mm thickness were placed at each channel opening, presented with the purple discs in Figure 8-8. The first manufacturing iteration involved the production of sections of the hip stem to demonstrate the internal geometry inside the proximal part while allowing for testing of loading and release screening of a blue dye to demonstrate the intended drug release capability through passive diffusion. The *Magics* build setup for the partial prototypes are presented in Figure 8-9(a) and the built parts in Figure 8-9(b). Splitting the proximal part in three sections, the interior surfaces are exposed and accessible for demonstration purposes. The distal stem parts were kept intact for the evaluation of antimicrobial efficacy with the addition of a foot piece to act as a jig to enable stable upright positioning.

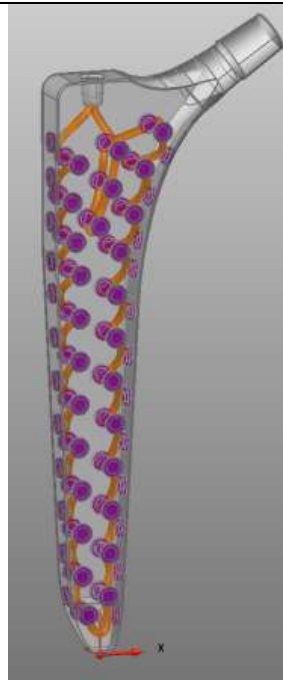
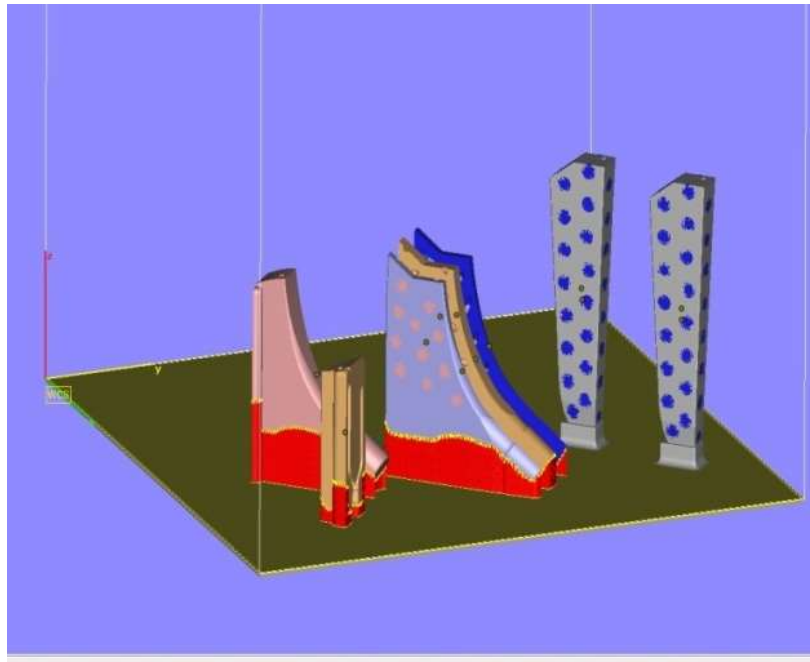
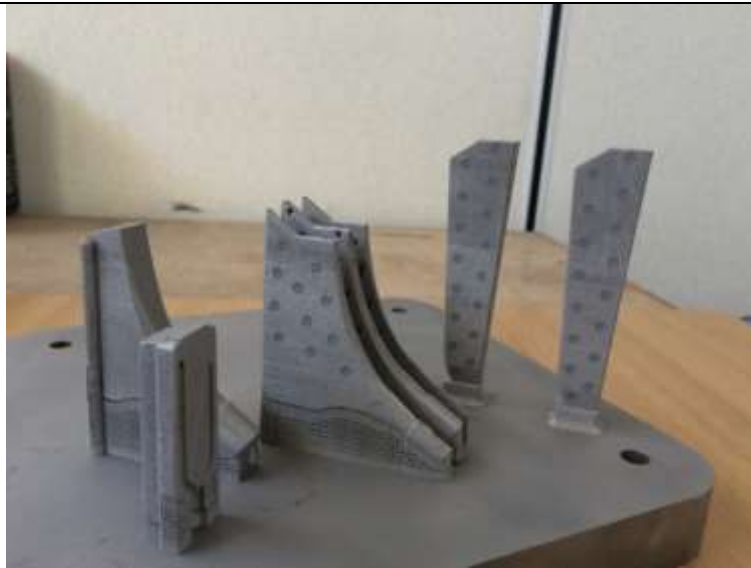


**Figure 8-8: Implant prototype CAD model with oversized individual permeable structures at channel openings**



(a)



(b)

**Figure 8-9: First iteration of LPBF prototype build with (a) *Magics* build setup and (b) actual parts.**

Solid parts were built with the default process parameters and permeable discs with PS-10 from Table 6-1. The support structure parameters are presented in Table 8-3 below.

**Table 8-3: First prototype build iteration support structure parameters**

<b>Support Parameters</b>	
<b>Hatching</b>	1 mm x 1 mm – no rotation
<b>Hatching Teeth</b>	
Height	1 mm
Top Length	0.5 mm
Base Length	1 mm
Base Interval	0.2 mm
<b>Fragmentation</b>	
X Interval	5 mm
Y Interval	5 mm
separation width	0.2 mm
<b>Border Teeth</b>	<i>Same as hatching teeth</i>
<b>Perforations</b>	
Beam	0.8 mm
Angle	60°
Height	1 mm
Solid Height	3 mm

### 8.2.2 Post Processing

Parts were removed with w-EDM. Removal of support remnants was done by hand. Reduction of surface roughness was done on the proximal parts for cosmetic purposes only as the parts were not subjected to mechanical testing. Silicon carbide sandpaper of various grit sizes (600 – 1200) was used for manual sequential grinding of the surfaces with support remnants using water as grinding fluid. Internal areas of the top sections were cleaned for demonstration purposes with an air drill and brass abrasive wheels.

Distal surfaces were kept in the as-built state (Figure 8-10) as the LPBF-produced mean surface roughness ( $11.99 \pm 3.49 \mu\text{m}$  measured at six randomly selected locations along the build direction) is advantageous for osseointegration (Maher et al., 2017). To remove unfused powder particles, parts were repeatedly cleaned with a sequence of compressed air and sonication in acetone, ethanol, and distilled water respectively, and air dried.

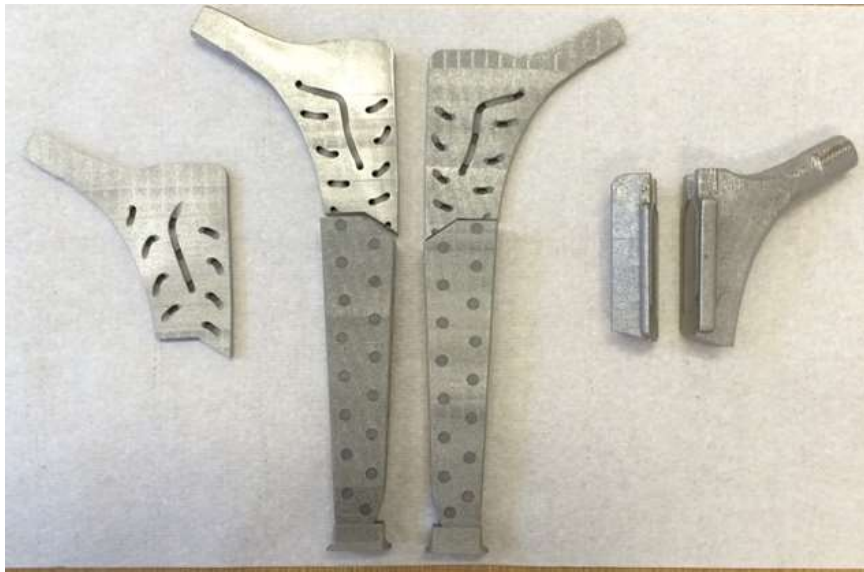


**Figure 8-10: First iteration prototypes for inspection and demonstration purposes**

### 8.2.3 Part Inspection

The main aspect for inspection was channel continuity and permeability of all PTWs. A qualitative demonstration has been performed with loading of a blue dye aqueous solution and passive diffusion through the PTWs into a reservoir containing distilled water (Figure 8-11). The aqueous dye solution was introduced with ease using a siphon method (Figure 8-11(a)). It was evident that no obstructions

existed within the channel and that all the channel openings could be sufficiently reached. The partial stem was then lowered into the distilled water reservoir (Figure 8-11(b)) and diffusion of the blue dye through all of the submerged PTWs continued unobstructed (Figure 8-11(c)).

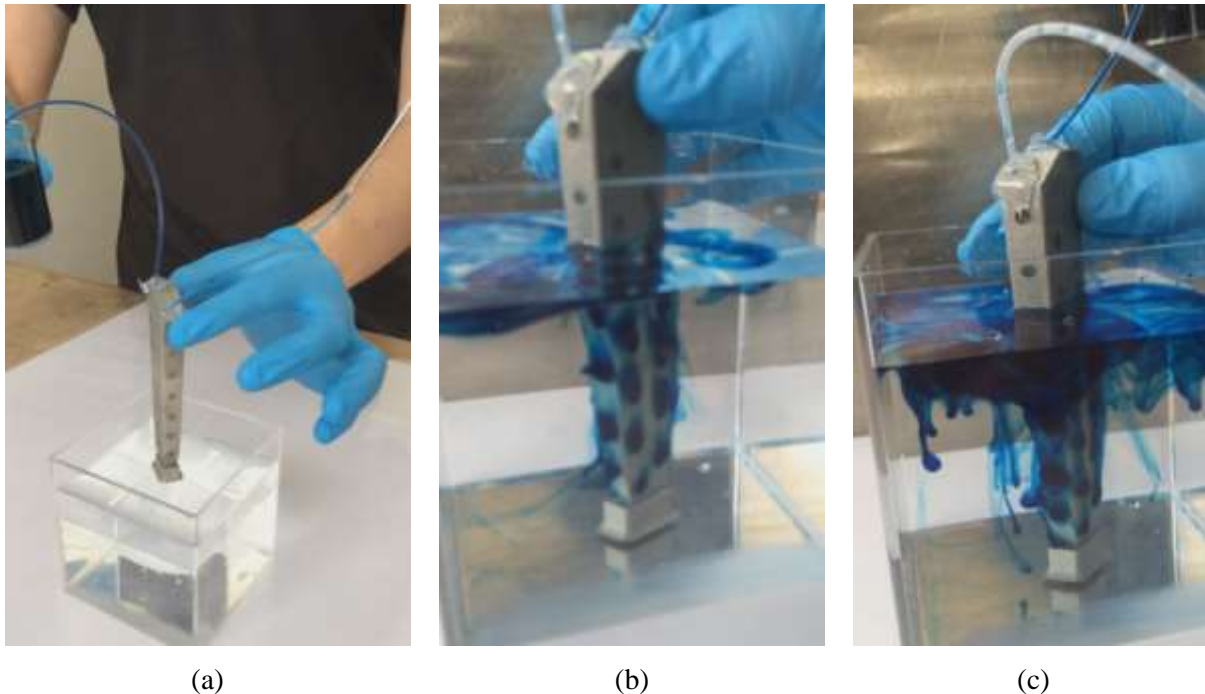


**Figure 8-11: Distal part of prototype blue dye diffusion screening with (a) dye loading, (b) stem immersion, (c) continued diffusion of blue dye**

### 8.3 Antimicrobial Testing of Prototype

#### 8.3.1 Experimental Setup and Design

The estimated channel volume within the partial stem was extracted from the 3D CAD model as ~ 3 mL. With reference to the vancomycin release and activity from integrated reservoirs discussed in Sections 7.2.2 and 7.2.3 the objective was to load the channel of the partial prototype with a vancomycin concentration which would near 1 mg per PTW channel opening. Considering the 47 PTWs in the partial prototype, the vancomycin concentration was rounded to 15 mg/mL (~45 mg of vancomycin) to yield a theoretical availability of ~ 957  $\mu\text{g}$  vancomycin per PTW. This approach was used as a guideline only and assumed total and even availability of the loaded vancomycin solution at the PTWs which in practice would not necessarily be the case. The physical setup for the vancomycin loading procedure is demonstrated in Figure 8-12.

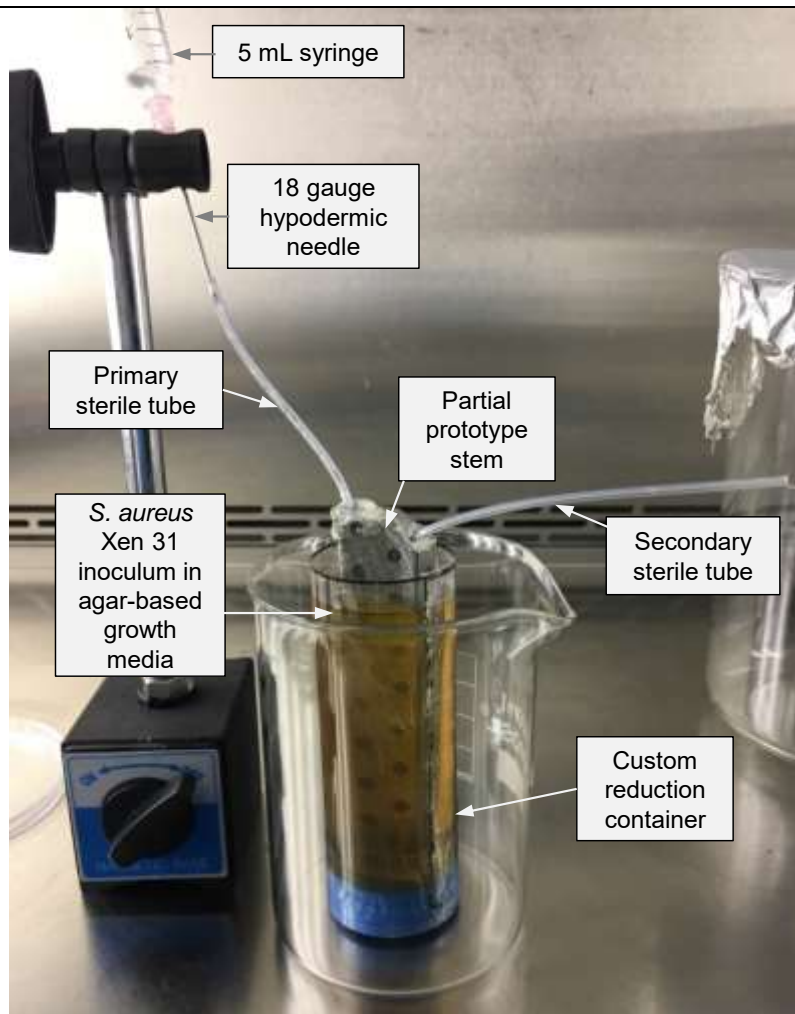
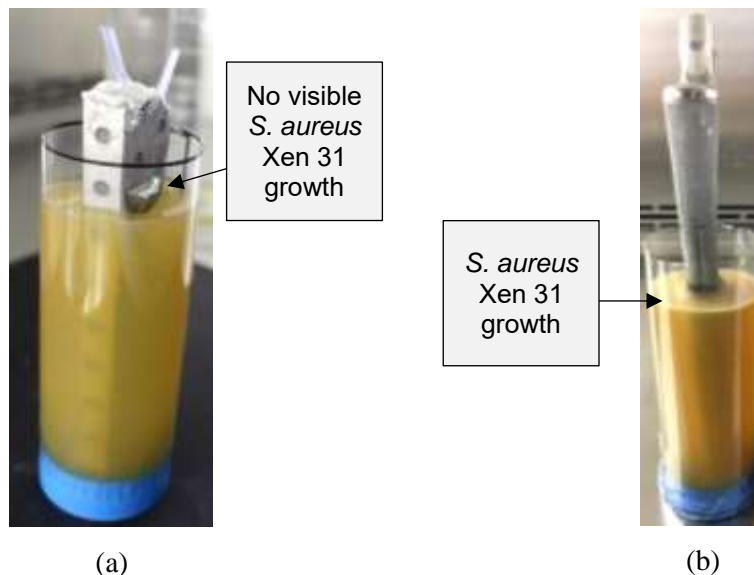


**Figure 8-12: Physical setup of vancomycin solution loading procedure**

A reduction container was made from cellulose acetate foil and placed inside a glass beaker. All equipment was sterilised by 70% ethanol and UV irradiation. Sterile tubing was fixed and sealed to the channel to enable loading of the vancomycin solution. A 5 mL syringe with an 18 gauge hypodermic needle was used to drop 3 mL of the 15 mg/mL vancomycin solution into the stem and an empty 5 mL syringe with an 18 gauge needle was connected to the secondary sterile tube (not present in Figure 8-12) to assist in removing air which may obstruct the flow of the vancomycin solution. Directly after introduction of the vancomycin solution the reduction container was filled with ~ 120 mL media containing an inoculum of *S. aureus* Xen 31 (MRSA strain) which was prepared by the Department of Microbiology with the same process as described in Section 6.2.2.2 and incubated at 37 °C for 24 hours. A retrieved commercial Ti6Al4V (ISO 5832-3 specification) cementless stem (the porous surface of  $Ra\ 15.66 \pm 1.44\ \mu\text{m}$  consists of plasma sprayed titanium and a hydroxyapatite coating) was kindly donated for research purposes and incubated with the same process as the prototype partial stem, but without any vancomycin to serve as a negative control.

### 8.3.2 Results

The prototype and commercial stems after 24 hours incubation are presented in Figures 8-13(a) and (b) respectively. Initial evaluation indicated that for the prototype stem no visible *S. aureus* Xen 31 growth was observed and subsequently, the results were treated in a qualitative manner to demonstrate the antimicrobial functionality of the partial prototype. The growth media surrounding the prototype stem had an absence of the typical observations for *S. aureus* Xen 31 proliferation on the top surface (Figure 8-13(a)), with the contrary observed for the commercial stem in Figure 8-13(b) as indicated by the annotations. Furthermore, when qualitatively considering the turbidity of the growth medium which increases with bacterial growth, visibility through the growth medium was noticeably greater for the prototype stem than for the commercial stem. In Figure 8-13(c) details such as the PTWs and the chamfer on the corner of the prototype stem are clearly distinguishable. In comparison, the embedded part of the commercial stem in Figure 8-13(d) is only visible as an indistinguishable dark mass and no features on the stem can be clearly identified. The lack of bacterial growth for the prototype stem is visually observed throughout the entire media surrounding the stem after removal of the stem (Figure 8-13(e)). For the commercial stem, *S. aureus* Xen 31 growth can be observed in the media surrounding the stem (Figure 8-13(e)). These observations corroborate both observations regarding bacteria proliferation on the top of the media as well as the differences in visibility related to the resulting turbidity caused by the absence and presence of *S. aureus* Xen 31 in the surrounding media of the prototype and commercial stems respectively. It is therefore concluded that vancomycin was effectively released from the prototype stem to prevent colonisation by *S. aureus* Xen 31.



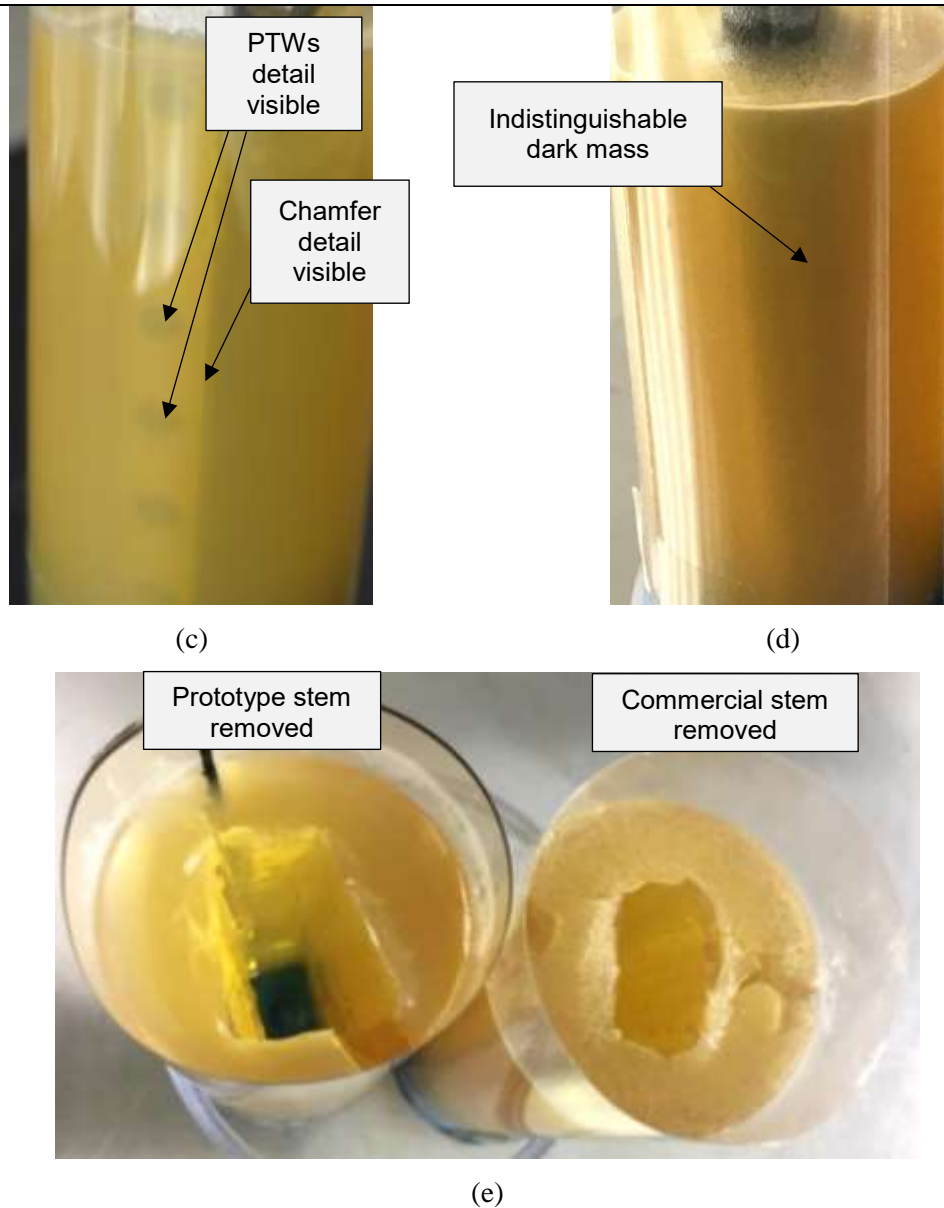


**Figure 8-13: Photographs after 24 hours incubation of (a) prototype stem, (b) commercial stem, (c) enlargement of prototype stem, (d) enlargement of commercial stem, (e) surrounding media of prototype and commercial stem visible after stem removal**

#### **8.4 Conclusion**

This chapter presented the design, manufacturing, and colonisation prevention potential testing of the prototype cementless hip stem. The process involved recombination of the preceding partial solutions to generate an overall solution which has effectively addressed the overall problem. Considering reports of 2 g vancomycin powder distribution in open wounds during THA (Heckmann et al., 2019),

the antibiotic resource consumption could potentially significantly be lowered through the concept developed in this study. The main conclusions are summarised as follows:

- A method has been developed to design an internal reservoir based on ZOI of the target pathogen and antibiotic combination. It could be defined as a circle packing problem for the minimum amount of circles of constant radius required to cover an arbitrary geometry. Therefore, a pseudo hexagonal approach was utilised.
- Based on a static stress analysis, the design was considered safe. However, fatigue testing would be required to truly determine this. This was outside of the scope due to the focus being on antimicrobial efficacy.
- The demonstrator components were manufacturing in-house using a basic LPBF process chain. The internal reservoir was open throughout and did not obstruct flow of aqueous solutions.
- Recomposition of partial solutions from the systematic investigation into LPBF for PTWs in Chapters 5-7 amounted to specifying PTWs which were successfully fabricated and assembled in-process. All PTWs were highly permeable when inspected with blue dye.
- A custom setup was developed to evaluate the potential for colonisation prevention of an MRSA strain. The demonstrator released vancomycin in sufficient concentrations to effectively prevent growth or subsequent surface colonisation of the prototype by *S.aureus* Xen 31.
- This provides a platform from which further research can be conducted regarding the optimisation of drug and device combination.

## 9. Framework Update and Implementation

This chapter presents an updated version of the high-level overall problem solving framework presented in Chapter 3. The implementation of the framework within the specifics of this study is then demonstrated in a table format. It provides a summary of the collaborative effort and the integrated concepts developed during the project to yield an overall solution prototype for prevention of cementless hip stem surface colonisation by pathogenic bacteria.

### 9.1 Updated Interdisciplinary Problem Solving Framework

The high-level overall problem solving framework consisting of five levels as presented in Figure 3-2 has been revised within the context of this study and is presented in Figure 9-1. The original five levels are now indicated with the shaded pillars. Each pillar is detailed with process steps with the aim of yielding an integrated outcome for input to the following level (indicated with the shaded document flowchart objects below the process steps). For the decomposition of partial and single problems, as well as the recomposition of single solutions to partial problems, the steps should be applied to each identified partial and single problem. Where possible, the single problems should be addressed concurrently to increase efficiency and provide real time information for the evaluation of interfacing and integration adequacy. Trade-offs and potentials identified as well as IKPs should be documented and stored with access for future projects.

The updated overall framework is considered to be a product of both a deductive and inductive process. Initially, a high-level framework was derived from literature to serve as a point of departure. During execution of the various interdisciplinary aspects of this project, each part of the overall problem was decomposed to partial and single problems. Within each of these problems, with the exception of the vancomycin sustained release alternative, an integrative approach from the main perspective of the LPBF was followed.

Recomposition of solutions to single problems thus does not blindly assemble generated elements to a functional whole, but strives to impart an IKP at each of these processes. This further aims to continuously develop creativity and innovation within each of the collaborative disciplines as project members are exposed to knowledge areas outside of their traditional focus area and perspective.

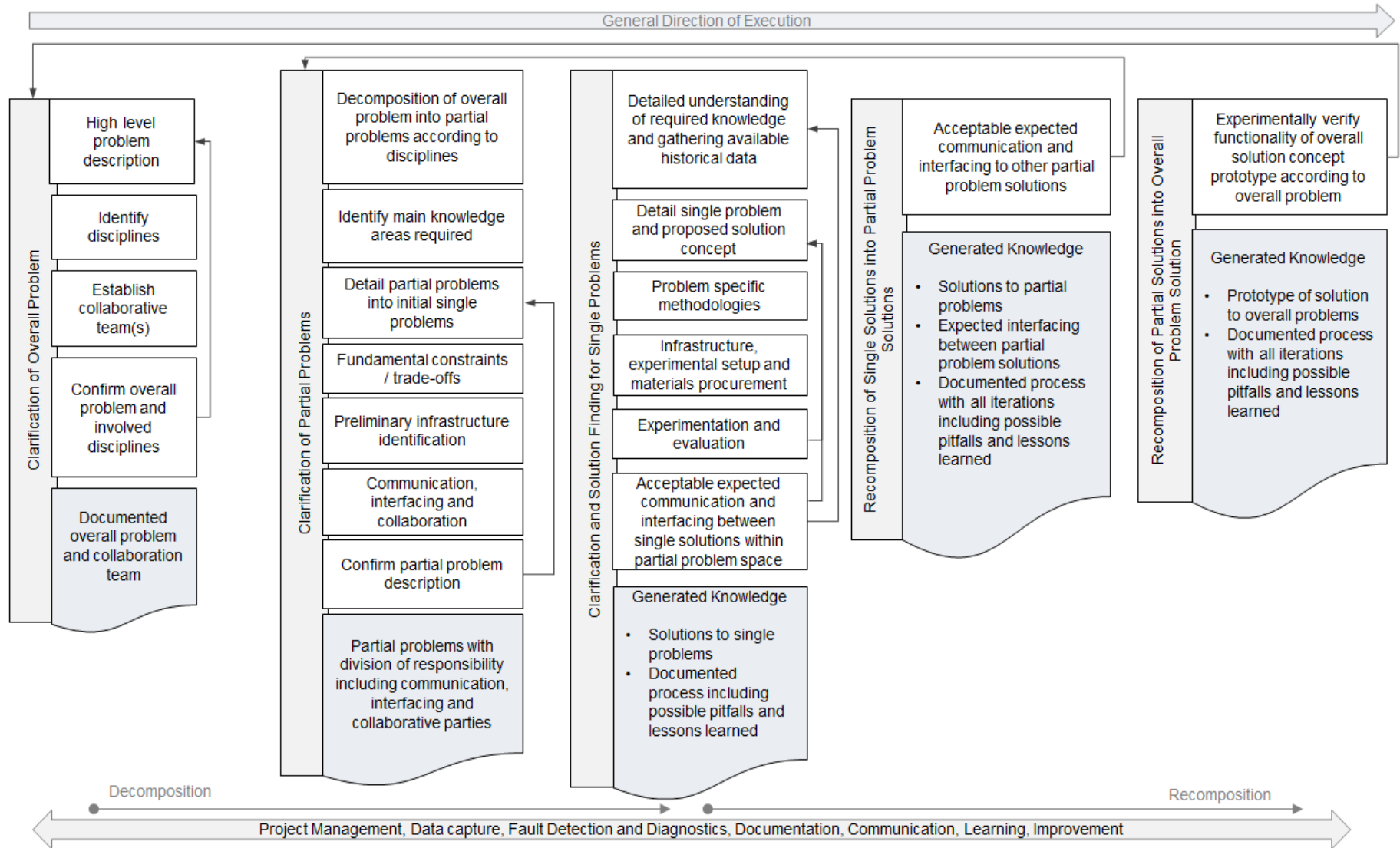
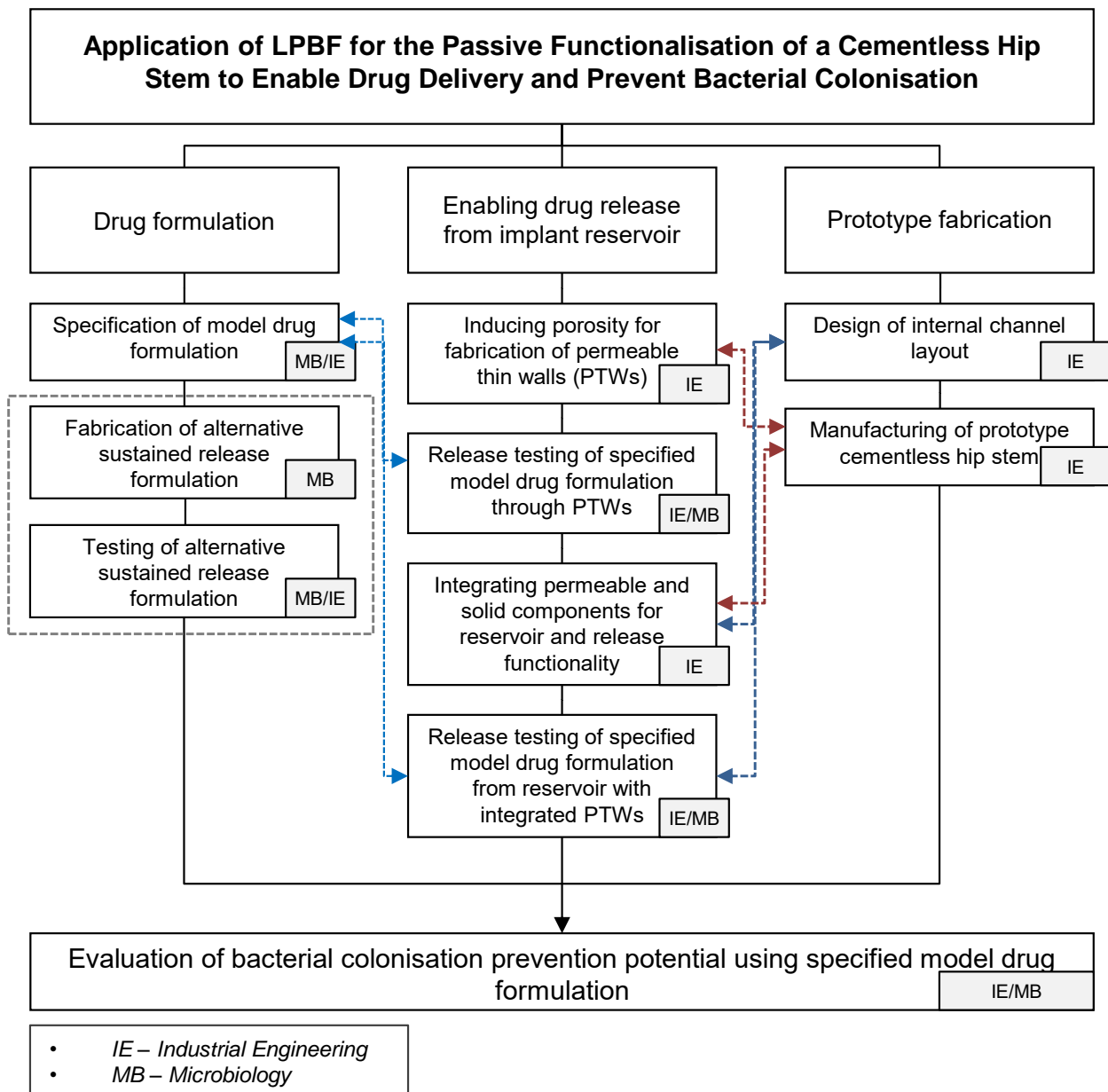


Figure 9-1: Updated overall framework

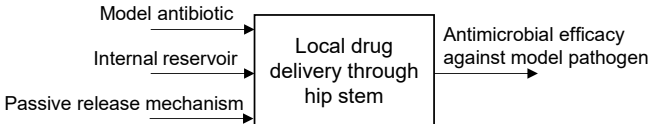
## 9.2 Framework Implementation Summary

As indicated in the framework, the implementation is based on the breakdown and clarification of overall, partial, and single problems. The initial problem breakdown structure is updated with communication lines between single problems and presented in Figure 9-2. Interdisciplinary communication was therefore essential in execution of the single problems. A summary of the framework implementation is presented in Table 9-1.



**Figure 9-2: Communication lines that developed between single problems during execution of the project**

**Table 9-1: Summary of overall framework implementation**

Level	Work Step	Team Member	Activity	Outcome
1 Clarification of Overall Problem	High level problem description	IE	Literature review and proposal for project based on high level description of overall problem and proposal of potential solution concept	<p>Description of problem of bacterial colonisation and biofilm formation of surfaces of cementless hip stems</p> <p>Proposal of research opportunity into identified potential overall solution concept of utilising LPBF for the production of implants with drug delivery functionality to prevent colonisation of the surface by a bacterial pathogen</p>  <pre> graph LR     MA[Model antibiotic] --&gt; LDD[Local drug delivery through hip stem]     IR[Internal reservoir] --&gt; LDD     PRM[Passive release mechanism] --&gt; LDD     LDD --&gt; AEA[Antimicrobial efficacy against model pathogen]   </pre> <p>Overall problem title: “Application of LPBF for the Passive Functionalisation of a Cementless Hip Stem to Enable Drug Delivery and Prevent Bacterial Colonisation”</p>
	Identify disciplines	IE	Approach departments and researchers with result from high level problem description to discuss collaboration opportunity.	Initial meetings between IE and MB regarding potential collaboration. Establishment of commitment and confirmation of feasibility to engage in the formal project proposal writing process.
	Establish collaborative team	IE/MB	In depth discussion of a collaboration commitment including initial budget requirements	Collaborative commitment between IE and MB: <ul style="list-style-type: none"> <li>• Two professors from IE</li> <li>• One professor from MB</li> <li>• One research student from IE</li> <li>• One research student from MB</li> </ul>
	Confirm overall problem and involved disciplines	IE/MB	Revision of problem description and involved disciplines - a single party may be able to account for more than one discipline	Confirmation of overall problem, involved disciplines and a suitable collaboration team for project execution. Agreement on preliminary high level budget and project time frame.

2. Clarification of Partial Problems	Decomposition of overall problem according to disciplines into partial problems	IE/MB	High level definition of partial problems and responsible members – first listed member takes main responsibility where responsibility is shared	MB/IE: Drug formulation IE/MB: Enabling drug release from implant reservoir IE: Prototype fabrication
		IE/MB	Breakdown of overall problem into specific disciplines present at the university	Manufacturing engineering Microbiology Polymer science
	Identify main knowledge areas required	IE/MB	Within each discipline, a literature review was done to identify key knowledge areas	Knowledge areas listed in Table 3-1
	Detail partial problems into initial single problems	IE/MB	Initial single problems were collaboratively defined for each of the partial problems to map out the objective logic towards obtaining a prototype solution for each partial problem. The specific methods and infrastructure required are not yet defined at this point.	Problem breakdown structure for overall problem, partial problems, and single problems (Figure 3-6)
	Fundamental constraints / trade-offs	IE/MB	Evaluation of work breakdown structure and identification of early fundamental constraints to aid in establishing initial boundaries for the solution search space	<ul style="list-style-type: none"> <li>• Model pathogens are strains of <i>S. aureus</i></li> <li>• Model drug formulation is aqueous vancomycin</li> <li>• Cementless hip stem (no head or cup)</li> <li>• Main manufacturing technology is LPBF</li> <li>• Feature size limitations of LPBF machine</li> <li>• Trade-off between formulation and demonstration of drug release from implant: at MB a sustained release vancomycin formulation was being developed while concurrent evaluations of drug release functionality of manufactured components at IE were done with aqueous vancomycin solutions at MB</li> </ul>

Preliminary infrastructure identification	IE/MB	Deeper evaluation of initial single problems within partial problems and identification of available infrastructure and feasibility of executing the work within the high-level budget limitations. Identified infrastructure can be available within the department, the university (other departments or analytical services), or third party, subject to the necessary non-disclosure agreements and costs.	<p><u>Within departments:</u></p> <ul style="list-style-type: none"> <li>• CAD, CAM, and CAE software</li> <li>• LPBF machine and material</li> <li>• Fused deposition modelling (FDM) machines</li> <li>• EDM wire cutter</li> <li>• Sandblaster</li> <li>• General power and hand tools</li> <li>• General microbiology laboratory equipment and consumables</li> <li>• BCA assay machine</li> <li>• HPLC machine and column</li> <li>• Optical microscopes</li> </ul> <p><u>Within university:</u></p> <ul style="list-style-type: none"> <li>• SEM facility</li> <li>• UHPLC facility</li> <li>• CT-scanning facility</li> <li>• Particle size analysers</li> </ul>
Communication, interfacing, and collaboration	IE/MB	From the initial problem structure, collaboration team members should identify and discuss the potential information flow between partial problems as well as required collaborative work efforts. The specifics regarding the collaborative work efforts are elucidated at the single problem stage.	<p>All partial problems interact.</p> <p>Drug formulation and Enabling release from implant reservoir:</p> <ul style="list-style-type: none"> <li>• PTWs were evaluated and specified for prototype based on tests with model drug formulation</li> </ul> <p>Drug formulation and Prototype fabrication:</p> <ul style="list-style-type: none"> <li>• Drug formulation should be introducible to prototype and sufficiently reach all channel openings</li> </ul> <p>Enabling drug release from implant reservoir and Prototype fabrication:</p> <ul style="list-style-type: none"> <li>• Developed PTWs were integrated into the actual prototype with an in-process assembly strategy</li> </ul>
Confirm partial problem description	IE/MB	Meetings to review preceding outcomes and compile a project proposal document.	The results from steps were above were consolidated into a project proposal document for evaluation by the project funders.

3. Clarification and Solution Finding for Single Problems	3.1 Specification of model drug formulation, Gain insight and specify materials for alternative formulation; Fabrication of alternative sustained release formulation, Testing of alternative sustained release formulation	Detailed understanding of required knowledge and gathering of available historical data	MB/IE	Specification of clinically relevant antibiotic and literature review on sustained release formulations of the identified; Study models for understanding polymer erosion to gain a functional understanding	Sections 2.2 and 4.1
		Detail single problem and proposed solution concept	MB/IE	Evaluate literature and propose a solution concept; adapt a computer simulation from literature to improve understanding of polymer erosion	For model drug formulation, release from the implant prototype and antimicrobial efficacy were evaluated with an aqueous vancomycin solution  For a sustained release alternative, a PLGA nanoparticle formulation was proposed as solution concept  A stochastic simulation program aids in the visualisation and functional understanding of PLGA bulk erosion
		Problem specific methodologies	MB/IE	Problem specific methodologies where available were identified from literature. Where literature did not provide clear guidelines, custom experimental setups were developed to allow experimentation.	Section 4.2
		Infrastructure, experimental setup, and materials procurement	MB/IE		Further details available in (Booyesen et al., 2019)
		Experimentation and evaluation	MB/IE		
		Acceptable expected communication and interfacing between single solutions within partial problem space	MB/IE	Evaluate results in terms of communication and interfacing with each other.	The prototype was required to release vancomycin formulated as an aqueous solution.  The alternative sustained drug formulation was developed as an independent branch to demonstrate that vancomycin could be supplied to a reservoir for an extended duration.

3. Clarification and Solution Finding for Single Problems	3.2 Inducing porosity for PTWs; Drug release through PTWs; Integration of PTWs, Drug release from reservoirs with integrated PTWs	Detailed understanding of required knowledge and gathering of available historical data	IE/MB	Literature was reviewed regarding inducing porosity with the LPBF process for drug delivery application	Little to no available literature on the specific LPBF application of inducing porosity to fabricate PTWs for drug delivery (Section 2.3.4), signalling an opportunity and the need for pilot experimentation to generate data for refinement of experiments.
		Detail single problem and proposed solution concept	IE/MB	Using available literature as a guide as well as LPBF process knowledge a solution concept was mapped out	Utilising the LPBF process to induce porosity with tailored process parameter settings and in-process of components using interference geometry for separate components and effectively a remelt strategy at geometric overlaps.
		Problem specific methodologies	IE/MB	Applicable methodologies were both identified from literature and drawn from in-house experience. Some trial and error approaches were required to develop custom experimental setups for vancomycin release testing.	Chapters 5, 6, and 7
		Infrastructure, experimental setup, and materials procurement	IE/MB		
		Experimentation and evaluation	IE/MB		
		Acceptable expected communication and interfacing between single solutions within partial problem space	IE/MB	Evaluate results in terms of communication and interfacing with each other.	The interfacing between PTWs and solid reservoirs for the release of vancomycin from an aqueous solution was deemed acceptable. Care should be taken to the placement of PTWs and potential effects on the accumulation of stresses. Although an in-depth investigation of this was outside the scope of this study, circular geometries in the dimensional ranges used were fabricated without cracks at the assembly interfaces.

3. Clarification and Solution Finding for Single Problems	3.3 Design of internal channel layout and manufacturing of demonstrator prototype cementless hip stem	Detailed understanding of required knowledge and gathering of available historical data	IE	Literature review on ZOI for vancomycin against <i>S. aureus</i> strains; Review of LPBF design guidelines; Studying LPBF machine specifications and capabilities; studying LPBF process chain	Categorised knowledge to utilise for detailing the proposed solution concept.
		Detail single problem and proposed solution concept	IE	Conversion of categorised knowledge for a strategy to design and manufacture the demonstrator prototype cementless hip stem	Strategy for the design of the channel layout (Section 8.1) and for the manufacturing of a demonstrator prototype cementless hip stem (Section 8.2)
		Problem specific methodologies	IE	Sections 8.1 and 8.2	Sections 8.1 and 8.2
		Infrastructure, experimental setup, and materials procurement	IE		
		Experimentation and evaluation	IE		
		Acceptable expected communication and interfacing between single solutions within partial problem space	IE	Evaluate design and manufacturing outcome in terms of communication and interfacing with each other.	The design of the prototype solution was fabricated with LPBF for a physical demonstrator model.

4. Recomposition of single solutions into Partial problem solutions	Acceptable expected communication and interfacing to other partial problem solution	IE/MB	Evaluate if partial problems are adequately fulfilled and integrated	Partial problems are fulfilled and no conflicts regarding integration were detected
5. Recomposition of partial solutions into overall problem solution	Experimentally verify functionality of overall solution concept prototype according to overall problem	IE/MB	Custom experimental setup to evaluate functionality of overall prototype solution (Section 8.3)	<i>S. aureus</i> Xen 31 (MRSA) was successfully prevented from colonising the demonstrator stem surface (Section 8.3) confirming the efficacy of the overall solution prototype

## 10. Conclusion and Future Research

The research presented aimed at contributing a prototype strategy for the prevention of periprosthetic joint infection (PJI) in the context of cementless hip stems by utilising the capabilities offered by metal additive manufacturing (MAM). This required an interdisciplinary approach. Therefore, in order to support the research aim, a framework was developed for systematic interdisciplinary problem solving from a laser powder bed fusion (LPBF)-centred perspective. An overall problem for investigation was defined as “*Passive Functionalisation of a Cementless Hip Stem Inner Structure to Enable Drug Delivery and Prevent Bacterial Colonisation*”. Using the high-level framework, the overall problem was decomposed into partial and single problems which were systematically investigated through further literature study and experimentation. The prototype solutions obtained for each single problem were recomposed for solutions to partial problems, which were finally recomposed to an overall prototype solution. This study therefore encompassed deductive as well inductive approaches as insights gained during the systematic problem solving were utilised to update the framework for a generically applicable detailed procedural representation. This project formed part of a larger international interdisciplinary collaborative project towards the development of intelligent implants under the lead of the Fraunhofer Institute for Machine Tools and Forming Technology (IWU).

A significant gap was identified between external and internal drug delivery strategies in research where external refers to the surface and internal to the incorporation of reservoir structures within the bulk of the implant. The systematic study and investigation of LPBF for an internal local drug delivery strategy resulted in the successful prevention of bacterial colonisation onto a prototype cementless hip stem surface, confirming that the research objectives were achieved. The original contributions of the study can be summarised in two main categories corresponding to the experimentation and framework development phases respectively.

In the first case, this involves the systematic application of LPBF to enable drug delivery from cementless hip stems and secondly, an LPBF-centred approach for interdisciplinary problem solving to develop an effective prototype solution for prevention of implant bacterial surface colonisation. It directly addressed the research gap in order to contribute to local drug delivery strategies for cementless implants. It also contributes to the advancement of LPBF as manufacturing technology by demonstrating the efficacy of the prototype solution. The contributions in this case can be summarised as follows:

- A method has been developed to directly integrate PTWs with dense components through an in-process assembly technique. Oversizing the components enables a re-melt at the interfering dimensions. This enables the production of in-process assemblies of components built with different process parameters without the need for expensive aftermarket software modules.
- A process window was developed for LPBF fabrication of permeable thin walls (PTWs) Ti6Al4V ELI structures based on lowering of the volumetric energy density (VED) through suitable values for laser power and scanning speed. Pores resulting from intermittent melting and sintering due to insufficient energy input are evenly distributed and interconnected to enable vancomycin diffusion across the PTWs. The process window constitutes a VED range of  $\sim 10 - 20 \text{ J}\cdot\text{mm}^{-3}$ . It is however subject to the specific LPBF system and should be adapted accordingly.
- VED as a criterion, however, should be considered in conjunction with the individual process parameters, especially at processing boundaries. At the lower processing boundary laser power became the main factor. Within the investigated ranges laser power had a significant effect on the resulting pore size and interconnectivity.
- For  $400 \mu\text{m}$  PTWs vancomycin release profiles from an aqueous solution could be altered by the induced porosity from constraint to near-free diffusion at a relative porosity above 21.17% (VED of  $13.89 \text{ J}\cdot\text{mm}^{-3}$ ).
- Pore shapes are irregular with constricting dimensions below  $50 \mu\text{m}$ , which is significantly smaller than pore sizes obtainable on current commercial LPBF machines with lattice structures and full density process parameters.
- The PTW structure can be altered from hydrophobic due to a Cassie-Baxter wetting state to highly hydrophilic by increasing the thickness of the PTW within the investigated range of  $0.4 - 1.5 \text{ mm}$ .
- Vancomycin released from Ti6Al4V ELI PTWs produced with LPBF retains its antibiotic efficacy.
- A method has been developed to design an internal reservoir for antimicrobial drug delivery based on the zone of inhibition of the target pathogen and antibiotic combination.
- The manufactured cementless hip stem released vancomycin effectively to prevent surface colonisation by *S. aureus* Xen 31, confirming the efficacy of the developed drug delivery strategy.

In the second case, a framework for interdisciplinary problem solving was developed that guided the creation of an LPBF-centred process chain aimed for enabling local drug delivery from cementless hip stems. During the conceptualisation phase of an LPBF-centred project, the interdisciplinary nature can be underestimated, especially the required depths of understanding within each of the involved disciplines. The framework can be used to provide insight for potential manufacturers into the necessary skills requirements for such projects. Due to its intended level of genericity, the framework can be adapted for other interdisciplinary overall problems based on the enabling technology through which the solution must be integrated. The framework promotes the continuous build of experience and lateral approaches spanning across disciplines. This has benefits specifically pertaining to finding customised solutions for experimental setup and infrastructure requirements within research organisations.

Through the research presented in this thesis, possible areas for further investigation and development have been identified. These are summarised as follows:

- Evaluation of the mechanical properties of PTWs in comparison to designed lattice structures to develop application limitations regarding load-bearing environments.
- The capillary action of the PTWs can be researched for wicking applications such as heat pipes. It can also be investigated for tissue engineering as capillary action may drive nutrients through the structure enhancing cell growth.
- The effects of increasing PTW thickness on cleaning and powder removal difficulties can be investigated. For example the use of piranha solution can potentially remove the loosely sintered powdered particles while avoiding significant material removal of the PTWs and simultaneously oxidise the entire PTW structure to enhance the biocompatibility.
- Different drugs and release formulations can be investigated to systematically build an application profile.
- Framework software can be developed to build a database of historic data and generated IKPs. This would enhance efficiency in future projects where trade-offs and potentials can already be studied from a database as well as relevant IKPs retrieved. Any insights regarding trade-offs, potentials, and generated IKPs should be fed back to the database to build an integrated knowledge system for interdisciplinary research projects.

---

## 11. References

- Abdallah, E., Khalid, A. and Ibrahim, N., 2009, 'Antibacterial activity of oleo-gum resins of commiphora molmol and Boswellia papyrifera against methicillin resistant Staphylococcus aureus', *Scientific Research and Essays*, 4(4), pp. 351-356.
- Abele, E., Stoffregen, H.A., Kniepkamp, M., Lang, S., and Hampe, M., 2015, 'Selective laser melting for manufacturing of thin-walled porous elements', *Journal of Materials Processing Technology*, 215, pp. 114-122.
- Aboulkhair, N., Everitt, N., Ashcroft, I., and Tuck, C., 2014, 'Reducing porosity in AlSi10Mg parts processed by selective laser melting', *Additive Manufacturing*, 1-4, pp. 77-86.
- Akindolire, J., Morcos, M.W., Marsh, J.D., Howard, J.L., Lanting, B.A., and Vasarhelyi, E.M., 2020, 'The economic impact of periprosthetic infection in total hip arthroplasty', *Canadian Journal of Surgery*, 63(1), pp. E52-E56.
- Aksoy, E.A., Yagci, B.S., Manap, G., Eroglu, I., Ozturk, S., Ekizoglu, M., and Ulubayram, K., 2019, 'Vancomycin Loaded Gelatin Microspheres Containing Wet Spun Poly( $\epsilon$ -caprolactone) Fibers and Films for Osteomyelitis Treatment', *Fibers and Polymers*, 20, pp. 2236-2246.
- Ali, H., Ghadbeigi, H., and Mumtaz, K., 2018, 'Effect of scanning strategies on residual stress and mechanical properties of Selective Laser Melted Ti6Al4V', *Materials Science and Engineering: A*, 712, pp. 175-187.
- Ali, M., Rai, R., Otte, J., and Smith, B., 2019, 'A product life cycle ontology for additive manufacturing' *Computers in Industry*, 105, pp. 191-203.
- Alshaibani, M., Jalil, J., Sidik, N.M., Edrada-Ebel, R., and Zin, N.M., 2016, 'Isolation and characterization of cyclo-(tryptophanyl-prolyl) and chloramphenicol from Streptomyces sp. SUK 25 with antimethicillin-resistant Staphylococcus aureus activity', *Drug Design, Development and Therapy*, 10, pp. 1817-1827.
- Amann, L.C., Gandal, M.J., Lin, R., Liang, Y., and Siegel, S.J., 2010, 'In Vitro-In Vivo Correlations of Scalable PLGA-Risperidone Implants for the Treatment of Schizophrenia', *Pharmaceutical Research*, 27(8), pp. 1730-1737.

- Ambrose, C.G., Clyburn, T.A., Mika, J., Gogola, G.R., Kaplan, H.B., Wanger, A., and Mikos, A., 2014, 'Evaluation of Antibiotic-Impregnated Microspheres for the Prevention of Implant-Associated Orthopaedic Infections', *The Journal of Bone and Joint Surgery, Incorporated*, 96(2), pp. 128-134.
- Anagnostakos, K., Schmid, N.V., Kelm, J., Grün, U., and Jung, J., 2009, 'Classification of hip joint infections', *International Journal of Medical Sciences*, 6(5), pp. 227-233.
- Anagnostakos, K., Wilmes, P., Schmitt, E., and Kelm, J., 2009, 'Elution of gentamicin and vancomycin from polymethylmethacrylate beads and hip spacers in vivo', *Acta Orthopaedica*, 80(2), pp. 193-197.
- Antoci, V., King, S.B., Jose, B., Parvizi, J., Zeiger, A.R., Wickstrom, E., Freeman, T.A., Composto, R.J., Ducheyne, P., Shapiro, I.M., Hickock, N.J., and Adams, C.S., 2007, 'Vancomycin Covalently Bonded to Titanium Alloy Prevents Bacterial Colonization', *Journal of Orthopaedic Research*, 25(7), pp. 858-866.
- Arciola, C., Campoccia, D., and Montanaro, L., 2018, 'Implant infections: adhesion, biofilm formation and immune evasion', *Nature Reviews Microbiology*, 16, pp. 397-409.
- Arciola, C., Campoccia, D., Speziale, P., Montanaro, L., and Costerton, J.W., 2012, 'Biofilm formation in Staphylococcus implant infections. A review of molecular mechanisms and implications for biofilm-resistant materials', *Biomaterials*, 33(26), pp. 5967-5982.
- Armillotta, A., Baraggi, R., and Fasoli, S., 2014, 'SLM tooling for die casting with conformal cooling channels', *The International Journal of Advanced Manufacturing Technology*, 71(1), pp. 573-583.
- Arullappan, S., Zakaria, A., and Basri, D., 2009, 'Preliminary Screening of Antibacterial Activity Using Crude Extracts of Hibiscus rosa sinensis', *Tropical Life Sciences Research*, 20(2), pp. 109-118.
- ASTM International, 2012, *F2792-12a: Standard Terminology for Additive Manufacturing Technologies*. West Conshohocken: ASTM International.
- ASTM International, 2013, *ASTM F136-13: Standard Specification for Wrought Titanium-6Aluminium-4Vanadium ELI (Extra Low Interstitial) Alloy for Surgical Implant Applications (UNS R56401)*. West Conshohocken: ASTM International.
- ASTM International, 2013, *D7334-08 Standard Practice for Surface Wettability of Coatings, Substrates and Pigments by Advancing Contact Angle Measurement*. West Conshohocken: ASTM International.

- ASTM International, 2014, *F3001 - 14: Standard Specification for Additive Manufacturing of Titanium-6 Aluminium -4 Vanadium ELI (Extra Low Interstitial) with Powder Bed Fusion*. West Conshohocken: ASTM International.
- Ayers, D.C., Zheng, H., Lemay, C., Yang, W., and Franklin, P.D., 2018, 'One-Year Total Hip Arthroplasty Revision Rates in the US: Incidence and Aetiology', *Orthopaedic Proceedings*, 100-B(SUPP\_13).
- Babis, G.C., Sakellariou, V.I., Pantos, P.G., Sasalos, G.G., and Stavropoulos, N.A., 2015, 'Two-Stage Revision Protocol in Multidrug Resistant Peroprosthetic Infection Following Total Hip Arthroplasty Using a Long Interval Between Stages', *The Journal of Arthroplasty*, 30(9), pp. 1602-1606.
- Bakhshandeh, S., Karaji, Z.G., Lietaert, K., Fluit, A.C., Boel, C.H.E., Vogely, H.C., Vermonden, T., Hennink, W.E., Weinans, H., Zadpoor, A.A., and Amin Yavari, S., 2017, 'Simultaneous Delivery of Multiple Antibacterial Agents from Additively Manufactured Porous Biomaterials to Fully Eradicate Planktonic and Adherent Staphylococcus aureus', *ACS Applied Materials and Interfaces*, 9(31), pp. 25691-25699.
- Baranowska, I., Wilczek, A., and Baranowski, J., 2010, 'Rapid UHPLC Method for Simultaneous Determination of Vancomycin, Terbinafine, Spironolactone, Furosemide and Their Metabolites: Application to Human Plasma and Urine', *Analytical Sciences*, 26(7), pp. 755-759.
- Barichello, J., Morishita, M., Takayama, K., and Nagai, T., 1999, 'Encapsulation of Hydrophilic and Lipophilic Drugs in PLGA Nanoparticles by the Nanoprecipitation Method', *Drug Development and Industrial Pharmacy*, 25(4), pp. 471-476.
- Barik, A. and Chakravorty, N., 2019, 'Targeted Drug Delivery from Titanium Implants: A Review of Challenges and Approaches', In: M. Pokorski, ed. *Trends in Biomedical Research. Advances in Experimental Medicine and Biology*. Cham: Springer Nature Switzerland AG, pp. 1-17.
- Bari, K., and Arjunan, A., 2019, 'Extra low interstitial titanium based fully porous morphological bone scaffolds manufactured using selective laser melting', *Journal of the Mechanical Behavior of Biomedical Materials*, 95, pp. 1-12.
- Barrack, R.L., Engh, G., Rorabeck, C., Sawhney, J., and Woolfrey, M., 2000, 'Patient satisfaction and outcome after septic versus aseptic revision total knee arthroplasty', *The Journal of Arthroplasty*, 15(8), pp. 990-993.

- Barthold, S., Kletting, S., Taffner, J., de Souza Carvalho-Wodarz, C., Lepeltier, E., Loretz, B., and Lehr, C.-M., 2016, 'Preparation of nanosized coacervates of positive and negative starch derivatives intended for pulmonary delivery of proteins', *Journal of Materials Chemistry B*, 4(13), pp. 2377-2386.
- Basri, D., Zainal, N., and Santhanam, J., 2014, 'The Potential of Canarium Odontophyllum MIQ. (Dabai) as Anti-Methicillin Resistant Staphylococcus Aureus Agent', *International Journal of Pharmacy and Pharmaceutical Sciences*, 6(9), pp. 290-293.
- Benedetti, M., Fontanari, V., Bandini, M., Zanini, F., and Carmignato, S., 2018, 'Low- and high-cycle fatigue resistance of Ti-6Al-4V ELI additively manufactured via selective laser melting: Mean stress and defect sensitivity', *International Journal of Fatigue*, 107, pp. 96-109.
- Benedetti, M., Torresani, E., Leoni, M., Fontanari, V., Bandini, M., Pederzoli, C., and Potrich, C., 2017, 'The effect of post-sintering treatments on the fatigue and biological behavior of Ti-6Al-4V ELI parts made by selective laser melting', *Journal of the Mechanical Behavior of Biomedical Materials*, 71, pp. 295-306.
- Bernard, L., Legout, L., Zürcher-Pfund, L., Stern, R., Rohner, P., Peter, R., Assal, M., Lew, D., Hoffmeyer, P., and Uçkay, I., 2010, 'Six weeks of antibiotic therapy is sufficient following surgery for septic arthroplasty', *Journal of Infection*, 61(2), pp. 125-132.
- Bertoli, U.S., Wolfer, A.J., Matthews, M.J., Delplanque, J.-P.M., and Schoenung, J.M., 2017, 'On the limitations of Volumetric Energy Density as a design parameter for Selective Laser Melting', *Materials & Design*, 113, pp. 331-340.
- Besheli, N.H., Mottaghitalab, F., Eslami, M., Gholami, M., Kundu, S.C., Kaplan, D.L., and Farokhi, M., 2017, 'Sustainable Release of Vancomycin from Silk Fibroin Nanoparticles for Treating Severe Bone Infection in Rat Tibia Osteomyelitis Model', *ACS Applied Materials & Interfaces*, 9(6), pp. 5128-5138.
- Bezuidenhout, M.B., Booysen, E., van Staden, A.D., Uheida, E.H., Hugo, P.A., Oosthuizen, G.A., Dimitrov, D.M., and Dicks, L.M.T., 2018, 'Selective Laser Melting of Integrated Ti6Al4V ELI Permeable Walls for Controlled Drug Delivery of Vancomycin', *ACS Biomaterials Science and Engineering*, 4(12), pp. 4412-4424.
- Bezuidenhout, M.B., van Staden, A.D., Oosthuizen, G.A., Dimitrov, D.M., and Dicks, L.M.T., 2015, 'Delivery of Antibiotics from Cementless Titanium-alloy cubes may be a Novel Way to Control Post-operative Infections', *BioMed Research International*, 2015, Article ID 856859, 7 pp.

- Bezuidenhout, M., Ter Haar, G., Becker, T., Rudolph, S., Damm, O., and Sacks, N., 2020, 'The effect of HF-HNO<sub>3</sub> chemical polishing on the surface roughness and fatigue life of laser powder bed fusion produced Ti6Al4V', *Materials Today Communications*, 25(101396), 10 pp.
- Bico, J., Thiele, U., and Quéré, D., 2002, 'Wetting of textured surfaces', *Colloids and Surfaces A: Physicochemical and Engineering Aspects*, 206(1-3), pp. 41-46.
- Bistolfi, A., Ferracini, R., Albanese, C., Vernè, E., and Miola, M., 2019, 'PMMA-Based Bone Cements and the Problem of Joint Arthroplasty Infections: Status and New Perspectives', *Materials*, 12(23), 16 pp.
- Bobbert, F.S.L., Lietaert, K., Eftekhari, A.A., Pouran, B., Ahmadi, S.M., Weinans, H., and Zadpoor, A.A., 2017, 'Additively manufactured metallic porous biomaterials based on minimal surfaces: A unique combination of topological, mechanical, and mass transport properties', *Acta Biomaterialia*, 53, pp. 572-584.
- Booyesen, E., Bezuidenhout, M., van Staden, A.D.P., Dimitrov, D., Deane, S.M., and Dicks, L.M.T., 2019, 'Antibacterial Activity of Vancomycin Encapsulated in Poly(DL-lactide-co-glycolide) Nanoparticles Using Electrospraying', *Probiotics and Antimicrobial Proteins*, 11, pp. 310-316.
- Bozic, K.J., Kamath, A.F., Ong, K., Lau, E., Kurtz, S., Chan, V., Vail, T.P., Rubash, H., and Berry, D.J., 2015, 'Comparative Epidemiology of Revision Arthroplasty: Failed THA Poses Greater Clinical and Economic Burdens Than Failed TKA', *Clinical Orthopaedics and Related Research*, 473(6), pp. 2131-2138.
- Bozic, K. and Ries, M., 2005, 'The Impact of Infection After Total Hip Arthroplasty on Hospital and Surgeon Resource Utilization', *The Journal of Bone & Joint Surgery*, 87(8), pp. 1746-1751.
- Braem, A., Van Mellaert, L., Mattheys, T., Hofmans, D., De Waelheyns, E., Geris, L., Anné, J., Schrooten, J., and Vleugels, J., 2014, 'Staphylococcal biofilm growth on smooth and porous titanium coatings for biomedical applications', *Journal of Biomedical Materials Research Part A*, 102(1), pp. 215-224.
- Brandt, C.M., Sistrunk, W.W., Duffy, M.C., Hanssen, A.D., Steckelberg, J.M., Ilstrup, D.M., and Osmon, D.R., 1997, 'Staphylococcus aureus Prosthetic Joint Infection Treated with Debridement and Prosthesis Retention', *Clinical Infectious Diseases*, 24(5), pp. 914-919.

- Brescó, M., Harris, L.G., Thompson, K., Stanic, B., Morgenstern, M., O'Mahony, L., Richards, R.G., and Moriarty, T.F., 2017, 'Pathogenic Mechanisms and Host Interactions in Staphylococcus epidermidis Device-Related Infection', *Frontiers in Microbiology*, 8(1401), 24 pp.
- Briggs, T., 2015, *A national review of adult elective orthopaedic services in England*, British Orthopaedic Association.
- Brown, A., 2001, 'A step-by-step guide to non-linear regression analysis of experimental data using a Microsoft Excel spreadsheet', *Computer Methods and Programs in Biomedicine*, 65(3), pp. 191-200.
- Brown, T.S., Fehring, K.A., Ollivier, M.m Mabry, T.M., Hanssen, A.D., and Abdel, M.P., 2018, 'Repeat two-stage exchange arthroplasty for prosthetic hip re-infection', *The Bone and Joint Journal*, 100-B(9), pp. 1157-1161.
- Broy, M. and Rausch, A., 2005, 'Das neue V-Modell XT: Ein anpassbares Modell für Software und System Engineering', *Informatik Spektrum*, 28, pp. 220-229.
- Brugnara, M., 2006, *Contact Angle*, [Online] Available at: <https://imagej.nih.gov/ij/plugins/contact-angle.html> [Accessed 31 August 2018].
- Bryskier, A. and Veyssier, P., 2005, 'Glycopeptides and Lipoglycopeptides', In: A. Bryskier, ed. *Antimicrobial Agents - Antibacterials and Antifungals*. Washington(District of Columbia): ASM Press, pp. 880-903.
- Buchholz, H.W., Elson, R.A., Engelbrecht, E., Lodenkamper, H., Rottger, J., and Siegel, A., 1981, 'Management of Deep Infection of Total Hip Replacement', *The Journal of Bone and Joint Surgery*, 63-B(3), pp. 342-353.
- Buijnsters, J., Zhong, R., Tsyntsar, N., and Celis, J.-P., 2013, 'Surface Wettability of Macroporous Anodized Aluminum Oxide', *ACS Applied Materials and Interfaces*, 5(8), pp. 3224-3233.
- Burghardt, I., Lüthen, F., Prinz, C., Kreikemeyer, B., Zietz, C., Neumann, H.-G., and Rychly, J., 2015, 'A dual function of copper in designing regenerative implants', *Biomaterials*, 44, pp. 36-44.
- Burton, H.E., Eisenstein, N.M., Lawless, B.M., Jamshidi, P., Segarra, M.A., Addison, O., Shepherd, D.E.T., Atallah, M.M., Grover, L.M., and Cox, S.C., 2019, 'The design of additively manufactured lattices to increase the functionality of medical implants', *Materials Science & Engineering C*, 94, pp. 901-908.

- Caggiano, A., Zhang, J., Alfieri, V., Caiazzo, F., Gao, R., and Teti, R., 2019, 'Machine learning-based image processing for on-line defect recognition in additive manufacturing', *CIRP Annals*, 68(1), pp. 451-454.
- Campoccia, D., Montanaro, L., and Arciola, C., 2013, 'A review of the biomaterials technologies for infection-resistant surfaces', *Biomaterials*, 34, pp. 8533-8554.
- Campoccia, D., Montanaro, L., Speziale, P., and Arciola, C., 2010, 'Antibiotic-loaded biomaterials and the risks for the spread of antibiotic resistance following their prophylactic and clinical use', *Biomaterials*, 31, pp. 6363-6377.
- Cardaropoli, F., Alfieri, V., Caiazzo, F., and Sergi, V., 2012, 'Dimensional analysis for the definition of the influence of process parameters in selective laser melting of Ti-6Al-4V alloy', *Proceedings of the Institution of Mechanical Engineers, Part B: Journal of Engineering Manufacture*, 226(7), pp. 1136-1142.
- Carter, L., Martin, C., Withers, P., and Atallah, M., 2014, 'The influence of the laser scan strategy on grain structure and cracking behaviour in SLM powder-bed fabricated nickel superalloy', *Journal of Alloys and Compounds*, 615, pp. 338-347.
- Cassie, A. and Baxter, S., 1944. 'Wettability of Porous Surfaces', *Transactions of the Faraday Society*, 40, pp. 546-551.
- Chandrasekaran, M., Kannathasan, K., and Venkatesalu, V., 2008, 'Antibacterial activity of some salt marsh halophytes and mangrove plants against methicillin resistant *Staphylococcus aureus*', *World Journal of Microbiology and Biotechnology*, 25, pp. 155-160.
- Chan, E.W.L., Gray, A.I., Igoli, J.O., Lee, S.M., and Goh, J.K., 2014, 'Galloylated flavonol rhamnosides from the leaves of *Calliandra tergemina* with antibacterial activity against methicillin-resistant *Staphylococcus aureus* (MRSA)', *Phytochemistry*, 107, pp. 148-154.
- Chavez-Diaz, M., Escudero-Rincon, M., Arce-Estrada, E., and Cabrera-Sierra, R., 2018, 'Effect of Heat-Treated Ti6Al4V Alloy on the Fibroblastic Cell Response', *Materials*, 11(21), 17 pp.
- Chen, Y.-J., Chen, Y.-M., and Chu, H.-C., 2009, 'Development of a mechanism for ontology-based product life cycle knowledge integration', *Expert Systems with Applications*, 36(Part 2), pp. 2759-2779.
- Chourifa, H., Bouloussa, H., Migonney, V., and Falentin-Daudré, C., 2019, 'Review of titanium surface modification techniques and coatings for antibacterial applications', *Acta Biomaterialia*, 83, pp. 37-54.

- Chua, P.-H., Neoh, K.-G., Kang, E.-T., and Wang, W., 2008, 'Surface functionalization of titanium with hyaluronic acid/chitosan polyelectrolyte multilayers and RGD for promoting osteoblast functions and inhibiting bacterial adhesion', *Biomaterials*, 29(10), pp. 1412-1421.
- Clijsters, S., Craeghs, T., Buls, S., Kempen, K., and Kruth, J.-P., 2014, 'In situ quality control of the selective laser melting process using a high-speed, real-time melt pool monitoring system', *International Journal of Advanced Manufacturing Technology*, 75, pp. 1089-1101.
- Conradie, P.J.T., Dimitrov, D., Oosthuizen, G.A., Hugo, P., and Saxer, M., 2017, 'Comparative assessment of process combination for Ti6Al4V components', *Rapid Prototyping Journal*, 23(3), pp. 624-632.
- Costa, P., Lobo, J.M., 2001, 'Modeling and comparison of dissolution profiles', *European Journal of Pharmaceutical Sciences*, 13(2), pp. 123-133.
- Costerton, J., Montanaro, L., and Arciola, C., 2005, 'Biofilm in Implant Infections: Its Production and Regulation', *The International Journal of Artificial Organs*, 28(11), pp. 1062-1068.
- Cox, S.C., Jamshidi, P., Eisenstein, N.E., Webber, M.A., Hassanin, H., Attallah, M.M., Shepherd, D.E.T., Addison, O., and Grover, L.M., 2016, 'Adding functionality with additive manufacturing: Fabricating titanium-based antibiotic eluting implants', *Materials Science and Engineering: C*, 64, pp. 407-415.
- Crawford, R.J., Webb, H.K., Truong, V.K., Hasan, J., and Ivanova, E.P., 2012, 'Surface topographical factors influencing bacterial attachment', *Advances in Colloid and Interface Science*, 179-182, pp. 142-149.
- Darouiche, R., 2001, 'Device-Associated Infections: A Macroproblem that Starts with Microadherence', *Clinical Infectious Diseases*, 33(9), pp. 1567-1572.
- Davidson, D., Spratt, D., and Liddle, A., 2019, 'Implant materials and prosthetic joint infection: the battle with the biofilm', *Efort Open Reviews*, 4(11), pp. 633-639.
- De Cremer, K., Braem, A., Gerits, E., De Brucker, K., Vandamme, K., Martens, J., Michiels, J., Vleugels, J., Cammue, B., and Thevissen, K., 2017, 'Controlled Release of Chlorhexidine from a Mesoporous Silica-Containing Macroporous Titanium Dental Implant Prevents Microbial Biofilm Formation', *European Cells and Materials*, 33, pp. 13-27.
- de Formanoir, C., Paggi, U., Colebrants, T., Thijs, L., Li, G., Vanmeensel, K., and Van Hooreweder, B., 2020, 'Increasing the productivity of laser powder bed fusion: Influence of the hull-bulk strategy on

- part quality, microstructure and mechanical performance of Ti-6Al-4V', *Additive Manufacturing*, 33(101129), 10 pp.
- De Pasquale, D., Luceri, F., and Riccio, M., 2019, 'Experimental Characterization of SLM and EBM Cubic Lattice Structures for Lightweight Applications', *Experimental Mechanics*, 59(4), pp. 469-482.
- Dilip, J.J.S., Zhang, S., Teng, C., Zeng, K., Robinson, C., Pal, D., and Stucker, B., 2017, 'Influence of processing parameters on the evolution of melt pool, porosity, and microstructures in Ti-6Al-4V alloy parts fabricated by selective laser melting', *Progress in Additive Manufacturing*, 2, pp. 157-167.
- Donachie, M., 2000, *Titanium A Technical Guide*. Second Edition. Materials Park: ASM International.
- Dordlofva, C. and Törlind, P., 2018, *Design for Qualification: A Process for developing Additive Manufacturing Components for Critical Systems*. Linköping, The Design Society.
- Doymus, B., Kerem, G., Karatas, A.Y., Kok, F.N., Önder, S., 2021, 'A functional coating to enhance antibacterial and bioactivity properties of titanium implants and its performance in vitro', *Journal of Biomaterials Applications*, 35(6), pp. 655-669.
- Du Plessis, A., 2019, 'Effects of process parameters on porosity in laser power bed fusion revealed by X-ray tomography', *Additive Manufacturing*, 30(100871), 9 pp.
- Du Plessis, A., Broeckhoven, C., Guelpa, A., and Le Roux, S., 2017, 'Laboratory X-ray micro-computed tomography: a user guideline for biological samples', *GigaScience*, 6(6), pp. 1-11.
- Du Plessis, A., and Macdonald, E., 2020, 'Hot isostatic pressing in metal additive manufacturing: X-ray tomography reveals details of pore closure', *Additive Manufacturing*, 34(101191), 12 pp.
- Du, L., Yang, S., Li, W., Li, H., Feng, S., Zeng, R., Yu, B., Xiao, L., Nie, H.-Y., and Tu, M., 2017, 'Scaffold composed of porous vancomycin-loaded poly(lactide-co-glycolide) microspheres: A controlled-release drug delivery system with shape-memory effect', *Materials Science and Engineering: C*, 78, pp. 1172-1178.
- Duvvuri, S., Janoria, K.G., and Mitra, A., 2006, 'Effect of Polymer Blending on the Release of Ganciclovir', *Pharmaceutical Research*, 23(1), pp. 215-223.
- Dydak, K., Junka, A., Szymczyk, P., Chodaczek, G., Toporkiewicz, M., Fijałkowski, K., Dudek, B., and Bartoszewicz, M., 2018, 'Development and biological evaluation of Ti6Al7Nb scaffold implants coated with gentamycin-saturated bacterial cellulose biomaterial', *PLoS ONE*, 13(10), 13 pp.

- Edwards, P. and Ramulu, M., 2014, 'Fatigue performance evaluation of selective laser melted Ti6Al4V', *Materials Science and Engineering: A*, 598, pp. 327-337.
- Eigner, M., Dickopf, T., and Huwig, C., 2016. *An Interdisciplinary Model-Based Design Approach For Developing Cybertronic Systems*. Dubrovnik, International Design Conference - Design 2016.
- Elmer, J.W., Palmer, T.A., 2004, 'Phase transformation dynamics during welding of Ti-6Al-4V', *Journal of applied physics*, 95(12), pp. 8327-8339.
- Emrouznejad, A. and Marra, M., 2017, 'The state of the art development of AHP (1979-2017): a literature review with a social network analysis', *International Journal of Production Research*, 55(22), pp. 6653-6675.
- Everton, S.K., Hirsch, M., Stravroulakis, P., Leach, R.K., and Clare, A.T., 2016, 'Review of in-situ process monitoring and in-situ metrology for metal additive manufacturing', *Materials and Design*, 95, pp. 431-445.
- Extrand, C. and Moon, S., 2010, 'When Sessile Drops Are No Longer Small: Transitions from Spherical to Fully Flattened', *Langmuir*, 26(14), pp. 11815-11822.
- Fagotti, L., Tatka, J., Salles, M., and Queiroz, M., 2018, 'Risk Factors and Treatment Options for Failure of a Two-Stage Exchange', *Current Reviews in Musculoskeletal Medicine*, 11, pp. 420-427.
- FDA, 2012, *Exactech Novation InteGrip Acetabular Augments Special 510(k) - 510(k) Summary of Safety and Effectiveness*. [Online] Available at: [http://www.accessdata.fda.gov/cdrh\\_docs/pdf11/K113609.pdf](http://www.accessdata.fda.gov/cdrh_docs/pdf11/K113609.pdf) [Accessed 27 February 2019].
- FDA, 2014, *510(k) Premarket Notification - 4WEB Spinal Implant Products*. [Online] Available at: [https://www.accessdata.fda.gov/cdrh\\_docs/pdf14/K142112.pdf](https://www.accessdata.fda.gov/cdrh_docs/pdf14/K142112.pdf) [Accessed 07 March 2019].
- FDA, 2015, *510(k) Premarket Notification - BioArchitects Patient Specific Cranial/Craniofacial Plate*. [Online] Available at: <https://www.accessdata.fda.gov/scripts/cdrh/cfdocs/cfPMN/pmn.cfm?ID=K151692> [Accessed 27 February 2019].
- FDA, 2016, *510(k) Premarket Notification - Additive Orthopaedics Bone Wedge System*. [Online] Available at: <https://www.accessdata.fda.gov/scripts/cdrh/cfdocs/cfPMN/pmn.cfm?ID=K153207> [Accessed 27 February 2019].

---

FDA, 2016, *510(k) Premarket Notification - Additive Orthopaedics Hammertoe Correction System*.

[Online]

Available at: <https://www.accessdata.fda.gov/scripts/cdrh/cfdocs/cfpmn/pmn.cfm?ID=K160264>

[Accessed 27 February 2019].

FDA, 2016, *510(k) Premarket Notification - Trident® II Tritanium® Acetabular Shells and 6.5 mm Low Profile Hex Screws*. [Online]

Available at: [https://www.accessdata.fda.gov/cdrh\\_docs/pdf16/K161569.pdf](https://www.accessdata.fda.gov/cdrh_docs/pdf16/K161569.pdf)

[Accessed 28 February 2019].

FDA, 2016, *510(k) Premarket Notification - Tritanium® PL Cage*. [Online]

Available at: [https://www.accessdata.fda.gov/cdrh\\_docs/pdf16/K162262.pdf](https://www.accessdata.fda.gov/cdrh_docs/pdf16/K162262.pdf)

[Accessed 28 February 2019].

FDA, 2017, *510(k) Premarket Notification - 3DMetal Tibial Cones*. [Online]

Available at: [https://www.accessdata.fda.gov/cdrh\\_docs/pdf17/K170149.pdf](https://www.accessdata.fda.gov/cdrh_docs/pdf17/K170149.pdf)

[Accessed 27 February 2019].

FDA, 2017, *510(k) Premarket Notification - Additive Orthopaedics Locking Lattice Plate*. [Online]

Available at: <https://www.accessdata.fda.gov/scripts/cdrh/cfdocs/cfpmn/pmn.cfm?ID=K170214>

[Accessed 27 February 2019].

FDA, 2017, *510(k) Premarket Notification - ARTiC-L 3D Ti Spinal System with TiONIC Technology, ARTiC-XL 3D Ti Spinal System with TiONIC Technology*. [Online]

Available at: [https://www.accessdata.fda.gov/cdrh\\_docs/pdf17/K171689.pdf](https://www.accessdata.fda.gov/cdrh_docs/pdf17/K171689.pdf)

[Accessed 27 February 2019].

FDA, 2017, *510(k) Premarket Notification - Foundation 3D Interbody*. [Online]

Available at: [https://www.accessdata.fda.gov/cdrh\\_docs/pdf16/K162496.pdf](https://www.accessdata.fda.gov/cdrh_docs/pdf16/K162496.pdf)

[Accessed 27 February 2019].

FDA, 2017, *510(k) Premarket Notification - Intervertebral Fusion Device With Bone Graft, Lumbar*.

[Online]

Available at: [https://www.accessdata.fda.gov/cdrh\\_docs/pdf17/K172888.pdf](https://www.accessdata.fda.gov/cdrh_docs/pdf17/K172888.pdf)

[Accessed 27 February 2019].

- FDA, 2017, *510(k) Premarket Notification - SPIRA Open Matrix ALIF*. [Online]  
Available at: [https://www.accessdata.fda.gov/cdrh\\_docs/pdf16/K162986.pdf](https://www.accessdata.fda.gov/cdrh_docs/pdf16/K162986.pdf)  
[Accessed 27 February 2019].
- FDA, 2017, *510(k) Premarket Notification - Tritanium C Anterior Cervical Cage*. [Online]  
Available at: [https://www.accessdata.fda.gov/cdrh\\_docs/pdf17/K171496.pdf](https://www.accessdata.fda.gov/cdrh_docs/pdf17/K171496.pdf)  
[Accessed 28 February 2019].
- FDA, 2017, *510(k) Premarket Notification - TruMatch CMF Titanium 3D Printed Implant System*.  
[Online]  
Available at: <https://www.accessdata.fda.gov/scripts/cdrh/cfdocs/cfPMN/pmn.cfm?ID=K170272>  
[Accessed 27 February 2019].
- FDA, 2018, *510(k) Premarket Notification - Osteotomy Truss System (OTS)*. [Online]  
Available at: [https://www.accessdata.fda.gov/cdrh\\_docs/pdf17/K172294.pdf](https://www.accessdata.fda.gov/cdrh_docs/pdf17/K172294.pdf)  
[Accessed 07 03 2019].
- FDA, 2018, *510(k) Premarket Notification - Tritanium® TL Curved Posterior Lumbar Cage*. [Online]  
Available at: [https://www.accessdata.fda.gov/cdrh\\_docs/pdf17/K173476.pdf](https://www.accessdata.fda.gov/cdrh_docs/pdf17/K173476.pdf)  
[Accessed 28 February 2019].
- Ferreira, I.S., Bettencourt, A.F., Gonçalves, L.M.D., Kasper, S., Bétrisey, B., Kikhney, J., Moter, A., Trampuz, A., and Almeida, A., 2015, 'Activity of daptomycin- and vancomycin-loaded poly-epsilon-caprolactone microparticles against mature staphylococcal biofilms', *International Journal of Nanomedicine*, 10(1), pp. 4351-4366.
- Fisman, D., Reilly, D., Karchmer, A., and Goldie, S., 2001, 'Clinical Effectiveness and Cost-Effectiveness of 2 Management Strategies for Infected Total Hip Arthroplasty in the Elderly', *Clinical Infectious Disease*, 32(3), pp. 41-430.
- Fousova, M., Vojtech, D., Doubrava, K., Daniel, M., and Lin, C.-F., 2018, 'Influence of Inherent Surface and Internal Defects on Mechanical Properties of Additively Manufactured Ti6Al4V Alloy: Comparison between Selective Laser Melting and Electron Beam Melting', *Materials*, 11(4), 18 pp.
- Francolini, I. and Donelli, G., 2010, 'Prevention and control of biofilm-based medical-device-related infections', *FEMS Immunol Med Microbiol*, 59(3), pp. 227-238.
- Freiberg, S. and Zhu, X., 2004, 'Polymer microspheres for controlled drug release', *International Journal of Pharmaceutics*, 282(1-2), pp. 1-18.

- Furnes, O., Gjertsen, J.-E., Hallan, G., Visnes, H., Gundersen, T., Fenstad, A.M., Dybvig, E., and Bartz-Johannessen, C., 2018, *Report June 2018 - Norwegian National Advisory Unit on Arthroplasty and Hip Fractures*, Bergen: Nasjonalt Register for Leddproteser.
- Gallo, J., Kolar, M., Novotny, R., Rihakova, P., and Ticha, V., 2003, 'Pathogenesis of Prosthesis-Related Infection', *Biomed. Papers*, 147(1), pp. 27-35.
- Garcia-Gareta, E., Davidson, C., Levin, A., Coathup, M.J., and Blunn, G.W., 2016. 'Biofilm formation in total hip arthroplasty: prevention and treatment', *RSC Advances*, 6, pp. 80244-80261.
- Garellick, G., Kärrholm, J., Lindahl, H., Malchau, H., Rogmark, C., and Rolfson, O., 2014, *Swedish hip arthroplasty register annual report 2013*, Swedish Hip Arthroplasty Register.
- Gaspar, L.M.D.A.C., Dorea, A.C.S., Droppa-Almeida, D., Silva, I.S.D.M., Montoro, F.M., Alves, L.L., Mecedo, M.L.H., and Padilha, F.F., 2018, 'Development and characterization of PLGA nanoparticles containing antibiotics', *Journal of Nanoparticle Research*, 20(289), 9 pp.
- Gavini, E., Chetoni, P., Cossu, M., Alvarez, M.G., Saettone, M.F., and Giunchedi, P., 2004, 'PLGA microspheres for the ocular delivery of a peptide drug, vancomycin using emulsification/spray-drying as the preparation method: in vitro/in vivo studies', *European Journal of Pharmaceutics and Biopharmaceutics*, 57(2), pp. 207-212.
- Geetha, M., Singh, A., Asokamani, R., and Gogia, A., 2009, 'Ti based biomaterials, the ultimate choice for orthopaedic implants - A review', *Progress in Materials Science*, 54(3), pp. 397-425.
- Gentile, P., Chiono, V., Carmagnola, I., and Hatton, P., 2014, 'An Overview of Poly(lactic-co-glycolic) Acid (PLGA)-Based Biomaterials for Bone Tissue Engineering', *International Journal of Molecular Sciences*, 15(3), pp. 3640-3659.
- George, D., Gant, V., and Haddad, F., 2015, 'The management of periprosthetic infections in the future', *The Bone and Joint Journal*, 97-B(9), pp. 1162-1169.
- Getzlaf, M.A., Lewallen, E.A., Kremers, H.M., Jones, D.L., Bonin, C.A., Dudakovic, A., Thaler, R., Cohen, R.C., Lewallen, D.G., and van Wijnen, A.J., 2016, 'Multi-Disciplinary Antimicrobial Strategies for Improving Orthopaedic Implants to Prevent Prosthetic Joint Infections in Hip and Knee', *Journal of Orthopaedic Research*, 34(2), pp. 177-186.
- Ghouse, S., Babu, S., Van Arkel, R.J., Nai, K., Hooper, P.A., and Jeffers, J.R.T., 2017, 'The influence of laser parameters and scanning strategies on the mechanical properties of a stochastic porous material', *Materials and Design*, 131, pp. 498-508.

- Gibbons, S., Ohlendorf, B., and Johnsen, I., 2002, 'The genus *Hypericum* - a valuable resource of anti-Staphylococcal leads', *Fitoterapia*, 73(4), pp. 300-304.
- Ginebra, M., Traykova, T., and Planell, J., 2006, 'Calcium phosphate cements as bone drug delivery systems: A review', *Journal of Controlled Release*, 113(2), pp. 102-110.
- Gogia, J., Meehan, J., Di Cesare, P., and Jamali, A., 2009, 'Local Antibiotic Therapy in Osteomyelitis', *Seminars in Plastic Surgery*, 23(2), pp. 100-107.
- Goldman, A.H., Osmon, D.R., Hanssen, A.D., Pagnano, M.W., Berry, D.J., and Abdel, M.P., 2020, 'The Lawrence D. Dorr Surgical Techniques & Technologies Award: Aseptic Reoperations Within One Year of Primary Total Hip Arthroplasty Markedly Increase the Risk of Later Periprosthetic Joint Infection', *The Journal of Arthroplasty*, 35(6 Supplement), pp. S10-S15.
- Gomez, M., Tan, T., Manrique, J., Deirmengian, G.K., and Parvizi, J., 2015, 'The Fate of Spacers in the Treatment of Periprosthetic Joint Infection', *The Journal of Bone and Joint Surgery, Incorporated*, 97-A(18), pp. 1495-1502.
- Gong, H., Rafi, K., Gu, H., Ram, J., Starr, T., and Stucker, B., 2015, 'Influence of defects on mechanical properties of Ti-6Al-4V components produced by selective laser melting and electron beam melting', *Materials & Design*, 86, pp. 545-554.
- Gong, H., Rafi, K., Gu, H., Starr, T., and Stucker, B., 2014, 'Analysis of defect generation in Ti-6Al-4V parts made using powder bed fusion additive manufacturing processes', *Additive Manufacturing*, 1-4, pp. 87-98.
- Göpferich, A., 1997, 'Polymer Bulk Erosion', *Macromolecules*, 30(9), pp. 2598-2604.
- Grammatopoulos, G., Kendrick, B., McNally, M., Athanasou, N.A., Atkins, B., McLardy-Smith, P., Taylor, A., and Gundle, R., 2017, 'Outcome Following Debridement, Antibiotics, and Implant Retention Retention in Hip Prosthetic Joint Infection - An 18-Year Experience', *The Journal of Arthroplasty*, 32(7), pp. 2248-2255.
- Graves, N., Wloch, C., Wilson, J., Barnett, A., Sutton, A., Cooper, N., Merollini, K., McCreanor, V., Cheng, Q., Burn, E., Lamagni, T., and Charlett, A., 2016, 'A cost-effective modelling study of strategies to reduce risk of infection following primary hip replacement based on a systematic review', *Health Technology Assessment*, 20(54), pp. 1-144.
- Grimm, T., 2004. *User's Guide to Rapid Prototyping*. 1st ed. Dearborn(Michigan): Society of Manufacturing Engineers.

- Gundtoft, P., Pedersen, A., Varnum, C., and Overgaard, S., 2017, 'Increased Mortality After Prosthetic Joint Infection in Primary THA', *Clinical Orthopaedics and Related Research*, 475, pp. 2623-2631.
- Günther, J., Krewerth, D., Lippmann, T., Leuders, S., Tröster, T., Weidner, A., Biermann, H., and Niendorf, T., 2017, 'Fatigue life of additively manufactured Ti-6Al-4V in the very high cycle fatigue regime', *International Journal of Fatigue*, 94(Part 2), pp. 236-245.
- Gusarov, A., Yadroitsev, I., Bertrand, P., and Smurov, I., 2007, 'Heat transfer modelling and stability analysis of selective laser melting', *Applied Surface Science*, 254(4), pp. 975-979.
- Hachicha, W., Kodjikian, L., and Fessi, H., 2006, 'Preparation of vancomycin microparticles: Importance of preparation parameters', *International Journal of Pharmaceutics*, 324(2), pp. 176-184.
- Haddad, F. S., Muirhead-Allwood, S. K., Manktelow, A. R. J., and Bacarese-Hamilton, I., 2000, 'Two-stage uncemented revision hip arthroplasty for infection', *The Journal of Bone and Joint Surgery (Br)*, July, 82-B(5), pp. 689-694.
- Hafeman, A., Zienkiewicz, K.J., Carney, E., Litzner, B., Stratton, C., Wenke, J.C., and Guelcher, S.A., 2010, 'Local Delivery of Tobramycin from Injectable Biodegradable Polyurethane Scaffolds', *Journal of Biomaterials Science*, 21(1), pp. 95-112.
- Hagedorn-Hansen, D., Bezuidenhout, M., Dimitrov, D., and Oosthuizen, G., 2017, 'The Effects of Selective Laser Melting Scan Strategies on Deviation of Hybrid Parts', *South African Journal of Industrial Engineering*, 28(3), pp. 200-212.
- Han, J., Yang, J., Yu, H., Yin, J., Gao, M., Wang, Z., and Zeng, X., 2017, 'Microstructure and mechanical properties of selective laser melted Ti6Al4V dependence on laser energy density', *Rapid Prototyping Journal*, 23(2), pp. 217-226.
- Hannan, A., Saleem, S., Chaudhary, S., Barkaat, M., and Arshad, M.U., 2008, 'Anti Bacterial Activity of Nigella Sativa Against Clinical Isolates of Methicillin Resistant Staphylococcus Aureus', *Journal of Ayub Medical College Abbottabad*, 20(3), pp. 72-74.
- Hann, D., Iammi, J., and Folkes, J., 2011, 'A simple methodology for predicting laser-weld properties from material and laser parameters', *Journal of Physics D: Applied Physics*, 44(44), 9 pp.
- Hansen, E., Tetreault, M., Zmistowski, B., Della Valle, C.J., Parvizi, J., Haddad, F.S., and Hozack, W.J., 2013, 'Outcome of One-stage Cementless Exchange for Acute Postoperative Periprosthetic Hip Infection', *Clinical Orthopaedics and Related Research*, 471, pp. 3214-3222.

- Hanssen, A. and Spanghehl, M., 2004, 'Practical Applications of Antibiotic-Loaded Bone Cement for Treatment of Infected Joint Replacements', *Clinical Orthopaedics and Related Research*, 427, pp. 79-85.
- Han, S., Yang, R., Li, C., and Yang, L., 2019, 'The Wettability and Numerical Model of Different Silicon Microstructural Surfaces', *Applied Sciences*, 9(3), 16 pp.
- Hassan, D., Omolo, C.A., Gannimani, R., Waddad, A.Y., Mocktar, C., Rambharose, S., Agrawal, N., and Govender, T., 2019, 'Delivery of novel vancomycin nanoplexes for combating methicillin resistant Staphylococcus aureus (MRSA) infections', *International Journal of Pharmaceutics*, 558, pp. 143-156.
- Hassanin, H., Finet, L., Cox, S.C., Jamshidi, P., Grover, L.M., Shepherd, D.E.T., Addison, O., Attallah, M.M., 2018, 'Tailoring selective laser melting process for titanium drug-delivering implants with releasing micro-channels', *Additive Manufacturing*, 20, pp. 144-155.
- Hassanin, H., Modica, F., El-Sayed, M.A., Liu, J., and Essa, K., 2016, 'Manufacturing of Ti-6Al-4V Micro-Implantable Parts Using Hybrid Selective Laser Melting and Micro-Electrical Discharge Machining', *Advanced Engineering Materials*, 18(9), pp. 1544-1549.
- Heckmann, N.D., Mayfield, C.K., Culvern, C.N., Oakes, D.A., Lieberman, J.R., and Della Valle, C.J., 2019, 'Systematic Review and Meta-Analysis of Intrawound Vancomycin in Total Hip and Total Knee Arthroplasty: A Call for a Prospective Randomized Trial', *The Journal of Arthroplasty*, 34(8), pp. 1815-1822.
- Herrera, M., Artunduaga, J., Ortiz, C., and Torres, R., 2017, 'Síntesis de nanopartículas de ácido poliláctico cargadas con antibióticos y su actividad antibacteriana contra Escherichia coli O157:H7 y Staphylococcus aureus resistente a meticilina', *Biomédica*, , pp. 11-21.
- Heufelder, M., Wilde, F., Pietzka, S., Mascha, F., Winter, K., Schramm, A., and Rana, M., 2017, 'Clinical accuracy of waferless maxillary positioning using customized surgical guides and patient specific osteosynthesis in bimaxillary orthognathic surgery', *Journal of Cranio-Maxillofacial Surgery*, 45(9), pp. 1578-1585.
- Hickock, N. and Shapiro, I., 2012, 'Immobilized antibiotics to prevent orthopaedic implant infections', *Advanced Drug Delivery Reviews*, 64(12), pp. 1165-1176.
- Hocking, L., Pramanik, A., Basak, A., and Chattopadhyaya, S., 2019, '2 - Designing and analysis of the femoral neck for an artificial hip joint prosthesis', In: J. Davim, ed. *Mechanical Behaviour of Biomaterials*. Aveiro: Woodhead Publishing, pp. 47-65.

- Høiby, N., Bjarnsholt, T., Givskov, M., Molin, S., and Ciofu, O., 2010, 'Antibiotic resistance of bacterial biofilms', *International Journal of Antimicrobial Agents*, 35(4), pp. 322-332.
- Holmström, J., Partanen, J., Tuomi, J., and Walter, M., 2010, 'Rapid manufacture in the spare parts supply chain: Alternative approaches to capacity deployment', *Journal of Manufacturing Technology Management*, 21(6), pp. 689-697.
- Hsieh, P.-H., Shih, C.-H., Chang, Y.-H., Lee, M.S., Yang, W.-E., and Shih, H.-N., 2004, 'Treatment of deep infection of the hip associated with massive bone loss: Two-stage revision with an antibiotic-loaded interim cement prosthesis followed by reconstruction with allograft', *The Journal of Bone & Joint Surgery (Br)*, 87-B(6), pp. 770-775.
- Hsu, Y.-H., Chen, D.W.-C., Li, M.-J., Yu, Y.-H., Chou, Y.-C., and Liu, S.-J., 2018, 'Sustained Delivery of Analgesic and Antimicrobial Agents to Knee Joint by Direct Injections of Electrospayed Multipharmaceutical-Loaded Nano/Microparticles', *Polymers*, 10(8), 16 pp.
- Hugo, P., Bezuidenhout, M., Oosthuizen, G., and Dimitrov, D., 2018. *Conceptual DFAM Frameworks for Part Life Cycle Resource Efficiency*. Berlin, Fraunhofer DDMC.
- Hu, H., Zhang, W., Qiao, Y., Jiang, X., Liu, X., and Ding, C., 2012, 'Antibacterial activity and increased bone marrow stem cell functions of Zn-incorporated TiO<sub>2</sub> coatings on titanium', *Acta Biomaterialia*, 8(2), pp. 904-915.
- Hu, L., Sun, Y., and Wu, Y., 2013, 'Advances in chitosan-based drug delivery vehicles', *Nanoscale*, 5, pp. 3103-3111.
- Iooss, P., Le Ray, A.-M., Grimandi, G., Daclusi, G., and Merle, C., 2001, 'A new injectable bone substitute combining poly( $\epsilon$ -caprolactone) microparticles with biphasic calcium phosphate granules', *Biomaterials*, 22(20), pp. 2785-2794.
- ISO 7206-4:2002(E), 2002. *Implants for surgery - Partial and total hip joint prostheses - Part4: Determination of endurance properties of stemmed femoral components*. Genève: ISO
- Jardini, A.L., Larosa, M.A., Filho, R.M., Zavaglia, C.A.D.C., Bernardes, L.F., Lambert, C.S., Calderoni, D.R., and Kharmandayan, P., 2014, 'Cranial reconstruction: 3D biomodel and custom-built implant created using additive manufacturing', *Journal of Cranio-Maxillofacial Surgery*, 42(8), pp. 1877-1884.
- Jeon, G., Yang, S., and Kim, J., 2012, 'Functional nanoporous membranes for drug delivery', *Journals of Materials Chemistry*, 22, pp. 24959-25506.

- Jhan, S., Lu, Y.-D., Lee, M.S., Lee, C.-H., Wang, J.-W., and Kuo, F.-C., 2017, 'The risk factors of failed reimplantation arthroplasty for periprosthetic hip infection', *BMC Musculoskeletal Disorders*, 18(255), 7 pp.
- Jiang, J., Xu, X., and Stringer, J., 2018, 'Support Structures for Additive Manufacturing: A Review', *Journal of Manufacturing and Materials Processing*, 2(4), 23 pp.
- Jiranek, W., Waligora, A., Hess, S., and Golladay, G., 2015, 'Surgical Treatment of Prosthetic Joint Infections of the Hip and Knee: Changing Paradigms?', *The Journal of Arthroplasty*, 30, pp. 912-918.
- Junaidah, A.S., Suhaini, S., Sidek, H.M., Basri, D.F., and Zin, N.M, 2015, 'Anti-Methicillin Resistant Staphylococcus aureus Activity and Optimal Culture Condition of Streptomyces sp. SUK 25', *Jundishapur Journal of Microbiology*, 8(5), e16784.
- Kamath, S., Bhattacharyya, D., Padukudru, C., Timmons, R.B., and Tang, L., 2008, 'Surface chemistry influences implant-mediated host tissue responses', *Journal of Biomedical Materials Research Part A*, 86A(3), pp. 617-626.
- Kandala, N.-B., Connock, M., Pulikottil-Jacob, R., Crowther, M.J., Grove, A., and Clarke, A., 2015, 'Setting benchmark revision rates for total hip replacement: analysis of registry evidence', *BMJ*, 350(h756), 16 pp.
- Kapadia, B.H., Banerjee, S., Cherian, J.J., Bozic, K.J., and Mont, M., 2016, 'The Economic Impact of Periprosthetic Infections After Total Hip Arthroplasty at a Specialized Tertiary-Care Center', *The Journal of Arthroplasty*, 31(7), pp. 1422-1426.
- Kapadia, B.H., Berg, R.A., Daley, J.A., Fritz, J., Bhave, A., and Mont, M.A., 2016, 'Periprosthetic joint infection', *The Lancet*, 387(10016), pp. 386-394.
- Kapoor, D.N., Bhatia, A., Kaur, R., Sharma, R., Kaur, G., and Dhawan, S., 2015, 'PLGA: a unique polymer for drug delivery', *Therapeutic Delivery*, 6(1), pp. 41-58.
- Kärrholm, J., Lindahl, H., Malchau, H., Mohaddes, M., Nemes, S., Rogmark, C., and Rolfson, O., 2018. *The Swedish Hip Arthroplasty Register Annual Report 2016*, Swedish Hip Arthroplasty Register.
- Kasimanickam, R.K., Ranjan, A., Asokan, G.V., Kasimanickam, V.R., and Kastelic, J.P., 2013, 'Prevention and treatment of biofilms by hybrid- and nanotechnologies', *International Journal of Nanomedicine*, 8, pp. 2809-2819.

- Kaspar, J., Bechtel, S., Häfele, T., Herter, F., Schneberger, J., Bähre, D., Griebisch, J., Hermann, H.-G., and Vielhaber, M., 2019, 'Integrated Additive Product Development for Multi-Material Parts', *Procedia Manufacturing*, 33, pp. 3-10.
- Kaspar, J., Stoffels, P., Schneberger, J.-H., and Vielhaber, M., 2018, *Early Phase Evaluation of Additive Manufacturing Technologies Within an Integrated Product and Production Engineering Approach*. Dubrovnik, International Design Conference - Design 2018.
- Kasperovich, G., Haubrich, J., Gussome, J., and Requena, G., 2016, 'Correlation between porosity and processing parameters in Ti6Al4V produced selective laser melting', *Materials & Design*, 105, pp. 160-170.
- Kasperovich, G. and Hausmann, J., 2015, 'Improvement of fatigue resistance and ductility of TiAl6V4 processed by selective laser melting', *Journal of Materials Processing Technology*, 220, pp. 202-214.
- Kelm, J., Anagostakos, K., Regitz, T., Schmitt, E., Schneider, G., and Ahlhelm, F., 2004, 'MRSA-Infektionen des Bewegungsapparats - Behandlung mit intraoperativ herstellbaren Gentamicin-Vancomycin-PMMA-Ketten', *Der Chirurgie*, 75, pp. 988-995.
- Khairallah, S., Anderson, A., Rubenchik, A., and King, W., 2016, 'Laser powder-bed fusion additive manufacturing: Physics of complex metal flow and formation mechanisms of pores, spatter, and denudation zones', *Acta Materialia*, 108, pp. 36-45.
- Kheir, M.M., Tan, T.L., Gomez, M.M., Chen, A.F., and Parvizi, J., 2017, 'Patients With Failed Prior Two-Stage Exchange Have Poor Outcomes After Further Surgical Intervention', *The Journal of Arthroplasty*, 32(4), pp. 1262-1265.
- Kiamco, M.M., Mohamed, A., Reardon, P.N., Marean-Reardon, C.J., Aframehr, W.M., Call, D.R., Beyenal, H., Renslow, R.S., 2018, 'Structural and metabolic responses of *Staphylococcus aureus* biofilms to hyperosmotic and antibiotic stress', *Biotechnology and Bioengineering*, 115(6), pp. 1594-1603.
- Kim, D., Witherell, P., Lipman, R., and Feng, S., 2015, 'Streamlining the additive manufacturing digital spectrum: A systems approach', *Additive Manufacturing*, 5, pp. 20-30.
- Kliushin, N., Ababkov, Y., Ermakov, A., and Malkova, T., 2016, 'Modified Girdlestone arthroplasty and hip arthrodesis using the Ilizarov external fixator as a salvage method in the management of severely infected total hip replacement', *Indian Journal of Orthopaedics*, 50(1), pp. 16-24.

- Klouche, S. Leonard, P., Zeller, V., Lhotellier, L., Graff, W., Leclerc, P., Mamoudy, P., and Sariali, E., 2012, 'Infected total hip arthroplasty revision: One- or two-stage procedure?', *Orthopaedics & Traumatology: Surgery & Research*, 98(2), pp. 144-150.
- Klouche, S., Sariali, E., and Mamoudy, P., 2010, 'Total hip arthroplasty revision due to infection: A cost analysis approach', *Orthopaedics & Traumatology: Surgery & Research*, 96(2), pp. 124-132.
- Kluin, O., van der Mei, H., Busscher, H., and Neut, D., 2013, 'Biodegradable vs non-biodegradable antibiotic delivery devices in the treatment of osteomyelitis', *Expert Opinion on Drug Delivery*, 10(3), pp. 341-351.
- Kok, Y., Tan, X.P., Wang, P., Nai, M.L.S., Loh, N.H., Liu, E., and Tor, S.B., 2018, 'Anisotropy and heterogeneity of microstructure and mechanical properties in metal additive manufacturing: A critical review', *Materials and Design*, 139, pp. 565-586.
- Kolb, T., Müller, L., Tremel, J., and Schmidt, M., 2018, 'Melt pool monitoring for laser beam melting of metals: inline-evaluation and remelting of surfaces', *Procedia CIRP*, 74, pp. 111-115.
- Kranz, J., Herzog, D., and Emmelmann, C., 2015. 'Design guidelines for laser additive manufacturing of lightweight structures in Ti6Al4V', *Journal of Laser Applications*, 27(S1), pp. S14001- 1-16.
- Krehmer, H., Eckstein, R., Lauer, W., Roelofsen, J., Stöber, C., Troll, A., Weber, N., and Zapf, J., 2009. *Coping with Multidisciplinary Product Development - a Process Model Approach*. Stanford, International Conference on Engineering Design, ICED'09.
- Kruth, J.-P., Froyen, L., Van Vaerenbergh, J., Mercelie, P., Rombouts, M., and Lauwers, B., 2004, 'Selective laser melting of iron-based powder', *Journal of Materials Processing Technology*, 149(1-3), pp. 616-622.
- Kumke, M., Watschke, H., and Vietor, T., 2016, 'A new methodological framework for design for additive manufacturing', *Virtual and Physical Prototyping*, 11(1), pp. 3-19.
- Kurtz, S., Hozack, W., Ray, R., and Edidin, A., 2001, *Biomechanical Analysis of Cementing an Acetabular Liner in a Metal Shell for Revision Total Hip Arthroplasty*. San Francisco, 47th Annual Meeting, Orthopaedic Research Society.
- Labek, G., Thaler, M., Janda, W., Agreiter, M., and Stöckl, B., 2011, 'Revision rates after total joint replacement - Cumulative results from worldwide joint register datasets', *The Bone & Joint Journal*, 93-B(3), pp. 293-297.

- Ladewig, A., Schlick, G., Fisser, M., Schulze, V., and Glatzel, U., 2016, 'Influence of the shielding gas flow on the removal of process by-products in the selective laser melting process', *Additive Manufacturing*, 10, pp. 1-9.
- Lai, K.-A., Shen, W.-J., Yang, C.-Y., Lin, R.-M., Lin, C.-J., and Jou, I.-M., 1996, 'Two-stage cementless revision THR after infection: 5 recurrences in 40 cases followed 2.5 - 7 years', *Acta Orthopaedica Scandinavica*, 67(4), pp. 325-328.
- Lanao, R.P.F., Jonker, A.M., Wolke, J.G.C., Jansen, J.A., van Hest, J.C.M., and Leeuwenburgh, S.C.G., 2013, 'Physicochemical Properties and Applications of Poly(lactic-co-glycolic acid) for Use in Bone Regeneration', *Tissue Engineering: Part B*, 19(4), pp. 380-390.
- Lan, Y., Li, W., Guo, R., Zhang, Y., Xue, W., and Zhang, Y., 2013, 'Preparation and characterisation of vancomycin-impregnated gelatin microspheres/silk fibroin scaffold', *Journal of Biomaterials Science, Polymer Edition*, 25(1), pp. 75-87.
- Laupacis, A., Bourne, R., Rorabeck, C., Feeny, D., Tugwell, P., and Wong, C., 2002, 'Comparison of Total Hip Arthroplasty Performed with and without Cement', *The Journal of Bone and Joint Surgery, Incorporated*, 84-A(10), pp. 1823-1828.
- Laverne, F., Segonds, F., D'Antonio, G., and Le Coq, M., 2017, 'Enriching design with X through tailored additive manufacturing knowledge: a methodological proposal', *International Journal on Interactive Design and Manufacturing*, 11(2), pp. 279-288.
- Le Ray, A.-M., Chiffolleau, S., Iooss, P., Grimandi, G., Gouyette, A., Daculsi, G., and Merle, C., 2003, 'Vancomycin encapsulation in biodegradable poly( $\epsilon$ -caprolactone) microparticles for bone implantation. Influence of the formulation process on size, drug loading, in vitro release and cytocompatibility', *Biomaterials*, 24(3), pp. 443-449.
- Le Ray, A.-M., Gautier, H., Laty, M.-K., Daculsi, G., Merle, C., Jacqueline, C., Hamel, A., and Caillon, J., et al., 2005, 'In Vitro and In Vivo Bactericidal Activities of Vancomycin Dispersed in Porous Biodegradable Poly( $\epsilon$ -Caprolactone) Microparticles', *Antimicrobial Agents and Chemotherapy*, 49(7), pp. 3025-3027.
- Learnmonth, I., Young, C., and Rorabeck, C., 2007, 'The operation of the century: total hip replacement', *The Lancet*, 370(9597), pp. 1508-1519.
- Lee, C., 2005, 'Properties of Bone Cement: The Mechanical Properties of PMMA Bone Cement', In: S. Breusch & H. Malchau, eds. *The Well-Cemented Total Hip Arthroplasty*. Berlin: Springer, pp. 60-66.

- Le, K. and Otto, M., 2015, 'Quorum-sensing regulation in staphylococci - and overview', *Frontiers in Microbiology*, 6, 8 pp.
- Lembach, A.N., Tan, H.-B., Roisman, I.V., Gambaryan-Roisman, T., Zhang, Y., Tropea, C., and Yarin, A.L., 2010, 'Drop Impact, Spreading, Splashing, and Penetration into Electrospun Nanofiber Mats', *Langmuir*, 26(12), pp. 9516-9523.
- Lenguerrand, E., Whitehouse, M.R., Beswick, A.D., Jones, S.A., Porter, M.L., and Blom, A.W., 2017, 'Revision for prosthetic joint infection following hip arthroplasty: Evidence from the National Joint Registry', *Bone and Joint Research*, 6(6), pp. 391-398.
- Leuders, S., Lieneke, T., Lammers, S., Tröster, T., and Niendorf, T., 2014, 'On the fatigue properties of metals manufactured by selective laser melting - The role of ductility', *Journal of Materials Research*, 29(17), pp. 1911-1919.
- Lin, C., Qiao, S.Z., Yu, C.Z., Ismadji, S., and Lu, G.Q., 2009, 'Periodic mesoporous silica and organosilica with controlled morphologies as carriers for drug release', *Microporous and Mesoporous Materials*, 117(1-2), pp. 213-219.
- Li, P., Warner, D., Fatemi, A., and Phan, N., 2016, 'Critical assessment of the fatigue performance of additively manufactured Ti-6Al-4V and perspective for future research', *International Journal of Fatigue*, 85, pp. 130-143.
- Lister, J. and Horswill, A., 2014, 'Staphylococcus aureus biofilms: recent developments in biofilm dispersal', *Frontiers in Cellular and Infection Microbiology*, 4, 9 pp.
- Li, T., Wang, N., Chen, S., Lu, R., Li, H., and Zhang, Z., 2017, 'Antibacterial activity and cytocompatibility of an implant coating consisting of TiO<sub>2</sub> nanotubes combined with a GL13K antimicrobial peptide', *International Journal of Nanomedicine*, 12, pp. 2995-3007.
- Liu, S. and Shin, Y., 2019, 'Additive manufacturing of Ti6Al4V alloy: A review', *Materials and Design*, 164, 23 pp.
- Liu, S.-J., Ueng, S.-N., Lin, S.-S., and Chan, E.-C., 2002, 'In vivo release of vancomycin from biodegradable beads', *Journal of Biomedical Materials Research*, 63(6), pp. 807-813.
- Liu, Z., Zhu, Y., Liu, X., Yeung, K.W.K., and Wu, S., 2017, 'Construction of poly (vinyl alcohol)/poly (lactide-glycolide acid)/vancomycin nanoparticles on titanium for enhancing the surface self-antibacterial activity and cytocompatibility', *Colloids and Surfaces B: Biointerfaces*, 151, pp. 165-177.

- Li, W., Ding, Y., Rai, R., Roether, J.A., Schubert, D.W., and Boccaccini, A.R., 2014, 'Preparation and characterization of PHBV microsphere/45S5 bioactive glass composite scaffolds with vancomycin releasing function', *Materials Science and Engineering: C*, 41, pp. 320-328.
- Li, Y., Na, R., Wang, X., Liu, H., Zhao, L., Sun, X., Ma, G., and Ciu, F., 2017, 'Fabrication of Antimicrobial Peptide-Loaded PLGA/Chitosan Composite Microspheres for Long-Acting Bacterial Resistance', *Molecules*, 22(10), p. 1637.
- Li, Z., Kucukkoc, I., Zhang, D., and Liu, F., 2018, 'Optimising the process parameters of selective laser melting for the fabrication of Ti6Al4V alloy', *Rapid Prototyping Journal*, 24(1), pp. 150-159.
- Lombardi Jr, A., Berend, K., and Adams, J., 2014, 'Why knee replacements fail in 2013. *The Bone & Joint Journal*, 96-B(11 Supplement A), pp. 101-104.
- Long, M. and Rack, H., 1998, 'Titanium alloys in total joint replacement - a materials science perspective', *Biomaterials*, 19(18), pp. 1621-1639.
- Luo, P., Wang, S.-N., Zhao, T.-T., and Li, Y., 2013, 'Surface characteristics, corrosion behavior, and antibacterial property of Ag-implanted NiTi alloy', *Rare Metals*, 32, pp. 113-121.
- Luthringer, T.A., Fillingham, Y.A., Okroj, K., Ward, E.J., and Della Valle, C., 2016, 'Periprosthetic Joint Infection After Hip and Knee Arthroplasty: A Review for Emergency Care Providers', *Annals of Emergency Medicine*, 68(3), pp. 324-334.
- Lütjering, G. and Williams, J., 2007. *Titanium*. 2nd Edition ed. Berlin: Springer-Verlag Berlin Heidelberg.
- Lyndon, J., Boyd, B., and Birbilis, N., 2014, 'Metallic implant drug/device combinations for controlled drug release in orthopaedic applications', *Journal of Controlled Release*, 179, pp. 63-75.
- Ma, D., Lin, F., and Chua, C., 2001, 'Rapid Prototyping Applications in Medicine. Part 2: STL File Generation and Case Studies', *International Journal of Advanced Manufacturing Technology*, 18, pp. 118-127.
- Maher, S., Kaur, G., Lima-Marques, L., Evdokiou, A., and Losic, D., 2017, 'Engineering of Micro- to Nanostructured 3D-Printed Drug-Releasing Titanium Implants for Enhanced Osseointegration and Localized Delivery of Anticancer Drugs', *ACS Applied Materials and Interfaces*, 9(35), pp. 29562-29570.

- Makadia, H. & Siegel, S., 2011, 'Poly Lactic-co-Glycolic Acid (PLGA) as a Biodegradable Controlled Drug Delivery Carrier', *Polymers*, 3(3), pp. 1377-1397.
- Mancuso, C.A, Ranawat, C.S., Esdaile, J.M., Johanson, N.A., and Charlson, M.E., 1996, 'Indications for total hip and total knee arthroplasties: Results of orthopaedic surveys', *The Journal of Arthroplasty*, 11(1), pp. 34-46.
- Martin, A.A., Calta, N.P., Khairallah, S.A., Wang, J., Depond, P.J., Fong, A.Y., Thampy, V., Guss, G.M., Kiss, A.M., Stone, K.H., Tassone, C.J., Weker, J.N., Toney, M.F., van Buuren, T., and Matthews, M.J., 2019, 'Dynamics of pore formation during laser powder bed fusion additive manufacturing', *Nature Communications*, 10(1987), 10 pp.
- Mascaretti, O., 2003, Inhibitors of Peptidoglycan Biosynthesis - Bacitracin and Glycopeptides. In: *Bacteria versus Antibacterial Agents - An Integrated Approach*. Washington(District of Columbia): ASM Press, pp. 203-214.
- Masri, B. and Salvati, E., 1998. Sepsis: Two-Stage Exchange. In: J. Callaghan, A. Rosenberg & H. Rubash, eds. *The Adult Hip: Volume II*. Philadelphia: Lippincott-Raven, pp. 1317-1330.
- Masuo, H., Tanaka, Y., Morokoshi, S., Yagura, H., Uchida, T., Yamamoto, Y., and Murakami, Y., 2018, 'Influence of defects, surface roughness and HIP on the fatigue strength of Ti-6Al-4V manufactured by additive manufacturing', *International Journal of Fatigue*, 117, pp. 163-179.
- Materialise, 2020. *Tutorial Video - What type of STL file errors can occur?*. [Online] Available at: <https://www.materialise.com/en/academy/software/magics/what-type-of-stl-file-errors-can-occur>  
[Accessed 3 May 2020].
- McGaffey, M., zur Linden, A., Bachynski, N., Oblak, M., James, F., and Weese, J.S., 2019, 'Manual polishing of 3D printed metals produced by laser powder bed fusion reduces biofilm formation', *PLoS ONE*, 14(2), 19 pp.
- Meehan, J., Jamali, A., and Nguyen, H., 2009, 'Prophylactic Antibiotics in Hip and Knee Arthroplasty', *The Journal of Bone and Joint Surgery, Incorporated*, 91-A(10), pp. 2480-2489.
- Mierzejewska, Z., 2019, 'Effect of Laser Energy Density, Internal Porosity and Heat Treatment on Mechanical Behavior of Biomedical Ti6Al4V Alloy Obtained with DMLS Technology', *Materials*, 12(14), 23 pp.

- Mingareev, I. and Richardson, M., 2017, 'Laser Additive Manufacturing Going Mainstream', Volume February 2017, pp. 24-31.
- Mirzendehtel, A. and Suresh, K., 2016, 'Support structure constrained topology optimization for additive manufacturing', *Computer-Aided Design*, 81, pp. 1-13.
- Mohammed, A., Elshaer, A., Sareh, P., Elsayed, M., and Hassanin, H., 2020, 'Additive Manufacturing Technologies for Drug Delivery Applications', *International Journal of Pharmaceutics*, 580, 24 pp.
- Mojab, F., Poursaeed, M., Mehragan, H., and Pakdaman, S., 2008, 'Antibacterial activity of Thymus daenensis methanolic extract', *Pakistan Journal of Pharmaceutical Sciences*, 21(3), pp. 210-213.
- Montgomery, D. and Runger, G., 2007, *Applied Statistics and Probability for Engineers*. 4th Edition ed. Hoboken: John Wiley & Sons, Inc..
- Mooney, J.A, Manasherob, R., Smeriglio, P., Bhutani, N., and Amanatullah, D.F., 2019, 'Effect of trabecular metal on the elution of gentamicin from Palacos cement', *Journal of Orthopaedic Research*, 37(5), pp. 1018-1024.
- Müller, B., Töppel, T., Rotsch, C., Böhm, A., Bräunig, J., and Neugebauer, R., 2012, 'New features and functions in implants through an innovative design approach and additive manufacturing technology', Brescia, PROMED, pp. 237-241.
- Murdoch, D.R., Roberts, S.A., Fowler, V.G., Shah, M.A., Taylor, S.L., Morris, A.J., and Corey, G.R., 2001, 'Infection of Orthopedic Prostheses after Staphylococcus aureus Bacteremia', *Clinical Infectious Diseases*, 32(4), pp. 647-649.
- Murr, L.E., Gaytan, S.A., Martinez, E., Medina, F., and Wicker, R.B., 2012, 'Next Generation Orthopaedic Implants by Additive Manufacturing Using Electron Beam Melting', *International Journal of Biomaterials*, 2012(245727), 14 pp.
- Murr, L.E., Quinones, S.A., Gaytan, S.M., Lopez, M.I., Rodela, A., Martinez, E.Y., Hernandez, D.H., Martinez, E., Medina, F., and Wicker, R.B., 2009, 'Microstructure and mechanical behavior of Ti-6Al-4V produced by rapid-layer manufacturing, for biomedical applications', *Journal of the Mechanical Behavior of Biomedical Materials*, 2(1), pp. 20-32.
- Myers, R. & Montgomery, D., 2002, *Response Surface Methodology Process and Product Optimization Using Designed Experiments*. 2nd ed. New York: John Wiley & Sons, Inc..

- Nettey, H., Haswani, D., Oettinger, C., and D'Souza, M., 2006, 'Formulation and testing of vancomycin loaded albumin microspheres prepared by spray-drying', *Journal of Microencapsulation*, 23(6), pp. 632-642.
- Nett, M., 2015, 'Single-Stage Revision Total Hip Arthroplasty', In: *Techniques in Revision Hip and Knee Arthroplasty*. Philadelphia: Elsevier Saunders, pp. 586-591.
- Neut, D., Dijkstra, R.J.B., Thompson, J.I., van der Mei, H.C., and Busscher, H.J., 2011, 'Antibacterial efficacy of a new gentamicin-coating for cementless prostheses compared to gentamicin-loaded bone cement', *Journal of Orthopaedic Research*, 29(11), pp. 1654-1661.
- Nickels, L., 2012, 'World's first patient-specific jaw implant', *Metal Powder Report*, March/April, 67(2), pp. 12-14.
- Ohldin, P., 2010, *Series Production of CE-Certified Orthopedic Implants with Integrated Porous Structures for Improved Bone Ingrowth*. Vienna, DAAAM International.
- Oliveira, W.F., Silva, P.M.S., Silva, R.C.S., Silva, G.M.M., Machada, Coelho, L.C.B.B., and Correia, M.T.S., 2018, 'Staphylococcus aureus and Staphylococcus epidermidis infections on implants', *Journal of Hospital Infection*, 98(2), pp. 111-117.
- Osmon, D.R., Berbari, E.F., Berendt, A.R., Lew, D., Zimmerli, W., Steckelberg, J.M., Rao, N., Hanssen, A., and Wilson, W.R., 2013, 'Diagnosis and Management of Prosthetic Joint Infection: Clinical Practice Guidelines by the Infectious Diseases Society of America', *Clinical Infectious Diseases*, 56(1), pp. e1-e25.
- Otto, M., 2013, 'Staphylococcal Infections: Mechanisms of Biofilm Maturation and Detachment as Critical Determinants of Pathogenicity', *Annual Review of Medicine*, 64, pp. 175-188.
- Oyesola, M., Mpofu, K., Mathe, N., and Daniyan, I., 2019, 'Development of an integrated design methodology model for quality and throughput of Additive Manufacturing processes', *Procedia CIRP*, 84, pp. 688-693.
- Özalp, Y., Özdemir, N., Kocagöz, S., and Hasirci, V., 2001, 'Controlled release of vancomycin from biodegradable microcapsules', *Journal of Microencapsulation*, 18(1), pp. 89-110.
- Pahl, G. & Beitz, W., 1988, *Engineering Design: A Systematic Approach*. Revised Edition (English) ed. Berlin: Springer-Verlag.

- Park, R., 2018, *Progressing Orthopedic Implants with Additive Manufacturing*. [Online] Available at: <https://www.3dprintingmedia.network/progressing-orthopedic-implants-additive-manufacturing/> [Accessed 26 11 2018].
- Parvizi, J., Pawasarat, I.M., Azzam, K.A., Joshi, A., Hansen, E.N., and Bozic, K.J., 2010, 'Periprosthetic Joint Infection: The Economic Impact of Methicillin-Resistant Infections', *The Journal of Arthroplasty*, 25(6 Supplement 1), pp. 103-107.
- Patel, H., Khoury, H., Girgenti, D., Welner, S., and Yu, H., 2016, 'Burden of Surgical Site infections Associated with Arthroplasty and the Contribution of Staphylococcus aureus', *Surgical Infections*, 17(1), pp. 78-88.
- Patti, J., Allen, B., McGavin, M., and Höök, M., 1994, 'MSCRAMM-Mediated Adherence of Microorganisms to Host Tissues', *Annual Review of Microbiology*, 48, pp. 585-617.
- Percival, S.L., Thomas, J.G., Slone, W., Linton, S., Corum, L., and Okel, T., 2011, 'The efficacy of silver dressings and antibiotics on MRSA and MSSA isolated from burn patients', *Wound Repair and Regeneration*, 19(6), pp. 767-774.
- Perez, L.M., Lalueza, P., Monzon, M., Puertolas, J.A., Arruebo, M., and Santamaria, J., 2011, 'Hollow porous implants filled with mesoporous silica particles as a two-stage antibiotic-eluting device', *International Journal of Pharmaceutics*, 409, pp. 1-8.
- Pesewu, G., Cutler, R., and Humber, D., 2008, 'Antibacterial activity of plants used in traditional medicines of Ghana with particular reference to MRSA', *Journal of Ethnopharmacology*, 116(1), pp. 102-111.
- Petrovic, V., Gonzalez, J.V.H., Ferrando, O.J., Gordillo, J.D., Puchades, J.R.B., and Grinan, L.P., 2011, 'Additive layered manufacturing: sectors of industrial application shown through case studies', *International Journal of Production Research*, February, 49(4), pp. 1061-1079.
- Petrovic, V., Haro, J., Blasco, J., and Portolés, L., 2012, 'Additive Manufacturing Solutions for Improved Medical Implants', In: C. Lin, ed. *Biomedicine*. InTech, pp. 147-180.
- Ploeg, H.-L., Bürgi, M., and Wyss, U., 2009, 'Hip stem fatigue test prediction', *International Journal of Fatigue*, 31(5), pp. 894-905.

- Post, V., Wahl, P., Richards, R., and Moriarty, T., 2017, 'Vancomycin displays time-dependent eradication of mature *Staphylococcus aureus* biofilms', *Journal of Orthopaedic Research*, 35(2), pp. 381-388.
- Prajapati, V., Jani, G., and Kapadia, J., 2015, 'Current knowledge on biodegradable microspheres in drug delivery', *Expert Opinion on Drug Delivery*, 12(8), pp. 1283-1299.
- Puhto, A.-P., Puhto, T.M., Niinimäki, T.T., Leppilahti, J.I., and Syrjälä, H.P.T., 2014, 'Two-Stage Revision for Prosthetic Joint Infection: Outcome and Role of Reimplantation Microbiology in 107 Cases', *The Journal of Arthroplasty*, 29(6), pp. 1101-1104.
- Qiu, C., Adkins, N., and Attallah, M., 2013, 'Microstructure and tensile properties of selective laser-melted and HIPed laser-melted Ti-6Al-4V', *Materials Science & Engineering A*, 578, pp. 230-239.
- Rack, H. and Qazi, J., 2006, 'Titanium alloys for biomedical applications', *Materials Science and Engineering: C*, 2006(8), pp. 1269-1277.
- Rafi, H.K., Karthik, N.V., Gong, H., Starr, T.L., and Stucker, B.E., 2013, 'Microstructures and Mechanical Properties of Ti6Al4V Parts Fabricated by Selective Laser Melting and Electron Beam Melting', *Journal of Materials Engineering and Performance*, 22(12), pp. 3872-3883.
- Rai, A., Senapati, S., Saraf, S., and Maiti, P., 2016, 'Biodegradable poly( $\epsilon$ -caprolactone) as a controlled drug delivery vehicle of vancomycin for the treatment of MRSA infection', *Journal of Materials Chemistry B*, 4(30), pp. 5151-5160.
- Ramchandani, M. and Robinson, D., 1998, 'In vitro and in vitro release of ciprofloxacin from PLGA 50:50 implants', *Journal of Controlled Release*, 54(2), pp. 167-175.
- Raphel, J., Holodniy, M., Goodman, S., and Heilshorn, S., 2016, 'Multifunctional coatings to simultaneously promote osseointegration and prevent infection of orthopaedic implants', *Biomaterials*, 84, pp. 301-314.
- Rava, A., Bruzzone, M., Cottino, U., Enrietti, E., and Rossi, R., 2019, 'Hip Spacers in Two-Stage Revision for Periprosthetic Joint Infection: A Review of Literature', *Joints*, 7(2), pp. 56-63.
- Renjith, S., Park, K., and Kremer, G., 2020, 'A Design Framework for Additive Manufacturing: Integration of Additive Manufacturing Capabilities in the Early Design Process', *International Journal of Precision Engineering and Manufacturing*, 21, pp. 329-345.
- Rezapoor, M. and Parvizi, J., 2015, 'Prevention of Periprosthetic Joint Infection', *The Journal of Arthroplasty*, 30(6), pp. 902-907.

- Rias, A.-L., Bouchard, C., Segonds, F., and Abed, S., 2016, '*Design for Additive Manufacturing: A Creative Approach*', Dubrovnik, The Design Society.
- Roach, R.A., Bishop, J.E., Johnson, K., Rodgers, T., Boyce, B.L., Swiler, L.P., van Bloemen Waanders, B.G., Chandross, M.E., Kammler, D., Balch, D.K., Jared, B.H., Martinez, M.J., Leathe, N., and Ford, K.R., 2018, '*Using additive manufacturing as a pathway to change the qualification paradigm*', [Online] Available at: <https://www.osti.gov/servlets/purl/1532627> [Accessed 6 May 2020].
- Rochford, E., Richards, R., and Moriarty, T., 2012, 'Influence of material on the development of device-associated infections', *Clinical Microbiology and Infection*, 18(12), pp. 1162-1167.
- Romanò, C., Romanò, D., Logoluso, N., and Meani, E., 2010, 'Septic versus aseptic hip revision: how different?', *Journal of Orthopaedics and Traumatology*, 11(3), pp. 167-174.
- Rosen, D., 2007, '*Design for Additive Manufacturing: A Method to Explore Unexplored Regions of the Design Space*', Austin, Solid Freeform Fabrication Symposium, pp. 402-415.
- Rumian, L., Tiainen, H., Cibor, U., Krok-Borkowicz, Brzychczy-Wloch, M., Haugen, H.J., and Pamula, E., 2017, 'Ceramic scaffolds with immobilized vancomycin-loaded poly(lactide-co-glycolide) microparticles for bone defects treatment', *Materials Letters*, 190, pp. 67-70.
- Rupp, F., Gittens, R.A., Scheideler, L., Marmur, A., Boyan, B.D., Schwartz, Z., and Geis-Gerstorfer, J., 2014, 'A review on the wettability of dental implant surfaces I: Theoretical and experimental aspects', *Acta Biomaterialia*, 10(7), pp. 2897-2906.
- Ryu, T.-K., Jun, D.-R., Kim, S., and Choi, S.-W., 2014, 'Sustained release of antibiotics from uniform poly( $\epsilon$ -caprolactone) microspheres prepared by a simple fluidic device with a tapered glass capillary', *Journal of Bioactive and Compatible Polymers*, 29(4), pp. 318-329.
- Sahiner, N., Suner, S., and Ayyala, R., 2019, 'Mesoporous, degradable hyaluronic acid microparticles for sustainable drug delivery application', *Colloids and Surfaces B: Biointerfaces*, 177, pp. 284-293.
- Saiful, A., Mastura, M., Mazurah, M., and Nuziah, H., 2011, 'Inhibitory Potential Against Methicillin-Resistant Staphylococcus aureus (MRSA) of Dolichandrone spathacea, a Mangrove Tree Species of Malaysia', *Latin American Journal of Pharmacy*, 30(2), pp. 359-362.
- Salih, S. and Hamer, A., 2013, 'Hip and knee replacement', *Surgery (Oxford)*, 31(9), pp. 482-487.

- Salmi, A., Calignano, F., Galati, M., and Atzeni, E., 2018, 'An integrated design methodology for components produced by laser powder bed fusion (L-PBF) process', *Virtual and Physical Prototyping*, 13(3), pp. 191-202.
- Sarigöl, E., Pehlivan, S.B., Ekizoglu, M., Sagiriglu, M., and Calis, M., 2017, 'Design and evaluation of gamma-sterilized vancomycin hydrochloride-loaded poly( $\epsilon$ -caprolactone) microspheres for the treatment of biofilm-based medical device-related osteomyelitis', *Pharmaceutical Development and Technology*, 22(6), pp. 706-714.
- Sarker, A., Tran, N., Rifai, A., Brandt, M., Tran, P.A., Leary, M., Fox, K., and Williams, R., 2019, 'Rational design of additively manufactured Ti6Al4V implants to control *Staphylococcus aureus* biofilm formation', *Materialia*, 5(100250), 13 pp.
- Sayin, B., Calis, S., Atilla, B., Marangoz, S., and Hincal, A.A., 2006, 'Implantation of vancomycin microspheres in blend with human/rabbit bone grafts to infected bone defects', *Journal of Microencapsulation*, 23(5), pp. 553-566.
- Scharfenberger, A., Clark, M., Lavoie, G., O'Connor, G., Masson, E., and Beaupre, L., 2007, 'Treatment of an infected total hip replacement with the PROSTALAC system Part 1: Infection resolution', *Canadian Journal of Surgery*, 50(1), pp. 24-28.
- Schmidt, M., Merklein, M., Bourell, D., Dimitrov, D., Hausotte, T., Wegener, K., Overmeyer, L., Vollertsen, F., and Levy, G.N., 2017, 'Laser based additive manufacturing in industry and academia', *CIRP Annals*, 66(2), pp. 561-583.
- Schrage, D., 1999, '*Technology for Rotorcraft Affordability Through Integrated Product/Process Development*', Montreal, The American Helicopter Society 55th Annual Forum.
- Segonds, F., 2018, 'Design By Additive Manufacturing: an application in aeronautics and defence', *Virtual and Physical Prototyping*, 13(4), pp. 237-245.
- Seifi, M., Gorelik, M., Waller, J., Hrabe, N., Shamsaei, N., Daniewicz, S., and Lewandowski, J.J., 2017, 'Progress Towards Metal Additive Manufacturing Standardization to Support Qualification and Certification', *The Journal of The Minerals, Metals & Materials Society*, 69(3), pp. 439-455.
- Shahi, A., Tan, T.L., Chen, A.F., Maltenford, M.G., and Parvizi, J., 2017, 'In-Hospital Mortality in Patients With Periprosthetic Joint Infection', *The Journal of Arthroplasty*, 32(3), pp. 948-952.e1.
- Shah, S., Henslee, A.M., Spicer, P.P., Yokota, S., Petrichenko, S., Allahabadi, S., Bennett, G.N., Wong, M.E., Kasper, F.K., and Mikos, A.G., 2014, 'Effects of Antibiotic Physicochemical Properties

- on Their Release Kinetics from Biodegradable Polymer Microparticles', *Pharmaceutical Research*, 31, pp. 3379-3389.
- Shi, X., Ma, S., Liu, C., Chen, C., Wu, Q., Chen, X., and Lu, J., 2016, 'Performance of High Layer Thickness in Selective Laser Melting of Ti6Al4V', *Materials*, 9(12), 15 pp.
- Shukla, S. and Della Valle, C., 2015, 'Two-Stage Revision Total Hip Arthroplasty', In: *Techniques in Revision Hip and Knee Arthroplasty*. Philadelphia: Elsevier Saunders, pp. 592-597.
- Sing, S., An, J., Yeong, W., and Wiria, F., 2016, 'Laser and Electron-Beam Powder-Bed Additive Manufacturing of Metallic Implants: A Review on Processes, Materials and Designs', *Journal of Orthopaedic Research*, 34(3), pp. 369-385.
- Siopack, J. and Jergesen, H., 1995, 'Total hip arthroplasty', *Western Journal of Medicine*, 162(3), pp. 243-249.
- Soffin, E. and YaDeau, J., 2016, 'Enhanced recovery after surgery for primary hip and knee arthroplasty: a review of the evidence', *British Journal of Anaesthesia*, 117(Supplement 3), pp. iii62-iii72.
- Sola, A. and Nouri, A., 2019, 'Microstructural porosity in additive manufacturing: The formation and detection of pores in metal parts fabricated by powder bed fusion', *Journal of Advanced Manufacturing and Processing*, 1(3), 21 pp.
- Song, B., Dong, S., Zhang, B., Liao, H., and Coddet, C., 2012, 'Effects of processing parameters on microstructure and mechanical property of selective laser melted Ti6Al4V', *Materials and Design*, 35, pp. 120-125.
- Song, R., Murphy, M., Li, C., Ting, K., Soo, C., and Zheng, Z., 2018, 'Current development of biodegradable polymeric materials for biomedical applications', *Drug Design, Development and Therapy*, 2018(12), pp. 3117-3145.
- Spears, T. and Gold, S., 2016, 'In-process sensing in selective laser melting (SLM) additive manufacturing', *Integrating Materials and Manufacturing Innovation*, 5(2), 25 pp.
- Spierings, A., Voegtlin, M., Bauer, T., and Wegener, K., 2016, 'Powder flowability characterisation methodology for powder-bed-based metal additive manufacturing', *Progress in Additive Manufacturing*, 1, pp. 9-20.

- Springer, B., 2015, 'The Diagnosis of Periprosthetic Joint Infection', *The Journal of Arthroplasty*, 30(6), pp. 908-911.
- Springer, B.D., Cahue, S., Etkin, C.D., Lewallen, D.G., and McGrory, B.J., 2017, 'Infection burden in total hip and knee arthroplasties: an international registry-based perspective', *Arthroplasty Today*, 3(2), pp. 137-140.
- Starov, V., Kostvintsev, S.R., Sobolev, V.D., Velarde, M.G., and Zhdanov, S.A., 2002, 'Spreading of Liquid Drops over Dry Porous Layers: Complete Wetting Case', *Journal of Colloid and Interface Science*, 252(2), pp. 397-408.
- Stat-Ease, I., 2020. *Response Transformations*, Minneapolis: Stat-Ease, Inc.
- Stoffels, P., Kaspar, J., Bähre, D., and Vielhaber, M., 2018, 'Integrated Product and Production Engineering Approach - A Tool-Based Method for a Holistic Sustainable Design, Process and Material Selection', *Procedia Manufacturing*, 21, pp. 790-797.
- Strondl, A., Lyckfeldt, O., Brodin, H., and Ackelid, U., 2015, 'Characterization and Control of Powder Properties for Additive Manufacturing', *The Journal of The Minerals, Metals & Materials Society (TMS)*, 67, pp. 549-554.
- Struers, 2016. *Metallographic preparation of titanium*. [Online]  
Available at: <https://www.struers.com/en/Knowledge/Materials/Titanium>  
[Accessed 22 February 2021].
- Sukeik, M. and Haddad, F., 2009, 'Two-stage procedure in the treatment of late chronic hip infections - spacer implantation', *International Journal of Medical Sciences*, 6(5), pp. 253-257.
- Sutton, A., Kriewall, C., Leu, M., and Newkirk, J., 2017, 'Powder characterisation techniques and effects of powder characteristics on part properties in powder-bed fusion processes', *Virtual and Physical Prototyping*, 12(1), pp. 3-29.
- Swearingen, M., Granger, J., Sullivan, A., and Stoodley, P., 2016, 'Elution of antibiotics from poly(methyl methacrylate) bone cement after extended implantation does not necessarily clear the infection despite susceptibility of the clinical isolates', *Pathogens and Disease*, 74(1), pp. 1-4.
- Ter Boo, G.-J.A., Grijpma, D.W., Moriarty, T.F., Richards, R.G., and Eglin, D., 2015, 'Antimicrobial delivery systems for local infection prophylaxis in orthopaedic- and trauma surgery', *Biomaterials*, 52, pp. 113-125.

- Ter Haar, G. and Becker, T., 2018, 'Selective Laser Melting Produced Ti-6Al-4V: Post-Process Heat Treatments to Achieve Superior Tensile Properties', *Materials*, 11(1), 15 pp.
- Thijs, L. V. F., Craeghs, T., Van Humbeeck, J., and Kruth, J.-P., 2010, 'A study of the microstructural evolution during selective laser melting', *Acta Materialia*, 58(9), pp. 3303-3312.
- Thöne, M., Leuders, S., Riemer, A., Tröster, T., and Richard, H.A., 2012, *Influence of heat-treatment on Selective Laser Melting products - e.g. Ti6Al4V*. Austin Texas, Solid freeform fabrication symposium SFF.
- Trampuz, A. and Zimmerli, W., 2005, 'Prosthetic joint infections: update in diagnosis and treatment', *Swiss Medical Weekly*, 135(17-18), pp. 243-251.
- Triantafyllopoulos, G.K., Memtsoudis, S.G., Zhang, W., Ma, Y., Sculco, T.P., and Poultsides, L.A., 2017, 'Periprosthetic Infection Recurrence After 2-Stage Exchange Arthroplasty: Failure or Fate?', *The Journal of Arthroplasty*, 32(2), pp. 526-531.
- Tsang, S., Gwynne, P., Gallagher, M., and Simpson, A., 2018, 'The biofilm eradication activity of acetic acid in the management of periprosthetic joint infection', *Bone & Joint Research*, 7(8), pp. 517-523.
- Tseng, Y.-Y., Kao, C.-W., Liu, K.-S., Tang, Y.-L., Liu, Y.-W., and Liu, S.-J., 2020, 'Treating Intracranial Abscesses in Rats with Stereotactic Injection of Biodegradable Vancomycin-Embedded Microparticles', *Pharmaceutics*, 12(2), 14 pp.
- Tsiapla, A.R., Bakola, V., Karagkiozaki, V., Pavlidou, E., and Logothetidis, S., 2019, 'Biodegradable Electrospayed NPs as Drug Carriers for Optimal Treatment of Orthopaedic Infections', *Materials Today: Proceedings*, 19(Part 1), pp. 110-116.
- Ulrich, S., Seyler, T.M., Bennett, D., Delanois, R.E., Saleh, K.J., Thongtrangan, I., Kuskowski, M., Cheng, E.Y., Sharkey, P.F., Parvizi, J., Stiehl, J.B., and Mont, M.A., 2008, 'Total hip arthroplasties: What are the reasons for revision?', *International Orthopaedics*, 32(5), pp. 597-604.
- Unwin, P., 2013, *willit3dprint.com*. [Online]  
Available at: <http://presentation.willit3dprint.com/presentations/Paul%20Unwin%20-%20The%20use%20of%20Additive%20Manufacturing%20for%20the%20fabrication%20of%20specialised%20orthopaedic%20implants.pdf> [Accessed 19 March 2014].

- van de Belt, H., Neut, D., Schenk, W., van Horn, J.R., van der Mei, H.C., and Busscher, H.J., 2001, 'Staphylococcus aureus biofilm formation on different gentamicin-loaded polymethylmethacrylate loaded bone cements', *Biomaterials*, 22(12), pp. 1607-1611.
- Vandenbroucke, B. and Kruth, J.-P., 2007, 'Selective laser melting of biocompatible metals for rapid manufacturing of medical parts', *Rapid Prototyping Journal*, 13(4), pp. 196-203.
- Vaneker, T., Bernard, A., Moroni, G., Gibson, I., and Zhang, Y., 2020, 'Design for additive manufacturing: Framework and methodology', *CIRP Annals*, 69(2), pp. 578-599.
- VDI, 1993. *VDI 2221: Methodik zum Entwickeln und Konstruieren technischer Systeme und Produkte*. Berlin: Beuth Verlag GmbH.
- Vincenten, C., Gosens, T., van Susante, J., and Somford, M., 2019, 'The Girdlestone situation: a historical essay', *Journal of Bone and Joint Infection*, 4(5), pp. 203-208.
- Vrancken, B., Thijs, L., Kruth, J.-P., and van Humbeeck, J., 2012, 'Heat treatment of Ti6Al4V produced by Selective Laser Melting: Microstructure and mechanical properties', *Journal of Alloys and Compounds*, 541, pp. 177-185.
- Waghmare, A., Saxena, N., Hupta, S., and Khan, S., 2019, 'Use of biodegradable materials as local antimicrobial carriers in orthopedic infections', *Journal of Orthopaedics and Spine*, 7(2), pp. 51-56.
- Wahl, P., Guidi, M., Benninger, E., Rönn, K., Gautier, E., Buclin, T., Magnin, J.-L., and Livio, F., 2017, 'The levels of vancomycin in the blood and the wound after the local treatment of bone and soft-tissue infection with antibiotic-loaded calcium sulphate as carrier material', *The Bone and Joint Journal*, 99-B(11), pp. 1537-1544.
- Waller, J., Walker, J., Burke, E., and Wells, D., 2016, *NASA OSMA NDE Program Additive Manufacturing Foundational Effort*. [Online]  
Available at: <https://ntrs.nasa.gov/archive/nasa/casi.ntrs.nasa.gov/20160011480.pdf>  
[Accessed 6 May 2020].
- Walls, R., Roche, S., O'Rourke, A., and McCabe, J., 2008, 'Surgical site infection with methicillin-resistant Staphylococcus aureus after primary total hip replacement', *The Journal of Bone and Joint Surgery*, 90-B(3), pp. 292-298.
- Wang, F., Ni, B., Zhu, Z., Liu, F., Zhu, Y.-Z., and Liu, J., 2011, 'Intra-discal vancomycin-loaded PLGA microsphere injection for MRSA discitis: an experimental study', *Archives of Orthopaedic and Trauma Surgery*, 131(1), pp. 111-119.

- Wang, L., Yang, Q., Chen, Y., Chai, Y., Li, J.J., Du, L., Tan, R., Yang, S., Tu, M., and Yu, B., 2017, 'A reformative shear precipitation procedure for the fabrication of vancomycin-loaded poly(lactide-co-glycolide) microspheres', *Journal of Biomaterials Applications*, 31(7), pp. 995-1009.
- Wang, X.-P., Chen, T.-N., and Yang, Z.-X., 2007, 'Modeling and simulation of drug delivery from a new type of biodegradable polymer micro-device', *Sensors and Actuators A: Physical*, 133(2), pp. 363-367.
- Wang, X., Xu, S., Zhou, S., Xu, W., Leary, M., Choong, P., Qian, M., Brandt, M., and Xie, Y.M., 2016, 'Topological design and additive manufacturing of porous metals for bone scaffolds and orthopaedic implants: A review', *Biomaterials*, 83, pp. 127-141.
- Warnke, P.H., Douglas, T., Wollny, P., Sherry, E., Steiner, M., Galonska, S., Becker, S.T., Springer, I.N., Wiltfang, J., and Sivananthan, S., 2009, 'Rapid Prototyping: Porous Titanium Alloy Scaffolds Produced by Selective Laser Melting for Bone Tissue Engineering', *Tissue Engineering: Part C*, 15(2), pp. 115-124.
- Wauthle, R., Vrancken, B., Beynaerts, B., Jorissen, K., Schrooten, J., Kruth, J.-P., and Van Humbeeck, J., 2015, 'Effects of build orientation and heat treatment on the microstructure and mechanical properties of selective laser melted Ti6Al4V lattice structures', *Additive Manufacturing*, 5, pp. 77-84.
- Wessels, H., Bode, T., Weissenfels, C., Wriggers, P., and Zohdi, T.I., 2019, 'Investigation of heat source modeling for selective laser melting', *Computational Mechanics*, 63, pp. 949-970.
- Westberg, M., Groggaard, B., and Snorrason, F., 2012, 'Early prosthetic joint infections treated with debridement and implant retention', *Acta Orthopaedica*, 83(3), pp. 227-232.
- Winkler, C., Dennison, J., Wooldridge, A., Larumbe, E., Caroom, C., Jenkins, M., and Brindley, G., 2018, 'Do local antibiotics reduce periprosthetic joint infections? A retrospective review of 744 cases', *Journal of Clinical Orthopaedics and Trauma*, 9(Supplement 1), pp. S34-S39.
- Winkler, H., 2009, 'Rationale for one stage exchange of infected hip replacement using uncemented implants and antibiotic impregnated bone graft', *International Journal of Medical Sciences*, 6(5), pp. 247-252.
- Wu, P. and Grainger, D., 2006. 'Drug/device combinations for local drug therapies and infection prophylaxis', *Biomaterials*, 27, pp. 2450-2467.

- Wycisk, E., Solbach, A., Siddique, S., Herzog, D., Walther, F., and Emmelmann, C., 2014, 'Effects of Defects in Laser Additive Manufactured Ti-6Al-4V on Fatigue Properties', *Physics Procedia*, 56, pp. 371-378.
- Wyles, C., Van Demark III, R., Sierra, R., and Trousdale, R., 2014, 'High Rate of Infection After Aseptic Revision of Failed Metal-on-Metal Total Hip Arthroplasty', *Clinical Orthopaedics and Related Research*, 472(2), pp. 509-516.
- Xiang, Z., Yin, M., Dong, G., Mei, X., and Yin, G., 2018, 'Modeling of the thermal physical process and study on the reliability of linear energy density for selective laser melting', *Results in Physics*, 9, pp. 939-946.
- Xia, W., Grandfield, K., Hoess, A., Ballo, A., Cai, Y., and Engqvist, H., 2012, 'Mesoporous titanium dioxide coating for metallic implants', *Journal of Biomedical Materials Research Part B: Applied Biomaterials*, 100B(1), pp. 82-93.
- Xie, C.-M., Lu, X., Wang, K.-F., Meng, F.-Z., Jiang, O., Zhang, H.-P., Zhi, W., and Fang, L.-M., 2014, 'Silver Nanoparticles and Growth Factors Incorporated Hydroxyapatite Coatings on Metallic Implant Surfaces for Enhancement of Osteoinductivity and Antibacterial Properties', *ACS Applied Materials and Interfaces*, 6(11), pp. 8580-8589.
- Yadroitsev, I., Gusarov, A., Yadroitsava, I., and Smurov, I., 2010, 'Single track formation in selective laser melting of metal powders', *Journal of Materials Processing Technology*, 210(12), pp. 1624-1631.
- Yadroitsev, I., Krakhmalev, P., Yadroitsava, I., and Du Plessis, A., 2018, 'Qualification of Ti6Al4V ELI Alloy Produced by Laser Powder Bed Fusion for Biomedical Applications', *The Journal of The Minerals, Metals & Materials Society (TMS)*, 70, pp. 372-377.
- Yang, H., Hao, Y., Liu, Q., Mi, Z., Wang, Z., Zhu, L., Feng, Q., and Hu, N., 2017, 'Preparation and in vitro study of hydrochloric norvancomycin encapsulated poly (d,l-lactide-co-glycolide, PLGA) microspheres for potential use in osteomyelitis', *Artificial Cells, Nanomedicine, and Biotechnology*, 45(7), pp. 1326-1330.
- Yang, J., Han, J., Yu, H., Yin, J., Gao, M., Wang, Z., and Zeng, X., 2016, 'Role of molten pool mode on formability, microstructure and mechanical properties of selective laser melted Ti-6Al-4V alloy', *Materials & Design*, 110, pp. 558-570.
- Yarwood, J., Bartels, D., Volper, E., and Greenberg, E., 2004, 'Quorum Sensing in Staphylococcus aureus Biofilms', *Journal of Bacteriology*, 186(6), pp. 1838-1850.

- Yau, H.-T., Kuo, C.-C., and Yeh, C.-H., 2003, 'Extension of surface reconstruction algorithm to the global stitching and repairing of STL models', *Computer-Aided Design*, 35, pp. 477-486.
- Young, S.W., Zhang, M., Freeman, J.T., Mutu-Grigg, J., Pavlou, P., and Moore, G.A., 2014, 'The Mark Coventry Award: Higher Tissue Concentrations of Vancomycin with Low-dose Intraosseous Regional Versus Systemic Prophylaxis in TKA', *Clinical Orthopaedics and Related Research*, 472(1), pp. 57-65.
- Yu, X., Pan, Q., Zheng, Z., Chen, Y., Chen, Y., Weng, S., and Huang, L., 2018, 'pH-responsive and porous vancomycin-loaded PLGA microspheres: evidence of controlled and sustained release for localized inflammation inhibition in vitro', *RSC Advances*, 8(65), pp. 37424-37432.
- Zadpoor, A., 2019, 'Additively manufactured porous metallic biomaterials', *Journal of Materials Chemistry B*, 7, pp. 4088-4117.
- Zagra, L., Gallazzi, E., Romano, D., Scarponi, S., and Romano, C., 2019, 'Two-stage cementless hip revision for per-prosthetic infection with an antibacterial hydrogel coating: results of a comparative series', *International Orthopaedics*, 43, pp. 111-115.
- Zakeri-Milani, P., Loveyemi, B., Jelvehgari, M., and Valizadeh, H., 2013, 'The characteristics and improved intestinal permeability of vancomycin PLGA-nanoparticles as colloidal drug delivery system', *Colloids and Surfaces B: Biointerfaces*, 103, pp. 174-181.
- Zaman, U., Rivette, M., Siadat, A., and Baqai, A., 2018, 'Integrated design-oriented framework for Resource Selection in Additive Manufacturing', *Procedia CIRP*, 70, pp. 96-101.
- Zhang, L., Yan, J., Yin, Z., Tang, C., Guo, Y., Li, D., Wei, B., Xu, Y., Gu, Q., and Wang, L., 2014, 'Electrospun vancomycin-loaded coating on titanium implants for the prevention of implant-associated infections', *International Journal of Nanomedicine*, 9, pp. 3027-3036.
- Zhang, S., Wei, Q., Cheng, L., Li, S., and Shi, Y., 2014, 'Effects of scan line spacing on pore characteristics and mechanical properties of porous Ti6Al4V implants fabricated by selective laser melting', *Materials and Design*, 63, pp. 185-193.
- Zhang, T., Wei, Q., Zhou, H., Zhou, W., Fan, D., Lin, X., Jing, Z., Cai, H., Cheng, Y., Liu, X., Li, W., Song, C., Tian, Y., Xu, N., Zheng, Y., Liu, Z., 2020, 'Sustainable release of vancomycin from micro-arc oxidised 3D-printed porous Ti6Al4V for treating methicillin-resistant *Staphylococcus aureus* bone infection and enhancing osteogenesis in a rabbit tibia osteomyelitis model', *Biomaterials Science*, 8, pp. 3106-3115.

- 
- Zhao, Z.-Y., Li, L., Bai, P.-K., Jin, Y., Wu, L.-Y., Li, J., Guan, R.-G., and Qu, H.-Q., 2018, 'The Heat Treatment Influence on the Microstructure and Hardness of TC4 Titanium Alloy Manufactured via Selective Laser Melting', *Materials*, 11(8), 12 pp.
- Zheng, L., Zhang, Q., Cau, H., Wu, W., Ma, H., Ding, X., Yang, J., Duan, X., and Fan, S., 2019, 'Melt pool boundary extraction and its prediction from infrared images in selective laser melting', *Materials and Design*, 183, 10 pp.
- Zhou, Z., Yao, Q., Li, L., Zhang, X., Wei, B., Yuan, L., and Wang, L., 2018, 'Antimicrobial Activity of 3D-Printed Poly( $\epsilon$ -Caprolactone) (PCL) Composite Scaffolds Presenting Vancomycin-Loaded Polylactic Acid-Glycolic Acid (PLGA) Microspheres', *Medical Science Monitor*, 24, pp. 6934-6945.
- Zilberman, M. and Elsner, J., 2008, 'Antibiotic-eluting medical devices for various applications', *Journal of Controlled Release*, 130, pp. 202-215.
- Zimmerli, W. and Moser, C., 2012, 'Pathogenesis and treatment concepts of orthopaedic biofilm infections', *FEMS Immunol Med Microbiol*, 65(2), pp. 158-168.
- Zimmerli, W. and Ochsner, P., 2003, 'Management of Infection Associated with Prosthetic Joints', *Infection*, 31, pp. 99-108.
- Zimmerli, W., Widmer, A.F., Blatter, M., Frei, R., and Ochsner, P.E., 1998, 'Role of Rifampin for Treatment of Orthopedic Implant-Related Staphylococcal Infections', *American Medical Association*, 279(19), pp. 1537-1541.
- Zmistowski, B., Karam, J.A., Durinka, J.B., Casper, D.S., and Parvizi, J., 2013, 'Periprosthetic Joint Infection Increases the Risk of One-Year Mortality', *The Journal of Bone and Joint Surgery, Incorporated*, 95-A(24), pp. 2177-2184.

## Appendix A: Supplementary Information to Chapter 1

**Table A-1: Commercially produced MAM medical implants (non-exhaustive list)**

Company	AM Type	Surgical Application	Material	Year	Reference
Adler Ortho S.R.L.	EBM	Acetabular cup	Ti-6Al-4V	2007	(Ohldin, 2010)
Lima-Lto	EBM	Acetabular cup	Ti-6Al-4V	2007	(Ohldin, 2010)
Advanced Medical Technologies	EBM	Interbody fusion cage	Cp Ti	2009	(Ohldin, 2010)
Stanmore Implants Worldwide Ltd	LPBF	Pelvic reconstruction	Ti-6Al-4V	2010	(Unwin, 2013)
Layerwise	LPBF	Facial reconstruction	Ti-6Al-4V	2012	(Nickels, 2012)
Exactech	EBM	Acetabular cup	Ti-6Al-4V	2012	(FDA, 2012)
4WEB Medical	EBM	Interbody fusion cage	Ti-6Al-4V	2014	(FDA, 2014)
BioArchitects	EBM	Patient specific cranioplasty plate	Ti-6Al-4V ELI	2015	(FDA, 2015)
Stryker	LPBF	Interbody fusion cage	Ti-6Al-4V	2016	(FDA, 2016)
	LPBF	Hex screws	Ti-6Al-4V ELI	2016	(FDA, 2016)
Additive Orthopaedics, LLC	Not specified	Bone fixation fastener	Ti-6Al-4V	2016	(FDA, 2016)
Emerging Implant Technologies GmbH	LPBF	Bone fixation plate	Ti-6Al-4V ELI	2016	(FDA, 2016)
		Locking lattice plate	Ti-6Al-4V ELI	2017	(FDA, 2017)
		Interbody fusion cage	Ti-6Al-4V ELI	2017	(FDA, 2017)
Materialise NV	LPBF	Maxillofacial reconstruction system	Cp Ti	2017	(FDA, 2017) (Heufelder, et al., 2017)
Medacta	EBM	Tibial cone	Ti-6Al-4V	2017	(FDA, 2017)
Stryker	LPBF	Interbody fusion cage	Ti-6Al-4V	2017	(FDA, 2017)
CoreLink, LLC	PBF	Interbody fusion cages	Ti-6Al-4V ELI	2017	(FDA, 2017)
Camber Spine	EBM	Interbody fusion cages	Ti-6Al-4V	2017	(FDA, 2017)
Medtronic Sofamor Danek, USA Inc.	LPBF	Interbody fusion cages	Stainless steel; Ti-6Al-4V ELI	2017	(FDA, 2017)
Stryker	LPBF	Interbody fusion cage	Ti-6Al-4V	2018	(FDA, 2018)
4WEB Medical	EBM	Bone fixation appliance	Ti-6Al-4V ELI	2018	(FDA, 2018)

---

Journal papers:

**Bezuidenhout, M.**, Ter Haar, G., Becker, T., Rudolph, S., Damm, O., Sacks, N., **2020**, “The effect of HF-HNO<sub>3</sub> chemical polishing on the surface roughness and fatigue life of laser powder bed fusion produced Ti6Al4V”, *Materials Today Communications*, Vol. 25, Article ID 101396.

Booyesen, E., **Bezuidenhout, M.**, van Staden, A.D., Dimitrov, D., Deane, S.M., and Dicks, L.M.T., **2019**, “Antibacterial Activity of Vancomycin Encapsulated in Poly(DL-lactide-co-glycolide) Nanoparticles Using Electrospraying”, *Probiotics and Antimicrobial Proteins*, Vol. 11, pp. 310-316.

**Bezuidenhout, M.B.**, Booyesen, E., van Staden, A.D., Uheida, E.H., Hugo, P.A., Oosthuizen, G.A., Dimitrov, D.M., and Dicks, L.M.T., **2018**, “Selective Laser Melting of Integrated Ti6Al4V ELI Permeable Walls for Controlled Drug Delivery of Vancomycin”, *ACS Biomaterials Science and Engineering*, Vol. 4, No. 12, pp. 4412-4424.

**Bezuidenhout, M.B.**, Dimitrov, D.M., van Staden, A.D., Oosthuizen, G.A., and Dicks, L.M.T., **2015**, “Titanium-Based Hip Stems with Drug Delivery Functionality through Additive Manufacturing”, *BioMed Research International*, Vol. 2015, Article ID 134093, 11 pages.

**Bezuidenhout, M.B.**, van Staden, A.D., Oosthuizen, G.A., Dimitrov, D.M., and Dicks, L.M.T., **2015**, “Delivery of Antibiotics from Cementless Titanium-Alloy Cubes May Be a Novel Way to Control Postoperative Infections”, *BioMed Research International*, Vol. 2015, Article ID 856859, 7 pages.

## Conference papers:

**Bezuidenhout, M.B.**, Booyesen, E., van Staden, A.D., Hugo, P.A., Oosthuizen, G.A., Dimitrov, D.M., and Dicks, L.M.T., **2018**, “Enabling Drug Delivery from Ti6Al4V ELI Reservoirs through Direct Fabrication of Parts with Integrated Permeable Structures”, *Proceedings of the Fraunhofer Direct Digital Manufacturing Conference 2018*, 14-15 March, Berlin, Germany.

Hugo, P., **Bezuidenhout, M.**, Oosthuizen, G., and Dimitrov, D., **2018**. “Conceptual DFAM Frameworks for Part Life Cycle Resource Efficiency”, *Proceedings of the Fraunhofer Direct Digital Manufacturing Conference 2018*, 14-15 March, Berlin, Germany.

Oettel, M.K., van der Schyff, H., **Bezuidenhout, M.B.**, Oosthuizen, G.A., **2016**, “Framework to Develop and Evaluate Process Chains for Resource Efficiency”, *Proceedings of the International Conference on Competitive Manufacturing*, 27-29 January, Stellenbosch, South Africa, pp 25-31.

---

## Appendix B: Vancomycin Encapsulation Biodegradable Polymers

The resulting publications list from the literature search described in Section 4.1.1 is summarised in Table B-1. The following notes accompany the table:

- In many of the studies the polydispersity index (measure of particle size uniformity) has not been reported and was therefore not included
- An important factor influencing the drug release is the pH of the release medium (Liu et al., 2017). Where studies investigated release at different pH levels, preference was given to release performed at pH values of or closest 7.4; that of the PBS buffer solution typically used in-house (Bezuidenhout et al., 2015).
- Burst release was evaluated according to whether more than 20% of the loaded drug was released in the first phase of release
- In the column “Release Testing Period” the duration was either approximated from reported release curves or in the case where testing was stopped prior to full release indicated with a greater than sign

Various notes related to the studies are listed below the table corresponding to the respective letter in superscript.

**Table B-1: Summary of publications for sustained vancomycin drug delivery formulations**

Polymer	Grade	Micro/Nano	Size [ $\mu\text{m}$ ]	Polydispersity Index	Encapsulation Efficiency [%]	Burst Release (<20%)	Release Testing Period (days)	Reference
Potato starch	1,300 kDa	Nanoparticles	0.164 – 0.165	0.05 - 0.08	43.50 – 81.10	n/a	n/a	(Barthold et al., 2016)
Dextran	500 kDa	Nano complex <sup>a</sup>	0.501 ± 0.0003 0.085 ± 0.004	0.29 ± 0.07 0.45 ± 0.02	95.26 ± 0.18 90.40 ± 0.77	N N	> 2 ~ 2	(Hassan et al, 2019)
Gelatin	n/a	Microspheres	20.8 ± 6.5	n/a	n/a	N	3	(Lan et al., 2013)
	Type A. gel, strength ~ 300 b Bloom	Microspheres	36.26 ± 0.2	n/a	67.40 ± 2.50	Y	36	(Aksoy et al., 2019)
Hyaluronic acid	HA-EP3, Injection grade	Microparticles <sup>c</sup>	< 500	n/a	69.80 ± 8.80 25.60 ± 7.80 21.50 ± 7.50	N N Y	> 7 > 7 > 7	(Sahiner et al., 2019)
Silk protein	n/a	Nanoparticles <sup>d</sup>	0.08 - 0.09	0.1	77.00 87.00 93.80	N Y Y	1 3 5	(Besheli et al., 2017)

					93.00	Y	11	
					94.20	Y	~14	
PHBV	PHBV with 12 wt% PHV	Microspheres	$D_{50} = 3.5$ , $d_{90} = 7.0$	n/a	27.30	N	~31	(Li et al., 2014)
Albumin	BSA	Microspheres <sup>e</sup>	< 16	n/a	n/a	N	> 2	(Nettey et al., 2006)
PLGA							+	
	(75:25) 10 kDa	Nanoparticles	$0.187 \pm 0.001$	$0.201 \pm 0.072$	$12.1 \pm 13$	n/a	n/a	(Barichello et al., 1999)
	(90:10) 12.25 kDa	Microparticles <sup>f,i</sup>	$d_{80} \sim 10$	n/a	97	N	>98	(Özalp et al., 2001)
					80	N	98	
					44	N	98	
					75.9	N	>98	
					83	N	>98	
	(70:30) 12.5 kDa	Microparticles <sup>f,i</sup>	n/a	n/a	71	Y	>98	(Özalp et al., 2001)
					48	Y	>98	
	(50:50) Resomer RG502H	Microspheres <sup>f</sup>	$11.75 \pm 1.31$	n/a	99.5	Y	< 1	(Gavini et al., 2004)
	inherent viscosity 0.16 dl/g		$10.96 \pm 0.08$		86.0	N	< 1	
			$11.15 \pm 0.69$		84.2	N	< 1	
	(50:50) 12kDa	Microparticles	1.6 11.8	n/a	94.33	N	< 1	(Hachicha et al., 2006)
	(75:25) 136 kDa	Microspheres	$77 \pm 1.7$	n/a	60	Y	> 60	(Sayin et al., 2006)
	(75:25) 30 kDa	Microspheres <sup>f</sup>	$61.57 \pm 4.37$	n/a	$75.27 \pm 1.60$	Y	> 30	(Wang et al., 2011)
			$64.33 \pm 6.96$		$68.67 \pm 1.78$	Y	> 30	
			$67.45 \pm 8.13$		$60.20 \pm 1.61$	Y	> 30	
	(50:50) 12 kDa	Nanoparticles <sup>f</sup>	$0.450 \pm 0.035$	0.006	$78.6 \pm 2.38$	N	1	(Zakeri-Milani et al.,

			0.461 ± 0.033	0.0053	67.1 ± 1.46	N	1	2013)
			0.466 ± 0.039	0.0069	38.38 ± 2.25	N	1	
(50:50) 36 kDa	Microparticles <sup>f</sup>		33.1 ± 28.7	n/a	83.3 ± 4.8 76.9	Y	50	(Shah et al., 2014)
			36.9 ± 28.1		± 6.2	Y	50	
(85:15) 100 kDa	Microparticles		5.2 ± 2.9	n/a	61 ± 6	N	~ 50	(Rumian et al., 2017)
(50:50) 30-60 kDa	Nanoparticles		0.05 – 0.1	n/a	n/a	n/a	> 20	(Liu et al., 2017)
(50:50) 30 kDa	Microspheres		n/a	n/a	n/a	N	> 8	(Du et al., 2017)
(75:25) 10 kDa	Microspheres		69.9	n/a	48.51 ± 14.83	Y	> 7	(Yang et al., 2017)
(50:50) 30 kDa	Microspheres		15.6 ± 3.1	n/a	30.2	Y	> 40	(Wang et al., 2017)
(75:25) 40 kDa	Microspheres		28.4 ± 0.59	n/a	10.34 ± 2.02	Y	> 50	(Yu et al., 2018)
(50:50) 33 kDa	Microparticles <sup>f</sup>		5 – 10	n/a	n/a	N	~ 3	(Hsu et al., 2018)
						N	~ 4	
						N	~ 20	
						N	17	
(75:25) 70 kDa	Microparticles		10	n/a	n/a	N	~ 17	(Hsu et al., 2018)
(75:25) 51 kDa	Microspheres <sup>f</sup>		~70	n/a	~70	N	> 28	(Zhou et al., 2018)
			~65		~65	N	> 28	
			~80		~60	N	> 28	
(50:50) Purasorb® PDLG 5002	Nanoparticles		~0.239 ± 0.1		28.3	N	~ 4	(Gaspar et al., 2018)
(50:50) Resomer RG503 33 kDa	Microparticles		3.7 ± 0.91	n/a	n/a	n/a	> 30	(Tseng et al., 2020)
PLA								
85 – 160 kDa	Nanoparticles		0.35 ± 0.089	0.299 ± 0.002	n/a	n/a	n/a	(Herrera et al., 2017)

PCL								
n/a	Microparticles	174.51 ± 9.20	n/a	n/a	Y	> 14	(Iooss et al., 2001)	
150 kDa	Microparticles <sup>g</sup>	195.80 ±	n/a	48.93 ± 5.29	Y	> 7	(Le Ray et al., 2003)	
		50.60		57.28 ± 4.18	N	> 7		
		208.00 ±		91.81 ± 3.79	Y	> 7 <sup>h</sup>		
		90.23						
		170.24 ±						
		56.26						
n/a	Microparticles	216.3 ± 66.0	n/a	49.6 ± 3.6	N	> 21	(Le Ray et al., 2005)	
65 kDa	Microspheres	25.49 ± 1.05	n/a	n/a	N	> 60	(Ryu et al., 2014)	
45 kDa	Microparticles	1.18 ± 0.05	n/a	54.6 ± 9.1	Y	> 3	(Ferreira et al., 2015)	
10 kDa	Microspheres <sup>i</sup>	58.05 ± 0.09	n/a	4.70 ± 0.01	N	~2	(Sarigöl et al., 2017)	
		58.08 ± 0.10		4.10 ± 0.08	N	~2		
42.5 kDa		71.84 ± 0.62		40.60 ± 0.21	N	~20		
		76.36 ± 1.93		47.10 ± 0.27	N	~15		
70 – 90 kDa		134.12 ± 1.98		54.80 ± 0.16	N	> 50		
		120.15 ± 1.43		58.40 ± 0.24	N	> 50		
45 kDa	Nanoparticles	n/a	n/a	n/a	N	~ 56	(Tsiapla et al., 2019)	

<sup>a</sup> Various vancomycin to dextran concentrations investigated and treatments classified according to charge ratios

<sup>b</sup> Generally accepted as safe

<sup>c</sup> Different crosslinker (divinyl sulfone) to hyaluronic ratios

<sup>d</sup> Different silk fibroin to vancomycin ratios

<sup>e</sup> Results for BSA microspheres cross-linked with 4% glutaraldehyde

<sup>f</sup> Different vancomycin to PLGA ratios used

<sup>g</sup> Different preparation methods

<sup>h</sup> Ineffective drug release, < 5% in 7 days

<sup>i</sup> Different stabiliser concentrations during preparation

## PLGA bulk erosion and drug delivery MATLAB code:

```

%Simulate Polymer Bulk Erosion as Poisson Process according to Göpferich 1997
%Author: M.B. Bezuidenhout

nloop = 1; %specify number of program loops
nt = 1000; %specify number of time steps
ft = linspace(1,nt,nt); %initiate timestep vector for plot
fetaveM = zeros(nloop, nt); %global erosion matrix for record keeping of loops
fdtaveM = zeros(nloop, nt); %global degradation matrix for record keeping of loops
fdrugtaveM = zeros(nloop, nt); %global drug release matrix for record keeping of loops

for loop = 1:nloop

    %Define elements of computational grid
    nx = 300; %number of pixels in x direction
    ny = 300; %number of pixels in y direction
    n = 300; %number of pixels per direction

    CSij = zeros(ny, nx);
    Pij = zeros(ny, nx); %initialise full black polymer matrix
    Drugij = zeros(ny, nx); %initialise drug distribution matrix
    p = 0.07; %specifiy mass ratio of drug-to-polymer
    Dij = zeros(ny, nx); %initialise effect matrix for degradation
    Eij = zeros(ny, nx); %initialise effect matrix for erosion

    tdegrade = zeros(ny, ny); %initialise matrix for interarrival times
    fdt = zeros(1, nt); %initialise row vector for degradation plot
    fet = zeros(1, nt); %initialise row vector for erosion plot
    fdrugt = zeros(1, nt); % initialise row vector for drug release plot

    %Poisson paramter
    lmdaA = 0.0001; %arrival rate for amorphous hydrolysis
    lmdaC = 0.000005; %arrival rate for crystalline hydrolysis
    pcs = 0.3; %probability of crystalline structure
    rnd = rand(); %random variable uniform dist [0,1]

    %specifiy indexes at which a pixel is a drug
    for i = 1:ny
        for j = 1:nx
            Drugij(i, j) = binornd(1,p,1,1);
        end
    end

    Drugs = sum(sum(Drugij)); %number of pixels that represent drugs

    %calculate interarrival times tij for each pixel
    for i = 1:ny
        for j = 1:nx
            cs = binornd(1,pcs,1,1); %assign structure according to Bernoulli
            trials
            if cs == 1
                CSij(i, j) = 0; %crystalline pixel set to black
                tdegrade(i, j) = (1/(lmdaC*log(n^2))) * (log(1-rand()));
            else
                CSij(i, j) = 0.5; %amorphous pixel set to grey
                tdegrade(i, j) = (1/(lmdaA*log(n^2))) * (log(1-rand()));
            end
        end
    end
end

```

---

```

        end
        if Drugij(i, j) == 1
            Pij(i, j) = 0.5; %set drug loaded indexes to behave as 'degraded
bond'
            tdegrade(i, j) = 0; %these pixels do not have life times
            CSij(i, j) = 1; %set drug loaded pixels white in structure matrix
        end
    end
end

figure
imshow(CSij);
title('Starting Polymer State: Crystalline(black), Amorphous(grey), and
Drug(white)');

figure
imshow(Drugij);
title('Drug Distribution through Polymer Matrix');

figure
imshow(Pij);
title('Starting Polymer Matrix');

for t = 1:nt %time steps
    %lmdat = lmda*t; %factor for degradation rate

    %loop for checking whether pixels should be degraded
    for i = 1:ny
        for j = 1:nx
            if Pij(i, j) == 0
                if t < abs(tdegrade(i, j))
                    Pij(i, j) = 0;
                else
                    Pij(i, j) = 0.5;
                end
            end
        end
    end
end

%loop for checking whether pixels should be eroded
%first row at surface in contact with erosion medium
for j = 1:nx
    if Pij(1, j) == 0.5
        Pij(1, j) = 1;
        Drugij(1, j) = 0;
    end
end

%loop for bulk of matrix except three boundaries
for i = 2:ny-1
    for j = 2:nx-1
        if Pij(i, j) == 0.5
            for a = i-1:i+1
                for b = j-1:j+1
                    if Pij(a, b) == 1;
                        Pij(i, j) = 1;
                        Drugij(i, j) = 0;
                    end
                end
            end
        end
    end
end

```

```

        end
    end
end

end

end

end

end

%loop to test for periodic right boundary
for i = 2:ny-1
    if Pij(i, nx) == 0.5
        for b = i-1:i+1
            if Pij(b, 1) == 1
                Pij(i, nx) = 1;
                Drugij(i, nx) = 0;
            end
        end
        for a = i-1:i+1
            if Pij(a, nx-1) == 1
                Pij(i, nx) = 1;
                Drugij(i, nx) = 0;
            end
        end
    end
end
end

%loop to test for periodic left boundary
for i = 2:ny-1
    if Pij(i, 1) == 0.5
        for b = i-1:i+1
            if Pij(b, nx) == 1
                Pij(i, 1) = 1;
                Drugij(i, 1) = 0;
            end
        end
        for a = i-1:i+1
            if Pij(a, 2) == 1
                Pij(i, 1) = 1;
                Drugij(i, 1) = 0;
            end
        end
    end
end
end

%loop to test for reflective bottom border
for j = 2:nx-1
    if Pij(ny, j) == 0.5
        for a = j-1:j+1
            if Pij(ny-1, a) == 1
                Pij(ny, j) = 1;
                Drugij(ny, j) = 0;
            end
        end
    end
end
end

%test for bottom left corner pixel
if Pij(ny, 1) == 0.5
    for j = 1:2
        if Pij(ny-1, j) == 1

```

---

```

        Pij(ny, 1) = 1;
        Drugij(ny, 1) = 0;
    end
end
if Pij(ny-1, nx) == 1
    Pij(ny, 1) = 1;
    Drugij(ny, 1) = 0;
end
end

%test for bottom right corner pixel
if Pij(ny, nx) == 0.5
    for j = nx-1:nx
        if Pij(ny-1, j) == 1
            Pij(ny, nx) = 1;
            Drugij(ny, nx) = 0;
        end
    end
    if Pij(ny-1, 1) == 1
        Pij(ny, nx) = 1;
        Drugij(ny, nx) = 0;
    end
end

%populate matrices for degradation and erosion
for i = 1:ny
    for j = 1:nx
        if Pij(i, j) == 0
            Dij(i, j) = 1;
        else
            Dij(i, j) = 0;
        end

        if Pij(i, j) == 1
            Eij(i, j) = 0;
        else
            Eij(i, j) = 1;
        end
    end
end

dt = (1/n^2)*sum(sum(Dij)); %fraction of non-degraded bonds in grid
fdt(1, t) = dt; %enter timestep-specific value into row vector
fdtaveM(loop, t) = dt; %enter into global matrix for record keeping
et = (1/n^2)*sum(sum(Eij)); %fraction of non-eroded pixels in grid
fet(1, t) = et; %enter timestep-specific value into row vector
fetaveM(loop, t) = et; %enter into global matrix for record keeping
drugt = (1/(Drugs))*sum(sum(Drugij)); %fraction of unreleased drugs
fdrugt(1, t) = (1-drugt); %Cumulative drug release at time step
fdrugtaveM(loop, t) = (1-drugt); %enter into global matrix for record
keeping
end

figure
imshow(Drugij);
title('Drug Distribution After Release Period');

figure

```

---

```
imshow(Pij);
title('Eroded Polymer After Release Period');

%section to calculate average values
if loop < 2
    fdtprevsum = fdt;
    fetprevsum = fet;
    fdrugtprevsum = fdrugt;
else
    fdtsum = fdtprevsum + fdt;
    fdtave = fdtsum / loop;
    fdtprevsum = fdtsum;

    fetsum = fetprevsum + fet;
    fetave = fetsum / loop;
    fetprevsum = fetsum;

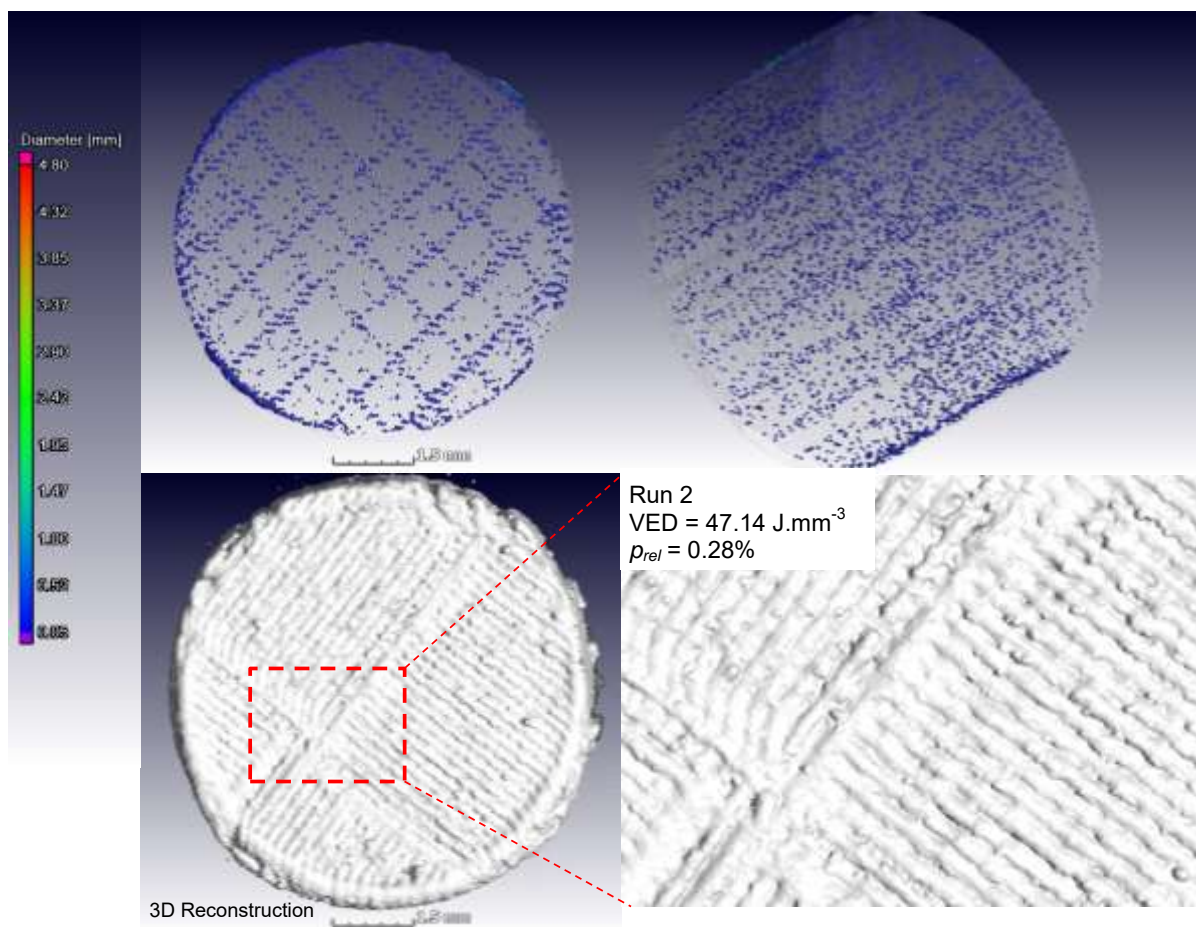
    fdrugtsum = fdrugtprevsum + fdrugt;
    fdrugtave = fdrugtsum / loop;
    fdrugtprevsum = fdrugtsum;
end
figure
plot(ft, fdt, 'k');
hold on
plot(ft, fet, 'r');
xlabel('Time Steps');
ylabel('Degradation(black) and Erosion(red)');
hold off

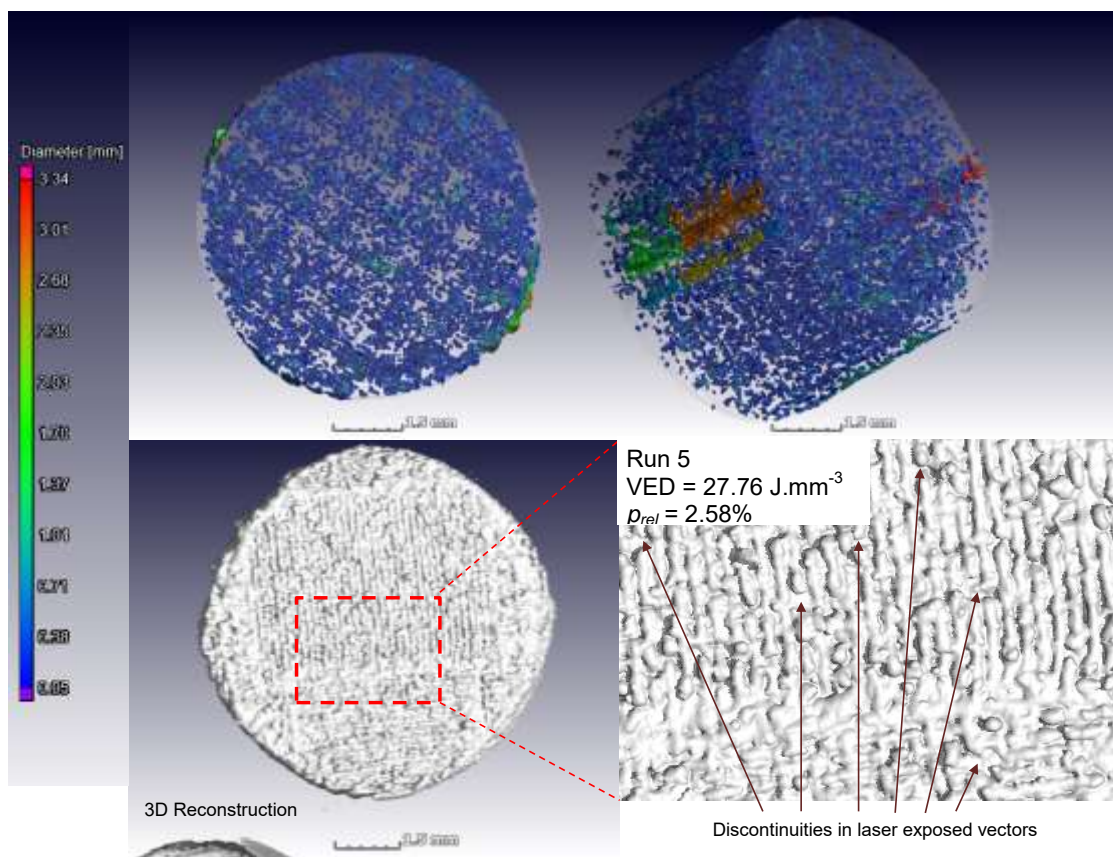
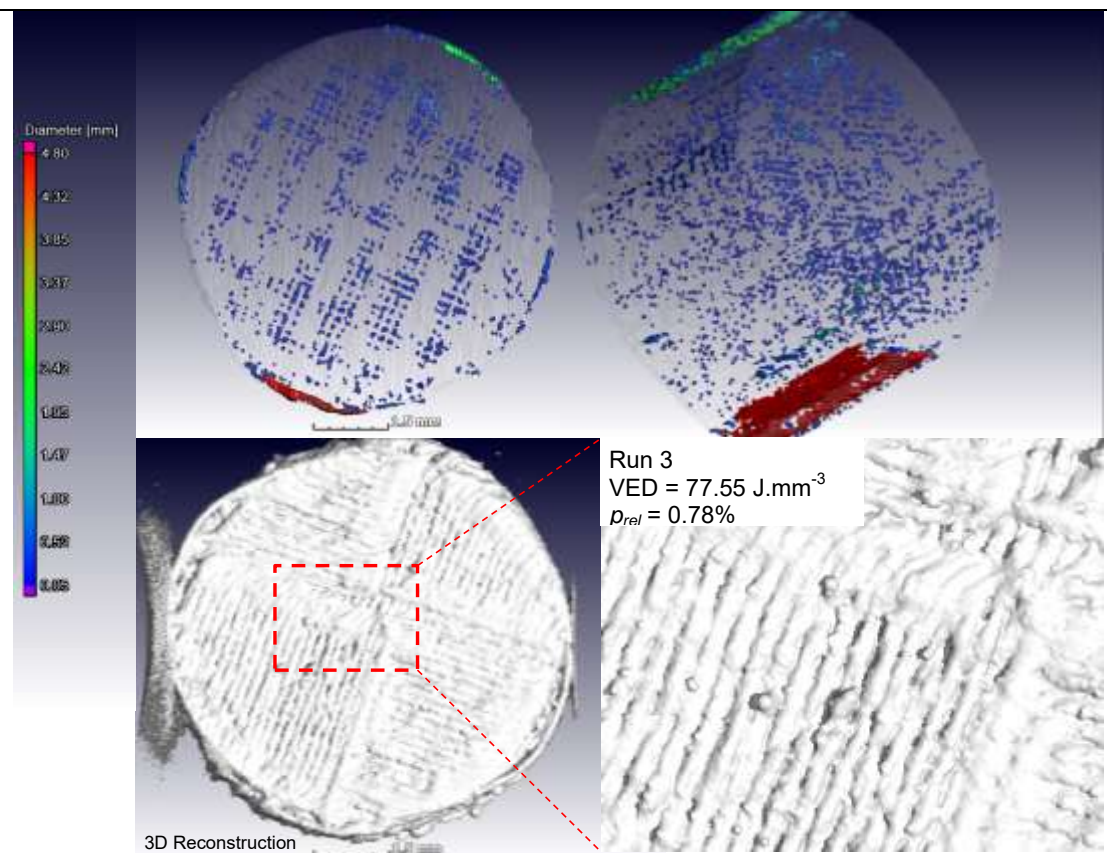
figure
plot(ft, fdrugt);
xlabel('Time Steps');
ylabel('Cumulative Fractional Drug Release');

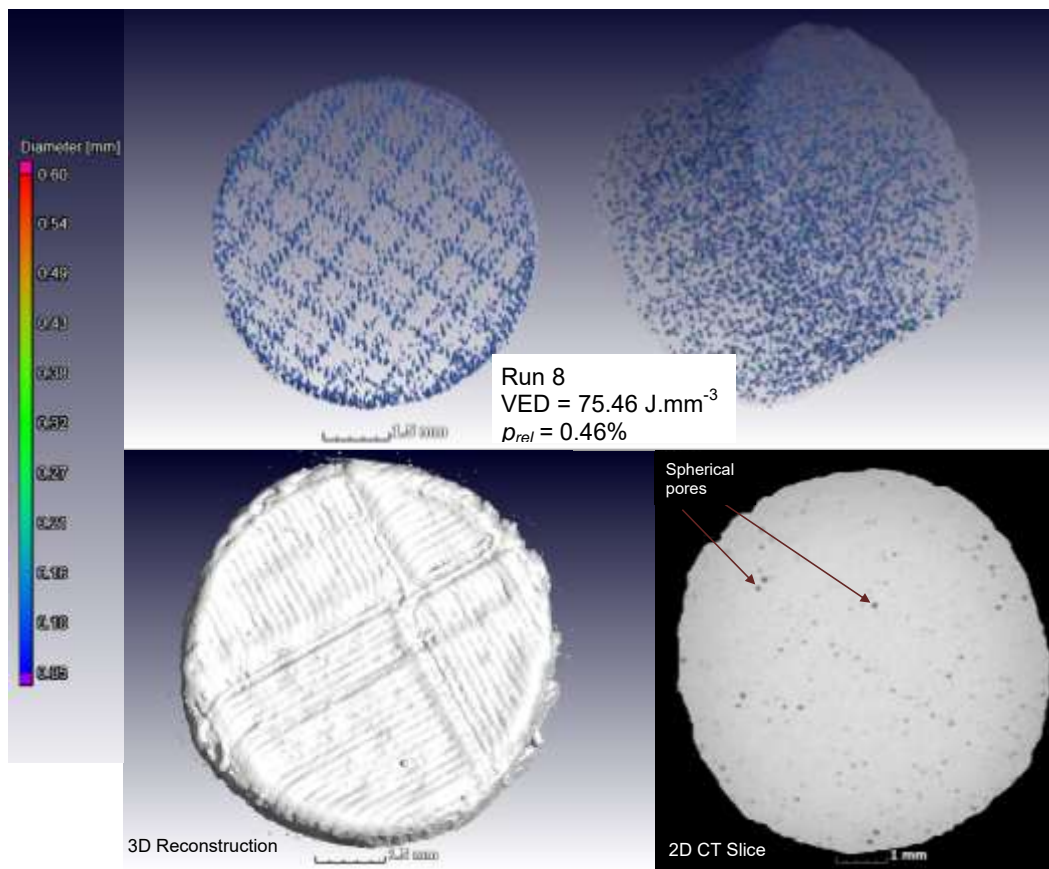
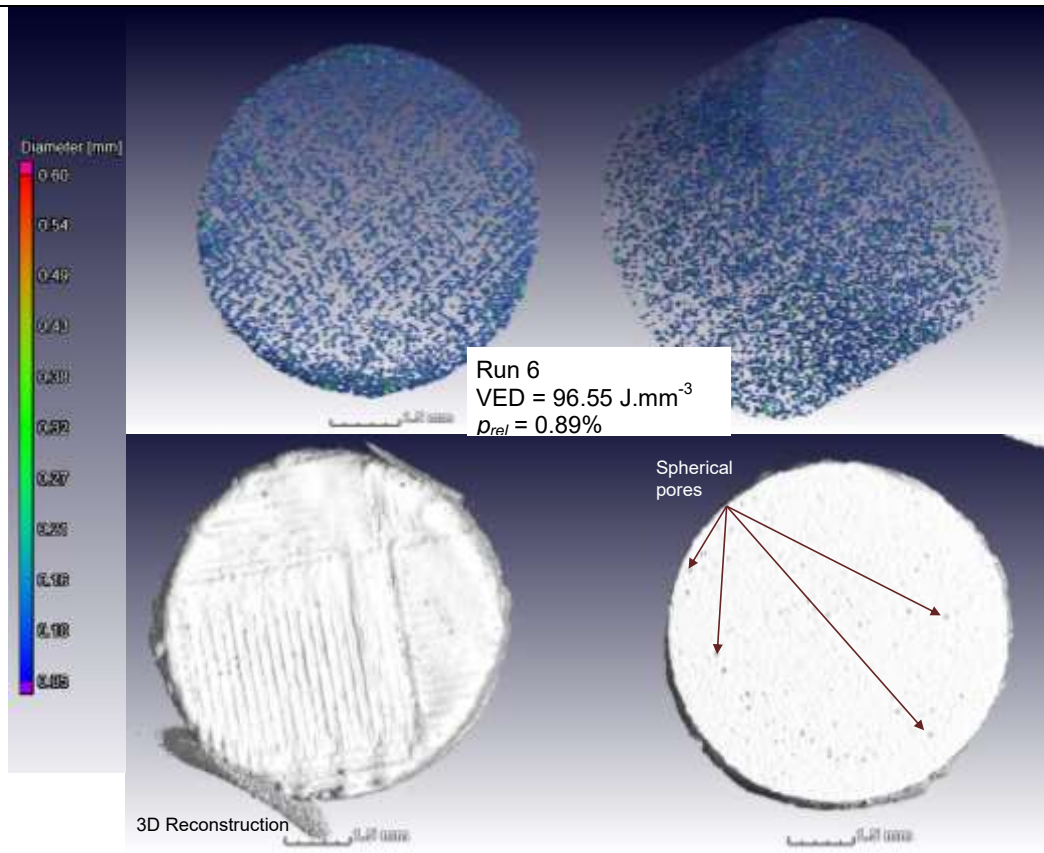
end
```

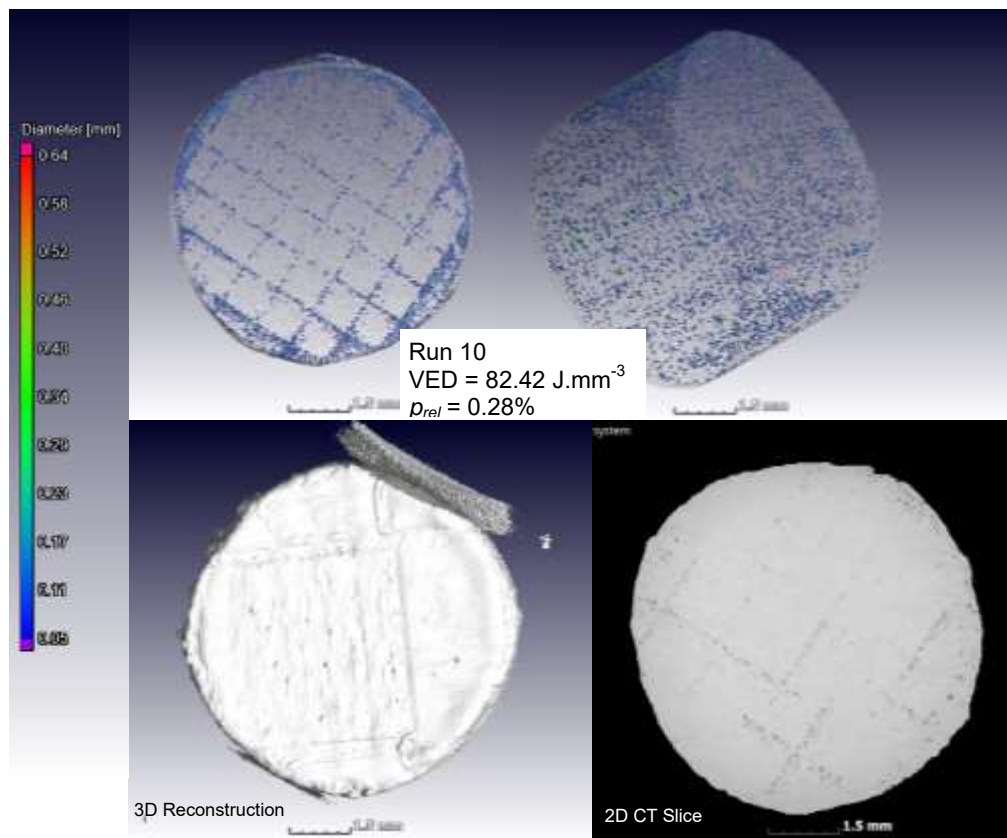
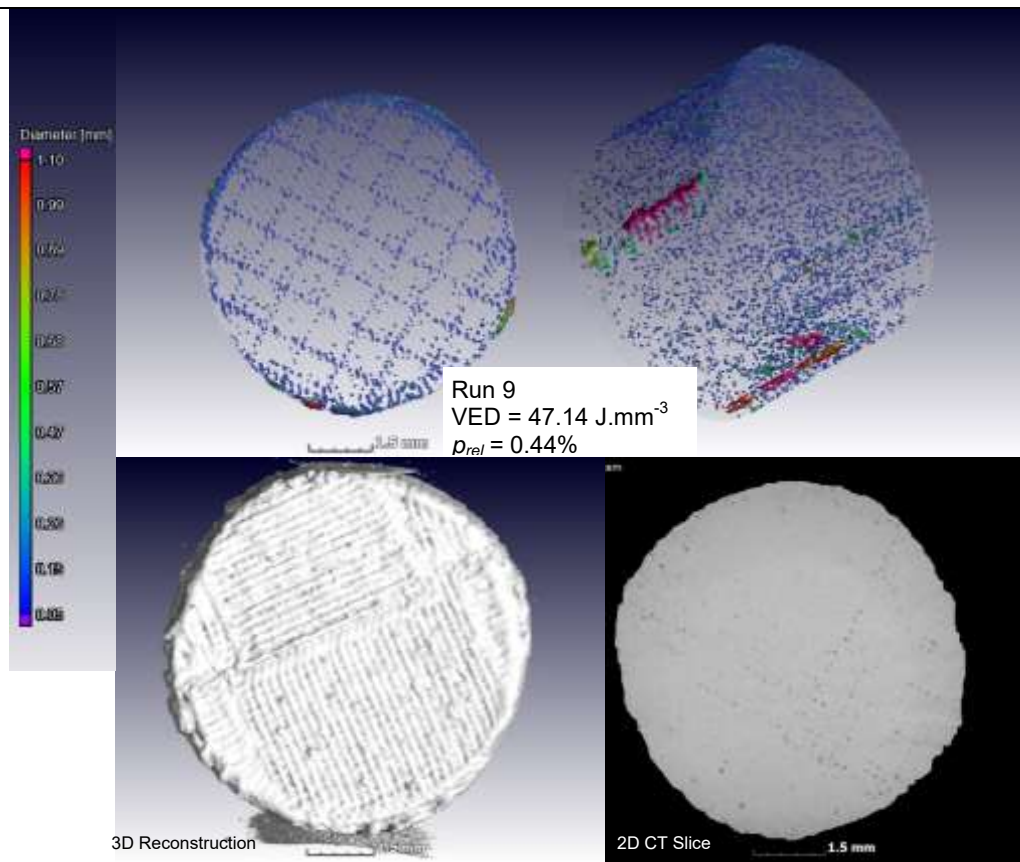
## Appendix C: LPBF-Induced Porosity Screening

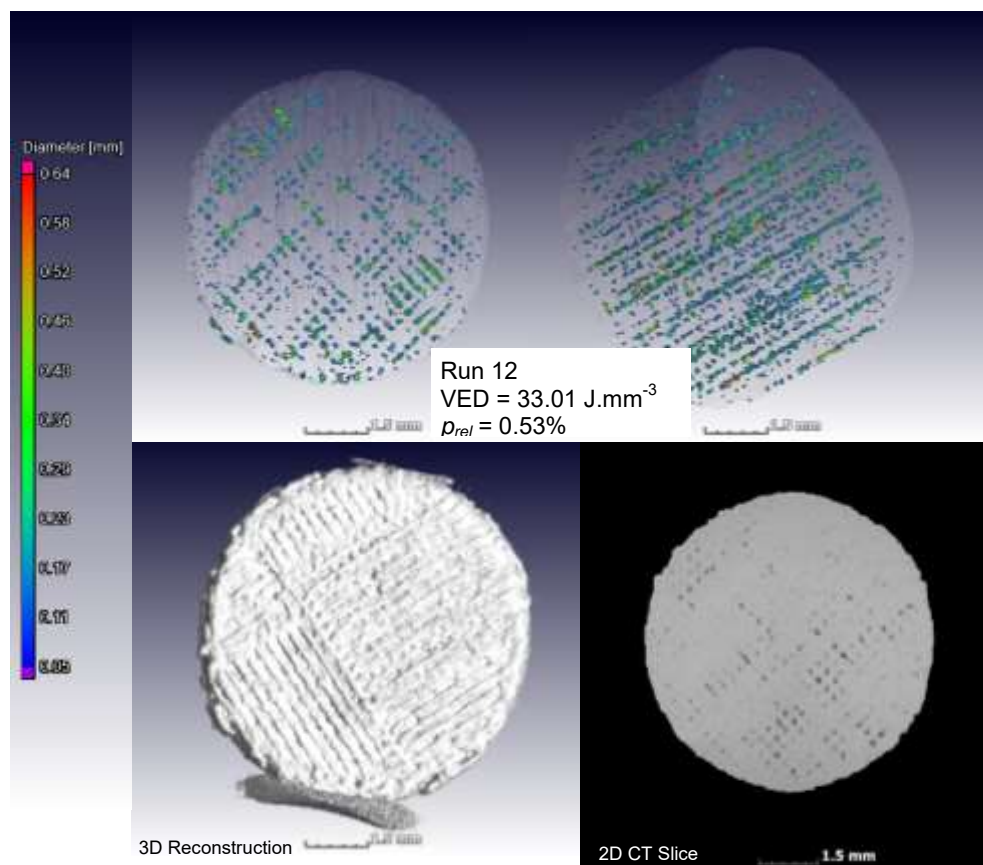
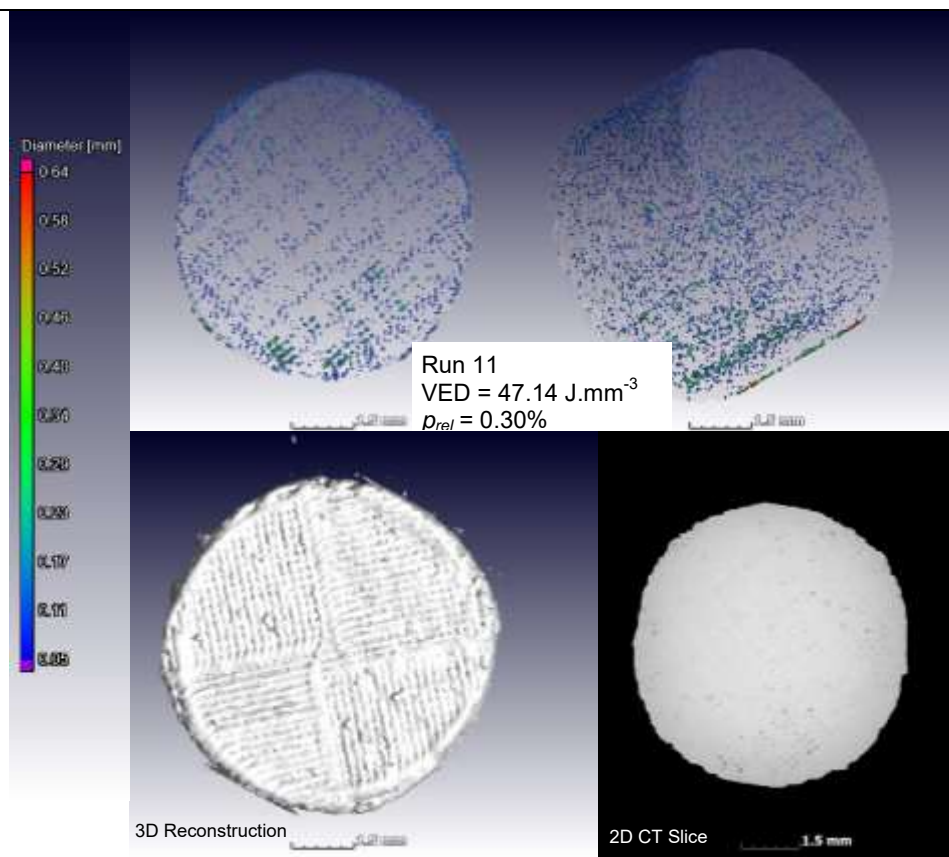
Images of 3D reconstructions from the CT data for the cylindrical specimens from runs 2,3,5,6,8,9,10,11,12,13,14,15,16,17,18 are presented in numerical order in Figure C-1 below.

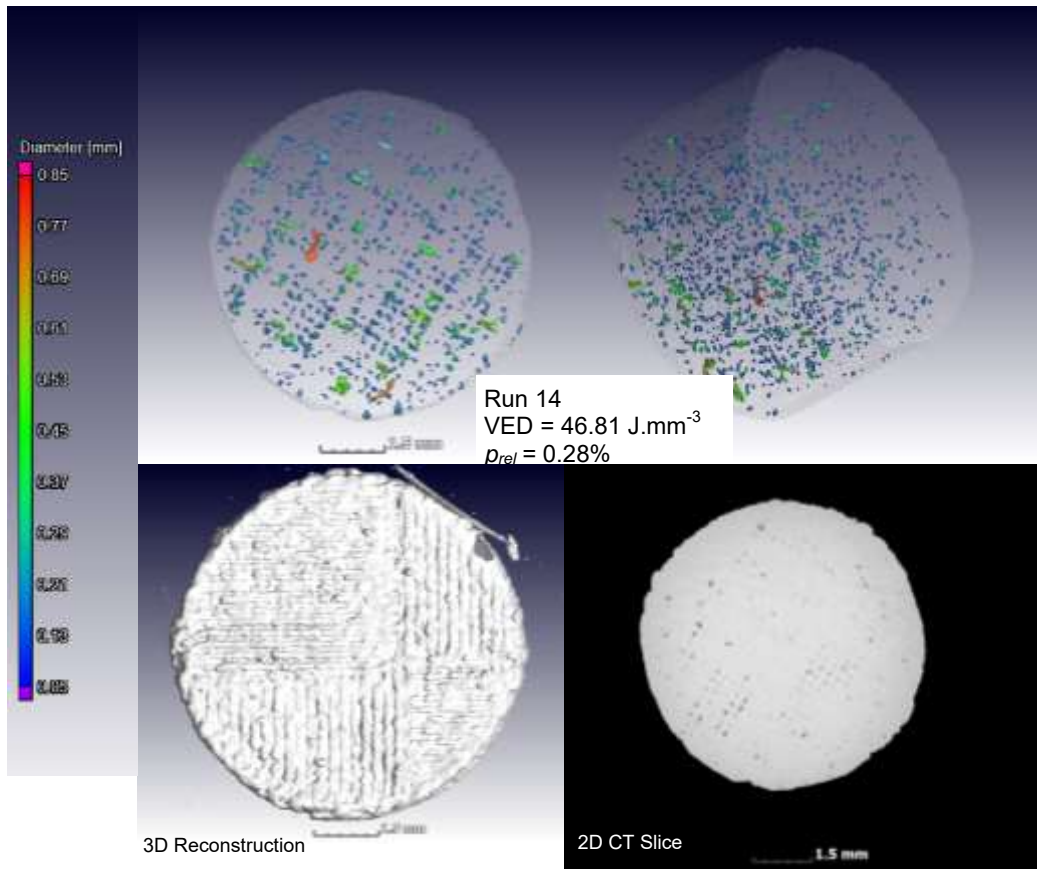
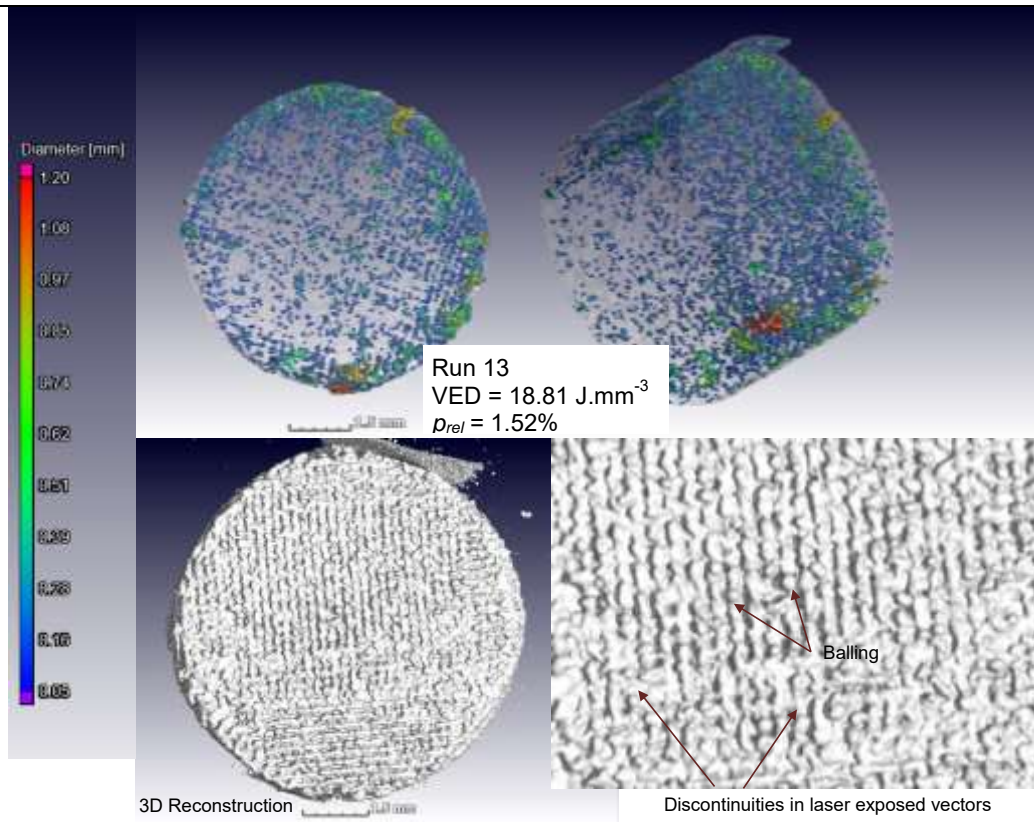


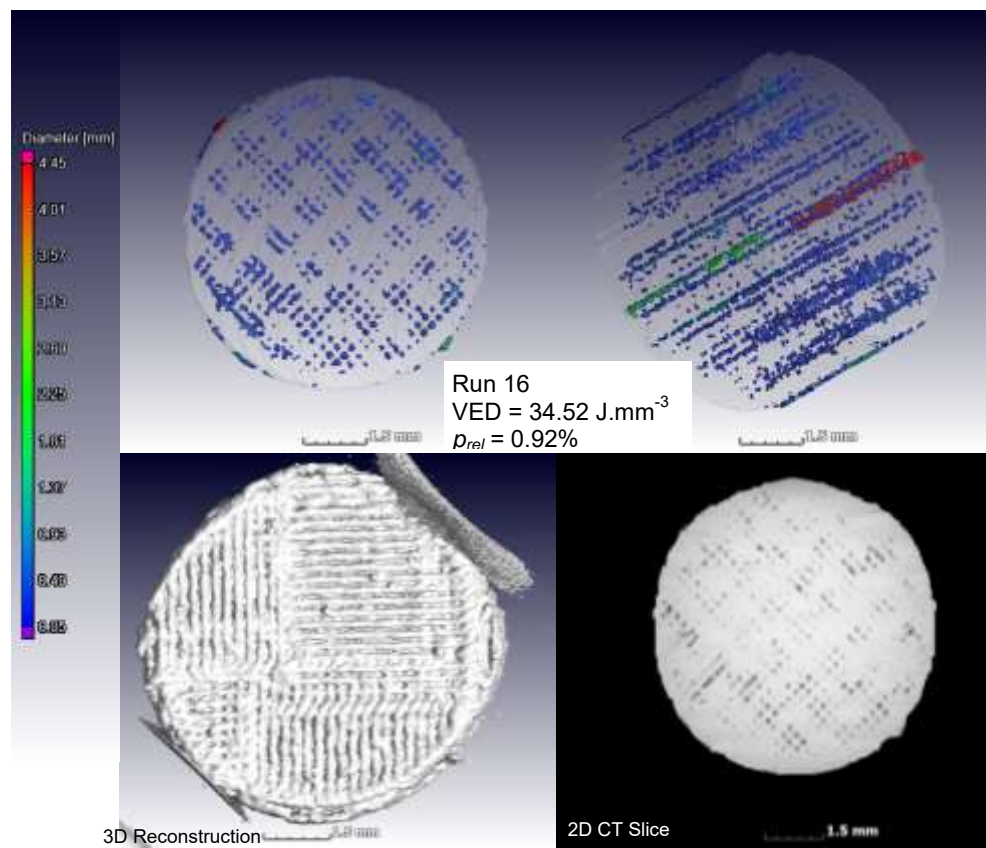
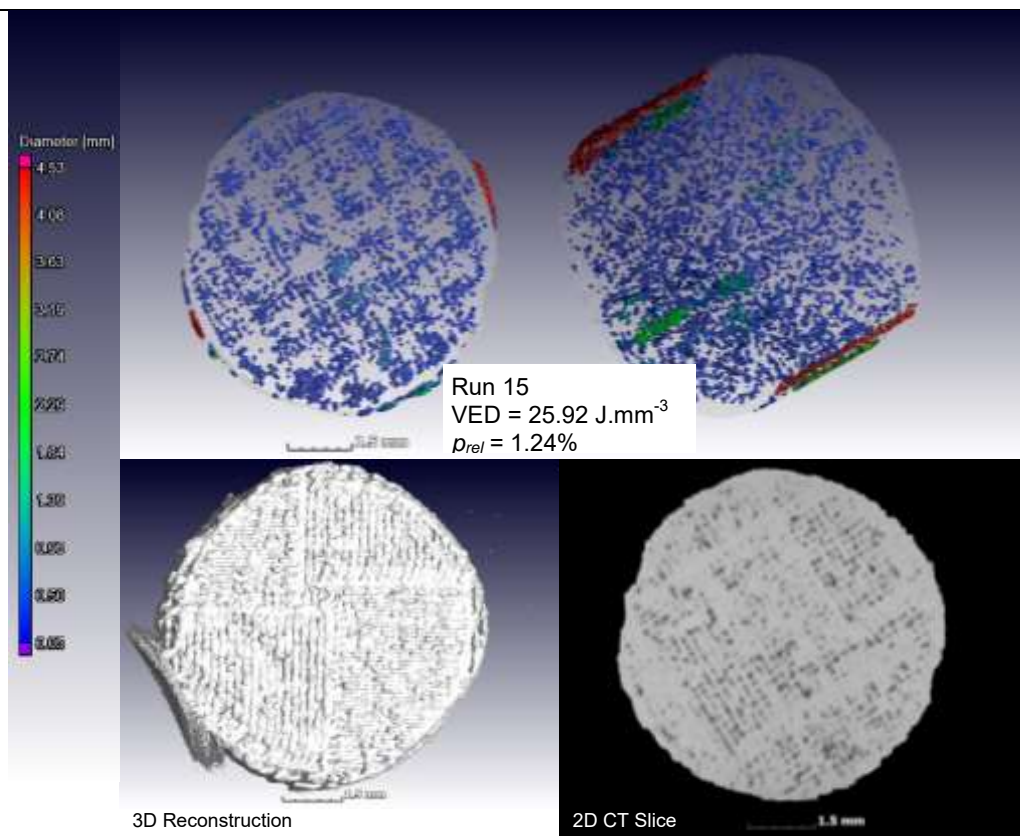












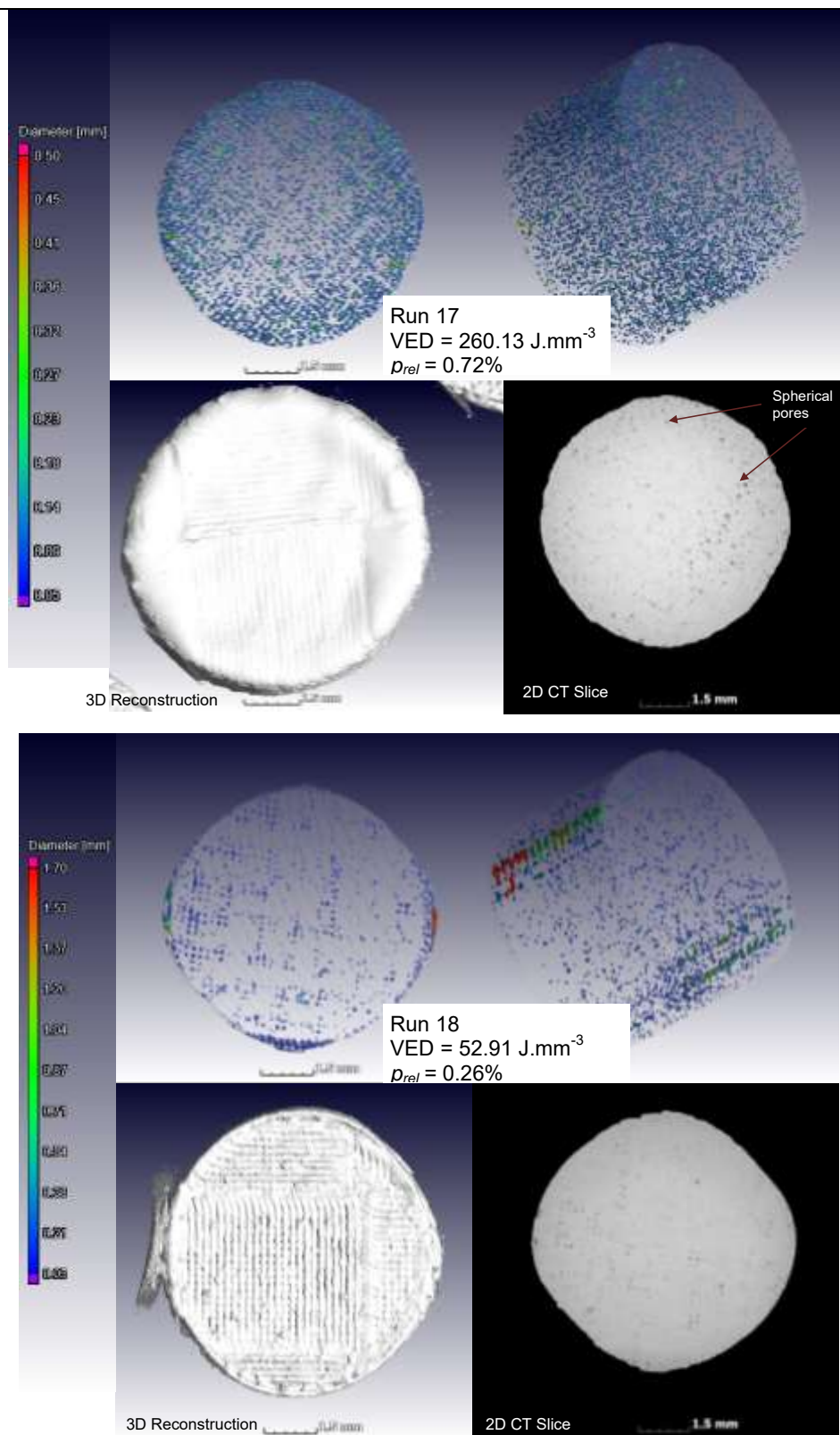
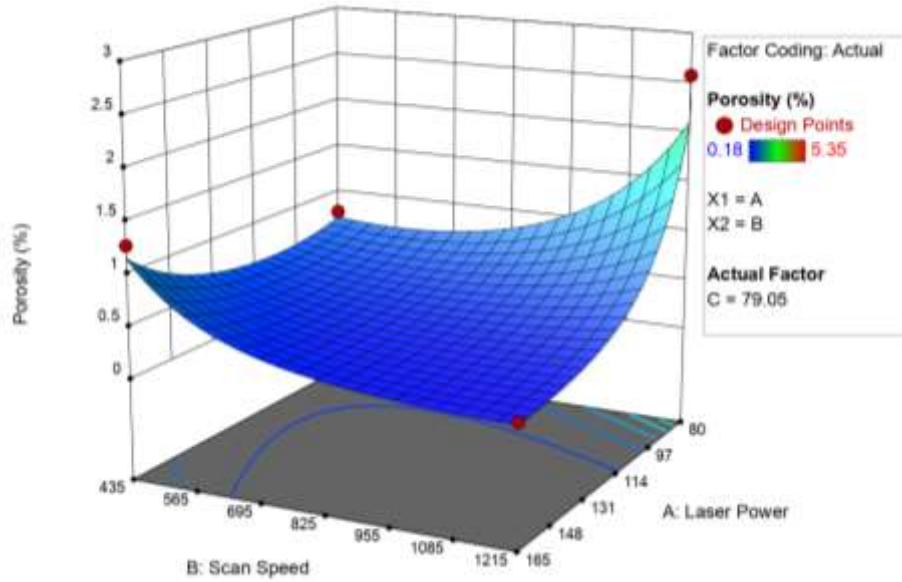
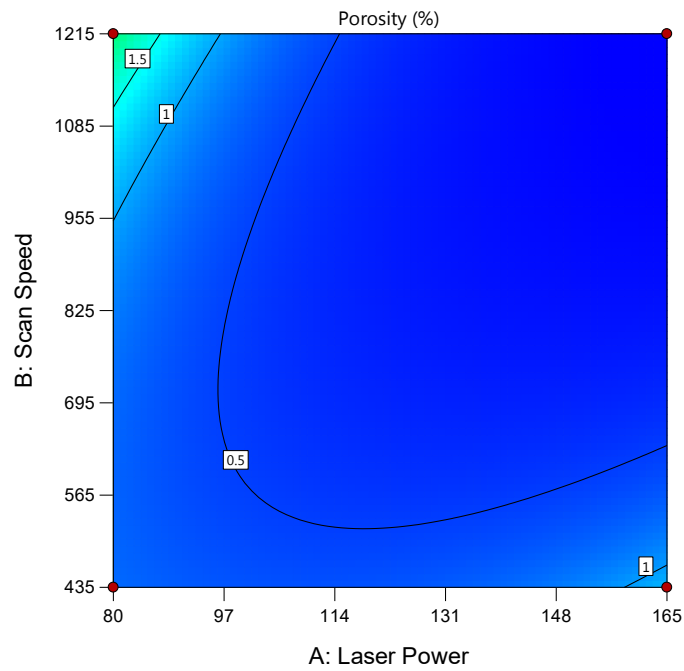


Figure C-1:  $\mu$ CT Porosity analysis of cylindrical specimens (Section 5.3)

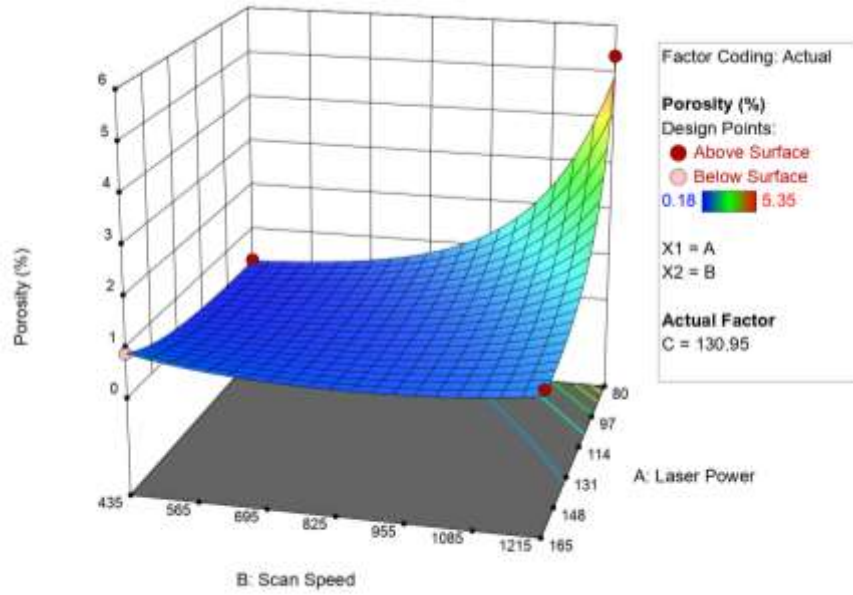
Response surfaces and contour plots for the quadratic model are presented below in Figure C-2. The responses are shown for the low and high level of hatch spacing (Factor C) respectively.



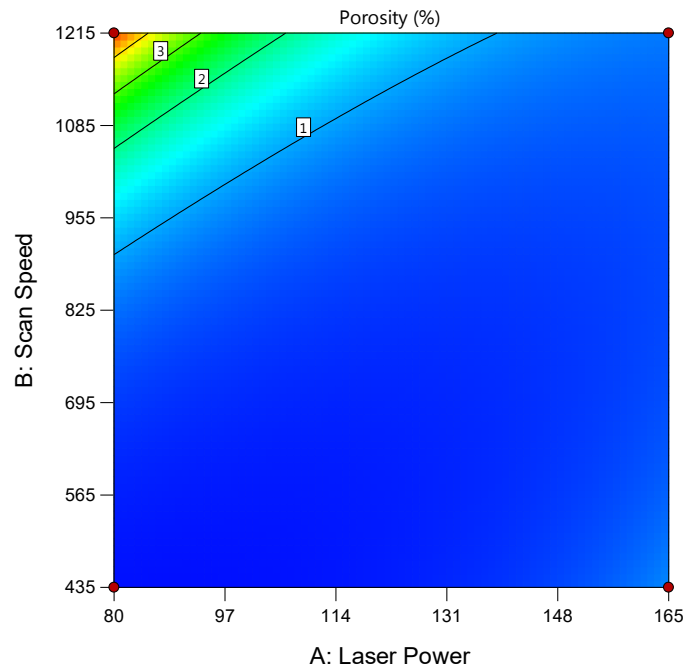
(a)



(b)



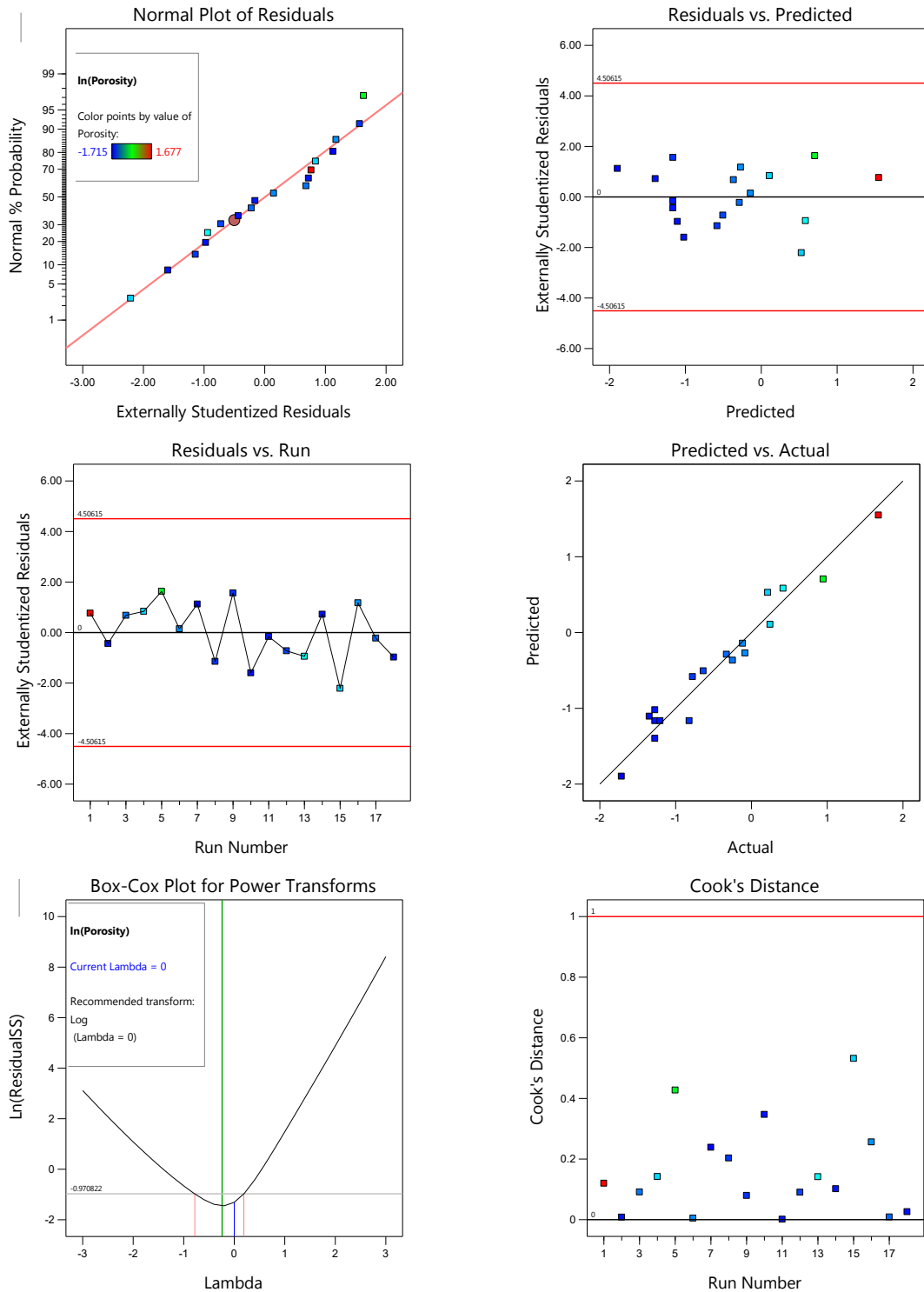
(c)

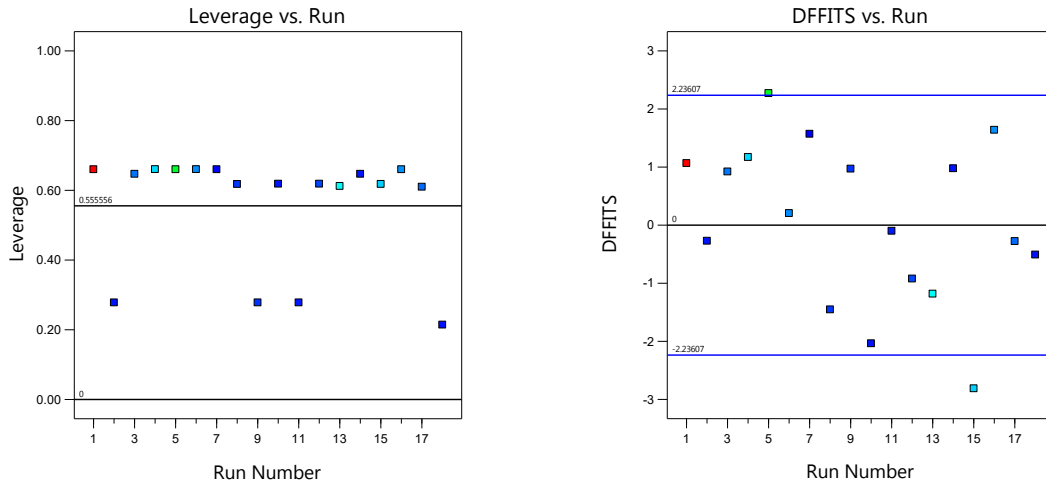


(d)

**Figure C-2: Response surfaces for the quadratic model with (a-b) the low level of hatch spacing and (c-d) the high level of hatch spacing**

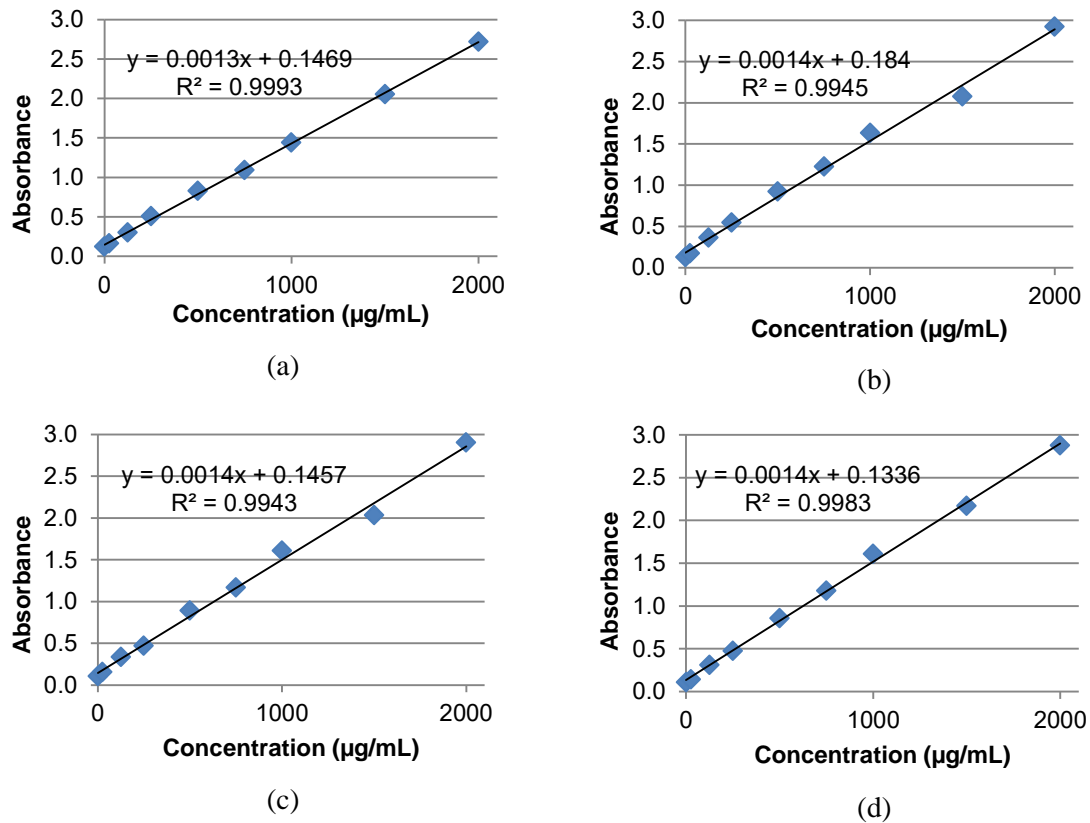
The diagnostic plots for the model fitting on the influences of the key LPBF process parameters on part porosity are presented in Figure C-3. All data points are coloured according to the legend of the *Normal Plot of Residuals* in the top left.

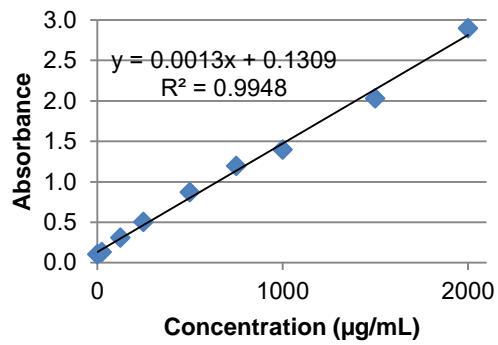




**Figure C-3: Diagnostic plots for quadratic model of porosity**

The calibration curves for the BCA vancomycin duplicate standard concentrations are presented for each analysis time point in Figure C-4





(e)

**Figure C-4: BCA assay calibration curves for a) 0 min, b) 15 min, c) 30 min, d) 45 min, and e) 60 min**

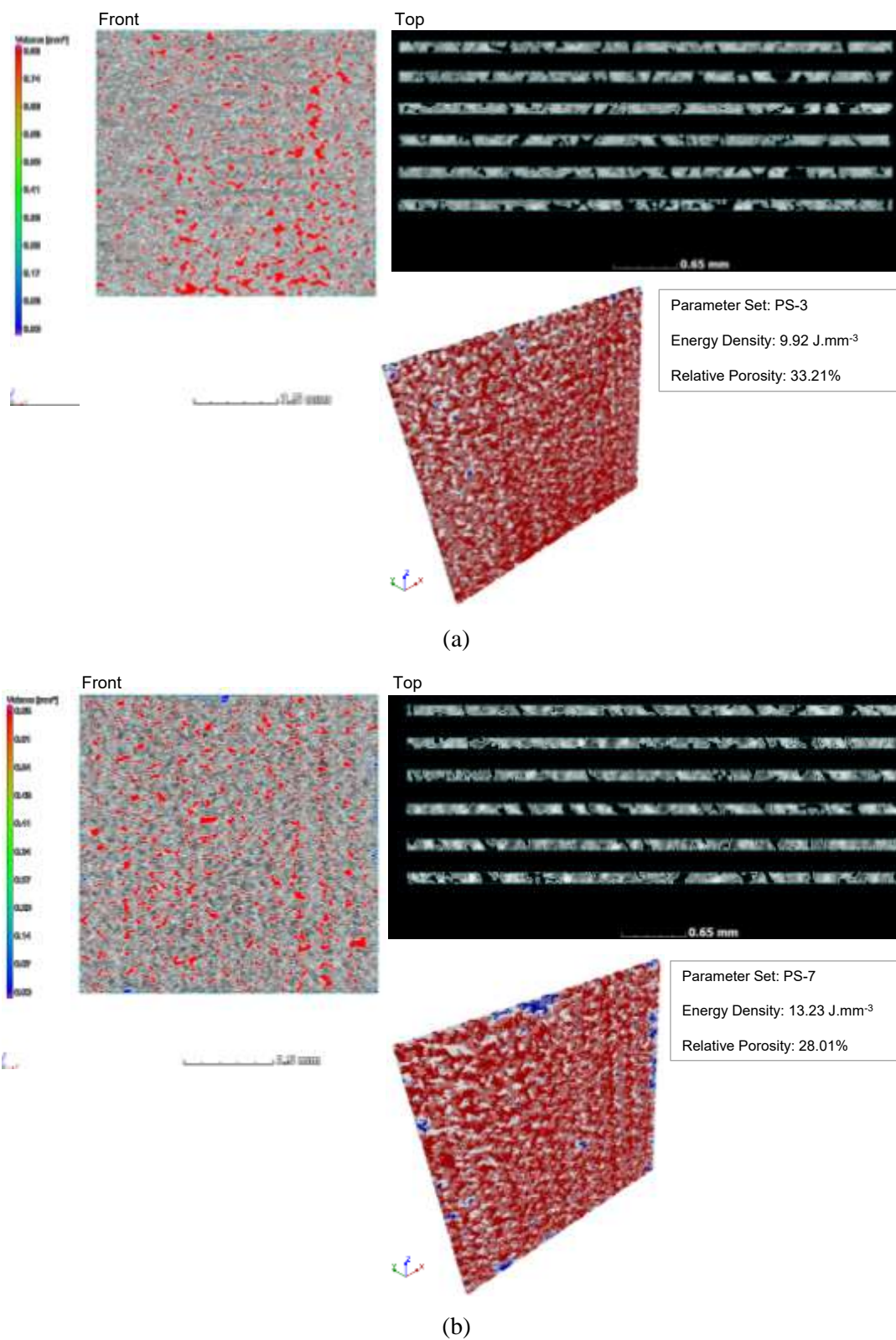
## Appendix D: PTWs for Vancomycin Release

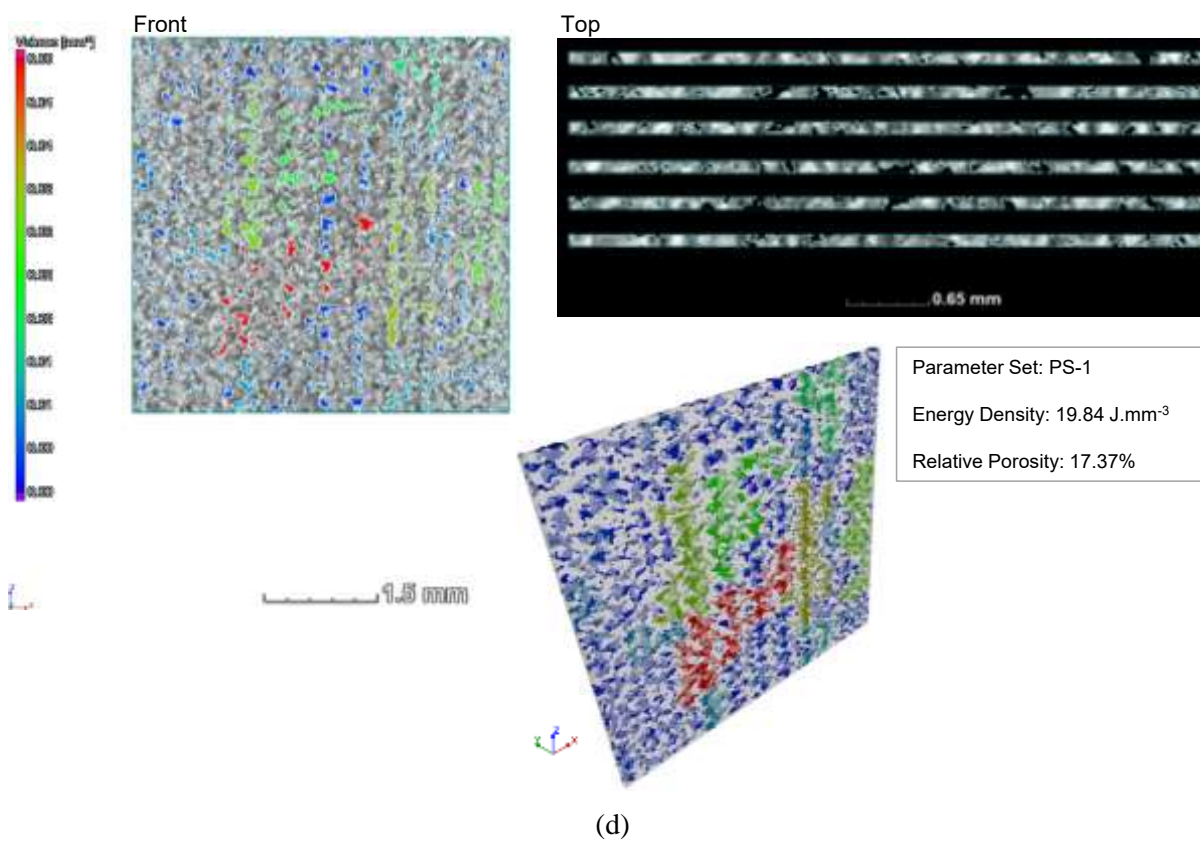
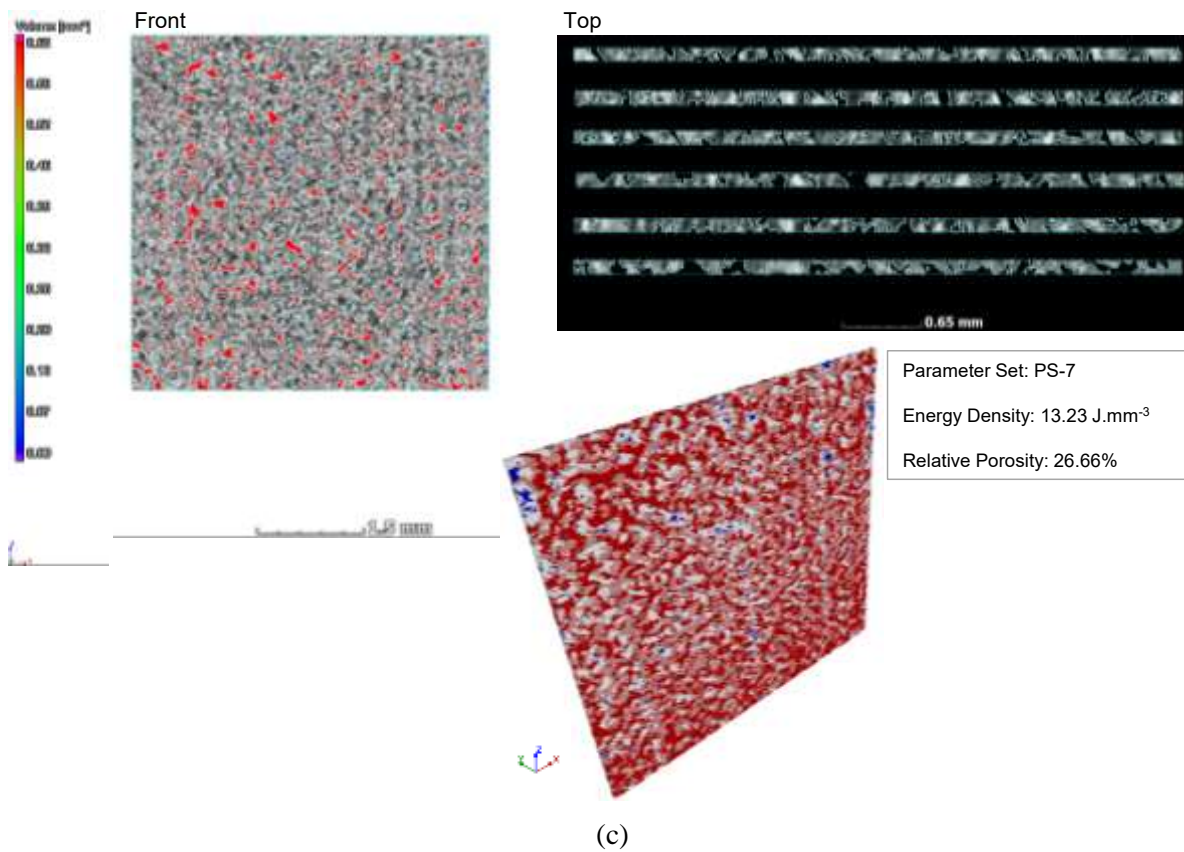
The measurements of the diameter and calculated area within the PVC masks used to standardise the contact area for the 400  $\mu\text{m}$  PTW reservoir vancomycin release are presented in Table D-1.

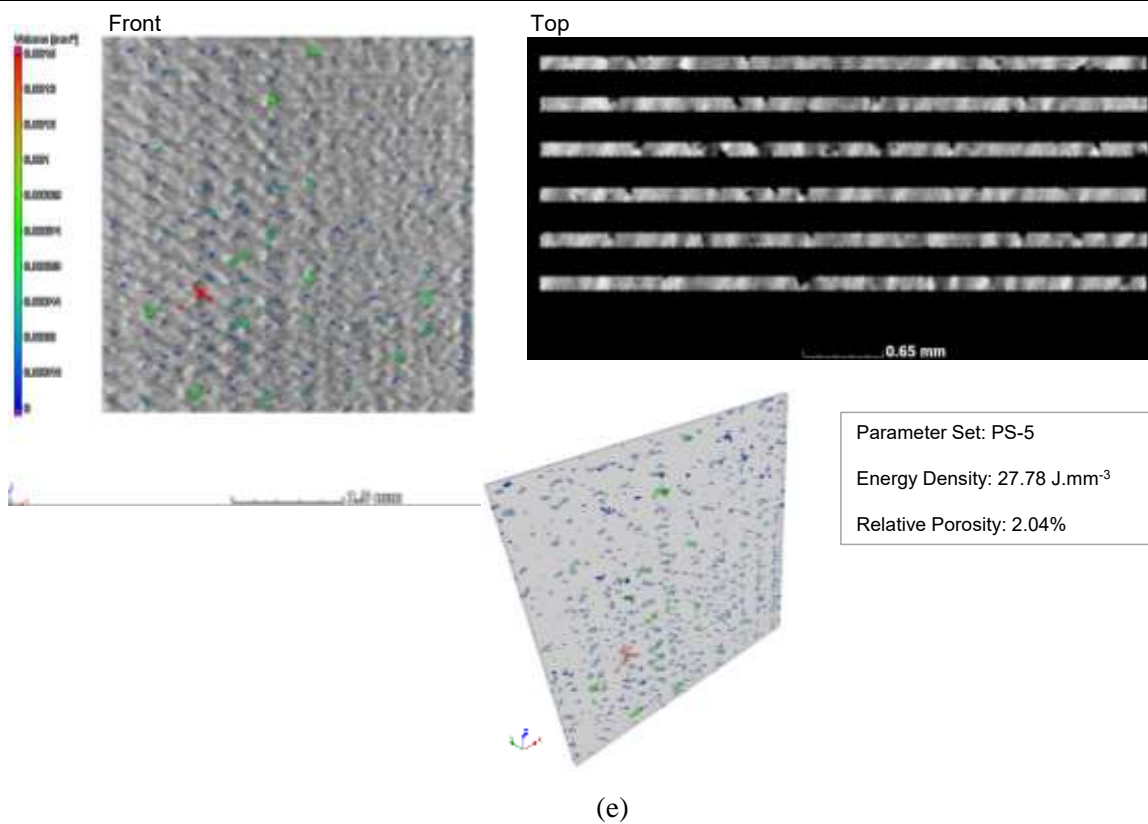
**Table D-1: Release contact area for permeable structures**

Reservoir	Diameter (mm)	Area (mm <sup>2</sup> )
D.	5.62	24.81
D..	5.61	24.72
D...	5.60	24.63
22	5.61	24.72
29	5.62	24.81
9	5.64	24.98
16	5.61	24.72
6	5.58	24.45
20	5.65	25.07
27	5.65	25.07
15	5.60	24.63
13	5.63	24.89
2	5.62	24.81
8	5.60	24.63
17	5.63	24.89
11	5.60	24.63
7	5.64	24.98
28	5.61	24.72
25	5.58	24.45
30	5.60	24.63
31	5.59	24.54
24	5.61	24.72
18	5.58	24.45
23	5.62	24.81
<b>Average</b>	<b>5.61</b>	<b>24.74</b>
<b>StdDev</b>	<b>0.02</b>	<b>0.18</b>

Images representing the relative porosity of 400  $\mu\text{m}$  PTWs CT-scanned for repeatability are presented in Figure D-1.

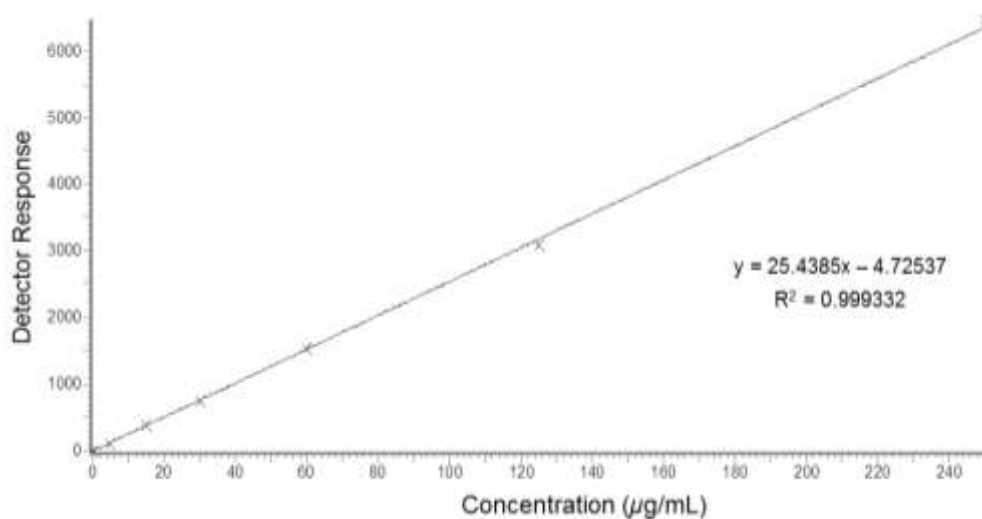






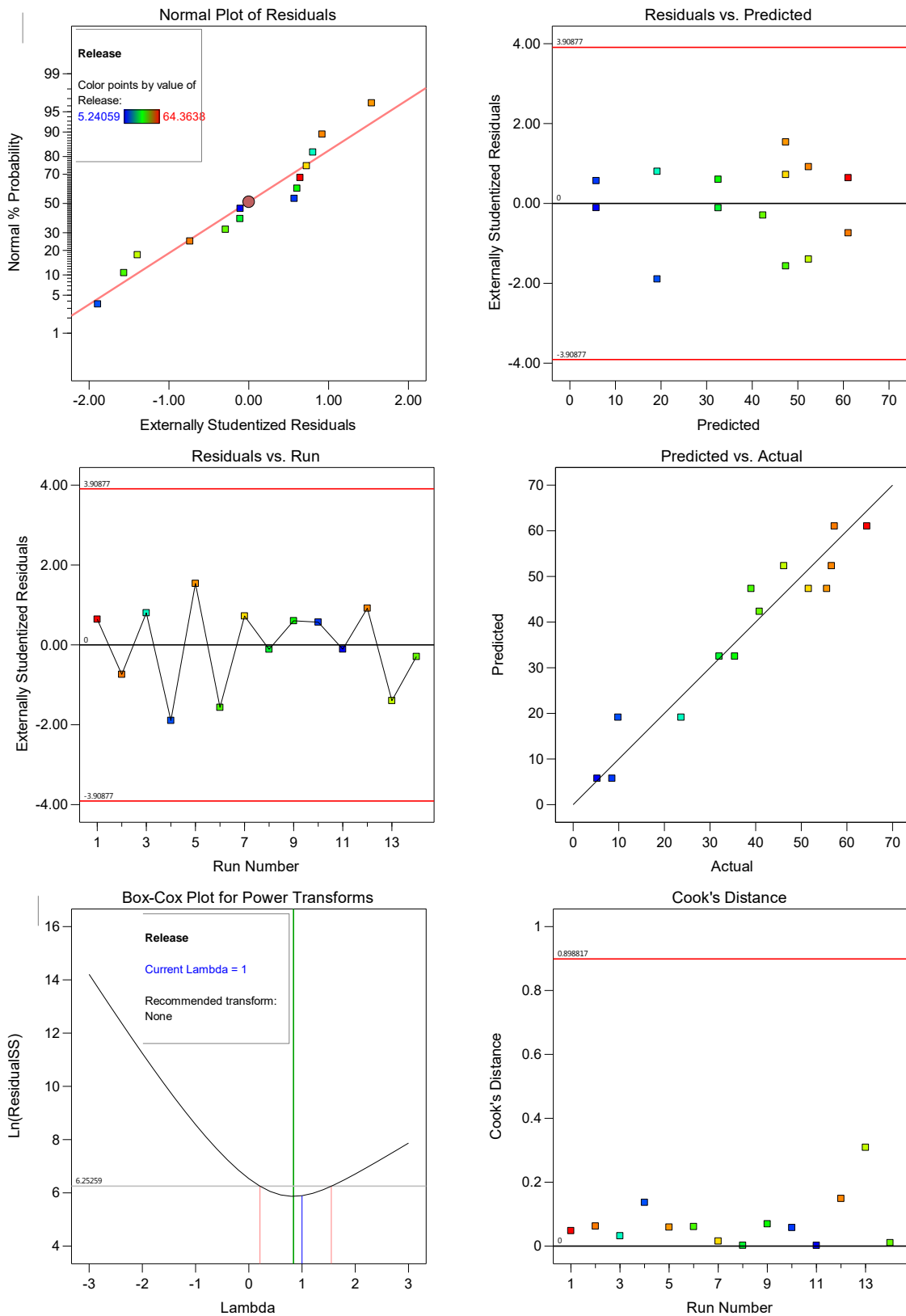
**Figure D-1: : Relative porosities of 400  $\mu\text{m}$  in order of ascending VED with (a) PS-3, (b) PS-7, (c) PS-7, (d) PS-1, and (e) PS-5**

The vancomycin RP-UHPLC calibration is shown in Figure D-2.



**Figure D-2: RP-UHPLC vancomycin calibration curve**

The diagnostic plots for two factor interaction the model fitting of the DoE investigation of vancomycin release across 400  $\mu\text{m}$  PTWs are presented in Figure D-3.



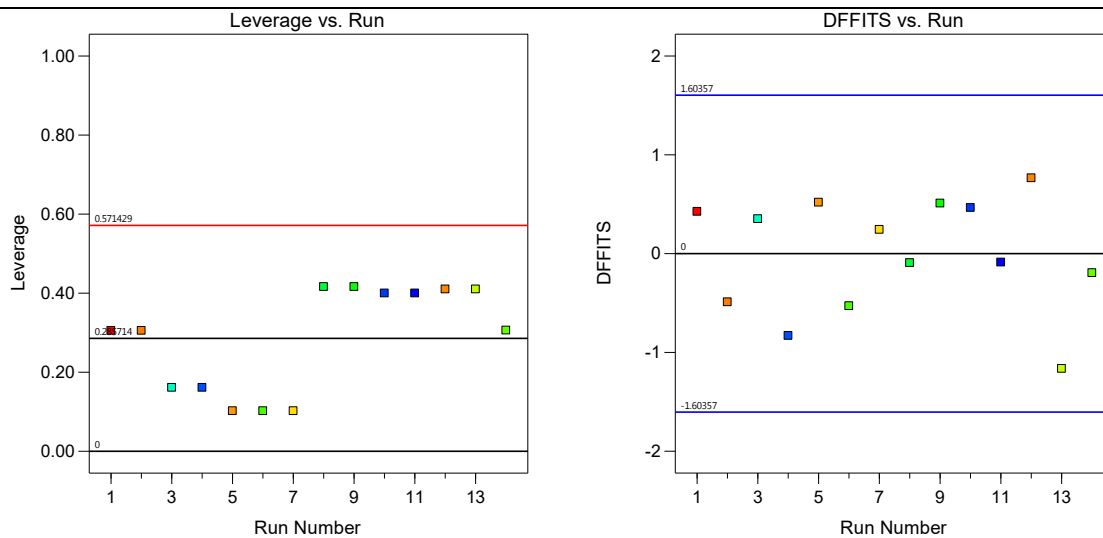


**Figure D-3: Diagnostic plots for two factor interaction model**

The vancomycin RP-HPLC calibration is shown in Figure D-4.

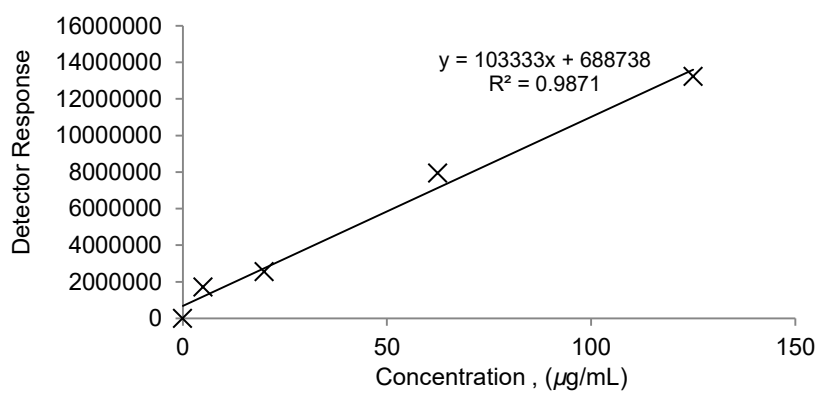
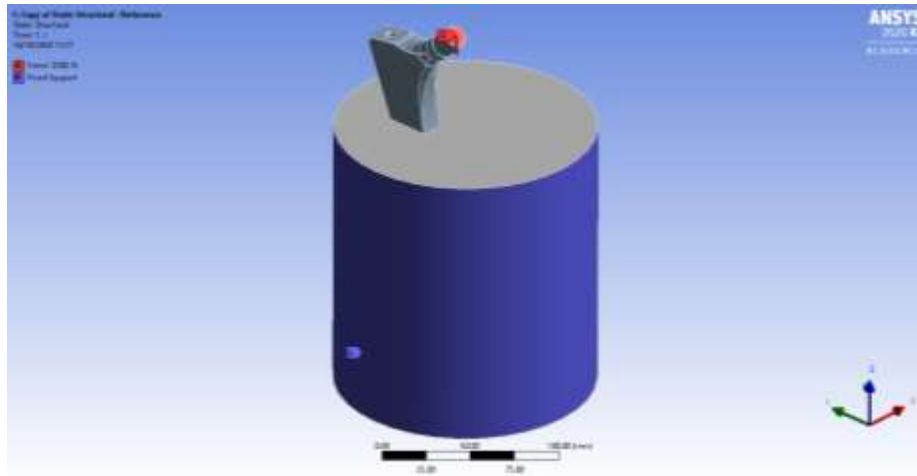


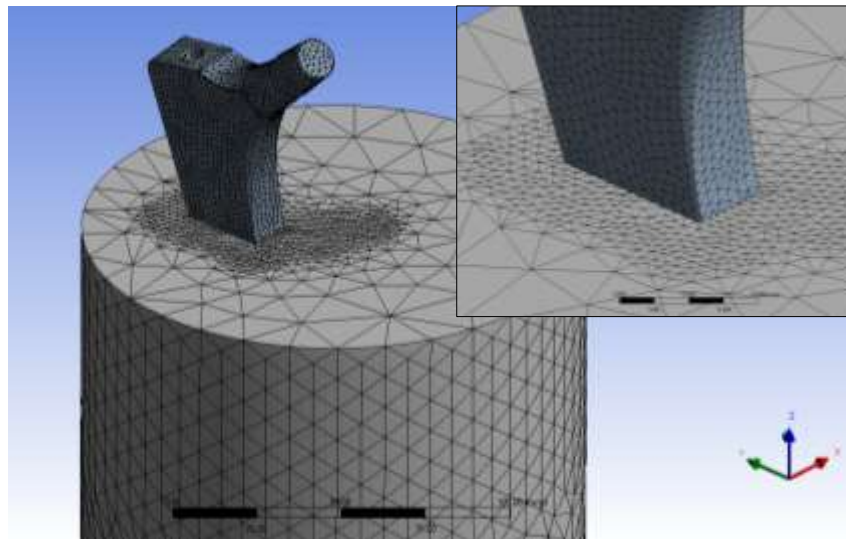
**Figure D-4: RP-HPLC vancomycin calibration curve**

## Appendix F: Prototype Design and Manufacturing

The orientation and load case applied to the reference stem model are presented in Figure F-1(a). Mesh refinement at the contact regions included reduction of element size and matching of the nodes of contacting elements between the two bodies (Figure F-1(b)). The resulting mesh consisted of 111,533 nodes and 70,470 elements.



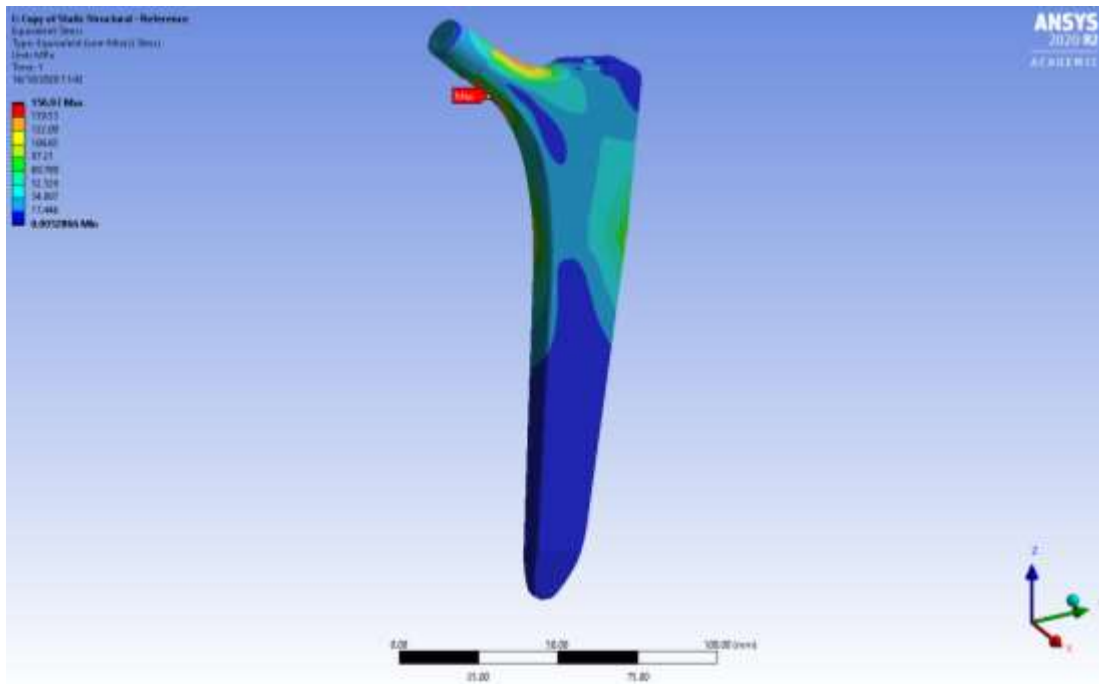
(a)



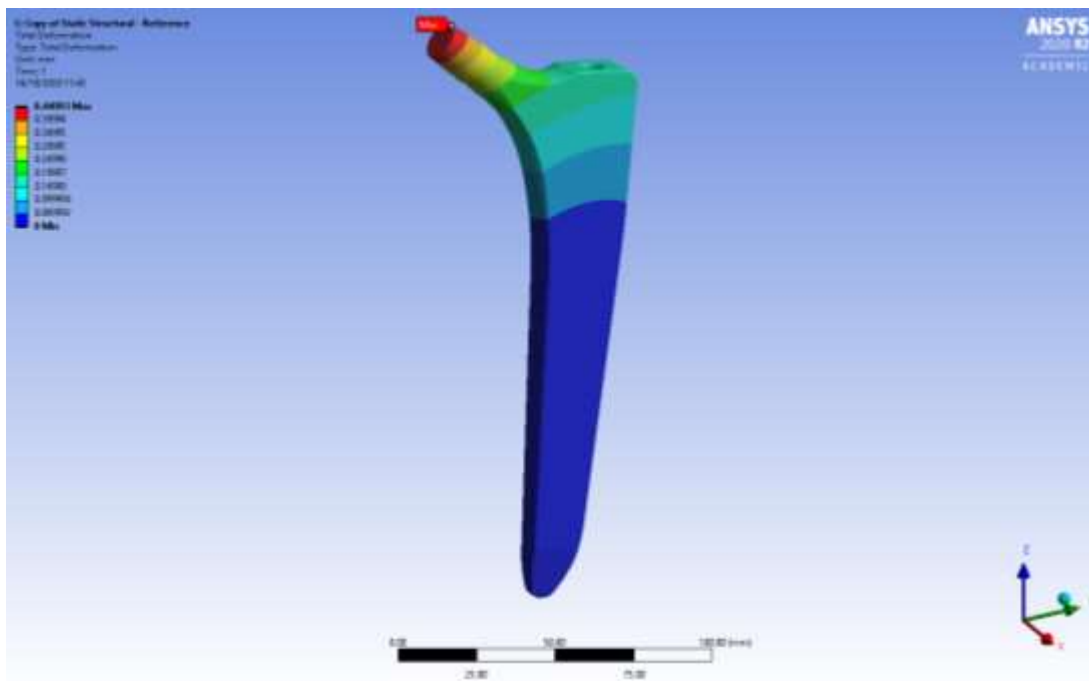
(b)

**Figure F-1: Static stress analysis setup for reference stem with (a) orientation, load, and boundary conditions and (b) mesh setup in ANSYS 2020 R2 with inset showing nodes matching at contact surfaces**

The von Mises equivalent stress and total deformation simulation results for the reference solid stem is presented in Figure F-2 below.



(a)



(b)

**Figure F-2: Simulation results for reference stem with (a) von Mises equivalent stress distribution and (b) the total deformation**